



**Institute of Cardiovascular Science &  
Great Ormond Street Hospital for Children  
University College London**

# Shape and function in congenital heart disease: a translational study using image, statistical and computational analyses

Submitted for the degree of Doctor of Philosophy  
University College London

**Jan Lukas Bruse**

SN: 13082317

Primary Supervisor:

Silvia Schievano, PhD

Secondary Supervisor:

Tain-Yen Hsia, MD

Tertiary Supervisor:

Andrew M. Taylor, MD

**London, April 2017**

All intellectual property rights are affiliated to the Institute of Cardiovascular Science,  
University College London. No liability is assumed for any content.

## Declaration of Originality

I, Jan Bruse, certify that the work presented in this thesis is solely my own work. I confirm that this work is original and that I only used the sources and means, which are mentioned throughout the thesis. Where information has been derived from other sources, I confirm that this has been indicated and that references are fully cited.

In particular, the presented clinical data from clinical reports stored at Great Ormond Street Hospital for Children, London, UK were collected and compiled with the help of Dr Hopewell Ntsinjana, Dr Elena Cervi, Dr Abbas Khushnood, Dr Catriona Baker and Dr Giuliano Giusti. Prof Andrew Taylor, Prof Tain-Yen Hsia and Dr Hopewell Ntsinjana performed expert scoring of shape abnormality. The multi-atlas automatic segmentation algorithm was provided by Dr Maria Zuluaga from the UCL Translational Imaging Group. The original algorithms of the statistical shape modelling framework were provided by Dr Kristin McLeod, Dr Maxime Sermesant and Dr Xavier Pennec from Inria Sophia-Antipolis, France.

---

Place, Date

---

Signature

## **Abstract**

While medical image analysis techniques are becoming technically more advanced, analysis of shape and structure in clinical practice is often limited to two-dimensional morphometry, neglecting potentially crucial three-dimensional (3D) anatomical information provided by the original images. This thesis aims at closing this gap by combining state-of-the-art medical image analysis, engineering and data analysis tools to elucidate relationships between 3D shape features and clinically relevant functional outcomes. In particular, patient cohorts affected by congenital heart disease were studied since shape and structure of the heart and its components are crucial for diagnosis, therapy and management of those patients.

At first, a statistical shape model was coupled with partial least squares regression to extract anatomical 3D shape biomarkers related to clinical parameters from cardiovascular magnetic resonance image data. After establishing a step-by-step protocol to guide the user with respect to parameter selection, results were shown to be in accordance with traditional morphometry as well as with clinical expert opinion. Novel aortic arch shape biomarkers relating to cardiac functional parameters were found in a cohort of patients post aortic coarctation repair (CoA). By combining statistical shape modelling results with computational fluid dynamics simulations, a mechanistic basis for the observed results was provided. Methods were then extended towards a hierarchical shape clustering framework, which achieved good unsupervised classification performance in a population of healthy and pathological aortic arch shapes. Applied to a cohort of CoA patients, previously unknown anatomical patterns were discovered.

This thesis demonstrates that combining medical image analysis and engineering tools with data mining and statistics provides a powerful platform to detect novel shape biomarkers and patient sub-groups. Results may ultimately improve risk-stratification, treatment-planning and medical device development, thereby promoting translation of advanced computational analysis techniques into clinical practice.

## Acknowledgements

First of all, I would like to sincerely thank my supervisors Silvia Schievano, Tain-Yen Hsia and Andrew Taylor for giving me the unique opportunity to be part of this research group. Your ideas and expertise, mentoring and trust were invaluable. It has been a great journey together.

I would like to extend my gratitude to my collaborators from Inria Sophia-Antipolis, Kristin McLeod, Maxime Sermesant and Xavier Pennec, who not only provided the core computational tool used in this work, but were most helpful and inspiring partners throughout. I would also like to thank Maria Zuluaga for being so kind to help me with the automatic segmentation algorithm and for her general support and input.

A large part of this work would not have been possible without the help of the fantastic clinical team at GOSH. Special thanks go to Hopewell Ntsinjana, Elena Cervi, Abbas Khushnood, Catriona Baker and Giuliano Giusti. Thanks for assisting me with data collection, for having great ideas and especially for being so open to new technologies. Further, I would like to thank Steven Kimberley for his reliable help.

A very big thank you goes to the Research Office team: Claudio, Giovanni, Giorgia, Benedetta, Daria, Emilie, Dilveer, Jakob; and also to the ones from “downstairs” Greg, Jenny and Vivek. Many thanks to all of you for being such bright, funny, kind and supportive colleagues and friends.

I wish to thank my family and friends at home for being such a strong backing along this way. Especially, I would like to thank my parents and my sisters, Katrin and Karoline, for their constant support and encouragement. Finally, I thank my wife Naiara for always being by my side – onena zara.

Vielen Dank.

This work has been funded by Fondation Leducq, Transatlantic Network of Excellence.

# Contents

<b>1</b>	<b>Introduction .....</b>	<b>14</b>
1.1	Tools to analyse shape and function .....	15
1.2	General objectives of this thesis .....	16
1.3	Outline of the thesis and questions to be answered by this work .....	18
<b>2</b>	<b>Background of phenomenological and mechanistic computational modelling: cardiac applications .....</b>	<b>22</b>
2.1	Basic concepts behind statistical shape modelling: parametric models .....	23
2.1.1	The computational atlas: the anatomical mean shape .....	23
2.1.2	Describing shape variability in 3D .....	25
2.2	Cardiac applications of SSM .....	27
2.3	Shape analysis of the aorta .....	29
2.3.1	Shape analysis of the healthy aorta .....	30
2.3.2	Shape analysis of the aorta in CoA .....	31
2.4	Mechanistic computational modelling .....	33
2.4.1	Mechanistic modelling of coarctation of the aorta .....	34
2.4.2	Combining mechanistic and phenomenological modelling .....	35
2.5	Summary .....	36
<b>3</b>	<b>Methods overview and processing pipeline .....</b>	<b>39</b>
3.1	Medical image data .....	41
3.2	Segmentation and anatomical reconstruction .....	41
3.2.1	Manual segmentation .....	42
3.2.2	Semi-automatic segmentation .....	43

3.2.3	Fully automatic segmentation .....	43
3.3	Meshing .....	44
3.4	Alignment .....	45
3.5	Morphometry – conventional shape analysis .....	46
3.6	A novel shape analysis method based on mathematical currents .....	48
3.6.1	Approaches to derive an anatomical mean or template shape .....	50
3.6.2	A framework based on mathematical currents .....	51
3.6.3	Defining the transformation function .....	55
3.6.4	Computing the template .....	56
3.7	Data processing of SSM results: supervised and unsupervised approaches ...	58
3.7.1	Unsupervised principal component analysis (PCA) .....	59
3.7.2	Supervised partial least squares regression (PLS) .....	60
3.7.3	Hierarchical clustering for sub-group detection .....	63
3.8	Clinical and functional parameters .....	63
3.8.1	Cardiac function .....	64
3.8.2	Ejection fraction .....	64
3.8.3	Left ventricular mass and left ventricular hypertrophy .....	65
3.8.4	Blood pressure and hypertension .....	66
3.8.5	Body surface area .....	66
3.9	Modelling fluid flow via computational fluid dynamics (CFD) .....	67
3.9.1	Fluid mechanics equations .....	67
3.9.2	Computational fluid dynamics simulations .....	69
3.9.3	Three-dimensional volume meshes for domain discretisation .....	70
3.9.4	Post-processing of CFD results .....	71
3.10	Summary .....	71

## **4 Extracting three-dimensional shape biomarkers from medical images ..... 72**

4.1	Abstract .....	73
4.2	Introduction.....	74
4.3	Methods .....	75
4.3.1	Patient population, image data and 2D morphometry .....	76
4.3.2	Pre-processing.....	77
4.3.3	Post-processing .....	85
4.3.4	Statistical analysis .....	88
4.4	Results .....	89
4.4.1	Computed template and validation .....	89
4.4.2	Shape patterns associated with differences in BSA.....	91
4.4.3	Shape patterns associated with differences in LVEF .....	94
4.5	Discussion .....	96
4.5.1	Detailed analysis of the identified correlations .....	98
4.5.2	Limitations and future work.....	99
4.6	Summary.....	100

## **5 Comparing computed statistical shape modelling results with clinical expert opinion ..... 102**

5.1	Abstract .....	103
5.2	Introduction.....	104
5.3	Methods .....	105
5.3.1	Patient population .....	105
5.3.2	Image processing and pre-processing of the surface models .....	105

5.3.3	Expert assessment of the aortic arch shapes .....	105
5.3.4	Control template and transformations towards CoA subject shapes ....	106
5.3.5	Analysing the transformations using PLS and PCA .....	107
5.4	Results .....	108
5.4.1	Control template .....	108
5.4.2	PLS and PCA results .....	109
5.4.3	Comparison of expert ranking with SSM results.....	111
5.5	Discussion .....	112
5.6	Summary.....	113

## **6 Aortic arch shape and function post coarctation repair: deriving 3D shape biomarkers ..... 115**

6.1	Abstract .....	116
6.2	Introduction.....	117
6.3	Methods .....	118
6.3.1	Patient population .....	118
6.3.2	Functional parameters.....	119
6.3.3	Segmentation and pre-processing.....	119
6.3.4	Statistical shape analysis method .....	120
6.3.5	Traditional 3D morphometrics.....	121
6.3.6	Statistical analysis .....	121
6.4	Results .....	122
6.4.1	Template aortic arch .....	122
6.4.2	Correlations of arch shape features with ejection fraction.....	122
6.4.3	Correlation of arch shape features with left ventricular mass .....	123

6.4.4	Correlation of arch shape features with resting blood pressure.....	124
6.5	Discussion .....	125
6.5.1	Associations between aortic arch shape features and CMR-derived functional parameters .....	125
6.5.2	Arch shape features and blood pressure response .....	127
6.5.3	Limitations and future work.....	128
6.6	Summary.....	129

## **7 Joint phenomenological and mechanistic computational modelling: CFD simulations on computed shape modes ..... 130**

7.1	Abstract .....	131
7.2	Introduction.....	132
7.3	Methods .....	134
7.3.1	Input shapes.....	134
7.3.2	Volume meshing .....	135
7.3.3	Boundary conditions .....	135
7.4	Results .....	137
7.5	Discussion .....	138
7.5.1	Limitations and future work.....	140
7.6	Summary.....	141

## **8 Detecting meaningful anatomical shape clusters: metrics analysis for hierarchical clustering of aortic arch shapes ..... 143**

8.1	Abstract .....	144
8.2	Introduction.....	145
8.3	Methods .....	147
8.3.1	Patient population .....	148
8.3.2	Segmentation and registration .....	148
8.3.3	Template and deformation matrix computation.....	149
8.3.4	Morphometric analysis and PCA.....	149
8.3.5	Hierarchical clustering.....	150
8.3.6	Clustering classification performance measures .....	153
8.3.7	Validation of clustering results .....	155
8.3.8	Statistical analysis .....	156
8.4	Results .....	156
8.4.1	Segmentation .....	156
8.4.2	Comparison of traditional shape parameters.....	156
8.4.3	PCA of 3D shape features.....	158
8.4.4	Determining best performing input and distance/linkage combination	159
8.4.5	Analysis of best performing distance/linkage combination .....	161
8.4.6	Subgroup analysis – clusters within clusters .....	162
8.5	Discussion .....	164
8.5.1	Optimal distance metric and linkage function.....	164
8.5.2	Classification performance .....	165
8.5.3	Subgroup detection.....	166
8.5.4	Limitations and future work.....	166
8.6	Summary.....	167

## **9 Hierarchical clustering applied to a patient population of repaired coarctation ..... 169**

9.1	Abstract .....	170
9.2	Introduction.....	171
9.3	Methods .....	172
9.3.1	Patient population and image processing .....	172
9.3.2	Hierarchical clustering analysis .....	173
9.3.3	Statistical analysis .....	173
9.4	Results .....	173
9.5	Discussion .....	177
9.5.1	Limitations and future work.....	179
9.6	Summary.....	180

## **10 Conclusions and future work ..... 181**

10.1	Contributions overview .....	182
10.2	Detailed contributions and outcomes.....	183
10.3	Limitations and future work.....	188
10.3.1	Sample size and patient populations .....	188
10.3.2	Automation and parameter setting .....	189
10.3.3	Post-processing of the data .....	190
10.4	Final remarks .....	191

## **11 Bibliography ..... 193**

## **12 List of publications arising during this thesis ..... 211**

12.1	Peer reviewed journal articles directly related to this work.....	211
------	---	-----

12.2	Peer reviewed journal articles not directly related to this work .....	212
12.3	Peer reviewed conference publications directly related to this work.....	213
<b>13</b>	<b>Copyright permissions .....</b>	<b>216</b>

## List of Figures

Fig. 1.1: Example of shape variability in CHD. Aortas of different adolescent patients post aortic coarctation repair .....	16
Fig. 1.2: Three-dimensional model of the aorta of a healthy subject (left) and of a patient post aortic coarctation (CoA) repair .....	18
Fig. 2.1: DIKW pyramid, adapted from (Frangi et al., 2016) .....	23
Fig. 2.2: Landmarks and point-to-point correspondence in 3D surface models of the left ventricle; apex marked.....	24
Fig. 2.3: General statistical shape modelling (SSM) pipeline from segmentation of the structure of interest to anatomical mean shape (template) computation and 3D shape variability description via principal component analysis (PCA), adapted from (Biglino et al., 2017) © 2017 BMJ Publishing Group Ltd .....	27
Fig. 2.4: Segmented 3D model of the aorta with annotations .....	29
Fig. 2.5: Aortic arch measurements and arch shape classification into three phenotypes, adapted from (Ou et al., 2004), © 2004 Oxford University Press .....	31
Fig. 2.6: : Image-based mechanistic modelling pipeline from image data to simulation results, adapted from (MacLeod et al., 2009) .....	34
Fig. 2.7: Shape variability in subjects with CHD makes landmarking difficult, adapted from (Bruse et al., 2016a) .....	37
Fig. 3.1: Modelling pipeline adopted in this thesis .....	39
Fig. 3.2: Segmentation of the aorta and the left ventricle from CMR images.....	42
Fig. 3.3: Semi-automatic segmentation in ITKSnap using seed points and snakes algorithm, respective 3D models shown below.....	43
Fig. 3.4: Automatic segmentation results before (red) and after (green) manual cleaning. Both segmentation labels and obtained 3D models are shown .....	44
Fig. 3.5: 3D surface mesh of a reconstructed aortic arch .....	45
Fig. 3.6: Alignment (rigid registration) of surface meshes.....	46
Fig. 3.7: Manual measurements of aortic arch height A and width T on CMR image slices in MIMICS (Materialise, Leuven, Belgium).....	47

Fig. 3.8: 3D morphometric parameters describing aortic arch shape, adapted from (Bruse et al., 2016a) .....	47
Fig. 3.9: Mathematical transformations $\phi$ define the shape of fishes, adapted from (Thompson, 1945) .....	49
Fig. 3.10: Laser beam probes arch surface mesh to obtain shape representation in the space of currents, adapted from (Bruse et al., 2016a) .....	52
Fig. 3.11: Effect of kernels to capture features of a distribution (coarse to smooth) adapted from (Izenman, A. J., 2008).....	53
Fig. 3.12: Dirac delta currents as shape representations and moment (deformation) vectors $\beta$ defined on currents drive the transformations, adopted from (Mansi et al., 2011), © 2011 IEEE .....	54
Fig. 3.13: Shape model of an aorta represented by currents; changing resolution $\lambda_w$ , adapted from (Bruse et al., 2016a) .....	54
Fig. 3.14: Each subject shape is uniquely parameterised by its deformation function $\phi$ ; all deformations concatenated in a matrix describe all 3D shape information within the population, adapted from (Bruse et al., 2017a) .....	55
Fig. 3.15: Shape data processing via PLS regression for visual and numerical shape feature extraction, adapted from (Bruse et al., 2016a).....	62
Fig. 3.16: Cross-section of centreline-adapted 3D volume mesh from VMTK .....	70
Fig. 4.1: Pre-processing steps required to prepare segmented arch models for subsequent 3D statistical shape analysis, adapted from (Bruse et al., 2016a) .....	75
Fig. 4.2: Higher or lower surface mesh resolution does not change the computed template shape .....	78
Fig. 4.3: Surface error compared to high resolution mesh relative to average surface mesh cell density.....	79
Fig. 4.4: Twenty input surface models of aortic arch shapes post CoA repair, adapted from (Bruse et al., 2016a) .....	79
Fig. 4.5: Different resolution $\lambda_w$ and stiffness $\lambda_v$ parameters result in different template shapes .....	81
Fig. 4.6: Influence of the $\lambda$ parameters on transformations of cylindrical shapes.....	82

Fig. 4.7: Influence of the $\lambda$ parameters on the template computation time.....	83
Fig. 4.8: Visual representation of the proposed understanding of the $\lambda$ parameters as covering a certain percentage of the arch surface area .....	84
Fig. 4.9: Setting $\lambda_V$ too small yields too local deformations, adapted from (Bruse et al., 2016a) .....	85
Fig. 4.10: Computed template shape (blue) based on the twenty input CoA models, adapted from (Bruse et al., 2016a) .....	90
Fig. 4.11: Arch shape features associated with low (-2SD) and high (+2SD) values of BSA represented by deforming the template shape along the computed BSA shape mode (a) and respective correlation between BSA shape vector and BSA, adapted from (Bruse et al., 2016a).....	92
Fig. 4.12: Shape features associated with LVEF shape mode deforming the template from low to high LVEF, adapted from (Bruse et al., 2016a) .....	94
Fig. 4.13: Correlation between LVEF shape vector and LVEF and comparison of shape features shown by the LVEF shape mode and actual patient shapes associated with low and high values of the LVEF shape vector, patients in line with PLS shape modes marked in green, outlying shapes marked in red. Adapted from (Bruse et al., 2016a).....	99
Fig. 5.1: Computed Control template aortic arch shape from different views (a-c) and cross-validated template shapes overlaid (d), adapted from (Bruse et al., 2016b) .....	109
Fig. 5.2: Distributional differences between Control and CoA PLS shape vector entries (** marks statistical significance at level $p < .01$ ), adapted from (Bruse et al., 2016b) .....	110
Fig. 5.3: Computed shape abnormality ranking from low (blue) to high (red) abnormality according to PLS shape vector results, adapted from (Bruse et al., 2016b).....	110
Fig. 5.4: Correlations between computed PLS shape vector and clinical expert ranking, outlying shape CoA12 marked (arrow), adapted from (Bruse et al., 2016b) .....	111
Fig. 5.5: Outlying shape CoA 12 with challenging arch shape features (narrowed transverse arch and indentation).....	113
Fig. 6.1: Input shape population of 53 aortic arch surface models and computed template shape (blue), adapted from (Bruse et al., 2017b) .....	118

Fig. 6.2: Arch shape features associated with low and high LVEF as represented by LVEF shape mode deformations (left) and respective correlations between patient-specific shape vector values and LVEF, adapted from (Bruse et al., 2017b) .....	123
Fig. 6.3: Arch shape features associated with low and high iLVM (left) and respective correlations between shape vector and iLVM, adapted from (Bruse et al., 2017b) ....	124
Fig. 6.4: Aortic arch shape features associated with low and high systolic resting BP (left) and respective correlations between PLS shape vector and BP, adapted from (Bruse et al., 2017b).....	124
Fig. 7.1: Computed arch shape features associated with low or high values of cardiac functional parameters as determined in previous chapter, adapted from (Bruse et al., 2017b) .....	132
Fig. 7.2: Definition of inflow and outflow boundaries for CFD simulations .....	134
Fig. 7.3: Power loss relative to average volume mesh cell density for mesh independence study.....	135
Fig. 7.4: Velocity encoded streamlines computed for the high/low arch shape cases derived by PLS in the previous chapter .....	137
Fig. 8.1: Representative arch shape models from each of the included cohorts .....	148
Fig. 8.2: Differences of aortic arch size (a-c) and shape (d-f) morphometric parameters between the three groups CTRL, COA and ASO, adapted from (Bruse et al., 2017c) ..	157
Fig. 8.3: PCA shape modes and shape vector differences between the three groups (a-c). Plotting the first two PCA modes against each other revealed clear grouping within the data according to primary diagnosis (d), adapted from (Bruse et al., 2017c).....	159
Fig. 8.4: Clustering classification performance in terms of F-score (a) and MCC (b) over 10 cross-validation runs for PCA dataset (light blue, left) and full deformation data. Only the respective best performing distance metric/linkage function is shown, adapted from (Bruse et al., 2017c) .....	160
Fig. 8.5: Means and 95CIs of all computed clustering classification performance measures for best performing Correlation distance metric / Weighted linkage function combination, adapted from (Bruse et al., 2017c).....	161

Fig. 8.6: Dendrogram obtained with the Correlation/Weighted distance/linkage combination on the full deformation dataset of 60 arch shapes. Cutting the dendrogram horizontally revealed known clusters (a) and novel subgroups (b), adapted from (Bruse et al., 2017c).....	163
Fig. 8.7: Scatterplot of PCA shape vector entries for modes 1 and 2 revealed that patients with similar 3D arch shape were grouped together by both PCA and the clustering algorithm (individual patients are symbol-coded according to subgroups obtained from cutting the dendrogram as in Fig. 8.6b), adapted from (Bruse et al., 2017c) .....	164
Fig. 9.1: Clustering dendrogram of 67 aortic arch shapes post CoA repair. Horizontal cutting revealed six larger shape clusters.....	174
Fig. 9.2: Distributional differences in morphometric parameters between the six derived arch shape groups from hierarchical clustering from Fig. 9.1 (** marks statistical significance at level $p<.01$ ; * at level $p<.05$ ) .....	175
Fig. 9.3: Distributional differences of cardiac functional parameters LVEF and systolic resting BP between the six derived shape clusters from Fig. 9.1 (* marks statistical significance at level $p<.05$ ).....	176
Fig. 9.4: Distributional differences of cardiac functional parameters iLVM and MVR between the six derived shape groups from Fig. 9.1.....	177
Fig. 9.5: Six CoA anatomical shape groups derived by the hierarchical clustering pipeline, see dendrogram in Fig. 9.1.....	178

## List of Tables

Tab. 3.1: Normal, averaged values for CMR-derived LVEF and iLVM for children aged 8 to 20 years. Data taken from (Sarikouch et al., 2010) .....	66
Tab. 4.1: Included 2D and 3D morphometric shape descriptors, adapted from (Bruse et al., 2016a).....	77
Tab. 4.2: Influence of the surface mesh resolution and resolution and stiffness parameters $\lambda_w$ and $\lambda_v$ on template computation runtime and template shape. $\uparrow$ denotes increase, $\downarrow$ decrease and $\uparrow \downarrow$ denotes an unpredictable change, adapted from (Bruse et al., 2016a) .....	82
Tab. 4.3: Comparison of computed mean population shape descriptors and respective template shape descriptors, adapted from (Bruse et al., 2016a).....	91
Tab. 4.4: Correlations between BSA, BSA Shape Vector, demographic and geometric parameters, adapted from (Bruse et al., 2016a) .....	93
Tab. 4.5: Correlations between LVEF, LVEF Shape Vector, demographic and geometric parameters, adapted from (Bruse et al., 2016a) .....	95
Tab. 5.1: Correlations between clinical expert shape ranking, computed PLS and PCA abnormality scores and traditionally used shape descriptors, adapted from (Bruse et al., 2016b) .....	112
Tab. 6.1: Detailed clinical information about the included patient cohort post CoA repair for shape biomarker extraction, adapted from (Bruse et al., 2017b) .....	119
Tab. 6.2: Correlations between functional parameters and respective computed PLS shape vectors, adapted from (Bruse et al., 2017b) .....	125
Tab. 7.1: Differences between computed hemodynamic parameters for respective PLS shape mode arch shapes associated with high or low functional parameters. Functional parameters associated with unfavourable cardiac function is highlighted in red; more favourable function in green.....	138
Tab. 8.1: Confusion matrix for unsupervised hierarchical clustering classification performance, adapted from (Bruse et al., 2017c) .....	162
Tab. 9.1: Detailed information about the included patient cohort post CoA repair for anatomical shape clustering .....	172

## List of Abbreviations

BCC	Brachiocephalic Artery
BP	Blood Pressure [mmHg]
BSA	Body Surface Area [m <sup>2</sup> ]
CHD	Congenital Heart Disease
CMR	Cardiovascular Magnetic Resonance
CoA	Coarctation of the Aorta
CT	Computed Tomography
ICP	Iterative Closest Point Algorithm
LCC	Left Common Carotid Artery
LDDMM	Large Deformation Diffeomorphic Metric Mapping
LSC	Left Subclavian Artery
LV	Left Ventricle
LVEF	Left Ventricular Ejection Fraction [%]
LVM	Left Ventricular Mass [g]
MVR	Mass to Volume Ratio [g/ml]
PCA	Principal Component Analysis
PDM	Point Distribution Model
PLS	Partial Least Squares Regression
SSM	Statistical Shape Model or Statistical Shape Modelling

## Nomenclature

This thesis outlines methods for analysing three-dimensional shape using medical image data. In current literature, many different terms associated with shape are used in various contexts. In order to guide the Reader, the following section briefly describes some of the most commonly used terminology and their mere definition based on the Oxford Dictionary. (Oxford University Press, 2014)

Starting from the most basic terms, “size” describes the *relative extent*, the *overall dimension* or magnitude of an object. “Form” is a particular way in which an object *exists or appears* and “shape” more specifically refers to its *external form, contours or outline*. A “structure” is defined as the *arrangement of and relations between components of something complex*. Note that the terms form, shape and structure are often used synonymously. (Oxford University Press, 2014)

The term “anatomical” relates to a *bodily structure* and “anatomy” is the *branch of science concerned with the bodily structure of humans* and other living organisms, as revealed by *dissection and separation of its components*. “Morphology” is the study of the form of objects and in particular the branch of biology or medicine that looks at the form (or shape) of living organisms and at the relationship between their structures. Morphology is sometimes used as a synonym for combining form, shape and structure. “Morphometry” characterises the *process of measuring the external shape* and dimensions of objects or living organisms. (Oxford University Press, 2014)

## 1 Introduction

Congenital heart disease (CHD) or congenital cardiovascular defects are structural cardiac defects that are present at birth. In CHD, the structure – the arrangement and relation between different cardiac components such as vessels, valves or heart chambers – is impaired or malformed such that connections are absent, predominant or switched, or single or multiple components are hypoplastic (underdeveloped) or atretic (abnormally narrowed). Mitchell et al (Mitchell et al., 1971) describe CHD as “a gross *structural* abnormality [...] that is actually or potentially of *functional* significance”. Structural problems accompany immediate functional impairment or might lead to functional impairment eventually. Yet, it remains debatable whether structure follows function or vice versa.

The American Heart Association (AHA) (Go et al., 2013) currently lists 21 specific anatomies or hemodynamic lesions, which fall into the category of CHD, ranging from small lesions to major malformations that require immediate intervention. With an incidence of about 8 per 1,000 live births in the US, which equals to a minimum of 32,000 infants expected to be affected each year, CHD is a serious condition that contributes significantly to morbidity, mortality and healthcare costs in children and later in adulthood (Go et al., 2013). Particularly complex conditions, such as hypoplastic left heart syndrome (HLHS) still result in low survival rates of about 70% until the age of five years (Feinstein et al., 2012).

Although advances in surgical techniques, diagnosis and intensive care have led to a considerable increase of survival rates of CHD patients (Warnes et al., 2001), (Marelli et al., 2007), (Go et al., 2013), (Fratz et al., 2013), there is still potential and need for improvements in diagnostic and therapeutic approaches for this group of patients.

As Mitchell defines it, the structure of the heart, the spatial relationship and arrangement of its components at birth, is crucial and defines CHD in the first instance. However as described above, in CHD it is not only the structure but also the shape and size of single cardiac components (such as the aorta), which may be affected and which

may constitute a cardiac defect leading to functional impairment. In fact, signs of cardiac anomaly or malformation in the foetus are often associated with a gross change of the shape and size of the heart (Cook, 2001). Ultimately, early and accurate diagnosis of CHD is based on discovering structural and shape related abnormalities, and both shape and structure have to be surgically altered to palliate CHD in order to restore an otherwise lost or impaired cardiac functionality (Feinstein et al., 2012). This highlights the importance of both shape and function for the management of CHD and justifies further detailed analysis of both.

## **1.1 Tools to analyse shape and function**

Information about cardiac anatomy in vivo can be acquired using various non-invasive medical imaging techniques such as ultrasound, X-Ray computed tomography (CT) or cardiovascular magnetic resonance (CMR) imaging. Particularly CMR imaging is today considered to be an integral part of early diagnosis and follow-up of patients with CHD (Ntsinjana et al., 2013a), (Fratz et al., 2013). It provides detailed and accurate structural information of cardiac anatomy in 3D combined with functional data such as valvular and vascular flows (Ntsinjana et al., 2013a).

Yet, in clinical practice, shape and structural analysis is often carried out in the fashion of simple morphometry, using 2D images. On single image slices traditional shape descriptors of cardiac anatomy such as lengths, diameters and angles are measured; some examples are given in studies (Agnoletti et al., 2008), (Ou et al., 2004). This however does not fully exploit the abundance of information that current medical imaging techniques offer. Several studies have shown that making use of 3D datasets for morphometric analysis proves to be beneficial (Schievano et al., 2007a), (Ntsinjana et al., 2014), (Craiem et al., 2012a) since, particularly in CHD, shape and structure (even of the same cardiac component) can be highly variable, and can be better appreciated and analysed using 3D data (Fig. 1.1).

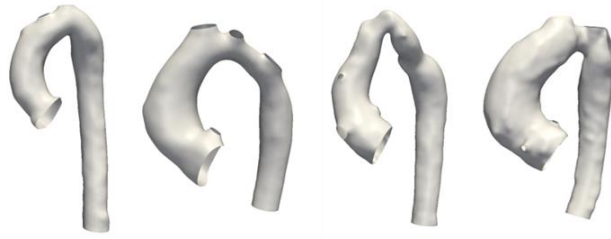


Fig. 1.1: Example of shape variability in CHD. Aortas of different adolescent patients post aortic coarctation repair

Due to advances in medical imaging techniques and ever-growing medical image databases paired with an increase in computational power, *statistical shape modelling* (SSM) has become a powerful computational tool to analyse detailed anatomical 3D shape information in a population-based manner (Lamata et al., 2014). In simple terms, statistical shape models allow the description of an average, mean anatomical 3D shape and of the shape variability around the mean, which can be used to build *descriptive* and *predictive* statistical models to investigate associations between 3D shape features and external (e.g. functional) parameters (Young and Frangi, 2009). This makes SSM an attractive tool to investigate relationships between shape and function in CHD.

## 1.2 General objectives of this thesis

The aims of this thesis are to present, validate and apply novel tools to investigate associations between cardiac shape and function in CHD. In particular, the focus lies on a recently introduced SSM approach, which allows the efficient analysis of such complex cardiac shapes found in CHD – without requiring point-to-point correspondence, landmarking or manual measurements. Instead of single morphometric parameters (diameters, lengths, etc.), 3D shape features can be analysed in their entirety. The SSM framework is based on parameterising 3D shape data as *mathematical currents* and was introduced to cardiac research by Mansi and Durrleman et al in 2009 (Mansi et al., 2009), (Durrleman et al., 2009).

The underlying motivation behind this work was to promote translation of advanced computational tools from the fields of engineering and data analytics into clinically driven research and eventually into clinical application. This is often hindered by too

complex and technical approaches, lacking clinical relevance or data, presented in mathematical terms that do not convey their potential power to a clinical or non-expert audience. This is particularly true for the SSM framework based on mathematical currents, which is in the focus of this thesis: while it offers large potential to efficiently analyse complex 3D shapes, the mathematical theory for a currents-based analysis is rather complex. In addition, cardiac applications to date are sparse, and often lack user-perspective and validation against more traditional approaches such as morphometrics or other computational modelling techniques.

Therefore, during my PhD work, I aimed to present SSM methods from a user-perspective, to validate and evaluate them against morphometry, clinical expert opinion and CFD results, to include clinical data and apply them to clinically relevant questions in order to make the developed methods attractive for a broader clinical and engineering community.

Specifically, 3D anatomical shape information was derived from CMR image data. As functional data, several clinically relevant parameters such as volumetric and blood pressure measurements were retrieved from clinical records. Further functional, blood flow related parameters were derived via computational fluid dynamics (CFD), which allows the computation of pressure and velocity fields within cardiac structures. The currents-based SSM was then used to jointly analyse associations between shape and functional data, thereby making use of data analysis tools from the fields of data mining and machine learning.

As an example clinical case of CHD, this work predominantly focusses on analysing shape and function in patients post aortic coarctation (CoA) repair. In this condition, the shape of the aortic arch is malformed, characteristically with a discrete narrowing (stenosis) in the arch that poses an obstruction for blood ejected from the left ventricle (Gunther and Grossman, 1979), (Rosenthal, 2005) (Fig. 1.2). Usually, the narrowing needs to be relieved via surgical or catheter intervention in order to restore an efficient distribution of blood to the lower body (Vergales et al., 2013). After CoA repair, patients are typically left with an abnormally shaped aortic arch, which may be associated with

cardiac function (Weber et al., 1993), (Ou et al., 2004), (Ou et al., 2006), (Ou et al., 2008a). Therefore, CoA provides an excellent platform to test and demonstrate the capabilities of a data-driven SSM approach that may provide novel insight into the relation between shape and function. As such, results may lead to improved, more informed diagnosis, follow-up and risk stratification strategies and may ultimately affect therapy and surgical decision making.

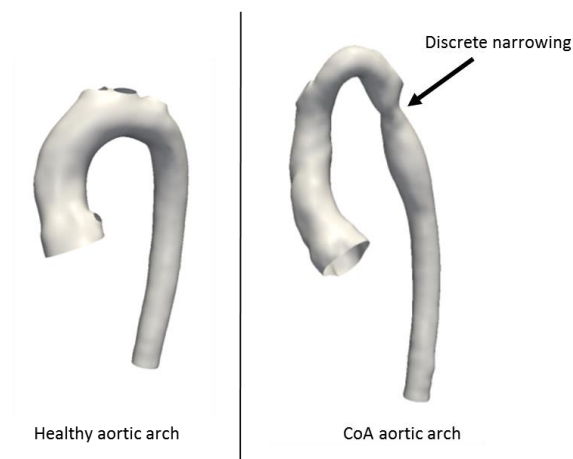


*Fig. 1.2: Three-dimensional model of the aorta of a healthy subject (left) and of a patient post aortic coarctation (CoA) repair*

### **1.3 Outline of the thesis and questions to be answered by this work**

The outline of this thesis is structured as follows. **Chapter 2** provides a general overview of phenomenological and mechanistic computational modelling with a focus on cardiac applications. First, basic concepts of traditional statistical shape modelling are described, followed by a brief discussion of relevant SSM applications to cardiac research. Since the focus of this thesis lies on the analysis of aortic arch shapes and arch shapes of patients affected by CoA in particular, an overview of morphometric and SSM-based studies of the aorta is given. Lastly, mechanistic computational modelling of the aorta is described as it has been used extensively by the engineering community to analyse shape and function.

**Chapter 3** presents a detailed description of the methods and the modelling pipeline used in this work – starting from medical image data to obtaining 3D anatomical models serving as input for the SSM framework, to data analysis strategies, to a discussion of the included cardiac functional parameters and tools used for mechanistic modelling. A particular focus lies on the description of the novel, mathematical currents-based SSM framework, building the core computational tool used in this thesis.

**Chapter 4** describes in detail how the currents-based SSM in combination with partial least squares (PLS) regression can be used to extract 3D “shape biomarkers” i.e. shape features associated with cardiac function in a robust and efficient way. This chapter extends the current literature by adopting the user-perspective, providing detailed insight into how to run the analysis, for the first time evaluating results against traditional morphometrics and by showcasing a potentially relevant clinical application of the framework in CoA. Chapter 4 aims to answer the following questions:

- Which parameters are relevant for the currents-based SSM framework and how can a robust and efficient analysis be ensured?
- How do the computed SSM results compare with traditional morphometric parameters and does the method offer the potential of discovering novel 3D shape biomarkers in CHD?

After establishing a protocol to set up and run the currents-based statistical shape analysis, and after demonstrating that results are in line with manually measured traditional shape descriptors, **Chapter 5** focusses on investigating whether results are in line with clinical expert opinion as well. Thereby, shape abnormality scores for aortic arch shapes post CoA repair are computed via PLS and principal component analysis (PCA) and compared against clinical expert ranking. The question to be answered by this chapter is:

- How do quantitative SSM results compare to subjective clinical expert opinion in terms of assessing cardiovascular anatomical shapes?

With confirmed objective and subjective meaningfulness of the SSM results, **Chapter 6** seeks to apply the currents-based SSM approach to a clinically relevant question, with the aim of extracting novel 3D shape biomarkers in a larger cohort of patients post CoA repair. While previous studies have suggested associations between aortic arch shape and cardiac function, no study to date has applied 3D SSM to analyse such relationships in CoA. The leading question behind this chapter is therefore:

→ Which 3D arch shape features are associated with clinically relevant parameters in CoA repair?

**Chapter 7** attempts to provide a mechanistic basis for the obtained phenomenological SSM results derived in Chapter 6. For the first time, computational fluid dynamics (CFD) simulations are carried out on computed SSM shape modes, which have been associated with “better” or “worse” cardiac function. Further hemodynamic performance parameters such as pressure drops and power losses are computed, hypothesising that the computed “worse” arch shapes relate to diminished computed hemodynamic performance as well. Chapter 7 therefore focusses on the question:

→ How do phenomenological SSM results compare to results from mechanistic computational modelling such as CFD?

Having exploited the capabilities of the SSM framework to extract clinically relevant aortic arch shape features via PLS regression, the framework was extended by another data mining technique known as hierarchical clustering in **Chapter 8**. Hierarchical clustering does not require any prior information about the dataset and may reveal novel anatomical shape clusters. Such anatomical clusters may be useful for risk stratification in CHD and for a potentially more cost-effective, cluster-adapted medical device development. To date, only few studies have applied hierarchical clustering to 3D medical image data and many different algorithms and parameter settings exist. Chapter 8 thus provides the technical basis required to be able to obtain meaningful clustering of the input data, aiming to answer the question:

→ How could the currents-based SSM framework be used to detect previously unknown 3D anatomical shape clusters and subgroups from CMR image data?

**Chapter 9** applies the developed clustering pipeline of Chapter 8 to a larger cohort of aortic arch shapes post CoA repair in order to investigate whether clinically relevant anatomical shape clusters can be found. The question to be answered is:

→ Can clinically relevant clusters or patterns be found in a larger patient cohort affected by CoA?

The established protocols and techniques that allowed me to extract clinically relevant 3D shape biomarkers as well as to discover novel anatomical shape clusters by making use of all 3D shape information within medical image data conclude this thesis.

**Chapter 10** presents the main outcomes, conclusions and achievements of this work and discusses potential future applications.

## 2 Background of phenomenological and mechanistic computational modelling: cardiac applications

*Part of the work described in this chapter has been published in: G. Biglino, C. Capelli, J. L. Bruse, G. Bosi, A. M. Taylor, and S. Schievano. Computational modeling for congenital heart disease: How far are we from clinical translation?, Heart, vol. 103, pp. 98–103, Jan. 2017. (Biglino et al., 2017). Copyright (2017) with permission of BMJ Publishing Group Ltd.*

This chapter first explains basic concepts behind “traditional” parametric (i.e. landmark-based) statistical shape modelling and moves on to present recent cardiac applications, with a focus on applications to the aorta. In the last section, an overview of mechanistic computational modelling commonly used in the engineering domain for the analysis of shape and function in cardiovascular research is presented.

## 2.1 Basic concepts behind statistical shape modelling: parametric models

Statistical shape modelling (SSM) constitutes an essential tool of “image-based phenomenological modelling” (Frangi et al., 2016), which focusses on extracting useful, structured information and knowledge from mere image data. In the context of clinical research, the general aim is to move upwards in the *data, information, knowledge and wisdom* pyramid (DIKW), towards higher meaning and value for clinical decision making (Frangi et al., 2016), (Rowley, 2007), (Fig. 2.1). This thesis applies various computational modelling tools to medical image and clinical data, in order to progress upwards in the DIKW pyramid. The core tool used here to extract information and knowledge from the input data is SSM. To be able to process, integrate and interpret large amounts of complex anatomical, functional and clinical data, a new “vehicle” is necessary. This vehicle is the *computational atlas* (Fonseca et al., 2011), an integral part of SSM, which is explained in the following section.

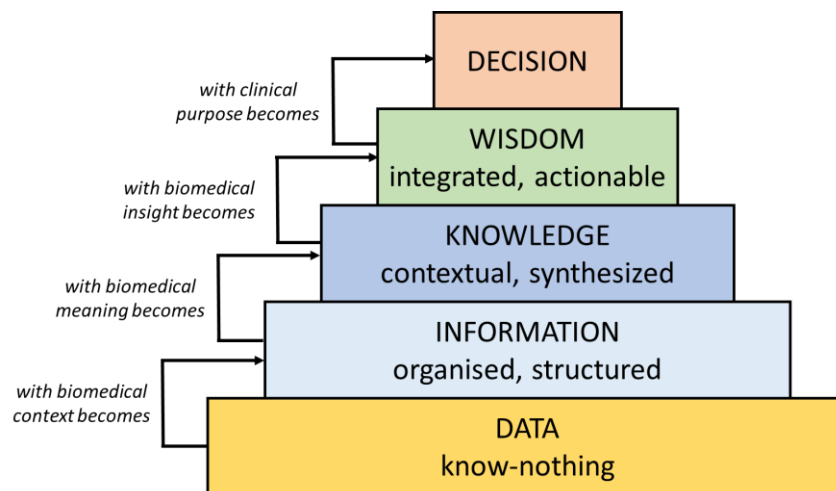


Fig. 2.1: DIKW pyramid, adapted from (Frangi et al., 2016)

### 2.1.1 The computational atlas: the anatomical mean shape

An atlas according to the definition of Young and Frangi is “an alignment of data maps from different domains, either population or individualized, which enables querying of relations [...] to construct the ‘big picture’” (Young and Frangi, 2009). In other words, an atlas integrates information from different sources by quantitatively describing

structural and functional variability with statistical and visual power. Thereby, an atlas helps to discover patterns of an internal logic or relationship within a population (Young and Frangi, 2009).

In cardiac research, computational atlases are often built from structural, anatomical data. In its simplest form, an atlas shows the average structural information as a *mean shape* and the respective *shape variations around the mean* – both being characteristic for a specific population. A simple “shape atlas” thus describes global and regional shape differences between two populations or the relation of a single shape (subject) to a normative mean shape (Bookstein, 1989), for example. Hence, it is a statistical tool as it allows “statistics on shapes” and is therefore an integral part for SSMs.

A widely used method to build a computational atlas for SSM goes back to the *Point Distribution Model* (PDM) as established by Cootes et al in 1994 (Cootes et al., 1994). In a PDM, the shape is parameterised by landmarks – therefore it belongs to the class of *parametric* computational shape analysis methods (Mansi, 2010). Bookstein et al (Bookstein, 1989) define landmarks as points on the structure’s surface for which “objectively meaningful and reproducible [...] counterparts” exist in all other structures present in the dataset. For the heart, such a landmark could be found at the apex, for example (Fig. 2.2). However for modern SSMs, landmarks do not necessarily have to be located at distinct feature points as required for strict anatomical landmarks (Heimann and Meinzer, 2009).

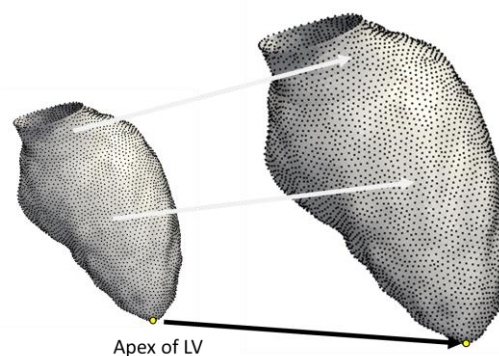


Fig. 2.2: Landmarks and point-to-point correspondence in 3D surface models of the left ventricle; apex marked

Each landmark is essentially a point with an  $x$ ,  $y$  and  $z$  coordinate in Euclidean space, so that each shape is parameterised by a vector  $S = (x_1, y_1, z_1, \dots, x_k, y_k, z_k)^T$  for a total of  $k$  landmark points. If additional connectivity information is given for each set of  $k$  points, the surface of the initial structure can be reconstructed and a computational mesh is obtained (Chapter 3.3). (Heimann and Meinzer, 2009), (Cootes et al., 1994)

In parametric computational shape analysis methods, each shape within the dataset is parameterised with the same number of  $k$  points and each point in one shape has its corresponding points in the other shapes; i.e. point number  $k = 1$  refers to the same landmark point  $k = 1$  in all the other shapes within the dataset. Thus, *point-to-point correspondence* is given and subsequent shape analysis becomes rather straightforward.

In this case, the mean position of the apex for example, can be obtained by simply averaging the point coordinates for all apex landmarks present in the dataset. Similarly, the entire mean shape  $\bar{S}$  for a set of  $N$  shapes can be calculated by averaging the landmark vector  $S$  in the following way, for each shape  $i \in [1, \dots, N]$  (Cootes et al., 1994)

$$\bar{S} = \frac{1}{N} \cdot \sum_{i=1}^N S_i \quad (2.1)$$

### 2.1.2 Describing shape variability in 3D

Statistical analysis of 3D shape falls into the domain of *multivariate statistical analysis*. Each of the  $N$  shapes of a dataset is defined by hundreds or thousands of landmarks and each of those points can vary arbitrarily in space. A collection of random variables has to be simultaneously statistically analysed. (Izenman, A. J., 2008)

Therefore, mathematical techniques for dimensionality reduction such as *principal component analysis* (PCA) can be applied to break down the high-dimensional variability of the entire dataset into a smaller set of independent variables that describe the principal contributors to shape variability (Cootes et al., 1994), (Jolliffe, I.T., 2002). These independent variables are called *principal components*, which are mathematically obtained by an orthonormal linear transformation. Here, PCA can be applied to the *covariance matrix*  $C$ , which describes the deviation of each shape from the mean:

$$C = \frac{1}{N-1} \sum_{i=1}^N (S_i - \bar{S}) \cdot (S_i - \bar{S})^T \quad (2.2)$$

A mathematical operation called eigendecomposition decomposes  $C$  into its *eigenvectors*  $p_i$  and their respective *eigenvalues*  $\mu_i$  describing their variance (Styner et al., 2003):

$$C \cdot p_i = p_i \cdot \mu_i \quad (2.3)$$

The eigenvectors  $p_i$  are typically called the *principal modes of variation* or *shape modes* and are used to quantify and visualise shape variability within a dataset. Note that each shape present in the dataset can be approximated by linearly combining the obtained shape modes. The shape  $S$  of subject  $i$  is characterised by a unique linear combination of  $K$  weights for  $K$  shape modes as exemplified in Eq. 2.4:

$$S_i = \sum_{m=1}^K \text{Weight}_i^m \cdot \text{Mode}^m \quad (2.4)$$

Once the population-specific shape modes are computed, each subject's 3D shape within the population can numerically be expressed by a unique, patient-specific set of weights, allowing a much lower dimensional shape representation than the original set of landmarks.

Usually, shape modes are ranked in order of highest to lowest variability, showing which shape variations are dominant and which can be neglected (Young and Frangi, 2009). The mean shape  $\bar{S}$  and the variations around the mean calculated by PCA finally constitute the PDM and hence a simple SSM. Fig. 2.3 shows a simplified “phenomenological modelling pipeline” (Frangi et al., 2016), typically used for SSM. It starts with the segmentation of the structure of interest (here the aorta and the left ventricle), which is then transferred into a computational shape representation – a 3D surface mesh. The meshes of a cohort of patients are then used to compute a common mean shape or atlas and shape variations around the mean are analysed using numerical techniques such as PCA to visually derive shape modes and numerically derive weights of shape modes, for instance.

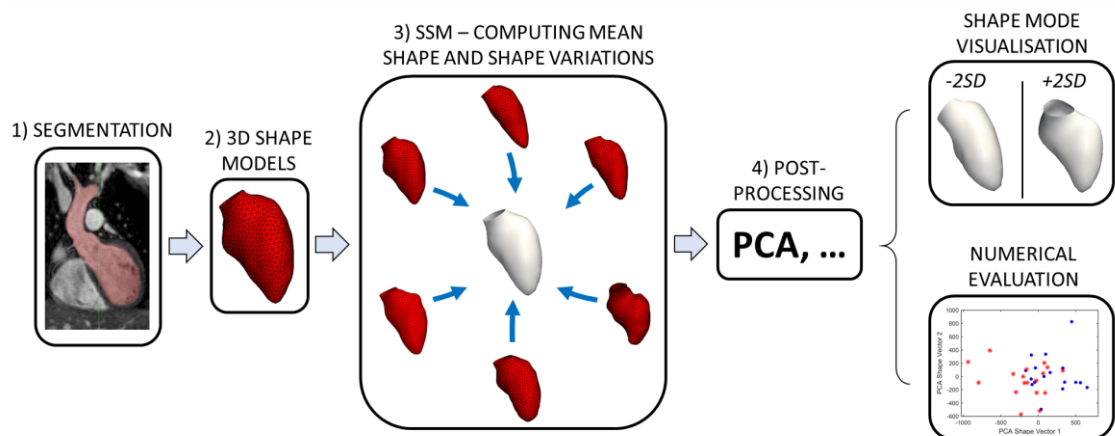


Fig. 2.3: General statistical shape modelling (SSM) pipeline from segmentation of the structure of interest to anatomical mean shape (template) computation and 3D shape variability description via principal component analysis (PCA), adapted from (Biglino et al., 2017) © 2017 BMJ Publishing Group Ltd

## 2.2 Cardiac applications of SSM

Using the mean shape and its principal modes of variation, *descriptive* or *predictive* statistical models of shape can be built. Descriptive statistical models help to explore particular characteristics of a population of shapes and can serve to discover unexpected patterns such as trends, clusters or outliers. Predictive statistical models in turn help to study relationships between shape and continuous or discrete parameters by applying regression or classification techniques, respectively. (Izenman, A. J., 2008), (Biglino et al., 2017)

Descriptive and predictive statistical approaches could be of great use in analysing shape in the context of cardiac research. Shape outliers could be automatically detected and could be followed-up more closely. Clustering techniques could uncover previously unknown shape sub-groups or morphological patterns and subsequent classification techniques could explore if any of these subgroups is at a higher risk of following a certain pathologic pathway. Regression and correlation of distinct anatomical shape features with clinical or functional parameters could identify potential biomarkers for adverse cardiac events (Lamata et al., 2014). In this way, cardiac SSMs could contribute to understanding cardiac disease and could support diagnosis and the development of new therapeutic approaches. (Fonseca et al., 2011), (Biglino et al., 2017)

Early SSMs in cardiac research described the variability of 2D heart ventricle shape contours based on a few subjects (Cootes et al., 1994). Models range now to elaborate 3D models of the whole heart (Lorenz and Berg, 2006) and models based on more than 2,000 subjects (Medrano-Gracia et al., 2013). Projects such as the *Cardiac Atlas Project* (Fonseca et al., 2011) aim to build up exhaustive image databases that fulfil the need of providing large amounts of data for population-based studies. (Biglino et al., 2017)

However to date, SSMs are predominantly used for isolating a structure of interest in medical image segmentation (Heimann and Meinzer, 2009), (Styner et al., 2003). Until recently, only few studies have recognised the power of computational atlases for diagnostic or prognostic purposes with a potential clinical impact. Examples include the work of Remme et al in 2004, who compared the shape of the left ventricle (LV) of healthy and diabetic subjects and found significant differences between regional shape features of the LV. In 2013, Lamata et al analysed the shape of ventricles in women with preeclampsia for risk assessment (Lamata et al., 2013) and Lewandowski et al found a unique LV shape in pre-term born subjects in adult life (Lewandowski et al., 2013). Recently, Dawes et al combined SSM and machine learning techniques, to predict outcome based on 3D right ventricular motion in a cohort of patients suffering from pulmonary hypertension (Dawes et al., 2017). They found that 3D cardiac motion parameters obtained via PCA significantly improved survival prediction, independent of conventional risk factors. In the field of CHD, Farrar et al analysed ventricular shapes and wall motion of adult single ventricle patients and compared them with a shape atlas of a healthy control population to derive shape z-scores as a measure of shape abnormality (Farrar et al., 2016). (Biglino et al., 2017)

The non-parametric currents-based approach used in this thesis had predominantly been applied to analyse brain structures (Vaillant and Glaunès, 2005), (Durrleman et al., 2007) until Mansi, McLeod et al introduced it to the field of CHD (Mansi et al., 2009), (Mansi et al., 2011), (McLeod et al., 2013). They analysed the shape of left and right ventricles of a population of Tetralogy of Fallot (TOF) patients and established correlations between distinct shape features of the ventricles and clinically

relevant parameters such as regurgitation fractions. Furthermore, they created a growth model that predicted ventricular shape changes based on changes in body surface area (BSA) (Mansi et al., 2011). It is noteworthy that the majority of previous work focussed on the analysis of heart ventricles; other cardiac structures were rarely considered.

## 2.3 Shape analysis of the aorta

In this thesis, the cardiac structure of interest is the aorta, the major cardiac vessel that serves as a conduit to distribute oxygenated blood ejected by the LV into the systemic vasculature to supply body organs. The aortic valve separates LV and aortic root, i.e. the portion of the aorta closest to the LV from where the coronary arteries originate (Fig. 2.4). The ejected blood then follows up the ascending aorta into the transverse arch section and downwards into the descending aorta and subsequent vessels, transporting oxygen to cells around the lower body. In this thesis, the term “aortic arch” refers to the ascending, transverse and descending portion of the aorta. From the transverse arch section, the brachiocephalic, left common carotid and left subclavian arteries originate, which deliver blood to the upper parts of the body. Here, these arteries are referred to as “head and neck vessels”. (Moeller, 2013), (Bogaert et al., 2012)

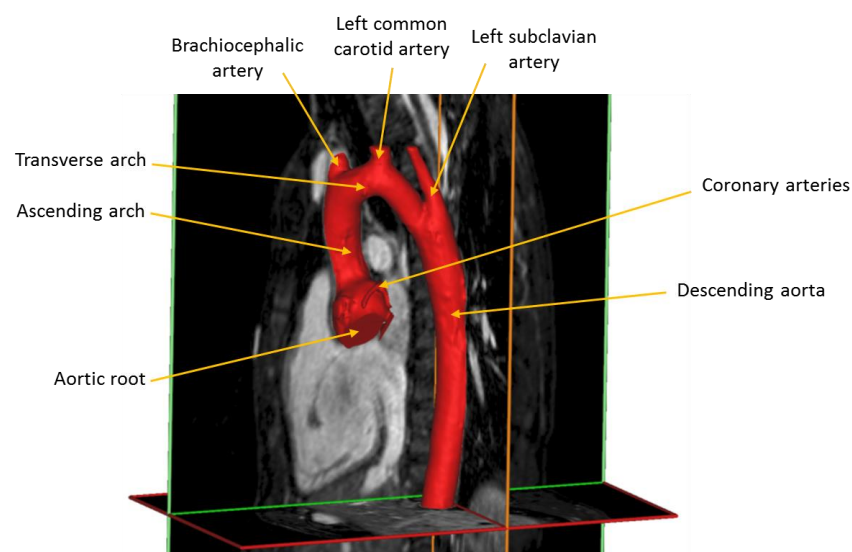


Fig. 2.4: Segmented 3D model of the aorta with annotations

### 2.3.1 Shape analysis of the healthy aorta

Methods for shape analysis of the aorta in vivo in the past two decades range from simple methods using 2D image analysis to more complex studies in 3D and recently, methods involving SSMs. One major topic of research has been age-related shape changes of the aorta by measuring diameters (Grimshaw and Thompson, 1995), (Wolak et al., 2008), lengths (Sugawara et al., 2008) or a combination of more elaborate 2D morphometric descriptors (Demertzis et al., 2010).

Later, Wörz et al and Craiem et al proposed elaborate semi-automatic segmentation methods to quantify aortic arch morphology from 3D CT data (Worz et al., 2010), (Craiem et al., 2012a), (Craiem et al., 2012b). Based on their approach, Casciaro et al (Casciaro et al., 2014) built a SSM for a population of 500 healthy subjects using 3D CT image data. They performed PCA – however not including the 3D shape in the fashion of a PDM (Chapter 2.1.1) – but on a data vector combining shape and size parameters measured from the 3D models. Further SSMs of the aorta can be found in (Chiu et al., 2013) and (Bosmans et al., 2013).

The studies (Casciaro et al., 2014), (Chiu et al., 2013) and (Bosmans et al., 2013) were all published in the past four years, proving the novelty of applying SSMs for shape analysis of the aorta. Furthermore, most of the previous studies were mainly based on measured geometric parameters, derived either from 2D medical images or from segmented 3D models. Just very few authors studied shape variability as deformations in 3D and the application of descriptive or predictive statistical models to derive clinically relevant results is still rare.

One study addressing those issues is by Zhao et al who compared 52 healthy subjects to 52 subjects with connective tissue disorder disease using CMR images (Zhao et al., 2009). They proposed an automatic segmentation method and also performed an elaborate shape analysis, employing a PDM. The derived PCA modes were used as a classifier to distinguish between healthy and diseased subjects, and reached a prediction accuracy of 82% to 90%. Those results were promising as they proved the feasibility of an

objective, quantitative assessment of aortic disease from CMR data via SSM and computational approaches.

### 2.3.2 Shape analysis of the aorta in CoA

Shape analysis of the aorta in patients affected by coarctation (CoA) is particularly interesting as there is an ongoing debate about how relevant the aortic arch shape is for morbidity and reduced life expectancy after successful repair. CoA accounts for about 8% of all CHD, which equals to an incidence of about 0.4 in a 1000 live births (Go et al., 2013). CoA can be defined as a narrowing, hypoplasia or obstruction of the aortic arch at the transverse (horizontal), isthmus or descending aorta level (O'Sullivan, 2014). Commonly, it is located in the juxtaductal position distal to the left-subclavian artery (LSC) as indicated by the arrow in Fig. 2.5. Although CoA is usually detected and treated early, patients show a reduced life-expectancy mostly related to late-complications post CoA repair (Cohen et al., 1989), (Canniffe et al., 2013), (Brown et al., 2013). One associated risk factor is *hypertension* (defined as a resting blood pressure exceeding around 140 mmHg in systole or 90mmHg in diastole), which occurs in around a third of CoA patients (Canniffe et al., 2013), see also Chapter 3.8.4.

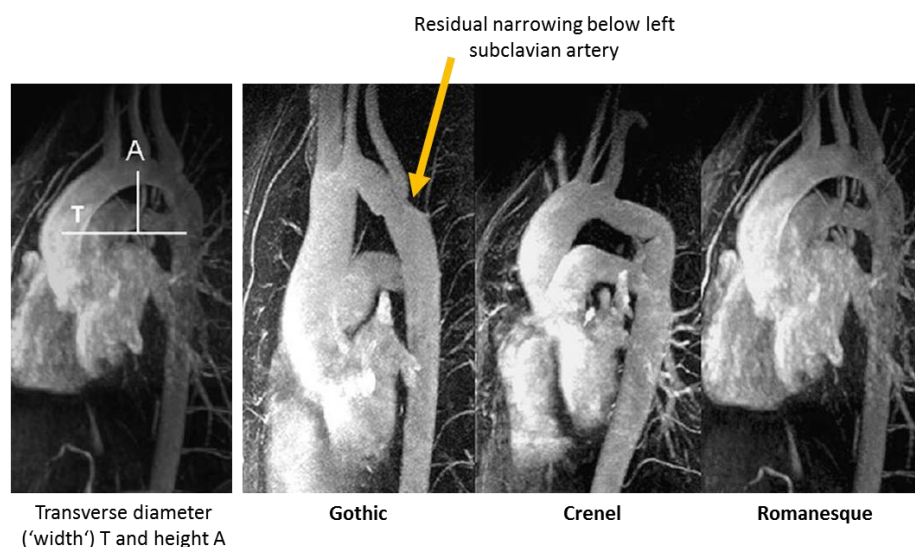


Fig. 2.5: Aortic arch measurements and arch shape classification into three phenotypes, adapted from (Ou et al., 2004), © 2004 Oxford University Press

In 2004, Ou et al laid out the basis for current shape analysis of aortic arches after CoA repair (Ou et al., 2004). They defined the ratio of aortic arch height  $A$  divided by arch width  $T$ ,  $A/T$  as shown in Fig. 2.5 to be a crucial shape parameter for CoA risk assessment. Thereby,  $A$  is the height of the aortic arch, defined as the maximal vertical distance between the plane in  $T$  and the highest mid-point of the arch, and  $T$  is the transverse width of the arch, defined as the maximal horizontal distance between the midpoints of the ascending and descending aorta close to an axial plane through the right pulmonary artery. Based on the  $A/T$  ratio, they found three dominant types of arch morphology in their CoA population.  $A/T$  ratios higher than around 0.8 defined an angulated or *Gothic* arch shape; lower values, around 0.68 and 0.66, defined more rounded shapes as *Romanesque* or *Crenel*, respectively. More specifically, they defined Gothic arches as being acutely angulated between ascending and descending aorta with the horizontal/transverse part being shortened or absent. Crenel arches were more “rectangular” with a normal length of the transverse aorta but a kink in the area around the isthmus. (Ou et al., 2004)

Several subsequent studies showed significant correlations between a Gothic arch shape (as defined by high  $A/T$  values) and resting (Ou et al., 2004) as well as exercise (Ou et al., 2006) hypertension, increased LV mass (Ou et al., 2004), (Ou et al., 2008a) and lower distensibility or other vascular abnormalities (Ou et al., 2007), (Ou et al., 2008a), (Donazzan et al., 2014). At the same time, other authors did not find respective correlations – particularly no correlation between a Gothic shape and hypertension, see (De Caro et al., 2007), (Ntsinjana et al., 2013b) and (Lee et al., 2012). Those authors suggest that rather a narrowing, general hypoplasia or residual obstruction at the level of the transverse arch or isthmus are likely to play a role in hypertension and associated risks in CoA patients. This controversy and the evidence that aortic arch shape features may be related to clinically important risk markers, generated the motivation for applying the currents-based SSM to 3D aortic arch shapes in this work.

## 2.4 Mechanistic computational modelling

Whilst SSM approaches can provide a data-driven, *observational* or *phenomenological* insight into relationships between shape and function, “image-based mechanistic modelling” (Frangi et al., 2016) has been widely applied in the biomedical engineering community to provide *mechanistic* insight by modelling physical principles associated with organs and body structures *in silico* (Viceconti, 2015). Computational models are considered a fundamental tool in cardiac research as they allow quantitative, mathematical analysis and prediction of cardiac biomechanical, biochemical and electrophysiological function based on physical laws, which can help to form and test novel hypotheses potentially yielding insight into underlying disease mechanisms and novel associations between shape and function (Lamata et al., 2014), (Quail and Taylor, 2013).

In an image-based mechanistic modelling pipeline (MacLeod et al., 2009), the anatomical structure of interest is segmented from medical images and is transformed into a geometric model represented by a computational mesh, which is then used to numerically solve equations describing functions of the original structure constrained by geometric and functional boundary conditions (Fig. 2.6). The biggest advantage of computational modelling is the possibility to *alter* certain geometric and/or functional boundary conditions, while controlling for others. This allows untangling the effect of changing one single parameter on the behaviour of the entire system.

The possibility of modelling cardiac structures has led to the development of *patient-specific* modelling (Taylor and Figueroa, 2009), which is transitioning from basic research into clinical application (Schievano et al., 2010) and into the field of CHD (Hsia et al., 2011). Various studies have analysed the effects of structural alterations due to surgical intervention in patient-specific models of CHD (Baretta et al., 2011), (Goubergrits et al., 2014). Applications range from computational models of cardiac structural mechanics (Capelli et al., 2012) to fluid dynamics and mass transport (Liu et al., 2009), and electrophysiology (Sermesant et al., 2012).

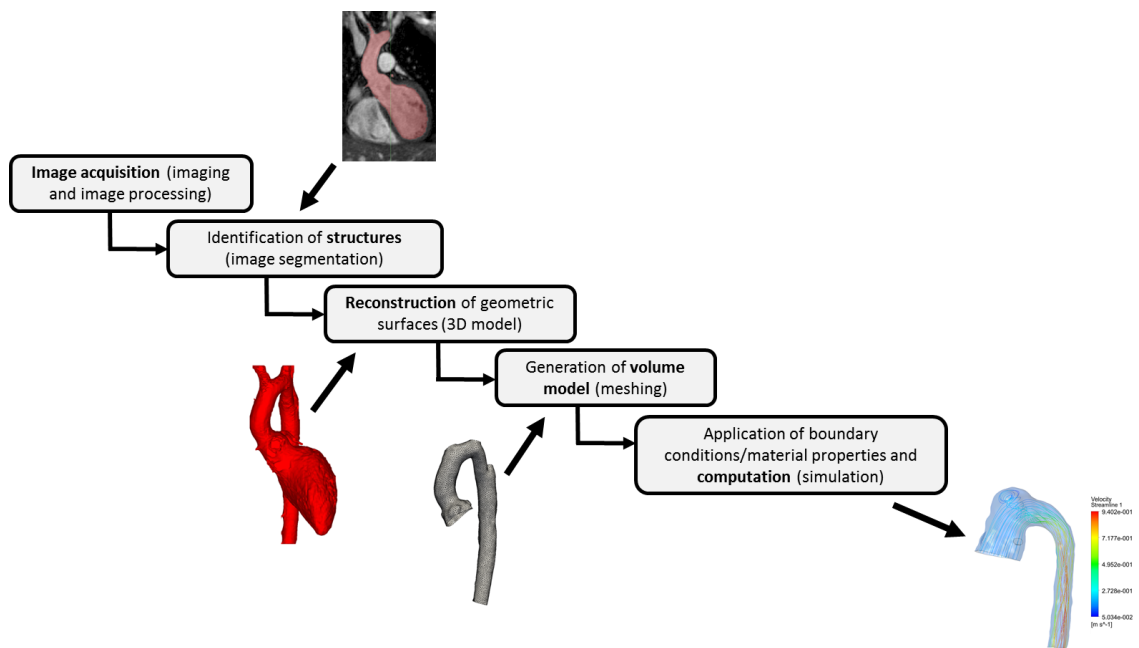


Fig. 2.6: : Image-based mechanistic modelling pipeline from image data to simulation results, adapted from (MacLeod et al., 2009)

Growing image databases combined with increasing computational resources allow now the transition from patient-specific towards *population-based* studies (Lamata et al., 2014), (Young and Frangi, 2009). In addition to individual structural and functional behaviour, variability can be quantified based on a population of image and clinical data. Hence, cardiac models are now able to implement natural and pathological variability to complement patient-specific models, allowing to add statistical power to simulation results (Lamata et al., 2014). Yet, due to the complex nature of computational modelling, involving many pre- and post-processing steps (Fig. 2.6) and due to lack of sharing clinical data, larger scale studies that involve modelling of cardiac functional aspects in a large number of subjects are still sparse.

### 2.4.1 Mechanistic modelling of coarctation of the aorta

To date, many studies have analysed blood flow through the aorta (Caballero and Laín, 2013), I focus here on computational mechanistic models of CoA only. The first sophisticated 3D computational models of CoA apply *virtual surgery*, i.e. keeping functional boundary conditions the same while relieving the narrowed CoA site in silico by changing the 3D geometry locally and computing pressure and velocity fields

from fluid dynamics simulations (Kim et al., 2009). The largest study to date applying virtual surgery in CoA included 13 patients and authors succeeded in reducing both pressure drops and wall shear stress (WSS) post virtual treatment (Goubergrits et al., 2014).

Further studies have performed computational fluid dynamics (CFD) simulations on small numbers of CoA patients and reported values such as pressure drop and wall shear stresses or cardiac workload (LaDisa et al., 2011a), (LaDisa et al., 2011b), (Olivieri et al., 2011), (Szopos et al., 2014), (Coogan et al., 2013). However, statistical power of such studies is limited by small sample sizes ( $N < 13$ ) and none of them incorporate statistical shape modelling. Further, correlations between computed parameters (such as WSS) and clinical outcomes are yet to be shown in order to ascertain clinical relevance.

A clinically important parameter in CoA is a peak systolic pressure drop  $\Delta p$  of more than 20mmHg across the coarctation site, defining a hemodynamically significant narrowing (Nielsen et al., 2005). Based on such measurements, usually performed via invasive cardiac catheterisation, a decision is made whether a patient requires intervention to relieve the narrowing. Therefore, recent studies focus on applying CFD approaches informed by CMR image and flow data to determine the pressure drop non-invasively in silico (Goubergrits et al., 2015), (Ralovich et al., 2015). Both studies show good agreement between CFD derived and catheterisation pressure drops, suggesting computational modelling-based approaches to be a potential alternative for invasive measurements. Yet, the largest study to date involves 13 CoA patients only, which is likely not to be sufficient for direct clinical translation.

#### **2.4.2 Combining mechanistic and phenomenological modelling**

A joint application of both image-based phenomenological (e.g. statistical shape modelling, SSM) and mechanistic computational modelling (e.g. computational fluid dynamics, CFD) may eventually allow further extraction of knowledge and wisdom from image data, moving towards improved clinical decision support at the top of the DIKW pyramid (Fig. 2.1). Such quantitative methods, integrating both phenomenological and

mechanistic computational modelling based on medical image data, targeted at optimising diagnosis and treatment strategies, were recently termed “Precision Imaging” by Frangi et al (Frangi et al., 2016) since they take into account individual patient variability for optimised diagnosis and treatment strategies, similar to the “Precision Medicine” maxim (Collins and Varmus, 2015). This thesis follows the Precision Imaging path and ultimately aims to transfer data into useful information.

While image-based statistical shape modelling is a powerful observational tool to build descriptive and predictive population-based models of shape and function that may complement (or may be complemented by) deterministic mechanistic modelling based on physical laws, both methods have not been applied jointly in cardiac research to date. Particularly when looking at SSM providing an observational basis and CFD adding mechanistic insight, previous studies have mainly applied both together with the aim of speeding up CFD simulations by mapping one full CFD solution to different anatomies (McGregor et al., 2008), (Guibert et al., 2014). In a recent study by Beier et al (Beier et al., 2016), previous SSM results (Medrano-Gracia et al., 2014) informed the creation of idealised Y-shaped bifurcation geometries for CFD analysis of coronary arteries. Yet, neither computed anatomical mean shapes nor derived shape modes have been implemented into the modelling pipeline to assess their functional behaviour, for instance. Larger scale studies, showing direct associations between functional data from CFD and 3D shape information are still missing. In this thesis, I therefore aim to bring observational and mechanistic computational modelling together by using SSM and CFD tools for the joint analysis of shape and function in CHD, see also Chapter 7.

## 2.5 Summary

This chapter explained basic concepts such as the calculation of mean shape and shape variations in 3D via PCA typically used in parametric SSM approaches. Crucial for these is the proper definition of landmarks and a consistent point-to-point correspondence between different shapes. Manual landmarking however, is labour-intensive and error-prone and particularly in highly variable sets of shapes corresponding landmarks are not easy to define (Huysmans et al., 2010). Although many automatic and semi-automatic

landmarking algorithms exist and are being developed, they are often still limited to sets of shapes with a confined shape variability. These methods may be difficult to be applied to arbitrary and highly complex shapes such as those present in CHD (Fig. 2.7) which is why a novel, non-parametric SSM approach based on parameterising shapes as mathematical currents has been adopted in this thesis (see Chapter 3.6).

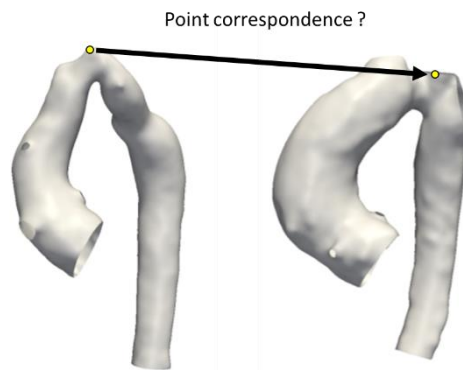


*Fig. 2.7: Shape variability in subjects with CHD makes landmarking difficult, adapted from (Bruse et al., 2016a)*

Further, relevant previous applications of SSM in cardiovascular research have been briefly described. While applications are still sparse, some studies have demonstrated clinical relevance of SSM results and found certain shape features to be risk markers or predictors of survival. A large part of the literature however, focusses on the analysis of ventricular shapes, only few SSMs of the aorta exist and most of them analyse the healthy aorta. In CHD, and particularly in CoA, most studies apply traditional morphometric shape analysis and to date, no SSM of aortic arches affected by CHD has been reported. In the literature, there is evidence of associations between arch shape and cardiac functional parameters in CoA, motivating the application of SSM approaches in this thesis.

Finally, concepts behind mechanistic computational modelling as typically used in biomedical engineering were elucidated and applications to simulations of blood flow through the aorta in CoA have been briefly summarised. Due to complexity and high computational efforts required for mechanistic modelling, cohort sizes are to date rather small, which hinders further statistical analysis of associations between computed functional parameters and clinical outcome.

To date, phenomenological and mechanistic modelling has never been combined to gain more clinically relevant insight into the relation of shape and function in a cardiac setting. While the focus of this thesis lies on phenomenological statistical shape modelling, this issue is addressed later in Chapter 7, where both modelling approaches are joined.

In the next chapter, the applied modelling methods are presented in detail. Thereby, I follow a modelling pipeline, which starts with the medical image data and ends with computed 3D shape features and anatomical shape clusters related to measured cardiac functional parameters and/or to computed hemodynamic parameters.

### 3 Methods overview and processing pipeline

Precision Medicine or “Precision Imaging” (Frangi et al., 2016) ultimately aims at achieving the best possible care for each individual patient by taking into account individual patient variability (Collins and Varmus, 2015). As presented in Chapter 2.4.2, a core component of such approaches is the integration of mechanistic and phenomenological modelling of a disease. This allows to move upwards in the DIKW pyramid Fig. 2.1, extracting information and further insight from a pool of data. Therefore, in this thesis, I join both MacLeod’s image-based mechanistic (MacLeod et al., 2009) and Frangi’s phenomenological modelling pipelines, by combining statistical shape modelling (SSM), data mining techniques and computational fluid dynamics (CFD) modelling. Fig. 3.1 shows the modelling pipeline schematically, as adopted in this work.

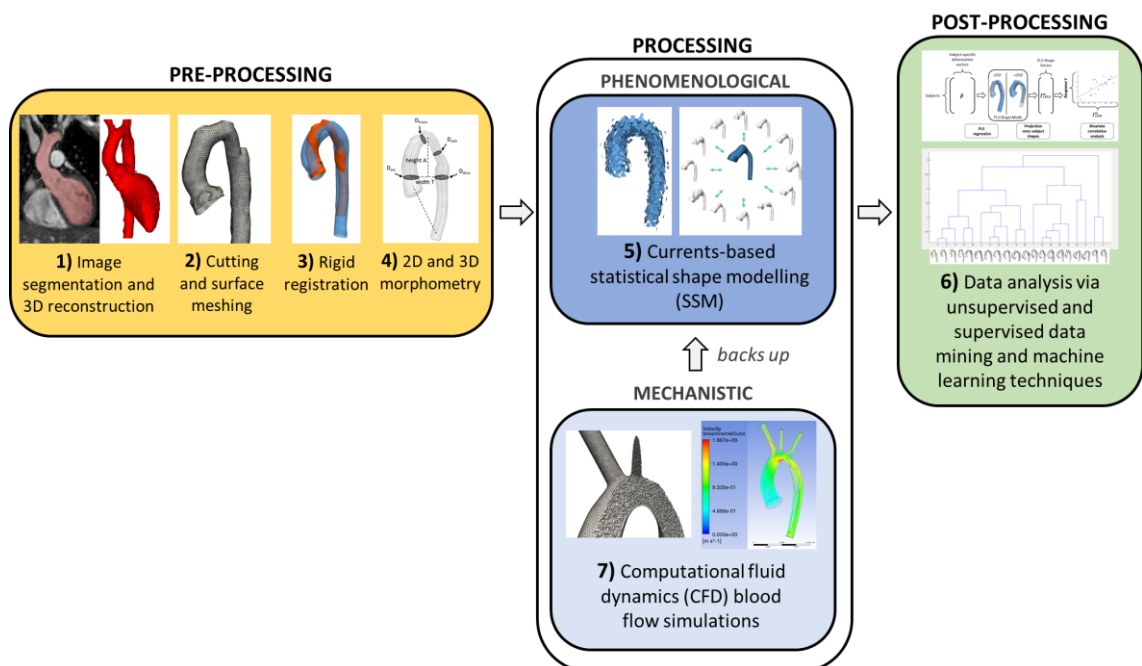


Fig. 3.1: Modelling pipeline adopted in this thesis

This chapter is organised by following the modelling pipeline in the same order a user would need to follow it to run it. First, the source and nature of the medical image data used in this thesis is described. Further, the methods used to segment the anatomical structures of interest from the image data are briefly introduced and basic concepts of

surface meshing and shape alignment are discussed, followed by a description of tools used for traditional morphometric measurements. The obtained 3D shape models are used as input for the non-parametric currents-based SSM framework, discussed in Chapters 3.6 and 3.7. The SSM framework and the adopted data post-processing techniques to extract 3D shape features constitute the key modelling tools used in this thesis. Further, the functional, clinically relevant parameters – here used as response parameters for the SSM and thus the descriptors of “cardiac function” – are introduced. Finally, basic concepts behind CFD analyses are discussed. CFD is used for mechanistic modelling of blood flow through the aorta and provides computed hemodynamic functional parameters, which are then used to evaluate the phenomenological SSM results in Chapter 7.

### 3.1 Medical image data

The processing pipeline starts with the acquisition of medical image data, which provide the initial bulk of information regarding shape and anatomy of body structures and – depending on the imaging modality – associated functional parameters. Due to its non-invasive and non-ionising nature, high spatial resolution, its reproducibility (Bogaert et al., 2012), (Fratz et al., 2013), (Robbers-Visser et al., 2009) and recent improvements in acquisition speed (Kowalik et al., 2012), cardiovascular magnetic resonance (CMR) imaging has been established as the modality of choice for a comprehensive assessment of CHD at Great Ormond Street Hospital for Children (GOSH), London, UK. The high quality images of 3D cardiac anatomy, combined with functional volumetric or flow data, constitute the input for the shape modelling pipeline.

In particular, all work presented in this thesis was based on 3D balanced steady-state free precession (bSSFP), wholeheart, free breathing, isotropic image data with iso-volumetric voxel size of 1.5mm x 1.5mm x 1.5mm acquired with a 1.5T Avanto MR scanner (Siemens Medical Solutions, Erlangen, Germany). While scan times for bSSFP acquisition are rather long (10 to 15 minutes per patient), this sequence provides excellent delineation of the blood pool and thus of the cardiac structures of interest such as the aorta (Bogaert et al., 2012), (Sørensen et al., 2004), (Razavi et al., 2003). In order to minimise cardiac motion artefacts, images are acquired during mid-diastolic rest and show cardiac anatomy at one distinct timepoint rather than averaged over the cardiac cycle. Cardiac and vessel motion is therefore not included (Fratz et al., 2013). All image data were analysed retrospectively and obtained from GOSH CMR data servers. Ethical approval for use of the image data was granted by the Institute of Child Health/Great Ormond Street Hospital for Children Research Ethics Committee, and all patients or legal parent or guardian gave informed consent for research use of the data.

### 3.2 Segmentation and anatomical reconstruction

Modern medical imaging techniques provide digitalised information about greyvalues in three dimensions of a region of interest (ROI). The anatomical structure of interest has

to be isolated, visualised and exported for further analysis. This process is called *segmentation* or delineation of anatomical boundaries and is based on the fact that connected anatomical structures are characterised by similar greyvalues within a specified range, (Fig. 3.2). Segmentation is a major branch of medical image processing and has evolved in the past years from manual to semi-automatic and automatic methods (Tavakoli and Amini, 2013). Medical image data used in this thesis were downloaded from GOSH CMR data servers in the DICOM (Digital Imaging and Communications in Medicine) file format, which were then further processed via different segmentation techniques.

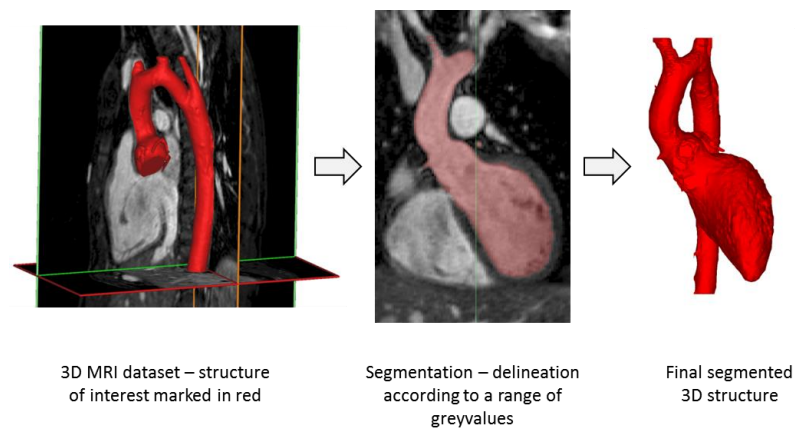


*Fig. 3.2: Segmentation of the aorta and the left ventricle from CMR images*

### 3.2.1 Manual segmentation

The first set of DICOM data was processed using commercial segmentation software (Mimics, Leuven, Belgium) via manual segmentation. The structures of interest were segmented using thresholding techniques (defining a range of greyvalues in 3D) and manual editing in a “top-down” approach. This means that via initial thresholding several connected structures characterised by a similar range of greyvalues were segmented as a bulk and then cut down until the single structure of interest (the aorta) remained. Depending on the intricacy of the selected bulk structure, this process takes in the order of 30-45 minutes to segment the aortic arch including head and neck vessels. An earlier study has shown that this manual approach yields average segmentation errors of around  $\pm 0.75\text{mm}$  (Schievano et al., 2007b), so about half the voxel size.

### 3.2.2 Semi-automatic segmentation

Since SSM requires large amount of 3D shape input data, the processing time required for segmentation was a crucial factor throughout my thesis. I therefore constantly tried different approaches and tools to improve efficiency. Active contour segmentation based on evolving snakes (Kass et al., 1988) have been shown to be both reliable and efficient for 3D segmentation of anatomical structures (Yushkevich et al., 2006) and have been implemented in the openly available software package ITKSnap ([www.itksnap.org](http://www.itksnap.org)). In this “bottom-up” approach, the user places seed points within the structure of interest (e.g. roughly along the centreline of a blood vessel) from where an active contour evolves towards the boundaries of the structure characterised by high greyvalue gradients (Yushkevich, 2016), (Fig. 3.3). The structure of interest is thus automatically “filled” until the segmented region contains the voxels defining the desired structure in 3D. This approach requires less user interaction than a fully manual approach and resulted in segmentation times of about 15-20 minutes for an aortic arch structure using a workstation with 32GB RAM and 24 CPUs.

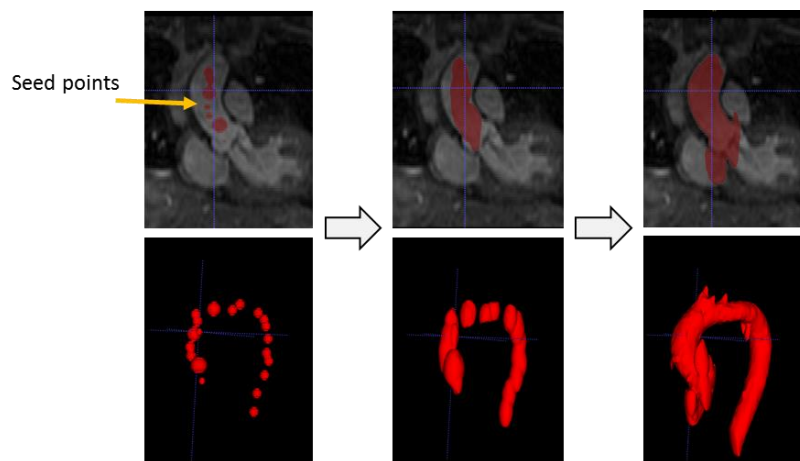


*Fig. 3.3: Semi-automatic segmentation in ITKSnap using seed points and snakes algorithm, respective 3D models shown below*

### 3.2.3 Fully automatic segmentation

Finally, I adopted a fully automated atlas-based segmentation approach, based on Python and C libraries, provided by Dr Maria A Zuluaga. This method uses multiple atlases (here, image data containing the intensity and labelled image data of a structure

of interest, i.e. the ground truth segmentation), which are propagated onto an unseen subject and then fused into a consensus segmentation of the unseen structure (Zuluaga et al., 2013). The method has been shown to perform well in segmenting pathological cardiac structures with a low number of atlases in the order of 20 (Zuluaga et al., 2015). The automatic segmentation process takes a computing time of about 30 minutes to segment LV and aortic arch for a single subject, and may require manual clean-up of the final segmentation label in ITKSnap for about 5 minutes. Fig. 3.4 shows the obtained automatic and cleaned (green) segmentation masks with the respective 3D reconstructed models of aorta and left ventricle for a challenging case with CHD.

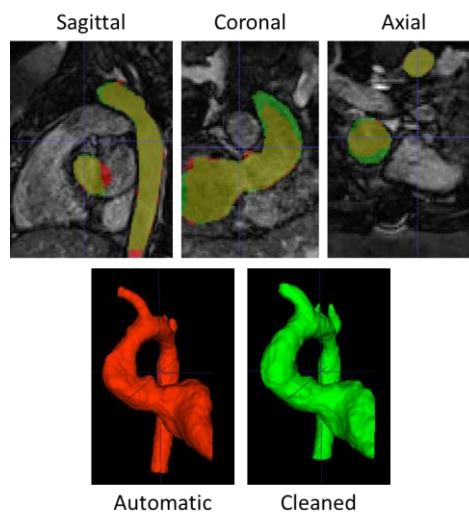


*Fig. 3.4: Automatic segmentation results before (red) and after (green) manual cleaning. Both segmentation labels and obtained 3D models are shown*

### 3.3 Meshing

In order to build a SSM with the proposed currents-based shape analysis method, the segmented 3D structures need to be transferred into a 3D computational surface mesh providing point coordinate and connectivity data. Each triangular surface element is made up of three nodes with respective  $x$ ,  $y$  and  $z$  coordinates in Cartesian space. The mesh file contains all node coordinates and information about which nodes are connected to each other to form the 3D surface of the structure of interest (Fig. 3.5).



Fig. 3.5: 3D surface mesh of a reconstructed aortic arch

Both Mimics and ITKSnap allow to transform a 3D segmentation label into a computational surface mesh. Since initial surface meshes directly obtained from segmentation labels are typically rough and include small and skewed mesh elements, models need to be re-meshed and smoothed. Therefore, files were exported from ITKSnap into the VTK (Visualization Toolkit) (Schroeder et al., 2006) file format and further processed using The Vascular Modeling Toolkit (VMTK) (Antiga et al., 2008), which integrates tools for image processing, morphometric analysis and mesh generation techniques in an open-source platform. Its code based functionality allows scripting for efficient processing of multiple input files. Within the scope of this thesis, I wrote respective scripts allowing to run sequential tasks on multiple files in VMTK via MATLAB (The MathWorks, Natick, MA). For re-meshing, the *vmtksurfacere meshing* function was used by varying the *area factor* parameter. In order to reduce small-scale bumps and surface irregularities stemming from the initial segmentation, meshes were smoothed using the *vmtksurfacesmoothing* function, which applies a passband filter. Final meshes were visualised in ParaView (Ahrens et al., 2005).

### 3.4 Alignment

Shape is defined as a property that is invariant to translation, rotation and scaling, and shape changes induced by any of these global transformations should not be modelled (Heimann and Meinzer, 2009). Therefore, it is important to align, i.e. rigidly register all surface meshes in a common reference (coordinate) system such that translational and rotational effects are minimised.

After manual pre-alignment of the exported surface meshes to one common reference subject mesh, the *vmtkicpregistration* function was used to automatically align each surface mesh to the chosen reference mesh by applying translation and rotation only (Fig. 3.6). The algorithm is based on a method proposed by Besl et al in 1992 (Besl and McKay, 1992), which makes use of the *iterative closest point* (ICP) algorithm. This algorithm iteratively minimises the Euclidean distances between two point, line or surface sets. Further details about the alignment procedure will be discussed in Chapter 4.3.2.2.

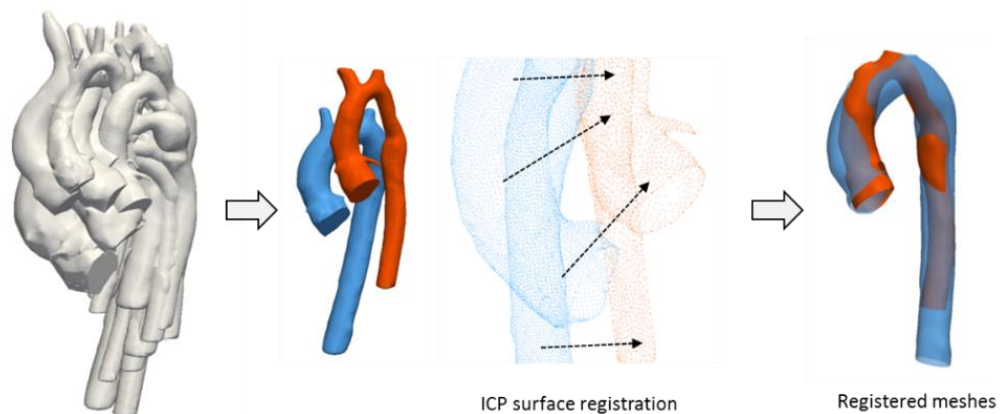


Fig. 3.6: Alignment (rigid registration) of surface meshes

### 3.5 Morphometry – conventional shape analysis

Traditional morphometry on 2D image slices was carried out on the DICOM data in Mimics, using ruler and diameter measuring tools (Fig. 3.7). In that way, lengths and diameters were measured manually as usually done in clinical practice.

3D shape parameters were measured automatically on the 3D surface meshes using VMTK functions in combination with MATLAB. Geometric parameters included volume  $V$  and surface area  $A_{surf}$ , extracted via the *vmtksurfaccmassproperties* function as well as parameters associated with the vessel centreline such as centreline length  $L_{CL}$ , curvature  $C$  and tortuosity  $To_{CL}$ , and inner vessel diameters along the centreline  $D_j$  (Fig. 3.8).

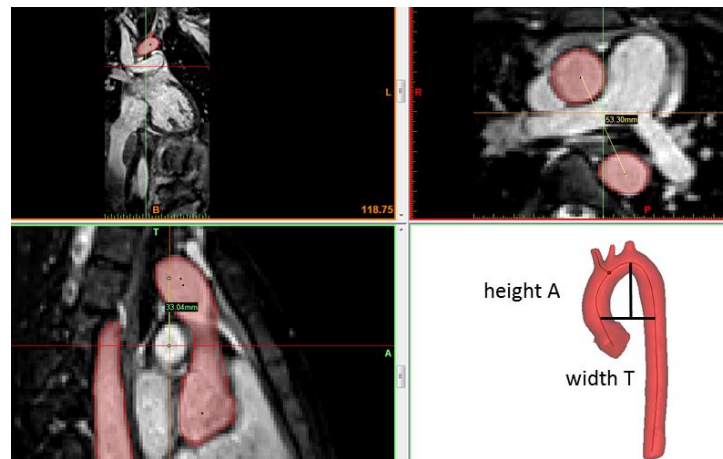


Fig. 3.7: Manual measurements of aortic arch height  $A$  and width  $T$  on CMR image slices in MIMICS (Materialise, Leuven, Belgium)

These were extracted via the `vmtkcenterlines` and `vmtkcenterlinegeometry` functions in VMTK. Note that the curvature measures the deviation of a curve from a straight line. At a given point of the centreline, curvature is the inverse of the radius of an inscribed circle tangent to the point (Piccinelli et al., 2009). Tortuosity is defined as the relative increment of the length of a curve deviating from a rectilinear line and calculated as  $To_{CL} = (L_{CL}/U) - 1$ , where  $U$  is the shortest distance between centreline start and end points. Further mathematical details are given in (Piccinelli et al., 2009) and (Antiga and Steinman, 2004).

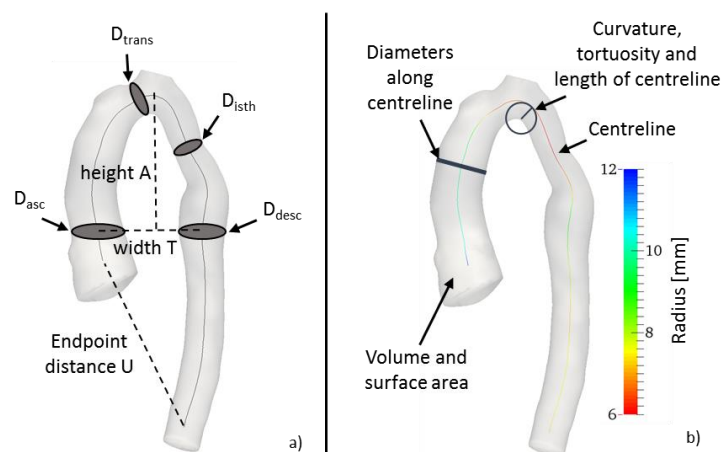


Fig. 3.8: 3D morphometric parameters describing aortic arch shape, adapted from (Bruse et al., 2016a)

### 3.6 A novel shape analysis method based on mathematical currents

As outlined in Chapter 2.1, many commonly applied methods for building a SSM in cardiac research can be classified as *parametric* methods. The major limitation of parametric models such as the PDM is that they rely on accurate landmarks, which need to ensure point-to-point correspondence between the shape representations. Particularly manual landmarking is error-prone, time-consuming and might introduce a bias, depending on how landmarks are positioned on the shapes to be analysed. (Mansi, 2010), (Huysmans et al., 2010)

The novelty and advantage of the approach used in this thesis is that neither prior landmarking nor point-to-point correspondence of the input shapes are necessary. This approach belongs to the class of *non-parametric* methods, which instead of directly looking at parameterised shapes, analyses how a representative atlas (here called an ideal “*template*”) *deforms* into each of the shapes that are present in the population. Hence, the focus does not lie on the shapes themselves but on the *transformations* that deform the atlas. (Durrleman et al., 2009)

In a simplified way, one could imagine an “ideal, prototype” aorta that – by applying the correct transformations – can be deformed into any possible aorta shape. This idea goes back to D’Arcy Thompson, who demonstrated in 1917 that only via mathematical transformations (via a change of the coordinate system) the shape of the existing porcupine fish can be transformed into the shape of a sunfish – another actually existing fish (Thompson, 1945), (Fig. 3.9).

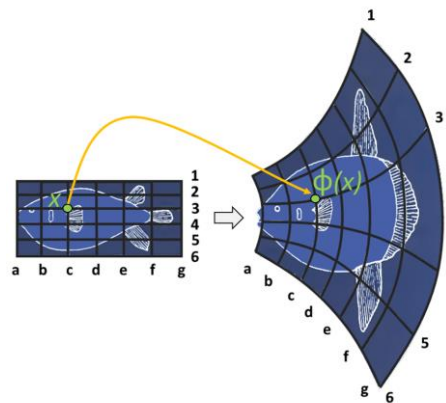


Fig. 3.9: Mathematical transformations  $\phi$  define the shape of fishes, adapted from (Thompson, 1945)

The problem of deforming a template shape towards an individual's shape becomes a *registration* problem. In medical image analysis, *registration* refers to finding an optimal geometric transformation that maximises the correspondence between two objects. Usually, a registration method consists of three components (Rueckert and Aljabar, 2010):

- A *similarity metric* measuring the *degree of correspondence* (alignment) between objects; in case of surfaces this can be the distance between corresponding surface features (with small distances being equal to a good correspondence)
- A *transformation model* defining the geometric transformation; the model can be *rigid* or *non-rigid* and suitable for small or large deformations
- An *optimisation method* that maximises (or minimises) the similarity metric

As mentioned above, there are different types of transformations. In general, geometric transformations define how the coordinates of two objects are related. A single coordinate transformation  $\phi$  maps each point  $x$  belonging to one object to a corresponding point  $\phi(x)$  on the other object, (Fig. 3.9). If this transformation can be achieved by only applying simple *translation*, *rotation* and *scaling*, the transformation is called *rigid*. In this case,  $\phi(x)$  can be written as a *linear combination* of the input coordinates. In *non-rigid* transformations, no such linear model exists, so that commonly a spatially varying displacement field  $u$  is used to describe the transformation;  $\phi(x)$  becomes  $\phi(x) = x + u(x)$ . (Rueckert and Aljabar, 2010)

By applying a *non-parametric SSM* using *non-rigid transformations* of a template towards each observation in the population, the entire 3D shape of objects can be assessed without introducing any prior knowledge. The difficulty however is to estimate the ideal template shape. The following sections will outline some concepts behind each of the components that are used here to build a SSM using *non-parametric registrations* of shapes.

### 3.6.1 Approaches to derive an anatomical mean or template shape

Generally, there are two different possibilities to construct an unbiased, ideal template of a population of shapes. The *backward approach* calculates the template as the average of the deformed objects plus some residuals that account for shape variability, which is not captured by the model. Let  $T_i$  be the computational representation that approximates the actual shapes  $S_i$  of the patient number  $i$ . Note that in the following, *shapes* are modelled as *surfaces* (represented by a computational surface mesh, (Fig. 3.5)). The *transformation* that maps  $T_i$  to the ideal template  $\bar{T}$  is denoted  $\phi_i$  and the residuals are written as  $\varepsilon_i$ . The ideal template  $\bar{T}$  can then be obtained from (Mansi, 2010):

$$\bar{T} = \phi_i(T_i) + \varepsilon_i \quad (3.1)$$

*“Template = Deformed Subject + Residuals”*

Starting from the observations (all shapes present in the population), the template  $\bar{T}$  can be calculated using iterative averaging techniques. However, there are uncertainties associated with this technique as it is not straightforward how to map back the residuals associated with each shape. It is not evident how to distinguish between actual shape variations of interest and variations due to noise and data artefacts – introduced by the initial image data, for example. (Mansi, 2010)

To overcome these issues, the *forward approach* reverses Eq. 3.1, such that the starting point is now an initial ideal template  $\bar{T}$  and each observation  $T_i$  is represented by transformations  $\phi_i$  of the template plus some residuals (Mansi, 2010):

$$T_i = \phi_i(\bar{T}) + \varepsilon_i \quad (3.2)$$

*“Subject = Deformed Template + Residuals”*

This reflects the initial idea of an ideal template that is able to deform into each of the shapes present in the population. The transformation  $\phi_i$  is the crucial component as it maps the template towards each individual observation and thereby encodes most of the shape information that is represented by the template.

The residuals  $\varepsilon_i$  correspond to shape features such as small topological changes or image artefacts that are not captured by the template or the deformations. This makes it easier to control for undesired residuals. To represent shapes (observations), deformations and residuals consistently in a SSM, a complex mathematical shape registration framework is necessary, which is introduced in the next section. (Mansi, 2010)

### 3.6.2 A framework based on mathematical currents

The novel method presented by Mansi, McLeod et al makes use of a SSM framework proposed by Durrleman et al (Durrleman et al., 2009), which employs *mathematical currents* as a non-parametric representation of shapes. Furthermore, it computes the ideal template and the deformations simultaneously and consistently and allows for easily controlling the shape information that is captured by both template and deformations.

The use of currents for SSMs in analysing anatomy was introduced by Glaunès and Vaillant in 2005 (Vaillant and Glaunès, 2005). Currents act here as a *similarity metric* measuring the similarity between computational meshes without assuming point-to-point correspondence. Mathematically, a current is a continuous linear mapping  $\omega$  from a vector space  $W$  to  $\mathbb{R}$ , thus it integrates vector fields. Vector spaces are mathematical structures formed by vectors, where certain rules of addition and multiplication of vectors apply. The current of a surface  $S$  is defined as the *flux of a test vector field* across that surface. The resulting shape  $T$  (the representation or surrogate of  $S$ ) is uniquely characterised by the variations of the flux as the test vector field varies. The definition of currents related to a flux stems from Faraday’s law in

electromagnetism, where a varying magnetic field induces a current in a wire (Durrleman, 2010). As the flux is a real number, each shape is characterised by a collection of real numbers within the same framework or coordinate system for all possible test vector fields. (Mansi, 2010), (Durrleman, 2010)

An analogy to currents representing shapes could be probing an object with a 3D laser scanner or beam (the “test vector field”) with a certain direction from all possible angles or positions around the object (Fig. 3.10). The shape is then characterised by how it deflects or repels (i.e. “integrates”) the laser beam at its surface and results are collected in the form of currents. Currents could thus be seen as an “indirect”, surrogate measure of shape as they model geometric objects via their action on a test vector field. (Durrleman, 2010)

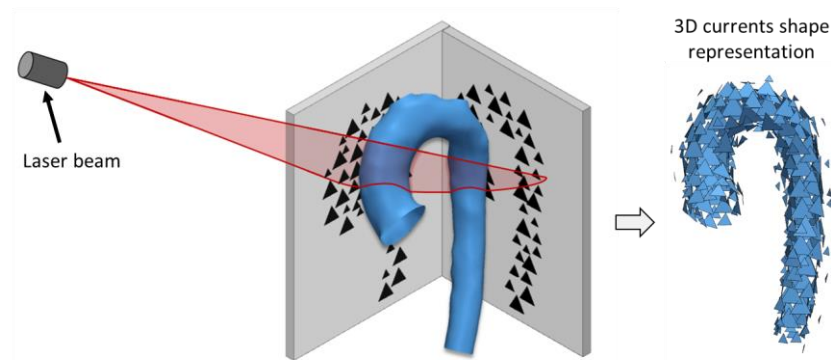


Fig. 3.10: Laser beam probes arch surface mesh to obtain shape representation in the space of currents, adapted from (Bruse et al., 2016a)

The crucial step is to define the test vector fields within a vector space, which is generated by a *Gaussian kernel*. In the univariate case, kernels are often used to obtain a smoother probability density estimate of a distribution than the histogram representation (Izenman, A. J., 2008), Fig. 3.11. Both give an intuitive idea of how likely a certain parameter value occurs within a population. Based on this idea, shape modelling via currents considers objects as a *distribution of shape features* without assuming any parameterisation. (Durrleman, 2010)

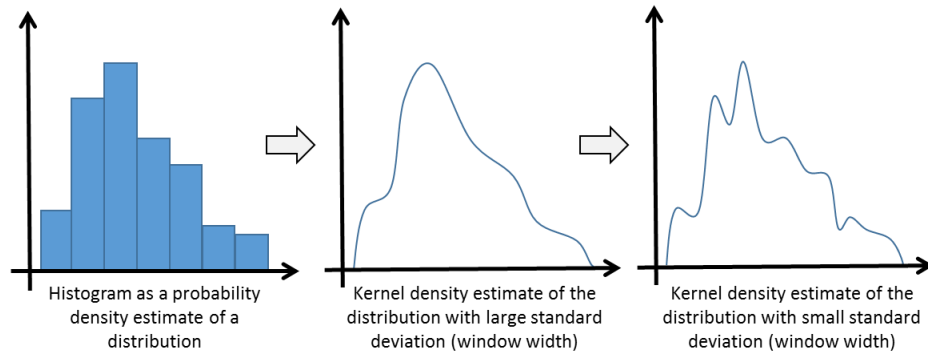


Fig. 3.11: Effect of kernels to capture features of a distribution (coarse to smooth) adapted from (Izenman, A. J., 2008)

In the multivariate case, the Gaussian kernel is typically a similarity measure between features. Everything with certain features that can be described by vectors can be compared by means of a kernel. The Gaussian kernel  $K_W$  that is used here is defined for any points  $x$  and  $y$  as (Mansi, 2010):

$$K_W(x, y) = e^{-\frac{\|x-y\|^2}{\lambda_w^2}} \quad (3.3)$$

The important parameter of this function is the *standard deviation* or *window width*  $\lambda_w$  which is the typical scale at which the vector fields can vary spatially. Therefore,  $\lambda_w$  defines the *smoothness* of the kernel – if  $\lambda_w$  is chosen too small, too many features are picked up and noise dominates whereas if  $\lambda_w$  is chosen too large, the function becomes so smooth that important features might not be picked up. The parameter  $\lambda_w$  allows to control the similarity metric and thus the measure of “distances” between shapes in this framework (Durrleman, 2010). The influence of kernel widths  $\lambda$  on the final SSM results will be investigated in Chapter 4.3.2.3.

Using the Gaussian kernel as defined in (Eq. 3.3) a vector space called *space of currents* can be built (mathematical details can be found in (Mansi, 2010) and (Durrleman, 2010)) and within this space, each surface that is represented by a computational mesh can be decomposed into its *current representation*  $T$  as the finite sum

$$T(\omega) = \sum_i \delta_{x_i}^{a_i}(\omega) \quad (3.4)$$

with  $\omega$  being the test vector field and  $\delta_x^a$  being a so called *Dirac delta current*. A Dirac delta current can be seen as an infinitesimal vector that is concentrated at the barycentres of the mesh faces  $x_k$  with their respective normal orientation  $a_k$  (Fig. 3.12). Durrleman et al developed an efficient “greedy” algorithm approximating each surface by a minimal yet optimal set of Dirac delta currents to keep the computational complexity low (Durrleman et al., 2009).

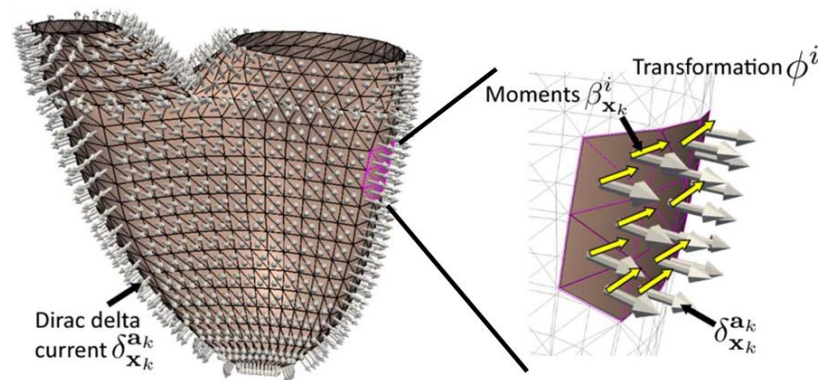


Fig. 3.12: Dirac delta currents as shape representations and moment (deformation) vectors  $\beta$  defined on currents drive the transformations, adopted from (Mansi et al., 2011), © 2011 IEEE

The user can control the resolution of the currents representation by changing the above mentioned parameter  $\lambda_w$ . The larger  $\lambda_w$ , the higher the spatial variation in the vector field and the coarser the resolution of the shape representation. Therefore,  $\lambda_w$  is here defined as the *resolution* of the shape analysis (Fig. 3.13).

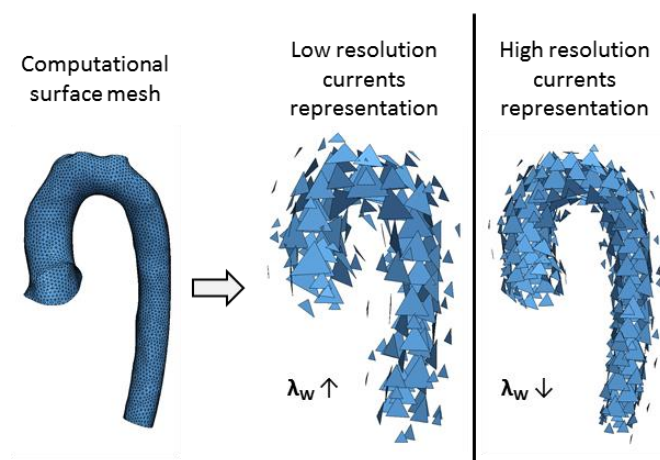


Fig. 3.13: Shape model of an aorta represented by currents; changing resolution  $\lambda_w$ , adapted from (Bruse et al., 2016a)

As currents are linear applications, the distance between two shapes can simply be computed as the difference between their currents. Hence, the space of currents allows to compute means, standard deviations and other descriptive statistics on 3D shapes. The empirical mean shape  $\bar{T}$  for example, can be simply computed by averaging over the individual currents  $T_i$  as shown in (Eq. 3.5) for a total of  $N$  input shapes (Durrleman et al., 2009):

$$\bar{T} = \frac{1}{N} \sum_{i=1}^N T_i \quad (3.5)$$

### 3.6.3 Defining the transformation function

Now that an appropriate representation of the shapes as currents is defined, a suitable *transformation model*  $\phi_i$  has to be found, which deforms the template shape towards the shape of each individual patient, Fig. 3.14. Here, the function  $\phi_i$  is defined using the *Large Deformation Diffeomorphic Metric Mapping* (LDDMM) approach (Beg et al., 2005). Diffeomorphic transformations are transformations that are smooth and invertible and thus crucial to ensure one-to-one mapping of two shapes (Durrleman, 2010), (Mansi, 2010).

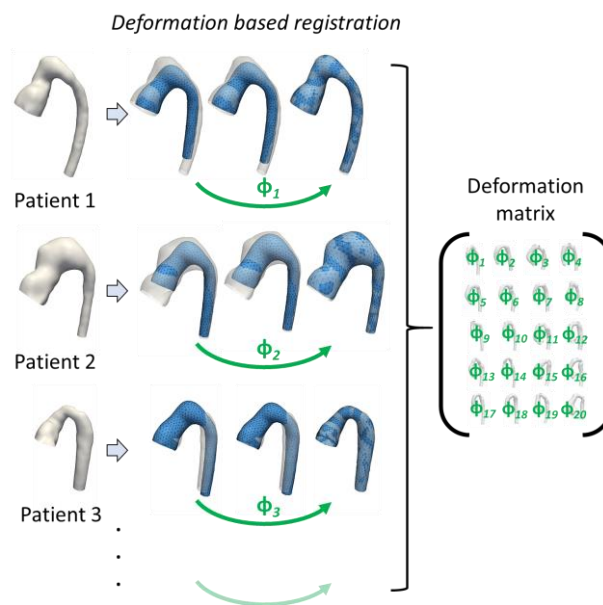


Fig. 3.14: Each subject shape is uniquely parameterised by its deformation function  $\phi$ ; all deformations concatenated in a matrix describe all 3D shape information within the population, adapted from (Bruse et al., 2017a)

To guarantee the consistency of the analysis, no material loss or change in topology is allowed. The transformation function  $\phi_i$  is computed by integrating the Lagrangian transport equation (see (Mansi, 2010) for details) and is determined by an *initial velocity field*  $v_o^i(x)$ , which is again defined within a vector space  $V$ , generated by another Gaussian kernel  $K_V$ , similar to Eq. 3.3:

$$K_V(x, y) = e^{-\frac{\|x-y\|^2}{\lambda_V^2}} \quad (3.6)$$

The initial velocities  $v_o^i(x)$  are associated with *moment* or *deformation vectors*  $\beta_i$ , which contain the initial kinetic energy that is necessary to cover the path of a transformation from one Dirac delta current to the other. Hence, for a computational surface mesh, moments are defined at the barycenters  $x_k$  of the Dirac delta currents and “drive” the transformation, see also Fig. 3.12 above. (Mansi, 2010)

Similar to the kernel width  $\lambda_W$  in Eq. 3.3, the kernel width  $\lambda_V$  controls the smoothness of the initial velocity field  $v_o^i(x)$  and thus of the transformation  $\phi_i$ . Intuitively,  $\lambda_V$  affects the size of the region of the shapes that is deformed consistently – the larger  $\lambda_V$ , the more *global* (“stiffer”) the deformation; the smaller  $\lambda_V$ , the more *local* (“less stiff”) the deformation. Therefore,  $\lambda_V$  will be referred to as the *stiffness* of the transformation. (Mansi et al., 2011). In the SSM framework *Deformetrica*,  $\lambda_V$  controls the number of so-called *control points*  $n_{CP}$ , i.e. the number and coordinates of the anchor points of the deformation vectors  $\beta_i$ .

The patient-specific transformation functions  $\phi_i = f(\beta_i)$  finally contain all 3D shape information present in the patient population, expressed as a unique deformation of the template shape. Combining the deformation vectors in one deformation matrix, yields a numerical data set of all 3D shape features within the population, which then allows further statistical analysis, see Chapter 3.7, Fig. 3.14.

### 3.6.4 Computing the template

The template  $\bar{T}$  and the associated transformations  $\phi_i$  are computed simultaneously using an alternate two-step minimisation algorithm, constituting the *optimisation*

*method* here. In simple terms, the aim is to minimise the distance between the deformed template and its respective target shape object in the space of currents, in the sense of a registration as outlined in Chapter 3.6.3. Eq. 3.7 shows the actual minimisation problem, which is solved iteratively (Mansi, 2010).

$$(\bar{T}, \phi_i) = \operatorname{argmin}_{\bar{T}, \phi_i} \left\{ \left\| \phi_i(\bar{T}) - T_i \right\|_W^2 + \tau \sum_{i=1}^N \left\| v_o^i \right\|_V^2 \right\} \quad (3.7)$$

The first term denotes the distance between the deformed template  $\phi_i(\bar{T})$  and the target shape  $T_i$ , which is to be minimised. The second term is a regularisation term associated with the transformation function  $\phi_i$ , which is typically introduced as a penalisation term to avoid overfitting. (Mansi, 2010)

To start the algorithm, an initial template shape has to be assumed. Typically, the template is initialised as the average of all the currents present in the population (the “mean shape”), see Eq. 3.5. Once the initial template is computed, Eq. 3.7 is first minimised *with respect to the transformations*  $\phi_i$  registering the initial template to each target shape independently (“first step”). Then the new, updated template is calculated based on those transformations and the initial template, in order to minimise equation Eq. 3.7 *with respect to the template*  $\bar{T}$  (“second step”). The second step aims to reduce the overall registration error and yields a template that is more centred with respect to the target shapes. This process is iterated until convergence. (Mansi, 2010)

The ideal template and its deformations towards each individual shape constitute the entire computational atlas containing mean shape and variations around the mean as represented by deformations of the template. Note that both template  $\bar{T}$  and transformations  $\phi_i$  are calculated based on currents in a vector space, not on the actual computational meshes. Therefore, results from the space of currents have to be mapped back to the Euclidean space of the computational surface meshes.

With the template  $\bar{T}$  and its transformations  $\phi_i$  towards each subject shape the currents-based SSM is defined. The entire SSM framework is published under the name “*exoshape*” (<https://team.inria.fr/asclepios/software/exoshape>) as a MATLAB code

(Mansi et al., 2011), (McLeod et al., 2013) and recently, under the name “*Deformetrica*” ([www.deformetrica.org](http://www.deformetrica.org)) (Durrleman et al., 2014) as libraries in C. In this thesis, *exoshape* was used for the work presented in Chapters 4-5 and *Deformetrica* for the following chapters as *Deformetrica* allowed me to reduce computational time for template and deformation estimation by more than 80%.

### 3.7 Data processing of SSM results: supervised and unsupervised approaches

The previous section described how to compute the template  $\bar{T}$  (i.e. the “anatomical mean shape”) and its transformations  $\phi_i$  towards each subject shape within a population. The output of this process is the template shape given as a surface mesh and a set of deformation vectors  $\beta$ , with each  $\beta_i$  sized  $3 \times n_{CP}$  ( $n_{CP}$  is the number of control points or number of deformation vectors, see 3.6.3) describing the unique deformation of  $\bar{T}$  towards each subject shape  $i$ , stored in a text file. The deformation vectors are thus a numerical representation of each input 3D shape within the same reference system, on the basis of a common template shape and allow further mathematical analysis.

Similarly as for the PDM (Chapter 2.1.2), principal component analysis (PCA) was used here to extract dominating features or patterns of 3D shape variability based on the deformation vectors. In the sense of a multivariate analysis, PCA can be considered a *descriptive* and *unsupervised* technique revealing structure and patterns, without the need for any prior knowledge or labelling of the data (Izenman, A. J., 2008). Furthermore, *partial least squares* regression (PLS) was used to find 3D shape features *most correlated* with a given continuous or discrete external parameter. Hence, PLS is a *predictive* and *supervised* technique trying to establish relations between variables, which requires additional information about the data to be analysed, such as known classes or covariates (Izenman, A. J., 2008). Both PCA and PLS have been used before in conjunction with the currents-based SSM framework (Mansi et al., 2011). In this thesis, I added unsupervised *hierarchical clustering* as a post-processing technique in order to automatically detect previously unknown shape clusters of patients with similar

anatomical shape within the 3D shape information provided by the deformation vectors, see Chapter 8.

### 3.7.1 Unsupervised principal component analysis (PCA)

PCA finds basis vectors of the space of the initial velocity fields  $v_o^i(x)$  (encoding the transformation of the currents) that best explain their variance (Mansi, 2010), (Mansi et al., 2009). Similar to Chapter 2.1.2, an eigenvalue problem is solved to compute the eigenvectors  $p$  with eigenvalues  $\mu$  according to

$$C \cdot p = p \cdot \mu \quad (3.8)$$

Here, the covariance matrix  $C$  is a function of the deformation vectors  $\beta$ ,  $C(\beta)$ . Let  $\{\beta\}$  be the *deformation matrix*, built from stacking all  $\beta^i$  to a matrix of size  $3 \times n_{CP} \times N$ , with  $N$  being the number of patient shapes. The deformation matrix  $\{\beta\}$  is first *centred* with respect to the mean deformation  $\bar{\beta}$ , with the centred deformation matrix  $\{\hat{\beta}\}$  defined as

$$\{\hat{\beta}\} = \{\beta\} - \bar{\beta} \quad (3.9)$$

For easier handling,  $\{\hat{\beta}\}$  (of size  $3 \times n_{CP} \times N$ ) is then reshaped into a two dimensional matrix of centred deformation vectors  $\{\hat{\beta}\}_{deformation}$  of size  $N \times (3 \cdot n_{CP})$ , which is used for the PCA decomposition. The covariance matrix  $C$  of size  $N \times N$  is now

$$C = \text{cov} \left( \left\{ \hat{\beta} \right\}_{deformation}^T \right) \quad (3.10)$$

and is used for the eigendecomposition to compute the eigenvectors  $p$ , sorted from high to low variance, according to the computed eigenvalues  $\mu$ . Usually, only the first  $K$  eigenvectors are retained, which explain a certain amount of the total variance (e.g. 90%) (Jolliffe, I.T., 2002). With these, the  $m^{\text{th}}$  PCA shape mode  $l_{PCA}^m$  is computed with  $m \in [1, K]$ , as (Mansi, 2010)

$$l_{PCA}^m = \sum_{i=1}^N p_i^m \cdot \hat{\beta}_i \quad (3.11)$$

with  $p_i^m$  being the  $i^{\text{th}}$  element of the  $m^{\text{th}}$  eigenvector of  $C$ . Each PCA shape mode  $l_{PCA}^m$  is of size  $3 \times n_{CP}$  and is a deformation vector itself. By deforming the template shape  $\bar{T}$  along the  $m^{\text{th}}$  mode with

$$\bar{\beta} \pm t\sqrt{\mu} \cdot l_{PCA}^m \quad (3.12)$$

the shape variability captured by the  $m^{\text{th}}$  mode can be visualised as a deformation of the template mesh around the mean with  $\pm t$  standard deviations (SD), for instance. All calculations were performed in MATLAB and PCA mode deformations of the template were visualised in ParaView.

To be able to quantitatively determine how 3D shape features described by the  $m^{\text{th}}$  PCA shape mode compare with an individual's 3D shape, the so-called *PCA shape vector*  $f_{i,PCA}^m$  can be computed by projecting each subject shape onto the mode. This is achieved by calculating the scalar product between the patient deformations and the  $m^{\text{th}}$  PCA shape mode (Mansi, 2010), (Mansi et al., 2011):

$$f_{i,PCA}^m = \langle \beta_i, l_{PCA}^m \rangle \quad (3.13)$$

The shape vector entries can thus be seen as the “weights” of a certain shape mode (see Eq. 2.4) and quantify how much of the mode's shape features are contained within a patient's shape. Shape vectors therefore provide a low dimensional parameterisation of a patient's 3D shape, reducing thousands of surface mesh nodes down to hundreds of deformation vectors and ultimately down to tens of shape vector entries or – in case of analysing one shape mode only – down to one single number. Shape vectors thus allow applying further statistical analyses on 3D shapes and are the essential quantity used in this thesis to analyse associations between 3D shape and function, see Chapter 4.

### 3.7.2 Supervised partial least squares regression (PLS)

PCA is a common technique used in statistical shape analysis to describe shape variability. PCA breaks down the shape variability at hand into its main contributors according to mathematical rules, without considering any additional information.

Results could thus be influenced if some other source of variability (such as a new patient with an abnormal or overly large shape) is added, leading to neglect of potentially important shape features with lower variance. (Mansi, 2010)

To overcome these issues, *partial least squares* (PLS) regression was introduced and has been shown to yield more compact results by finding the minimal number of *relevant* shape modes (Mansi et al., 2011), (McLeod et al., 2013). PLS combines dimensionality reduction in the fashion of a PCA with linear regression techniques. It is a supervised technique and allows the extraction of dominant 3D shape features, which *correlate most* with a specific response variable, thus avoids potentially discarding shape information with low variance.

Given two sets of variables  $X$  (predictors) and  $Y$  (response), PLS computes the shape modes which best explain the variance of  $X$ ,  $Y$  and the covariance of  $X$  and  $Y$  (Hastie et al., 2009), (Singh et al., 2014). As predictor matrix  $X$  the centred deformation matrix  $X = \{\hat{\beta}\}_{deformation}$  (see Eq. 3.9) that parameterises subject-specific 3D shape features was used. As response variables  $Y$ , any external – here functional – parameter such as blood pressure, for example, can be used. PLS was performed using the *plsregress(X,Y)* function in MATLAB, which yields the  $(3*n_{cp}) \times m$  matrix of predictor loadings  $X_L$  containing coefficients used for a linear combination of the  $m$  predictor scores  $X_S$  to approximate the original predictors  $X$ . Thereby  $X$  and  $Y$  are approximated by (The Mathworks, Inc., 2016)

$$X \cong X_S \cdot X_L^T \quad (3.14)$$

$$Y \cong X_S \cdot Y_L^T \quad (3.15)$$

and

$$Y_S = Y \cdot Y^T \cdot X_S \quad (3.16)$$

with  $Y_L$  containing the response coefficients and  $Y_S$  being the response scores i.e. the linear combinations of  $Y$  with which the  $X_S$  have maximum covariance.

Mathematical details regarding the PLS algorithm can be found in (Mansi et al., 2011) and (Mansi, 2010). From the loadings  $X_L$ , the PLS shape modes  $l_{PLS}^m$  can be constructed, similarly to above. The  $l_{PLS}^m$  were ordered according to their correlation with the response variable  $Y$ , with the first one being most correlated and accounting for a certain percentage of variability in both the response  $Y$  and the predictors  $X$ . Similarly to Eq. 3.13, the *PLS shape vector*  $f_{i,PLS}^m$  can then be derived from the scalar product (Mansi, 2010)

$$f_{i,PLS}^m = \langle \hat{\beta}_i, l_{PLS}^m \rangle \quad (3.17)$$

projecting each patient deformation onto the PLS shape modes. Each PLS shape vector entry describes how much of the 3D shape information captured by the PLS shape mode is contained within a patient's shape. Since a PLS shape mode captures shape features *most associated* with a given external response parameter  $Y$  such as high or low blood pressure, for example, direct correlations between the patients' 3D shapes and blood pressure response can be studied. This concept will be used for shape biomarker derivation in Chapter 4.

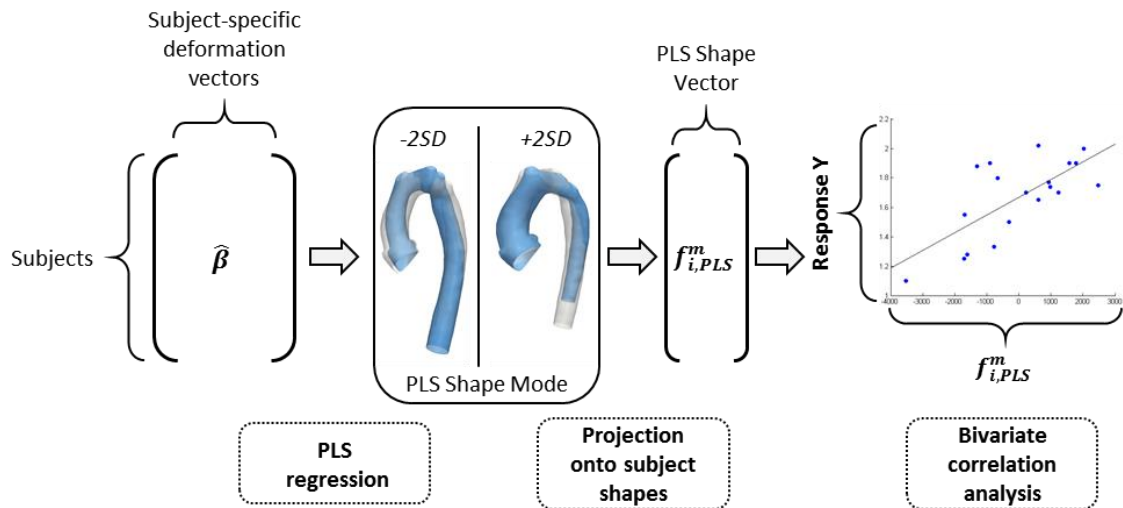


Fig. 3.15: Shape data processing via PLS regression for visual and numerical shape feature extraction, adapted from (Bruse et al., 2016a)

Note however, that PLS is not symmetric, which means that  $Y = f(X)$  cannot be easily inverted to  $X = f(Y)$ . In fact, PLS yields a model *clinical parameter* =  $f(\text{shape})$  predicting the response parameter based on the shape, not vice versa.

### 3.7.3 Hierarchical clustering for sub-group detection

Hierarchical clustering is a data mining technique used to detect underlying patterns and structure within a larger dataset without any prior knowledge. Specifically, it is able to uncover similarities among subjects, each defined by a characteristic set of features (here 3D shape features parameterised by the deformation vectors  $\beta_i$ ). Similar subjects form a cluster or confined subgroup and are grouped close together in one branch of the clustering tree, while dissimilar subjects are placed on another branch. In this way, a hierarchical structure, the *dendrogram*, is built, which provides an intuitive visual representation of previously unknown clusters within the data. At the lowest level of the hierarchy, each subject forms a single cluster by itself. (Hastie et al., 2009)

Within this thesis, hierarchical clustering strategies were applied for the first time to the deformation vector data provided by the currents-based SSM. A detailed description of the methodology is provided in Chapter 8.

## 3.8 Clinical and functional parameters

To analyse the clinical relevance of 3D anatomical shape features derived via the currents-based SSM approach as detailed above, associations with external, cardiac functional parameters need to be assessed. The following describes briefly key functional aspects of the heart and some of the clinically used parameters included here as response parameters for the SSM, serving as descriptors or surrogates of “cardiac function”.

The heart is essentially a sophisticated muscle that – in case of a healthy, normal heart – pumps, via its left side, oxygenated blood to the systemic vascular system and via its right side deoxygenated blood into the pulmonary system. Each side is two-chambered, consisting of an atrium serving as a reservoir and a ventricle creating the driving force to eject blood into the great vessels: the pulmonary artery on the right and the aorta on

the left side. Atria and vessels are separated from the ventricles by valves. The pump function is characterised by repetitive phases of myocardial contraction and ventricular emptying or *ejection*, called *systole*, and myocardial relaxation and ventricular filling, called *diastole*. *Systole* starts with contraction, i.e. myocardial deformation and motion and a subsequent rise in ventricular pressure. Once this pressure is higher than the pressure in the receiving vessel (afterload), the valve between ventricle and vessel opens and ejection of blood occurs accompanied by a decrease of ventricular volume, until the pressure relation is reversed and the valve closes again. (Bogaert et al., 2012)

### 3.8.1 Cardiac function

The heart's ability to drive blood through the vascular system is often paraphrased by the term "cardiac function" and is crucial for the clinical assessment of patients suffering from CHD, where this function may be severely impaired. Since the focus of this thesis is the shape of the aortic arch and potential associations between arch shape and cardiac function, I focus in this section on functional parameters associated with the *left side* of the heart only, concerning the pump function of the left ventricle (LV).

Following the description above, LV pump function and the amount of blood being ejected during systole are directly related to changes in left ventricular volume, occurring during ejection (volume decrease) and filling phase (volume increase). In clinical practice, systolic cardiac function or "global ventricular performance" (Bogaert et al., 2012) is therefore assessed by measuring ventricular volumes from CMR image data at the time of maximal filling (end of diastole, largest volume) and maximal emptying (end of systole, smallest volume). The difference between *end-diastolic volume* (EDV) and *end-systolic volume* (ESV) yields the *stroke volume* (SV), which represents the amount of blood ejected during systole. Multiplying SV with the heart rate (HR) yields the total *cardiac output* (CO) in [ml/min]. (Bogaert et al., 2012)

### 3.8.2 Ejection fraction

One of the key cardiac functional parameters is *ejection fraction* (EF): it is calculated as  $EF = SV/EDV$  and describes the percentage of the maximal volume (EDV) that is ejected during systole. Low EF thereby characterises a decreased pumping efficiency. Values for

left ventricular EF (LVEF) between 40% and 50% are often referred to as “reduced LVEF”, while anything above 50% typically describes “preserved LVEF” (Bhatia et al., 2006).

### 3.8.3 Left ventricular mass and left ventricular hypertrophy

Another functional parameter associated with ventricular performance obtainable from CMR image data is *left ventricular mass* (LVM), which is thought to increase in the presence of pressure or volume overload of the ventricle (Katz, 1990), (Gardin and Lauer, 2004). High indexed LVM values above 116g/m<sup>2</sup> for men or above 104g/m<sup>2</sup> for women (Cuspidi et al., 2010) mark *LV hypertrophy* (LVH), i.e. a pathological increase of cardiac muscular mass. LVH is an important independent risk factor for adverse cardiac events (Levy et al., 1990), (Verdecchia et al., 1998), (Lorell and Carabello, 2000), (Vakili et al., 2001), (Bluemke et al., 2008), (Takx et al., 2017) and has particularly been associated with the presence of CoA posing an obstruction for the LV that leads to a higher workload and subsequent compensatory increase in muscular mass (Gunther and Grossman, 1979), (Rosenthal, 2005), (Maceira and Mohiaddin, 2012) or increased aortic stiffness in CoA (Ong et al., 1992), (Ou et al., 2008b). Another outcome marker derived from LVM that has been associated with adverse cardiac events (Bluemke et al., 2008) and CoA (Crepaz et al., 2005), (Krieger et al., 2013) is an increased *mass to volume ratio* (MVR), defined as  $MVR = LVM/EDV$  above 1.16 g/ml (Maceira and Mohiaddin, 2012).

At GOSH, all ventricular volumes (i.e. EDV and ESV) and LVM are measured manually using a *volumetric* approach on the short-axis stack by segmenting ventricular borders slice by slice at either end-diastole or end-systole, multiplying each segmented ventricular cross-sectional area by the distance between respective slices and adding up all of the created sub-volumes. For EDV and ESV, only endocardial borders are taken into account during segmentation, while for LVM the area between endocardial and epicardial border is used. The derived volume is then multiplied by the specific density of myocardium of 1.05g/cm<sup>3</sup> (Bogaert et al., 2012) to obtain LVM. In order to define which values are “low” or “high” in an adolescent population, normal ranges of

CMR-derived LVEF and LVM indexed to body surface area (Chapter 3.8.5) (iLVM) are reported in Tab. 3.1.

Tab. 3.1: Normal, averaged values for CMR-derived LVEF and iLVM for children aged 8 to 20 years. Data taken from (Sarikouch et al., 2010)

Gender	LVEF [%]	iLVM [g/m <sup>2</sup> ]
Girls (N=59)	63.4±6.1	47.6±8.2
Boys (N=55)	64.4±4.9	55.9±12.3

### 3.8.4 Blood pressure and hypertension

Another clinical parameter related to cardiac function is *blood pressure* (BP), with elevated BP marking *hypertension* (HT), a particular risk factor in patients suffering from CoA (Presbitero et al., 1987), (Cohen et al., 1989), (Hager et al., 2007), (Brown et al., 2013). At GOSH, resting systolic BP is routinely recorded during CMR acquisition using a cuff in the right arm. HT is defined by resting systolic BP values over 140mmHg (Cuspidi et al., 2010).

### 3.8.5 Body surface area

In order to account for size differences between the studied patients, *body surface area* (BSA) was used as a surrogate measure of body size. BSA was calculated following the Haycock formula (Haycock et al., 1978) (Eq. 3.18) as it was previously found to be the most suitable method for describing growth related differences of cardiovascular structures (Sluysmans and Colan, 2005). Size-dependent parameters such as EDV and LVM were accordingly indexed with BSA, denoted with a preceding lower case *i* (i.e. iLVM = LVM/BSA).

$$BSA_{Haycock} [m^2] = 0.024265 \cdot height[cm]^{0.3964} \cdot weight[kg]^{0.5378} \quad (3.18)$$

The mentioned functional parameters EF, iLVM and BP were chosen as the principal clinical parameters to be included in this thesis. They are routinely acquired and used for clinical risk stratification of CHD patients at GOSH. Data used in this thesis were retrieved from clinical CMR reports.

To summarise, low LVEF, LVH as marked by high LVM and HT as marked by high BP characterise impaired or altered cardiac function and an increased risk profile for adverse cardiac events, particularly in CHD patients affected by CoA. In patients post CoA repair, several studies suggest associations between aortic arch shape and LVH and HT (Ou et al., 2004), (Ou et al., 2006), (Ou et al., 2008a), (Lee et al., 2012), (Donazzan et al., 2014), providing the motivation for this work.

### **3.9 Modelling fluid flow via computational fluid dynamics (CFD)**

For *mechanistic* computational modelling, *computational fluid dynamics* (CFD) is used in this thesis to compute additional functional parameters related to hemodynamic performance of the aorta. Generally, modelling flow via CFD follows the mechanistic modelling pipeline as introduced in Fig. 2.6.

In the past decades, CFD has been used extensively for computing flow fields in cardiovascular structures. CFD allows solving the fundamental fluid mechanic equations numerically for complex geometries and various types of boundary conditions. Thus, the flow of blood through a vessel can be modelled *in silico* to determine the pressure drop across the vessel or the location and magnitude of peak velocity, for instance. (Caballero and Laín, 2013)

Starting point for numerical simulation of blood flow via CFD are the fundamental equations of conservation of mass, momentum and energy for a fluid particle, which can be used to determine characteristic flow variables such as velocity vectors, pressure and temperature. As heat transfer processes or temperature distributions are not of interest in this work, I neglect energetic considerations here.

#### **3.9.1 Fluid mechanics equations**

The continuity equation describing the conservation of mass can be derived from the assumption that the mass flow exiting an infinitesimal volume element must be equal to the entering mass flow, and can be written in differential form for Cartesian coordinates as (Lecheler, 2014)

$$\frac{\partial}{\partial t}(\rho) + \frac{\partial}{\partial x}(\rho \cdot u) + \frac{\partial}{\partial y}(\rho \cdot v) + \frac{\partial}{\partial z}(\rho \cdot w) = 0 \quad (3.20)$$

with  $\rho = f(x, y, z, t)$  being the density of the fluid as a function of  $x, y, z$  coordinates and time  $t$ , and  $u, v, w$  being the fluid velocities in  $x, y$  and  $z$  direction. This means that the variation of density with time together with the changes in mass flow in  $x, y$  and  $z$  direction equal to zero. Similarly, the equations characterising conservation of momentum can be derived from the equilibrium of forces of an infinitesimal volume element, here for the  $x$  direction only, as (Lecheler, 2014)

$$\frac{\partial}{\partial t}(\rho \cdot u) + \frac{\partial}{\partial x}(\rho \cdot u \cdot u + p - \tau_{xx}) + \frac{\partial}{\partial y}(\rho \cdot u \cdot v - \tau_{yx}) + \frac{\partial}{\partial z}(\rho \cdot u \cdot w - \tau_{zx}) - \rho \cdot g_x = 0 \quad (3.21)$$

with  $p$  being the pressure of the fluid,  $\tau_{xx}$  being the principal stress in  $x$  direction,  $\tau_{yx}$  being the shear stress in  $x$  direction along the surface where  $y$  is constant,  $\tau_{zx}$  being the shear stress in  $x$  direction along the surface where  $z$  is constant and  $g_x$  being the gravitational force in  $x$  direction. The stresses  $\tau$  can further be expressed as a function of velocity gradients. In Newtonian fluids, for example,  $\tau$  is proportional to the local shear velocity with proportionality factor  $\eta$  being the viscosity of the fluid, a material parameter to be defined by the user. (Lecheler, 2014)

The set of equations describing conservation of mass Eq. 3.20 and momentum Eq. 3.21 in  $x, y$  and  $z$  direction combined constitute the so-called *Navier-Stokes-Equations* (NVS), a system of coupled, non-linear differential equations, which is the basis for fully describing all flow features, i.e. all sorts of forces, shear and stresses a fluid particle experiences. Analytical solutions for the NVS only exist for certain specific flow scenarios assuming simplifications. For flow through or around complex geometries involving fluids such as blood, which has a shear rate dependent viscosity (Johnston et al., 2004), the NVS can only be solved numerically with suitable boundary conditions such as pressures and velocities defined at the inlets and outlets or other boundaries of the computational domain. Those boundary parameters can be constant or variable themselves. (Lecheler, 2014)

To further reduce complexity, one can assume certain general simplifications regarding flow characteristics. The most common simplifications concern the time-dependency of the flow, i.e. whether flow can be considered *stationary* or *non-stationary*. In stationary flows, the local velocity on a particle is only dependent on the location in the flow field. A fluid particle only experiences *convective* accelerations during its change of location while in non-stationary flows, additional *local* accelerations lead to time-dependent local velocities. Further, the fluid can be considered *compressible* or *incompressible*, where the latter refers to fluids with constant density throughout the flow field. The last crucial assumption to be mentioned here is whether flow can be considered *laminar* or *turbulent*. In laminar flows fluid particles travel on their streamlines without any mixing. In turbulent flows, there can be vortices of different size leading to mixing and transversal movements of particles, making the flow field much more complex. (Lecheler, 2014), (ANSYS Inc., 2016)

### 3.9.2 Computational fluid dynamics simulations

CFD is based on approximating solutions for the NVS via a numerical iteration process. In this thesis, the commercial software ANSYS FLUENT v17.0 was used to compute flow fields. FLUENT uses a so-called Finite-Volume approach to discretise the partial differential equations into a system of algebraic equations. Thus, the flow domain is subdivided into a computational grid or mesh of discrete control volumes represented by cell elements that are connected via nodes. In each control volume, the NVS are discretised and transferred into algebraic equations, which allow the computation of dependent variables (velocities, pressures etc.) for each cell. The discretised equations are then linearised to create a numerically solvable linear equation system for the entire flow domain. (Lecheler, 2014), (ANSYS Inc., 2016)

Under the constraints of the boundary conditions defined by the user, the flow field is then computed iteratively until convergence, reached once residuals (quantifying the imbalance between the discretised equations) fall below a certain cut-off value. This assures that all equations in all cells are fulfilled within certain tolerance limits and that

physical fluid variables of interest do not change significantly with further iterations. (Lecheler, 2014), (ANSYS Inc., 2016)

In general, it is to be taken into account that CFD solutions are always an approximation of the real flow field under the constraints of set boundary conditions, chosen material properties and underlying simplifying assumptions regarding the nature of the flow.

### 3.9.3 Three-dimensional volume meshes for domain discretisation

For complex and arbitrary geometries such as cardiovascular structures, an *unstructured* computational mesh is often used to subdivide the flow domain. Here, tetrahedral cell elements were used. Volume meshes were created in a two-step approach. First, a centreline-adaptive volume mesh was computed using VMTK and its *vmtkmeshgenerator* function, which creates volume meshes that are locally refined in regions of high curvature and small domain size, i. e. in regions where high velocity gradients occur (Fig. 3.16). In a second step, volume meshes were cleaned and improved in ANSYS ICEM.

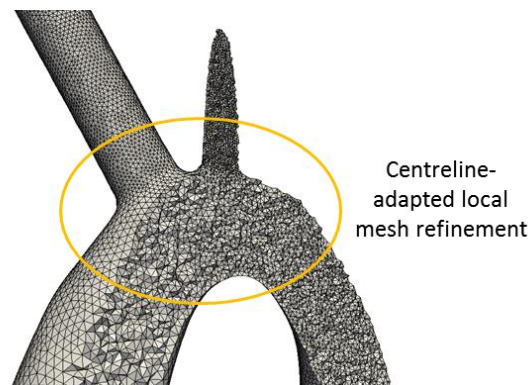


Fig. 3.16: Cross-section of centreline-adapted 3D volume mesh from VMTK

Generally, flow phenomena are resolved better, yet computational time increases dramatically, the more elements are used (Vignon-Clementel et al., 2010b). I therefore performed mesh-independence studies by volume meshing the same geometry with varying number of elements from low to high resolution prior to CFD analysis. This was done in VMTK by modifying the *edgelenghfactor* parameter in the *vmtkmeshgenerator* function. CFD runs were then performed using each of the meshes of varying size, but maintaining the same boundary conditions and material properties. Output flow

parameters of interest, such as power loss  $PL$  (see Chapter 7) across the flow domain were recorded and plotted for each of the input meshes. Mesh independency was achieved once the output variable did not differ by more than 5% from one run to the other when increasing the mesh size. The same number of cells per  $\text{mm}^3$  were then used to mesh all the other input geometries.

#### **3.9.4 Post-processing of CFD results**

The computed pressure or velocity fields and derived parameters such as shear stresses can be visualised at each point or mesh node of the fluid domain via post-processing in ANSYS CFD-Post. It allows visualisation of results in the form of pressure maps, velocity vectors or streamlines and to compute variables of interest such as the pressure difference between domain inlet and outlet or energy loss.

### **3.10 Summary**

This chapter provided a detailed description of the methodologies used in this thesis to follow both phenomenological and mechanistic computational modelling with the aim of investigating associations between shape and function in CHD. Software packages as well as fundamental concepts adopted in this thesis were described following a processing pipeline that allows extracting 3D shape features and anatomical shape clusters from medical image data, assessing their relationship with clinically used cardiac functional parameters and parameters computed via fluid flow simulations. Based on this state-of-the-art, methods are extended and refined over the following chapters. Application of the currents-based SSM in combination with PLS regression with the aim of extracting functionally relevant 3D shape features in CoA is described in detail from the user perspective in the next chapter.

## 4 Extracting three-dimensional shape biomarkers from medical images

*Part of the work described in this chapter has been published in: J. L. Bruse, K. McLeod, G. Biglino, H. N. Ntsinjana, C. Capelli, T.-Y. Hsia, M. Sermesant, X. Pennec, A. M. Taylor, and S. Schievano. A statistical shape modelling framework to extract 3D shape biomarkers from medical imaging data: assessing arch morphology of repaired coarctation of the aorta, BMC Medical Imaging, vol. 16, no. 40, May 2016. (Bruse et al., 2016a). Copyright (2016) with permissions of Springer Nature.*

As discussed in the previous chapter, the currents-based SSM offers huge potential to analyse complex, pathological shapes in 3D. However, the framework and underlying concepts have only been presented in mathematically complex terms, with only few concrete suggestions for potential users on how to run a robust and efficient analysis, thus limiting its use to technically highly skilled audiences. Furthermore, it has not been investigated how the non-parametric SSM results compare to traditionally measured morphometric parameters upon which, to date, most clinicians rely. These unresolved issues are addressed in this chapter by applying SSM methods step-by-step to extract functionally relevant “3D shape biomarkers” from medical image data of an exemplary cohort of 20 patients post coarctation repair (CoA).

## 4.1 Abstract

*Background:* In this chapter, the currents-based statistical shape modelling framework (SSM), introduced in the previous chapter, was used in combination with PLS regression to detect 3D shape features most associated with functional parameters in a cohort of repaired CoA shapes. The method is presented from the user-perspective and is evaluated by comparing results with traditional morphometric measurements.

*Methods:* Steps required to set up the SSM analysis, from pre-processing of the medical images to parameter setting and strategies to account for size differences and outliers, are described in detail. The template shape of 20 aortic arches post CoA repair was computed and partial least squares (PLS) regression was applied to the deformation vector data to extract shape patterns related to differences in body surface area (BSA) and left ventricular ejection fraction (LVEF). Resulting shape vectors, describing shape features in 3D, were compared with traditionally measured 2D and 3D morphometric parameters.

*Results:* The computed 3D template (i.e. anatomical mean shape) was close to population mean values of geometric shape descriptors and visually integrated characteristic shape features associated with the population of CoA shapes. After removing size effects due to differences in BSA between patients, distinct 3D shape features of the aortic arch correlated significantly with LVEF ( $r=0.521$ ,  $p=.022$ ) and were well in agreement with trends as shown by traditional shape descriptors.

*Conclusions:* Insight in how to set relevant SSM parameters is provided. Results were in agreement with traditional morphometrics and the combination of the currents-based SSM with PLS showed potential to discover previously unknown 3D shape biomarkers from medical image data.

## 4.2 Introduction

This chapter aims to provide a detailed description of how to run the currents-based SSM in combination with PLS regression to extract 3D shape features most associated with external (functional) parameters. Detecting such “shape biomarkers” could provide novel insight and may improve risk stratification.

Specifically, I present in a step-by-step manner how to run the analysis, highlight the influence of crucial parameters and provide guidance on how to set them to ensure robust and efficient analyses. Further, I extend the PLS regression approach so that size differences between input shapes and shape outliers can be taken into account. I also demonstrate how the SSM framework could be used to detect novel “shape biomarkers” and – for the first time – how results compare with conventional morphometric parameters.

As a relevant application, I focus here on aortic arch shapes of patients post CoA repair (O’Sullivan, 2014), (Vergales et al., 2013) as they typically present highly variable, complex shapes, which have been extensively described in terms of traditional morphometric analyses (Ou et al., 2004), (De Caro et al., 2007), (Lee et al., 2012). To demonstrate the capabilities of the proposed methods, I derive global and regional shape features potentially associated with left ventricular ejection fraction (LVEF), introduced in Chapter 3.8.2, as novel 3D shape biomarkers. CMR-derived low or reduced LVEF has been shown to be a predictor of outcomes in congenital conditions other than CoA, for instance in Tetralogy of Fallot (ToF) (Knauth et al., 2008) or hypoplastic left heart syndrome (Hughes et al., 2011). The hypothesis was that low LVEF, which characterises poor ventricular function, may be associated with distinct 3D shape patterns of the aortic arch. With this chapter I therefore aimed to answer the following questions as posed in the introduction of this thesis:

- Which parameters are relevant for the currents-based SSM framework and how can a robust and efficient analysis be ensured?

→ How do the computed SSM results compare with traditional morphometric parameters and does the method offer the potential of discovering novel 3D shape biomarkers in CHD?

### 4.3 Methods

The *exoshape* SSM framework was applied to the aortic arch shapes following the general pipeline described in Chapter 4.3. Specific steps and considerations required to set up the SSM analysis are explained in detail in the next sections (Fig. 4.1): i) Segmentation of patient CMR images to reconstruct the 3D surface models of the structures of interest; the models and CMR data were also used to compute traditional morphometric parameters (Fig. 4.1a); ii) meshing and smoothing of the segmented models to create the computational input for template calculation (Fig. 4.1b); iii) registration of the input shapes (Fig. 4.1c); and iv) setting of resolution  $\lambda_w$  and stiffness  $\lambda_v$ , which are the crucial parameters the user needs to provide along with the input shapes prior to calculating the template.

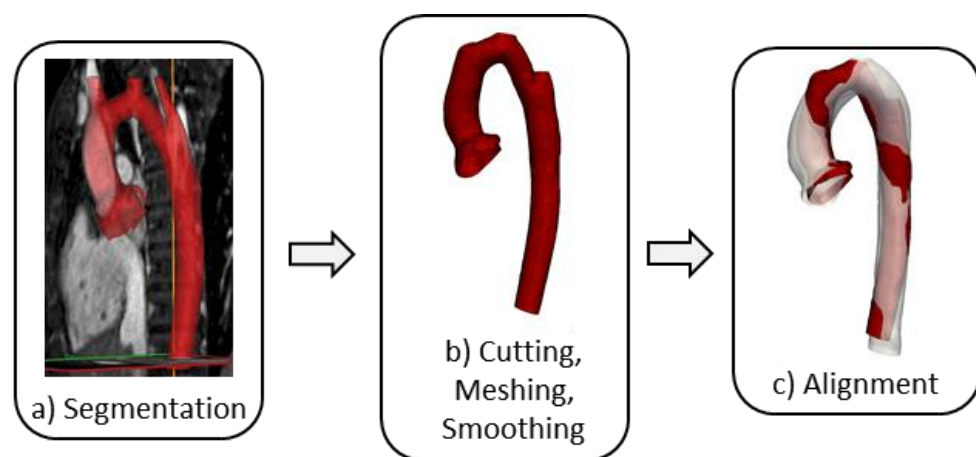


Fig. 4.1: Pre-processing steps required to prepare segmented arch models for subsequent 3D statistical shape analysis, adapted from (Bruse et al., 2016a)

After the template shape was computed, the following post-processing analyses were carried out: i) removing confounders such as size differences between subjects prior to extracting shape features related to the functional parameter LVEF as they can hide potentially important shape features; ii) accounting for outliers and influential subjects; iii) validating the template as robustly representing the mean shape of the population

and iv) analysing associations between extracted shape features (represented by shape vectors as well as by traditional 2D and 3D measured geometric parameters) and demographic (BSA) and functionally relevant parameters (LVEF) via standard bivariate correlation analysis (Fig. 3.15).

#### 4.3.1 Patient population, image data and 2D morphometry

CMR image data from 20 CoA patients post-repair ( $16.5 \pm 3.1$  years, range 11.1 to 20.1 years; CoA repair performed at 4 days to 5 years of age) were included in this study.

Three-dimensional volumes of the left ventricle (LV) and the aorta during mid-diastolic rest period were obtained from CMR wholeheart data, together with a measurement of left ventricular ejection fraction (LVEF) (Ntsinjana et al., 2013b). Images were segmented using thresholding techniques combined with manual editing in commercial software (Mimics, Leuven, Belgium). In order to reduce irrelevant shape variability, aortas were cut such that only the root, the arch and the descending aorta up to the diaphragm were kept. As the focus of this analysis lies on the arch shape, coronary arteries and head and neck vessels were cut as close as possible to the arch. This is a common pre-processing step in shape analysis of aortic arches (Casciaro et al., 2014), (Bosmans et al., 2013), (Zhao et al., 2009). The final segmented surface models of the aortas were stored as computational surface meshes.

Conventional 2D morphometry was carried out manually on CMR image data to measure the ratio of aortic arch height ( $A$ ) and width ( $T$ ) as well as the ascending and descending aortic arch diameters ( $D_{asc}$  and  $D_{desc}$ , respectively) at the level of the pulmonary artery as proposed by Ou et al (Ou et al., 2004) (Fig. 2.5). Diameters at the transverse arch level ( $D_{trans}$ ) and at the isthmus level ( $D_{isth}$ ) were measured manually as described in (Ntsinjana et al., 2013b).

3D shape parameters were computed semi-automatically from the segmented arch surface models using VMTK in combination with MATLAB. Extracted geometric parameters included volume  $V$  and surface area  $A_{surf}$ , as well as parameters associated with the vessel centreline such as centreline length, curvature and tortuosity

(Piccinelli et al., 2009), (Antiga and Steinman, 2004), and inner vessel diameters along the centreline (minimum  $D_{min}$ , maximum  $D_{max}$  and median diameters  $D_{med}$ ). Tab. 4.1 provides an overview of all geometric parameters that were assessed via correlation analyses. Note that all measured geometric parameters were indexed to patient body surface area (BSA, Chapter 3.8.5), where applicable.

Tab. 4.1: Included 2D and 3D morphometric shape descriptors, adapted from (Bruse et al., 2016a)

2D measured parameters (manually)	3D measured parameters (VMTK)
<ul style="list-style-type: none"> <li>• Arch height <math>A</math> [mm]</li> <li>• Arch width <math>T</math> [mm]</li> <li>• Ratio <math>A/T</math></li> <li>• Diameters at ascending, transverse, isthmus and descending level of the aorta: <math>D_{asc}</math>, <math>D_{trans}</math>, <math>D_{isth}</math>, <math>D_{desc}</math> [mm]</li> <li>• Ratios <math>D_{asc}/D_{desc}</math>, <math>D_{trans}/D_{desc}</math> and <math>D_{isth}/D_{desc}</math></li> </ul>	<ul style="list-style-type: none"> <li>• Volume <math>V</math> [mm<sup>3</sup>]</li> <li>• Surface Area <math>A_{surf}</math> [mm<sup>2</sup>]</li> <li>• Ratio <math>A_{surf}/V</math> [1/mm]</li> <li>• Centreline length <math>L_{CL}</math> [mm]</li> <li>• Centreline Tortuosity <math>TO_{CL}</math></li> <li>• Median curvature along centreline <math>C_{med}</math> [1/mm]</li> <li>• Maximum, minimum and median diameter along centreline <math>D_{max}</math>, <math>D_{min}</math>, <math>D_{med}</math> [mm]</li> </ul>

### 4.3.2 Pre-processing

#### 4.3.2.1 Meshing and smoothing

Previous studies have not specifically considered the effects that mesh size and thus the resolution of the surface mesh might have on the 3D shape analysis. However, Durrleman et al suggested (Durrleman, 2014) that a high resolution mesh (high number of cells per mm<sup>2</sup>) increases computational time.

To investigate this further, I performed a sensitivity analysis on a test set of 5 subjects. The segmented 3D models were meshed from high (5 cells/mm<sup>2</sup>; average cell size 0.2mm<sup>2</sup>) to low (0.3 cells/mm<sup>2</sup>; average cell size 2.5mm<sup>2</sup>) mesh resolution. Meshing was performed using VMTK. Keeping all other parameters constant, the template shape (Chapter 3.6.4) was calculated for each of the differently meshed test sets. All computations were performed on a workstation with 32GB RAM and 12 CPUs and computational time was recorded. Fig. 4.2 shows that the computed template was not substantially affected by changing the mesh resolution, and template calculation time could be reduced by up to 85% when using a lower mesh resolution.

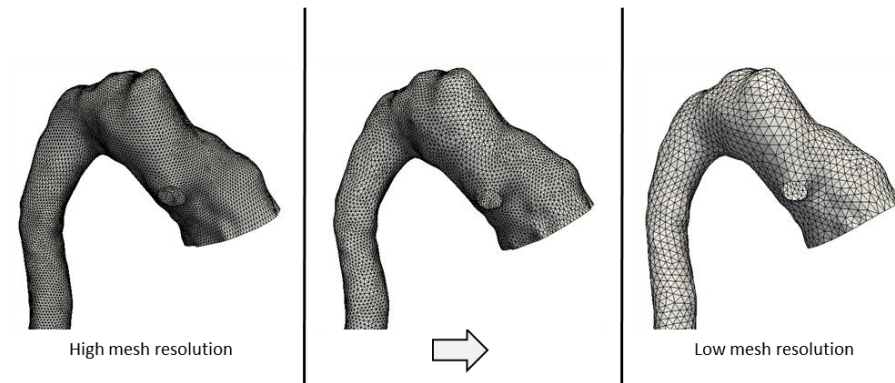


Fig. 4.2: Higher or lower surface mesh resolution does not change the computed template shape

To determine an optimally low, yet *sufficient* mesh resolution, I focussed on the smallest subject present in the population of shapes as it defines a lower limit for mesh resolution. Starting from the original surface model of the smallest subject obtained from segmentation (in this case, subject CoA3), re-meshed surface models were created from low ( $\sim 0.3$  cells/mm<sup>2</sup>) to high ( $\sim 1.5$  cells/mm<sup>2</sup>) mesh resolution. To quantify deviations from the original segmented shape, the surface area  $A_{surf}$  of each re-meshed model was measured and compared to the respective values of the original, high resolution mesh ( $A_{surf,orig} = 8825$  mm<sup>2</sup>). Surface area deviations were calculated according to:

$$Error_{Surface} = \frac{A_{surf} - A_{surf,orig}}{A_{surf,orig}} \cdot 100\% \quad (4.1)$$

A cut-off value for tolerable surface errors was chosen to be 0.5% compared to the original subject mesh, which was reached for a surface mesh resolution of 0.75 cells/mm<sup>2</sup>, Fig. 4.3.

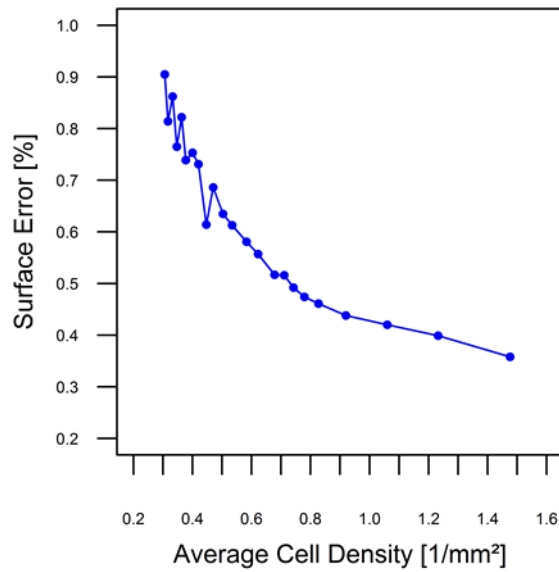


Fig. 4.3: Surface error compared to high resolution mesh relative to average surface mesh cell density

All CoA arch surface models (Fig. 4.4) were meshed with this resolution, applying additional mesh smoothing to further reduce unnecessary shape variability introduced by small bumps.



Fig. 4.4: Twenty input surface models of aortic arch shapes post CoA repair, adapted from (Bruse et al., 2016a)

#### 4.3.2.2 Alignment of input meshes

To reduce possible bias introduced by misaligned surface models, a two-step approach is proposed. First, each input shape was aligned (i.e. rigidly registered using translation and rotation only) to an initial reference shape using registration functions based on the iterative closest point (ICP) algorithm available in VMTK (Besl and McKay, 1992). The initial reference shape was determined as the closest shape to the centre or “mean” of the population (in this case subject CoA4; Fig. 4.4) according to gross geometric parameters (volume  $V$ , surface area  $A_{surf}$ , centreline length  $L_{CL}$  and median diameter along the centreline  $D_{med}$ ).

After computing an initial template shape based on the shapes aligned to the initial reference shape (subject CoA4), the final alignment of all input meshes was obtained in a second step by adopting a *Generalised Procrustes Analysis* (GPA) (Heimann and Meinzer, 2009) approach in the following manner:

1. The input meshes were re-aligned, with the reference shape this time being the computed template;
2. a new template based on the newly aligned meshes was computed;
3. the *model compactness* was computed as proposed by Styner et al (Styner et al., 2003);
4. if the compactness was decreased, the reference shape was set to the new template and the procedure continued with step 1, otherwise the meshes were aligned sufficiently.

Here, sufficient alignment was obtained after one iteration of the outlined procedure.

#### 4.3.2.3 A priori setting of resolution and stiffness $\lambda$ parameters

Although the entire mathematical framework behind the proposed method is rather cumbersome and complex, as shown in Chapter 3.6, the user only has to provide the input shapes as surface meshes and has to set two parameters prior to calculating the

template. Those parameters are the resolution  $\lambda_W$  and the stiffness  $\lambda_V$ , both defined in millimetres. Preliminary studies on shapes of aortic arches showed that changing them within a range of tens of millimetres does affect the final template considerably as shown in Fig. 4.5.

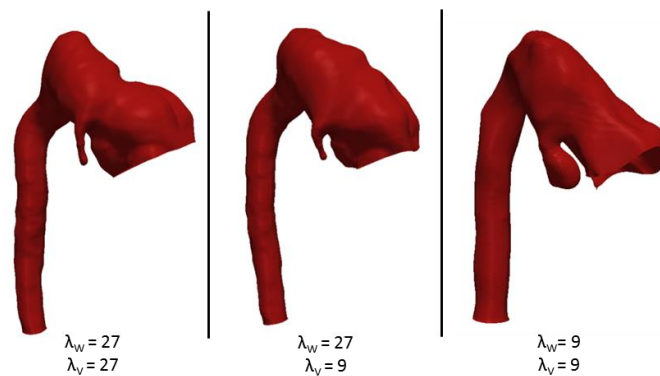


*Fig. 4.5: Different resolution  $\lambda_W$  and stiffness  $\lambda_V$  parameters result in different template shapes*

Generally, it is recommended to set the resolution parameter  $\lambda_W$  in the order of magnitude of the shape features to be captured (Mansi et al., 2011); however, clear indication for parameter setting is missing, in particular for the stiffness  $\lambda_V$ , which cannot be intuitively estimated. Therefore, I performed several tests on real patient data as well as on simple shapes to investigate how the two parameters influence the calculation.

Fig. 4.6 shows the effects on a simple transformation when setting the resolution  $\lambda_W$  too high and the stiffness  $\lambda_V$  too small. In the first case, small shape features (the groove in the big cylinder) cannot be captured when deforming the small cylinder towards the big cylinder; in the latter case, the transformation is too local, so that the two cylinders cannot be matched correctly.

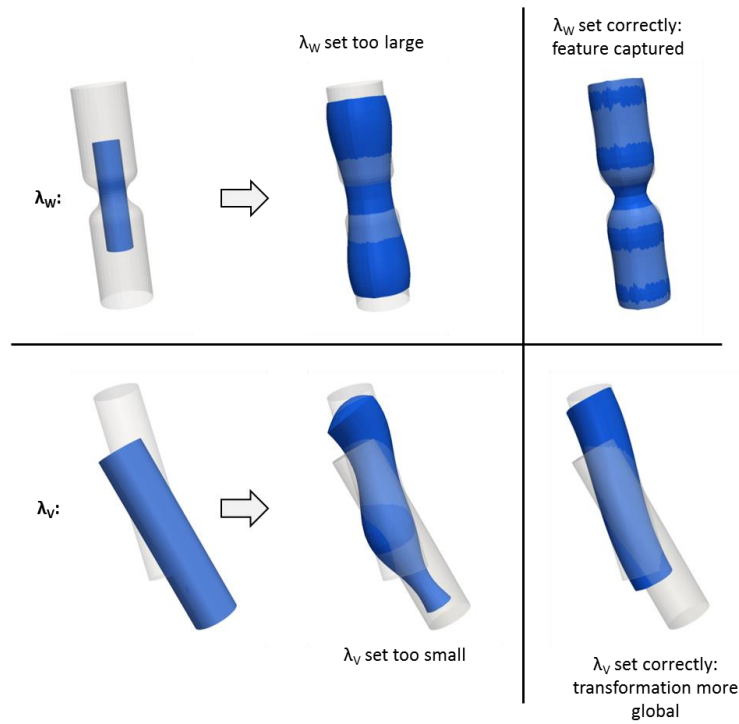


Fig. 4.6: Influence of the  $\lambda$  parameters on transformations of cylindric shapes

Another crucial aspect to take into consideration is the computational time. Trials have shown that both  $\lambda_W$  and  $\lambda_V$  do affect the template calculation considerably as shown in Fig. 4.7. Particularly setting the resolution parameter too small, can lead to a 5-fold increase in computational time. The times shown in Fig. 4.7 were calculated in *exoshape* on a test set of 5 aortas keeping either one of the parameters constant. The results of the sensitivity analyses are summarised in Tab. 4.2.

Tab. 4.2: Influence of the surface mesh resolution and resolution and stiffness parameters  $\lambda_W$  and  $\lambda_V$  on template computation runtime and template shape.  $\uparrow$  denotes increase,  $\downarrow$  decrease and  $\uparrow \downarrow$  denotes an unpredictable change, adapted from (Bruse et al., 2016a)

Parameter	Runtime	Template Shape
Mesh Resolution $\uparrow$	$\uparrow$	-
Currents Resolution $\lambda_W \uparrow$	$\downarrow$	$\uparrow \downarrow$
Deformation Stiffness $\lambda_V \uparrow$	$\uparrow \downarrow$	$\uparrow \downarrow$

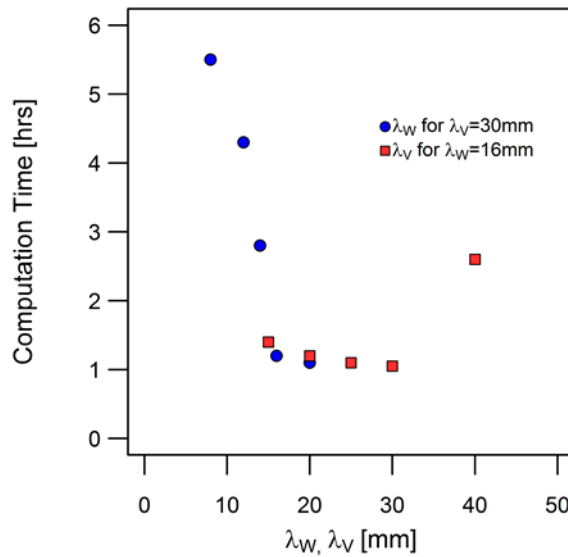


Fig. 4.7: Influence of the  $\lambda$  parameters on the template computation time

To summarise,  $\lambda_W$  needs to be small enough to be able to capture all the features of interest, while being large enough to discard noise and to allow efficient template computation.

The following approach is proposed to obtain an *a priori estimation* of a suitable set of  $\lambda$  parameters. Essentially, the shape analysis algorithm deforms a template shape towards each individual subject shape present in the population. The quality of the matching of source and target shape depends on the setting of the  $\lambda$  parameters. The suggested approach is based on the idea that the subject with the *most challenging* shape features to be captured defines a lower limit in terms of transformation resolution ( $\lambda_W$ ) and stiffness ( $\lambda_V$ ) to obtain an appropriate matching. Here I assume this to be the smallest subject within the shape population. I therefore transformed an initial template towards the smallest subject shape present in the set of shapes, starting from coarse initial values and decreasing both resolution  $\lambda_W$  and stiffness  $\lambda_V$  incrementally until a sufficient matching was achieved. Note that incorrectly chosen  $\lambda$  parameters will ultimately result in high matching errors and in unrealistic shape deformations, which can be examined by the user – visually and numerically. To determine starting values for  $\lambda_W$  and  $\lambda_V$  for computing the initial template, I suggest a “rule of thumb” method, based on the fact that the  $\lambda$  parameters are inherently associated with probing ( $\lambda_W$ ) or

deforming surfaces ( $\lambda_V$ ). As both parameters are given as a length in millimetres, they can be squared to define a plane quadratic surface. With this definition, they are interpreted as a percentage of the surface area to be probed or deformed, Fig. 4.8.

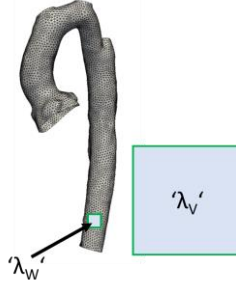


Fig. 4.8: Visual representation of the proposed understanding of the  $\lambda$  parameters as covering a certain percentage of the arch surface area

Based on the smallest surface area  $A_{surf,min}$  within the population,  $\lambda_W$  and  $\lambda_V$  can be initialised using the following equation for a given percentage  $p_W$  or  $p_V$ , respectively

$$\lambda_W = \sqrt{p_W \cdot A_{surf,min}} ; \lambda_V = \sqrt{p_V \cdot A_{surf,min}} \quad (4.2)$$

For the resolution  $\lambda_W$ , this approach can be interpreted as probing  $p_W$  % of the smallest aorta surface area if it was cut open and laid out flat. Note that for large aortas the percentage drops below the chosen percentage values as the same parameters are applied to all shape models. Reasonable ranges for the percentage  $p_W$  could be in the order of about 1% to 5% and for  $p_V$  within 10% to 40%. Here, I set  $p_W$  to 2.5% and  $p_V$  to 25%, which yielded an initial  $\lambda_W$  of 15mm and a  $\lambda_V$  of 47mm, with the minimal surface area present in the set of shapes being  $A_{surf,min} = 8825\text{mm}^2$ . Those values were used to compute an initial template based on all 20 subjects. The initial template was then transformed towards the smallest subject (CoA3, Fig. 4.4) while incrementally decreasing  $\lambda_W$  and  $\lambda_V$  in 1mm steps until the matching error between source (initial template) and target (CoA3) was reduced by >80%. Matching error was defined as

$$Error_{\text{Matching}} = \frac{Dist_{\text{max}} - Dist_{\text{max,initial}}}{Dist_{\text{max,initial}}} \cdot 100\% \quad (4.3)$$

with  $Dist_{max}$  being the maximal surface distance between target shape and matched (registered or deformed) source shape and  $Dist_{max,initial}$  being the maximum surface distance between target shape and source prior to matching, computed with the *vmtksurfacelistance* function in VMTK.

Note that the range of values for  $\lambda_V$  was fixed from 47mm down to 40mm in order to avoid too local deformations, Fig. 4.9. Starting from  $\lambda_W = 15$ mm, transformations were computed in parallel for the range of  $\lambda_V$  values (47 to 40mm). If the matching error was not reduced sufficiently by decreasing  $\lambda_V$ , then  $\lambda_W$  was decreased by 1mm. In this way, I prioritised high  $\lambda_W$  values in order to ensure low runtimes for the final template calculation. Following this procedure, a resolution of  $\lambda_W = 11$ mm and a deformation stiffness of  $\lambda_V = 44$ mm were found to sufficiently reduce the matching error and were used for all further template computations.

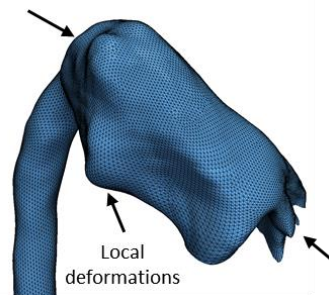


Fig. 4.9: Setting  $\lambda_V$  too small yields too local deformations, adapted from (Bruse et al., 2016a)

The template shape, PLS shape modes and PLS shape vectors  $l_{PLS}^m$  were then computed in MATLAB as detailed in Chapter 3.7.2 based on the 20 arch surface models on a 32GB workstation using 10 cores (runtime for simultaneous template computation and transformation estimation approximately 15 hours in *exoshape*).

### 4.3.3 Post-processing

#### 4.3.3.1 Controlling for confounders and influential observations

Due to the “supervised” nature of PLS, it is possible to control for confounding factors in the analysis. Factors such as age or body size can be confounders affecting the shape analysis and can hide potentially important shape features. Size differences between

patients were assumed to be reflected in differences in patient body surface area (BSA). To “normalise” the extraction of functionally relevant shape features, I aimed to remove dominant size-related shape features first. For that, shape features most related to a change in BSA were computed using PLS based on the original predictors  $X_{orig}$  (the moment vectors deforming the template towards each subject, Chapter 3.7). In previous publications this approach has been used to build a statistical growth model (Mansi et al., 2011), (McLeod et al., 2013). Here, on the contrary, I aimed to *remove* shape patterns related to size differences between subjects prior to further analyses. A second PLS was then performed on the predictor residuals  $X_{resid}$ , which were obtained by subtracting the result of the first PLS (the product of PLS predictor scores  $X_{S,BSA}$  and predictor loadings  $X_{L,BSA}$ ) from the original predictors  $X_{orig}$  as (The Mathworks, Inc., 2016)

$$X_{resid} = X_{orig} - X_{S,BSA} \times X'_{L,BSA} \quad (4.4)$$

In this way, 3D shape features most related to size differences could be removed prior to analysing correlations of PLS shape vectors with geometric and clinical parameters normalised to BSA (Singh et al., 2014).

#### 4.3.3.2 Number of PLS modes to retain

The number of shape modes (either PCA or PLS) is limited to  $m_{max} = N - 1$  with  $N$  being the number of subjects. All  $N$  shape modes explain 100% of the shape variability and would lead to a higher dimensional analysis. The last few shape modes only account for a very low percentage of the overall shape variability and are likely not to represent relevant shape features. Therefore, a cut-off value needs to be defined to decide how many modes should be retained. Here (and throughout the thesis), only the *first* PLS shape mode was retained in order to capture only shape features *most related* to the chosen external parameter (here: BSA and LVEF). This ensures to avoid overfitting (The Mathworks, Inc., 2016), (Hastie et al., 2009).

#### 4.3.3.3 Detecting outliers or influential subjects

In my preliminary studies, PLS regression proved to be prone to be influenced by outliers, which is a known issue in PLS regression (Daszykowski et al., 2007). Outliers in

terms of shape are common in clinical data of pathological shapes; particularly in the field of CHD, where inter-subject shape variability is often large. In order to detect influential observations in the PLS regression, the *Cook's distance*  $Dist_{Cook,i}$  for each subject  $i$  was measured. The Cook's distance measures how much a specific subject influences the final regression result by leaving out that subject and comparing all remaining fitted values to the original, full data fitted values. It is defined as (The Mathworks, Inc., 2016)

$$Dist_{Cook,i} = \frac{\sum_{j=1}^N (y_j - y_{j(i)})^2}{c \cdot MSE} ; MSE = \frac{1}{N} \sum_{i=1}^N (y_j - y_{j(i)})^2 \quad (4.5)$$

with  $y_j$  being the  $j^{\text{th}}$  fitted response variable and  $y_{j(i)}$  being the  $j^{\text{th}}$  fitted response variable if the fit does not include observation  $i$ ;  $c$  is the number of coefficients in the regression model and MSE is the mean square prediction error. The Cook's distance was computed for each subject by leaving out the subject and performing PLS regression on the remaining subjects. PLS regression was thus repeated  $N$  times, with  $N$  being the number of subjects. Here, observations with Cook's distances exceeding four times the mean Cook's distance were discarded from the analysis as potentially influential observations.

#### 4.3.3.4 Validation of the template – geometric approach

Standard geometric parameters (Tab. 4.1) were computed for each patient shape, averaged over the entire population and compared with the respective parameter measured on the final template shape. The deviations  $\Delta Dev$  from the mean population values were calculated for  $x$  being one of the parameters ( $V$ ,  $A_{surf}$ ,  $L_{CL}$ ,  $D_{med}$ ) calculated on the template and  $\bar{x}$  being the respective population mean as

$$\Delta Dev = \frac{x - \bar{x}}{\bar{x}} \cdot 100\% \quad (4.6)$$

The overall deviation  $\Delta Dev_{total}$  of the template from population means was calculated as the absolute average of the deviations from each of the above mentioned parameters.

A template shape yielding a low overall deviation  $\Delta Dev_{total}$  from population mean values of below 5% was considered to represent a good approximation of the mean shape.

#### 4.3.3.5 K-fold cross-validation of the template shape

In order to assure that the final template shape is not overly influenced by adding or leaving out a specific subject shape, k-fold cross-validation was performed (Mansi et al., 2011), (Hastie et al., 2009). The entire dataset was divided into  $k = 10$  randomly assigned subsets. The template calculation was run  $k$  times, each time leaving out one of the subsets until each patient had been left out once. As the entire set consists of  $N = 20$  datasets in total, in each of the  $k$  runs  $N/k = 2$  patients were left out. The 10 resulting templates should all be close to the template calculated on the full dataset of  $N = 20$  patients. This was assessed by overlaying the final template meshes and by measuring the surface distances between each of the 10 templates and the original template using the *vmtksurfacelistance* function.

#### 4.3.4 Statistical analysis

The ultimate aim of this study is to analyse *correlations* between 3D shape features (visually represented by shape modes and numerically by shape vectors) and functional parameters to derive 3D shape biomarkers. Note that the aim is not to *predict* shape from any of the parameters or vice versa but to discover statistically significant correlations, hence *associations* between those variables.

As the SSM framework in combination with PLS (see Chapter 3.7.2) essentially condenses 3D shape information into PLS shape vectors  $l_{PLS}^m$ , traditional *bivariate correlation analysis* can be used to analyse associations between those numerical predictors and the chosen response parameters BSA and LVEF.

Conceptually, each shape vector entry describes in one subject-specific number how much the template shape has to be deformed along the derived shape mode in order to match the specific subject shape as well as possible. A perfect correlation between shape vector and response would imply that the derived shape mode showed exactly

those 3D shape patterns associated with low or high response values (such as high or low LVEF) when moving along the shape mode from low to high shape vector values.

First, to back up the findings of the SSM, correlations between the parameters of interest, BSA and LVEF, with the traditionally measured geometric parameters and demographic parameters (patient age and height) were computed using bivariate correlation analysis. For correlations with BSA, non-indexed geometric shape descriptors were used.

In a second step, shape vectors most related to BSA and LVEF (after removing size effects as outlined in Chapter 4.3.3.1) were extracted via PLS and were correlated with the response variables BSA, LVEF, demographic parameters and the 2D and 3D geometric shape descriptors (Tab. 4.1). For parameters that were normally distributed, the standard parametric Pearson correlation coefficient  $r$  is reported. For non-normally distributed parameters, non-parametric Kendall's  $\tau$  is given. Non-normality was assumed if the Shapiro-Wilk test was significant. Parameters were considered significant (2-tailed) for  $p$ -values  $< .05$ . All statistical tests were performed in SPSS (IBM SPSS Statistics v.22, SPSS Inc., Chicago, IL).

## 4.4 Results

### 4.4.1 Computed template and validation

The template shape showed distinct narrowed sections in the transverse arch and isthmus region. The root was slightly dilated and the overall arch shape could be described as rather “Gothic” with a narrow arch width  $T$  and large height  $A$ , Fig. 4.10.

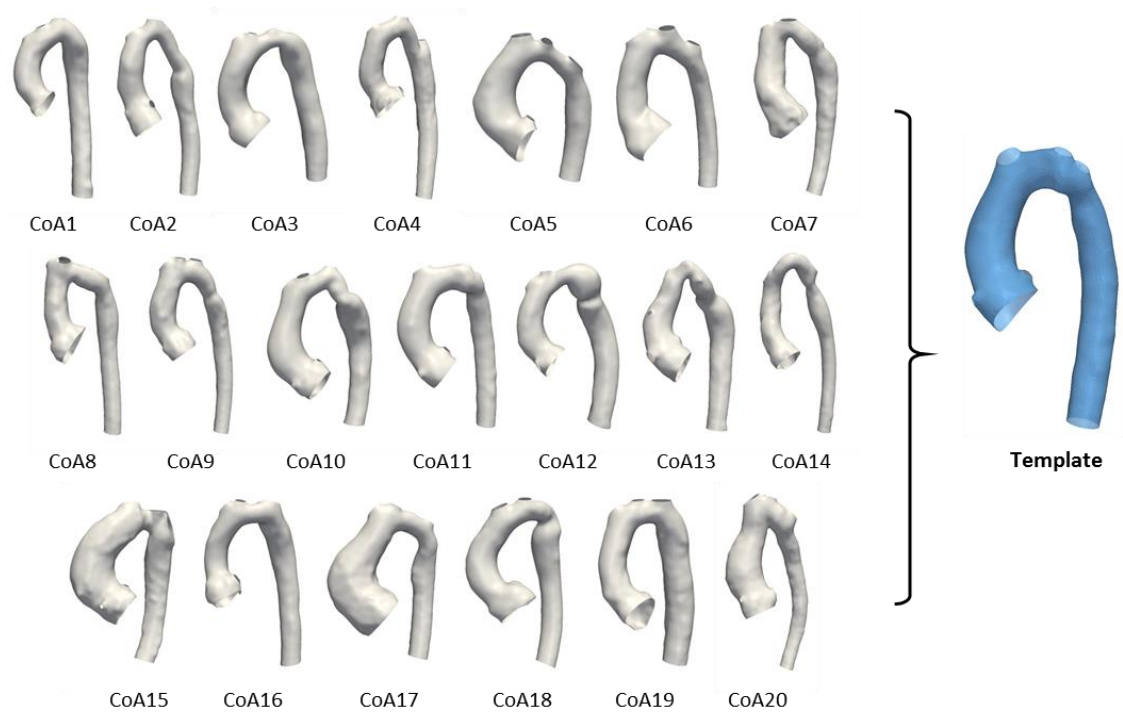


Fig. 4.10: Computed template shape (blue) based on the twenty input CoA models, adapted from (Bruse et al., 2016a)

Key geometric parameters of the template such as surface area  $A_{surf}$ , volume  $V$ , centreline length  $L_{CL}$  and median diameter along the centreline  $D_{med}$  were all close to their respective means as measured on the entire population of shapes (Tab. 4.3). Overall average deviation from those mean geometric population values was 3.1%. Thus, the template was considered to be a good representation of the “mean shape” of the CoA population. The cross-validation templates matched the original template well on visual assessment. Using gross geometric parameters ( $A_{surf}$ ,  $V$ ,  $L_{CL}$  and  $D_{med}$ ), cross-validation templates showed average total deviations from the original template ranging from 2.8% to 6.6%. Average surface distances between the template shapes ranged from 0.21mm to 1.07mm. Hence, the computed template was considered to be minimally influenced by adding or removing another patient shape.

Tab. 4.3: Comparison of computed mean population shape descriptors and respective template shape descriptors, adapted from (Bruse et al., 2016a)

Parameters	Surface Area $A_{surf}$ [mm <sup>2</sup> ]	Volume $V$ [mm <sup>3</sup> ]	Centreline Length $L_{cl}$ [mm]	Median Diameter $D_{med}$ [mm]
Mean population values	15392.5	82839.0	224.3	17.1
Template values ( $\lambda_w = 11\text{mm}$ , $\lambda_v = 44\text{mm}$ )	15351.5	81552.7	215.2	18.2
Deviation from population values	0.3%	1.5%	4.1%	6.4%
Overall deviation	<b>3.1%</b>			

#### 4.4.2 Shape patterns associated with differences in BSA

##### 4.4.2.1 Associations of geometric shape descriptors with changes in BSA

Correlations of the traditionally measured 2D and 3D geometric parameters (Tab. 4.1) and demographic parameters with BSA were analysed using non-indexed geometric descriptors. BSA was significantly positively correlated with age ( $r = 0.705$ ;  $p = .001$ ) and height ( $r = 0.838$ ;  $p < .001$ ) and thus accounted for overall size differences between subjects. Further significant positive correlations of BSA were found with volume  $V$  (Kendall's  $\tau = 0.385$ ;  $p = .019$ ) and surface area  $A_{surf}$  ( $r = 0.537$ ;  $p = .015$ ) of the arch models, the maximum and minimum diameter along the centreline,  $D_{max}$  ( $\tau = 0.460$ ;  $p = .005$ ) and  $D_{min}$  ( $r = 0.628$ ;  $p = .003$ ), ascending aortic diameter  $D_{asc}$  ( $r = 0.550$ ;  $p = .012$ ), transverse diameter  $D_{trans}$  ( $r = 0.453$ ;  $p = .045$ ) and isthmus diameter  $D_{isth}$  ( $r = 0.523$ ;  $p = .018$ ) as well as the arch width  $T$  ( $r = 0.555$ ;  $p = .011$ ), (Tab. 4.4). Significant negative correlations were found with the ratio of arch surface area and volume  $A_{surf}/V$  ( $r = -0.641$ ;  $p = .002$ ) and the median curvature along the centreline  $C_{med}$  ( $r = -0.603$ ;  $p = .005$ ).

#### 4.4.2.2 Associations of shape modes and shape vectors with changes in BSA derived from SSM

A first PLS regression of shape features with BSA revealed subject CoA20 to be influential to the regression as CoA20 exceeded the computed Cook's distance threshold of 0.77. CoA20 was considered as an outlier in terms of its overall shape as it presented with a highly Gothic ( $A/T$  ratio = 0.94) arch with a bended descending aorta (Fig. 4.11) that is considerably larger than other subjects. Thus, CoA20 (Fig. 4.4) is likely to skew the subsequent shape feature extraction and was therefore removed from the following analyses.

Subsequent PLS regression with BSA on the remaining 19 subjects extracted a BSA shape mode, which accounted for 24% of the shape variability present in the population. Visually, the BSA shape mode showed an overall enlargement of the deformed template arch shape with an increase in ascending, transverse, isthmus and descending aorta diameter while moving from low towards higher BSA values (Fig. 4.11a). The overall arch shape for low BSA was slim and rather straight, with a rounded arch; whereas for high BSA values the arch shape was more Gothic and more tortuous with a slightly dilated root and descending aorta.

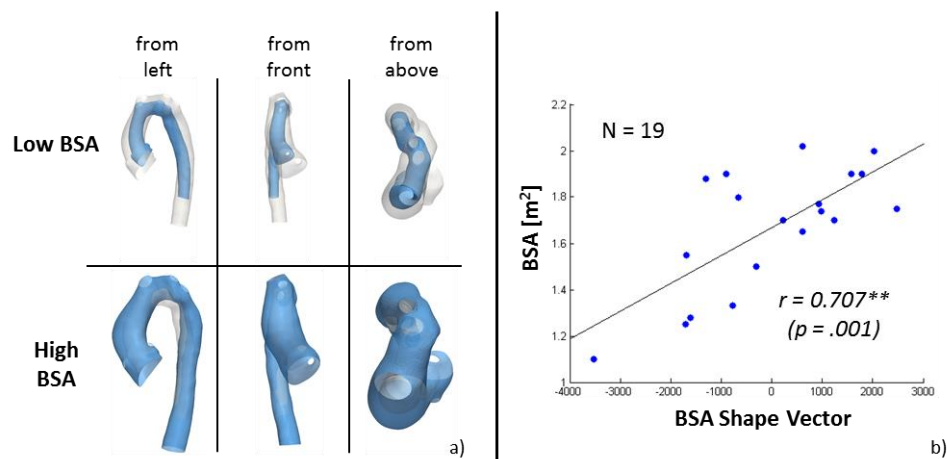


Fig. 4.11: Arch shape features associated with low ( $-2SD$ ) and high ( $+2SD$ ) values of BSA represented by deforming the template shape along the computed BSA shape mode (a) and respective correlation between BSA shape vector and BSA, adapted from (Bruse et al., 2016a)

The correlation between the associated BSA shape vector and BSA was significant with ( $r = 0.707$ ;  $p = .001$ ), implying that the BSA shape mode captured shape features

associated with differences in BSA well (Fig. 4.11b). Furthermore, the computed BSA shape vector correlated positively and significantly with age ( $r = 0.696$ ;  $p = .001$ ) and height ( $r = 0.872$ ;  $p < .001$ ), volume  $V$  ( $\tau = 0.743$ ;  $p < .001$ ) and surface area  $A_{surf}$  ( $r = 0.902$ ;  $p < .001$ ), centreline length  $L_{CL}$  ( $r = 0.853$ ;  $p < .001$ ), diameters  $D_{max}$  ( $r = 0.602$ ;  $p < .001$ ),  $D_{min}$  ( $r = 0.763$ ;  $p < .001$ ),  $D_{med}$  ( $r = 0.709$ ;  $p = .001$ ),  $D_{asc}$  ( $r = 0.708$ ;  $p = .001$ ),  $D_{trans}$  ( $r = 0.646$ ;  $p = .003$ ),  $D_{isth}$  ( $r = 0.746$ ;  $p < .001$ ),  $D_{desc}$  ( $r = 0.740$ ;  $p < .001$ ) and arch height  $A$  ( $r = 0.632$ ;  $p = .004$ ) and width  $T$  ( $r = 0.626$ ;  $p = .004$ ) (Tab. 4.4). Significant negative correlations were found for the surface volume ratio  $A_{surf}/V$  ( $r = -0.787$ ;  $p < .001$ ) and the median curvature  $C_{med}$  ( $r = -0.718$ ;  $p = .001$ ). Those associations were correctly depicted by the BSA shape mode, Fig. 4.11a.

Tab. 4.4: Correlations between BSA, BSA Shape Vector, demographic and geometric parameters, adapted from (Bruse et al., 2016a)

Correlations Pearson's $r$ (p-value) Kendall's $\tau$ (p-value)	Body Surface Area BSA [m <sup>2</sup> ] $N = 20$	BSA Shape Vector $N = 19$
Body Surface Area BSA [m <sup>2</sup> ]	-	$r = 0.707^{**}$ ( $p = .001$ )
Age [years]	$r = 0.705^{**}$ ( $p = .001$ )	$r = 0.696^{**}$ ( $p = .001$ )
Height H [mm]	$r = 0.838^{**}$ ( $p < .001$ )	$r = 0.872^{**}$ ( $p < .001$ )
Volume V [mm <sup>3</sup> ]	$\tau = 0.385^*$ ( $p = .019$ )	$\tau = 0.743^{**}$ ( $p < .001$ )
Surface Area $A_{surf}$ [mm <sup>2</sup> ]	$r = 0.537^*$ ( $p = .015$ )	$r = 0.902^{**}$ ( $p < .001$ )
Centreline length $L_{CL}$ [mm]	$r = 0.398$ ( $p = .083$ )	$r = 0.853^{**}$ ( $p < .001$ )
Centreline Tortuosity $T_{O_{CL}}$	$r = 0.022$ ( $p = .928$ )	$r = 0.206$ ( $p = .398$ )
Ratio $A_{surf}/V$ [1/mm]	$r = -0.641^{**}$ ( $p = .002$ )	$r = -0.787^{**}$ ( $p < .001$ )
Median Curvature $C_{med}$ [1/mm]	$r = -0.603^{**}$ ( $p = .005$ )	$r = -0.718^{**}$ ( $p = .001$ )
Maximum Diameter $D_{max}$ [mm]	$\tau = 0.460^{**}$ ( $p = .005$ )	$\tau = 0.602^{**}$ ( $p < .001$ )
Minimum Diameter $D_{min}$ [mm]	$r = 0.628^{**}$ ( $p = .003$ )	$r = 0.763^{**}$ ( $p < .001$ )
Median Diameter $D_{med}$ [mm]	$r = 0.386$ ( $p = .092$ )	$r = 0.709^{**}$ ( $p = .001$ )
Ascending Diameter $D_{asc}$ [mm]	$r = 0.550^*$ ( $p = .012$ )	$r = 0.708^{**}$ ( $p = .001$ )
Transv. Diameter $D_{trans}$ [mm]	$r = 0.453^*$ ( $p = .045$ )	$r = 0.646^{**}$ ( $p = .003$ )
Isthmus Diameter $D_{isth}$ [mm]	$r = 0.523^*$ ( $p = .018$ )	$r = 0.746^{**}$ ( $p < .001$ )
Descending Diameter $D_{desc}$ [mm]	$r = 0.332$ ( $p = .152$ )	$r = 0.740^{**}$ ( $p < .001$ )
Ratio $D_{asc}/D_{desc}$	$r = 0.264$ ( $p = .260$ )	$r = 0.025$ ( $p = .918$ )
Ratio $D_{isth}/D_{trans}$	$r = 0.190$ ( $p = .422$ )	$r = 0.315$ ( $p = .189$ )
Ratio $D_{isth}/D_{desc}$	$r = 0.364$ ( $p = .115$ )	$r = 0.278$ ( $p = .250$ )
Ratio $D_{trans}/D_{desc}$	$r = 0.074$ ( $p = .757$ )	$r = -0.188$ ( $p = .442$ )
Arch height A [mm]	$r = 0.198$ ( $p = .402$ )	$r = 0.632^{**}$ ( $p = .004$ )
Arch width T [mm]	$r = 0.555^*$ ( $p = .011$ )	$r = 0.626^{**}$ ( $p = .004$ )
Ratio A/T	$r = -0.170$ ( $p = .473$ )	$r = 0.116$ ( $p = .637$ )

### 4.4.3 Shape patterns associated with differences in LVEF

#### 4.4.3.1 Associations of indexed geometric shape descriptors with changes in LVEF

Significant positive correlations were found between LVEF and the ratio of transverse and descending arch diameter  $D_{trans}/D_{desc}$  ( $r = 0.456$ ;  $p = .050$ ). LVEF correlated negatively and significantly with the indexed arch surface area  $iA_{surf}$  ( $r = -0.571$ ;  $p = .011$ ).

#### 4.4.3.2 Associations of shape modes and shape vectors with changes in LVEF derived from SSM

A second PLS regression based on the residuals of the first PLS regression with BSA was performed with LVEF as response. This two-step approach allowed removing shape features due to size differences between subjects prior to extracting shape modes related to LVEF. This second “normalised” PLS regression yielded the LVEF shape mode, which accounted for 19% of the remaining shape variability. The LVEF shape mode deformed the template from a large, overall rather straight but slightly Gothic arch shape with a slim ascending aorta and a dilated descending aorta for low LVEF values towards a rather compact but rounded arch shape with a dilated aortic root and a slim descending aorta for high LVEF (Fig. 4.12).

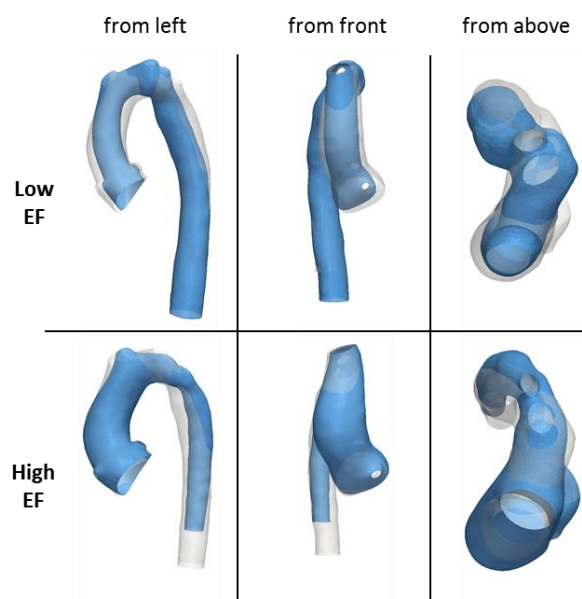


Fig. 4.12: Shape features associated with LVEF shape mode deforming the template from low to high LVEF, adapted from (Bruse et al., 2016a)

The associated LVEF shape vector correlated significantly with LVEF ( $r = 0.521$ ;  $p = .022$ ) (Fig. 4.13). By analysing correlations of the LVEF shape vector with measured geometric parameters, further significant positive correlations with the ratio of ascending to descending aorta diameter  $D_{asc}/D_{desc}$  ( $r = 0.753$ ;  $p < .001$ ) and the ratio of transverse and descending aorta diameter  $D_{trans}/D_{desc}$  ( $r = 0.457$ ;  $p < .049$ ) were found; corroborating the visual results. Negative significant correlations were found with the indexed descending aorta diameter  $iD_{desc}$  ( $r = -0.527$ ;  $p < .020$ ). All further correlations are given in Tab. 4.5.

Tab. 4.5: Correlations between LVEF, LVEF Shape Vector, demographic and geometric parameters, adapted from (Bruse et al., 2016a)

Correlations Pearson's r (p-value) Kendall's $\tau$ (p-value)	Ejection Fraction LVEF [%] N = 19	LVEF Shape Vector N = 19
Ejection Fraction LVEF [%]	-	<b><math>r = 0.521^*</math> (<math>p = .022</math>)</b>
Body Surface Area BSA [m <sup>2</sup> ]	$r = -0.147$ ( $p = .548$ )	$r = 0.000$ ( $p = .999$ )
Age [years]	$r = -0.243$ ( $p = .316$ )	$r = -0.142$ ( $p = .561$ )
Height H [mm]	$r = -0.391$ ( $p = .098$ )	$r = -0.246$ ( $p = .310$ )
Volume $iV$ [mm <sup>3</sup> /m <sup>2</sup> ]	$\tau = -0.322$ ( $p = .058$ )	$\tau = -0.228$ ( $p = .172$ )
Surface Area $iA_{surf}$ [mm <sup>2</sup> /m <sup>2</sup> ]	<b><math>r = -0.571^*</math> (<math>p = .011</math>)</b>	$r = -0.320$ ( $p = .181$ )
Centreline length $iL_{CL}$ [mm/m <sup>2</sup> ]	$r = -0.255$ ( $p = .293$ )	$r = -0.338$ ( $p = .157$ )
Centreline Tortuosity $iTo_{CL}$	$r = -0.039$ ( $p = .874$ )	$r = 0.267$ ( $p = .269$ )
Ratio $A_{surf}/V$	$r = -0.386$ ( $p = .103$ )	$r = 0.072$ ( $p = .770$ )
Median Curvature $iC_{med}$ [1/mm m <sup>2</sup> ]	$r = 0.269$ ( $p = .265$ )	$\tau = 0.158$ ( $p = .345$ )
Maximum Diameter $iD_{max}$ [mm/m <sup>2</sup> ]	$\tau = -0.096$ ( $p = .574$ )	$\tau = 0.064$ ( $p = .064$ )
Minimum Diameter $iD_{min}$ [mm/m <sup>2</sup> ]	$r = -0.409$ ( $p = .082$ )	$r = -0.239$ ( $p = .324$ )
Median Diameter $iD_{med}$ [mm/m <sup>2</sup> ]	$r = -0.363$ ( $p = .127$ )	$\tau = -0.228$ ( $p = .172$ )
Ascending Diameter $iD_{asc}$ [mm/m <sup>2</sup> ]	$\tau = 0.000$ ( $p = 0.999$ )	$\tau = 0.170$ ( $p = .310$ )
Transverse Diameter $iD_{trans}$ [mm/m <sup>2</sup> ]	$r = 0.020$ ( $p = .937$ )	$r = -0.018$ ( $p = .942$ )
Isthmus Diameter $iD_{isth}$ [mm/m <sup>2</sup> ]	$r = -0.407$ ( $p = .083$ )	$r = -0.441$ ( $p = .059$ )
Descending Diameter $iD_{desc}$ [mm/m <sup>2</sup> ]	$r = -0.442$ ( $p = .058$ )	<b><math>r = -0.527^*</math> (<math>p = .020</math>)</b>
Ratio $D_{asc}/D_{desc}$	$r = 0.312$ ( $p = .193$ )	<b><math>r = 0.735^{**}</math> (<math>p &lt; .001</math>)</b>
Ratio $D_{isth}/D_{trans}$	$r = -0.362$ ( $p = .128$ )	$r = -0.453$ ( $p = .052$ )
Ratio $D_{isth}/D_{desc}$	$r = -0.152$ ( $p = .535$ )	$r = 0.083$ ( $p = .736$ )
Ratio $D_{trans}/D_{desc}$	<b><math>r = 0.456^*</math> (<math>p = .050</math>)</b>	<b><math>r = 0.457^*</math> (<math>p = .049</math>)</b>
Arch height $iA$ [mm/m <sup>2</sup> ]	$r = -0.154$ ( $p = .529$ )	$\tau = -0.146$ ( $p = .382$ )
Arch width $iT$ [mm/m <sup>2</sup> ]	$r = 0.000$ ( $p = .999$ )	$r = 0.018$ ( $p = .943$ )
Ratio A/T	$r = -0.224$ ( $p = .357$ )	$r = -0.269$ ( $p = .265$ )

## 4.5 Discussion

In this chapter, the currents-based SSM method has been described and evaluated in detail, and its potential for discovering 3D shape biomarkers in a complex anatomical shape population of patients post CoA repair has been demonstrated. Steps to run the analysis were explained from the user-perspective, with the aim of making the process more accessible to the broader research community.

The SSM framework in combination with PLS was applied to CMR image data of the aorta from 20 patients post CoA repair. The computed template shape was in good agreement with conventional 2D and 3D measurements when averaged across the population (e.g. centreline length of the template = the average of the centreline length measured from each patient). Biomarker information – the 3D shape features – for each individual were then extracted by deforming the template aorta to each patient's aorta. These extracted shape features, unique to each individual, were shown to: i) Accurately represent individual characteristics of the arch, as measured by patient-specific 2D/3D morphometric parameters, and ii) have correlations with BSA and LVEF, which may show them to be important biomarkers of biological processes. Even though preliminary, the found associations of aortic arch shape with LVEF were not known previously, which is why the extracted 3D shape features are considered as potential novel shape biomarkers. These results constitute the first statistical shape model of the aorta affected by coarctation.

A description of the currents-based SSM framework adopted in this chapter is reported elsewhere in mathematically rather complex terms. Here, the method is presented from the user's perspective with the aim of raising the awareness of the importance of necessary modelling parameters such as the meshing, smoothing and  $\lambda$  parameters for 3D shape analysis of complex anatomical structures.

The mesh resolution for the input surfaces mainly affected the computational time needed to compute the template, but did not affect the final template shape substantially. Conversely, the analysis parameters (resolution  $\lambda_W$  and stiffness  $\lambda_V$ )

affected both computational time and the final template shape considerably, requiring careful setting according to the shape population to be analysed.

Insight is provided as to how to mesh input models and a new way of determining the  $\lambda$  parameters is proposed, which ensures robust and efficient template computation. Furthermore, a modified PLS regression technique is described, which enables extraction of shape features independent of size differences between subjects. By measuring the Cook's Distance during PLS regression, I was able to account for outliers such as one subject with an overly large, "abnormal" aortic shape and indeed a highly impaired cardiac function (LVEF = 17%) that had to be excluded in order not to affect the shape feature extraction (subject CoA20). This suggests that the methodology could potentially be used to detect outlying shapes in a complex shape population – which, in turn, might be associated with outlying functional behaviour.

The calculated template shape based on the 20 CoA cohort showed characteristic shape features associated with CoA such as a slightly Gothic arch shape, a dilated root, and a distinct narrowing of the transverse and isthmus arch section. The template shape was validated by comparing its geometry with the population average geometric parameters and by applying cross-validation techniques in order to ensure that removing or adding shapes had no influence. Such a template could serve as a representative of the "normal of the abnormal"; a reference mean shape that might facilitate the diagnosis of highly abnormal cases within a pathologic shape population.

Three-dimensional global and regional shape features associated with differences in size (represented by BSA) and function (represented by LVEF) were extracted and found to be well in agreement with trends confirmed by traditional morphometrics. BSA correlated strongly and significantly with conventional geometric parameters, as expected. Those results confirmed the visual results shown by the SSM, whereby an increase in BSA was associated with an overall increase in aorta length and vessel diameters as well as with a shape development towards a slightly dilated root and a more Gothic arch shape. For the first time, high LVEF was associated with a more compact, rounded arch shape with a slightly dilated aortic root and a slim descending

aorta, whereas low LVEF was associated with a more Gothic arch shape, a slim ascending aorta and a slightly dilated descending aorta, which may increase flow resistance across the arch and therefore left ventricular afterload.

#### **4.5.1 Detailed analysis of the identified correlations**

##### **4.5.1.1 Correlations with traditionally measured geometric parameters**

While BSA correlated strongly with multiple measured 2D and 3D shape descriptors, LVEF correlated significantly only with two geometrical parameters (the ratio of transverse to descending aortic diameter and the indexed surface area). One reason for this may be that the shape of the aortic arch marginally affects LVEF. However, these discrepancies could also emphasise that complex 3D shapes cannot always be sufficiently described by traditional individual morphometric measurements. Shape features associated with differences in body size between subjects are typically dominant and contribute to the largest portion of shape variability in natural pathologic shape populations (Jolliffe, I.T., 2002). An increase in body size usually results in an overall size increase of the structure of interest, reflected in increased diameters and vessel length in the case of the aorta. This is why shape features associated with size differences are likely to be picked up by traditional 2D and 3D measurements. For the functional parameter LVEF though, I was interested in shape features independent of size effects, which, however, may be less prominent and may only be captured by a complex combination and collection of different morphometric parameters. Herein lies the power of 3D statistical shape modelling: results such as the mean shape and its variability are derived as visual, intuitively comprehensible and less biased 3D shape representations taking into account the entire 3D shape, instead of an unhandy collection of multiple measured parameters that might miss out crucial shape features.

##### **4.5.1.2 Correlations with shape vectors describing shape features most related to a specific parameter in 3D**

I found a strong significant correlation between the BSA shape vector and BSA, whereas LVEF correlated less with its LVEF shape vector. Overall, these results imply that shape features shown by the respective shape modes accounted well for differences in both

BSA and LVEF in the given shape population. In a strong correlation between functional parameter and shape vector, all subjects with low LVEF values would show those shape features given by the LVEF shape mode for low shape vector values, and vice versa for all subjects with high LVEF values. Nevertheless, those trends visually confirmed that the method was able to correctly extract 3D shape features from a population of shapes, which are potentially associated with a functional parameter of clinical relevance, Fig. 4.13. Therefore, the presented method can be used as a research tool to explore a population of 3D shapes, in order to detect where crucial shape changes occur and whether specific geometric parameters are likely to be of functional relevance.

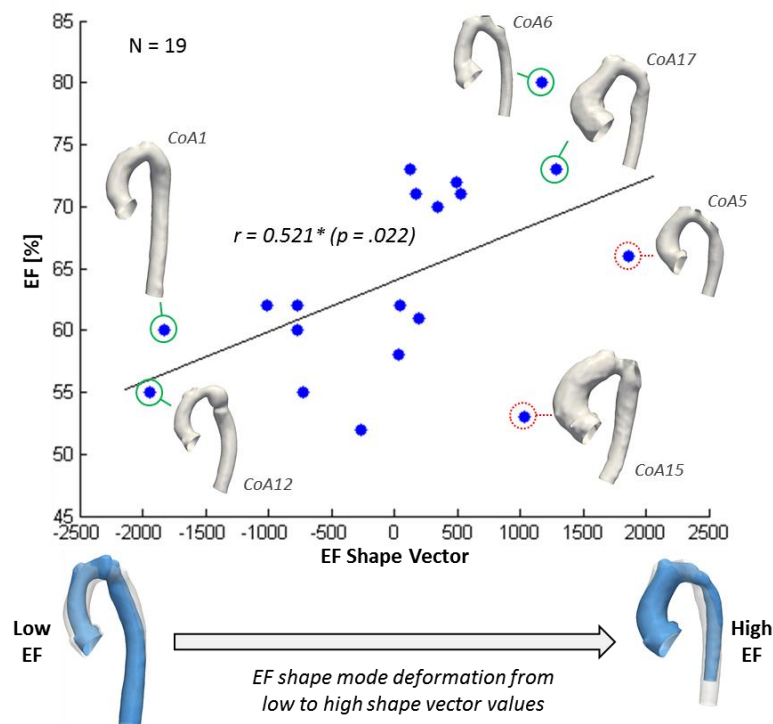


Fig. 4.13: Correlation between LVEF shape vector and LVEF and comparison of shape features shown by the LVEF shape mode and actual patient shapes associated with low and high values of the LVEF shape vector, patients in line with PLS shape modes marked in green, outlying shapes marked in red. Adapted from (Bruse et al., 2016a)

#### 4.5.2 Limitations and future work

The main limitation of this study is the small sample size of 20 subjects, with rather inhomogeneous characteristics in terms of age (range 11.1 to 20.1 years), age at arch intervention (4 days to 5 years after birth) and type of surgery (Ntsinjana et al., 2013b).

Furthermore, in order not to inflate Type II error of not detecting actual effects, computed correlation significances were not adjusted for multiple comparisons. Therefore, all results have to be considered as exploratory.

Results presented in this chapter are primarily meant to demonstrate the potential of the currents-based SSM by studying the association of complex 3D shape features with functional, clinically relevant parameters such as LVEF. This could improve the derivation of novel shape biomarkers in future studies. Applying the methods proposed here to a larger cohort of CoA patients could provide additional insight as to whether specific arch morphologies such as the Gothic arch shape are associated with hypertension post-aortic coarctation repair (O'Sullivan, 2014), (Canniffe et al., 2013). Chapter 6 will apply the developed methods to a larger cohort of CoA patients to derive such further arch shape biomarkers.

## 4.6 Summary

The main outcomes of this chapter were:

- Pre- and post-processing steps necessary to run the currents-based SSM analysis in *exoshape* with the aim of extracting shape biomarkers via PLS were described in detail.
- Specifically, new rules were derived on how to set surface meshing and  $\lambda$  parameters for an efficient shape analysis; and how to ensure PLS regression is not influenced by size differences between input shapes nor by shape outliers.
- For the first time, currents-based SSM results such as the computed template shape as well as extracted PLS shape modes and shape vectors were compared against traditional 2D and 3D morphometric parameters, showing good agreement.
- After accounting for size differences between patients, significant associations between 3D aortic arch shape features and LVEF could be found in patients post CoA repair, highlighting the potential of detecting novel, clinically relevant shape biomarkers from CMR image data via the proposed methods.

Having determined a protocol of how to run the shape analysis and being confident that 3D SSM results are in agreement with measured 2D and 3D shape descriptors, I was interested in exploring whether results derived with the currents-based framework are also in agreement with subjective clinical expert opinion. This question is addressed in the next chapter.

## 5 Comparing computed statistical shape modelling results with clinical expert opinion

*Part of the work described in this chapter has been published in: J. L. Bruse, K. McLeod, G. Biglino, H. N. Ntsinjana, C. Capelli, T.-Y. Hsia, M. Sermesant, X. Pennec, A. M. Taylor, and S. Schievano. A non-parametric statistical shape model for assessment of the surgically repaired aortic arch in coarctation of the aorta: How normal is abnormal?, Proceedings of STACOM 2015, vol. 9534, Editors: Camara, Mansi, Pop, Rhode, Sermesant, Young, Jan. 2016. (Bruse et al., 2016b). Copyright (2016) with permission of Springer.*

The previous chapter established protocols to run the currents-based statistical shape model (SSM) efficiently with the aim of extracting clinically relevant anatomical 3D shape features from medical image data via PLS regression techniques. Further, I showed that SSM results compare well with traditional shape descriptors, but potentially provide more detailed 3D shape information. Whilst recent studies suggest that regular screening via cardiovascular magnetic resonance (CMR) imaging is warranted for patients post CoA repair, shape assessment in clinical practice is often subjective or based on simple morphometric measurements. Therefore, this chapter investigates how numerical 3D SSM results compare with the subjective opinion of clinical experts who deal with anatomical shape assessment on a daily basis. An objective, quantitative measure of “shape abnormality” is computed based on the established SSM protocols and compared to both expert shape abnormality ranking and traditional shape descriptors.

## 5.1 Abstract

*Background: Many CoA patients suffer from complications post-repair, which are commonly associated with aortic arch shape abnormalities. Determining the degree of shape abnormality could improve risk stratification in recommended screening procedures. Yet, traditional morphometry struggles to capture the highly complex arch geometries. Therefore, the currents-based SSM framework was used here to fully account for 3D shape features.*

*Methods: By computing a template aorta of a population of healthy subjects and combining PLS and PCA to analyse its deformation vectors towards CoA arch shape models, (supervised) PLS shape vectors and (unsupervised) Mahalanobis distances were derived as quantitative measures of subject-specific shape abnormality. Computed results were compared with a shape ranking performed by three clinical experts and with manually measured height to width ratio (A/T) and coarctation index (CoAi).*

*Results: Both supervised and unsupervised measures of shape abnormality computed from SSM results correlated better with average expert shape ranking than the traditional metrics. Specifically, best agreement with average expert ranking was achieved for the supervised PLS shape vectors (Kendall's  $\tau = 0.359$ ,  $p = .033$ ), followed by the Mahalanobis distance based on 10 principal components, explaining 90% of shape variability (Kendall's  $\tau = 0.336$ ,  $p = .045$ ).*

*Conclusion: This study suggested that the currents-based SSM approach constitutes a promising diagnostic tool for improved objective screening of complex cardiac defects, as results were in better agreement with clinical expert opinion than traditional shape descriptors.*

## 5.2 Introduction

Although survival rates have improved over the last decades, many patients with coarctation of the aorta (CoA) suffer from late complications post-aortic arch repair such as hypertension, which have been associated with shape abnormalities of the arch (Ou et al., 2004), Chapter 2.3.2. Recent studies therefore suggest long-term follow-up and regular screening via cardiac imaging (Ou et al., 2007), (Craiem et al., 2012a), (Lee et al., 2012), (Brown et al., 2013), (Canniffe et al., 2013).

Being able to quantify the degree of shape abnormality could be beneficial for such screening procedures as it assists in identifying highly abnormal cases that are potentially associated with a higher risk profile. Yet, in clinical practice, aortic arch shape is commonly assessed via conventional 2D morphometry, which – as found in the previous chapter – fails to capture the full 3D shape complexity of aortic arch shapes. SSM instead provides a visual, thus intuitively comprehensible tool to assess the entire 3D anatomy of a population of shapes (Young and Frangi, 2009). Furthermore, mathematical currents as non-parametric anatomical shape descriptors circumvent the process of landmarking (Vaillant and Glaunès, 2005) and following the steps described in Chapter 4, a robust and efficient analysis of 3D shape features can be ensured.

In this chapter, I aimed to use the deformation vector data (Chapter 3.7) to quantify the degree of shape abnormality of CoA arch shapes compared to the healthy aorta. The idea was that by analysing how a template shape of a healthy (not surgically altered) aortic arch deforms towards each CoA arch shape, subject-specific measures of shape abnormality can be derived. I followed a supervised approach using PLS shape vectors and an unsupervised approach using PCA. The PLS shape vector essentially condenses 3D shape features down to a single number for each CoA patient (Chapter 3.7.2), which allows a ranking of CoA shapes according to their overall shape deviation from the template. Furthermore, the Mahalanobis distance is a common distance measure used in high-dimensional space to detect outliers (Jolliffe, I.T., 2002). It can be derived from PCA shape vectors and was used here as an unsupervised measure of shape abnormality.

Both PLS shape vector and various Mahalanobis distances were compared with an expert ranking of shape abnormality performed by three clinical experts in order to explore to which degree the SSM results reflect the experts' opinion. Further, I analysed associations between the expert ranking and conventional 2D shape descriptors that are commonly used in clinical practice. The leading question behind this study was:

→ How do quantitative SSM results compare to subjective clinical expert opinion in terms of assessing cardiovascular anatomical shapes?

## 5.3 Methods

### 5.3.1 Patient population

This is a retrospective study based on a population of 20 healthy Control subjects and 20 age- and body surface area (BSA)-matched patients post-aortic arch repair (CoA) (Ntsinjana et al., 2013b). Average age was  $15.2 \pm 2.0$  years (mean  $\pm$  standard deviation) for the Control and  $16.5 \pm 3.1$  years for the CoA group. CoA patients had surgical arch repair four days to five years after birth. Control subjects did not have any intervention on the aortic arch and were considered "normal" in terms of shape.

### 5.3.2 Image processing and pre-processing of the surface models

The 40 aortas were segmented manually (Mimics, Leuven, Belgium) from wholeheart images and pre-processed further as described in Chapter 4.3.2. Prior to computing the template shape, Control arches were rigidly aligned to an initial reference subject from the Control population using an Iterative Closest Point (ICP) algorithm in VMTK (Besl and McKay, 1992). As conventional 2D morphometric shape descriptors, the coarctation index ( $CoAi$ ) and the ratio of arch height  $A$  to width  $T$ ,  $A/T$  were measured manually on CMR images as proposed by (Tan et al., 2005) and (Ou et al., 2004), respectively.

### 5.3.3 Expert assessment of the aortic arch shapes

Three clinical experts (radiologist, cardiac surgeon and cardiologist; each with >10 years of experience) qualitatively ranked the CoA shapes according to their distance from a

normal arch shape (1=close; 2=fairly close; 3=mid-range; 4=far away; 5=very far away from normal). Control arch shapes were accessible for comparison. The experts assessed the arch surface models, merely using a 3D viewer (viewable models of the arches available under [http://www.ucl.ac.uk/cardiac-engineering/research/library-of-3d-anatomies/congenital\\_defects/coarctations](http://www.ucl.ac.uk/cardiac-engineering/research/library-of-3d-anatomies/congenital_defects/coarctations)), without knowing the patients' clinical history or results of the shape analysis.

### 5.3.4 Control template and transformations towards CoA subject shapes

The template shape of the Control group  $\bar{T}_{Control}$  was computed with the *exoshape* code framework following steps detailed in Chapter 4. In order to find an adequate set of  $\lambda$  parameters, an initial template of the Control group  $\bar{T}_{Control,initial}$  was computed using starting values of  $\lambda_{W,initial}=15\text{mm}$  and  $\lambda_{V,initial}=47\text{mm}$ . As the analysis is based on transformations that match the Control template with CoA shapes, the final set of  $\lambda$  parameters was obtained by matching  $\bar{T}_{Control,initial}$  with a specific target shape from the CoA group  $T_{i\ CoA,Target}$ , while incrementally decreasing  $\lambda_{W,initial}$  and  $\lambda_{V,initial}$  until the registration error between the deformed source shape  $\phi_i(\bar{T}_{Control,initial})$  and  $T_{i\ CoA,Target}$  was reduced by at least 80%. Being one of the arch models that posed the most challenging shape features to be captured, the CoA subject with the smallest surface area was chosen as  $T_{i\ CoA,Target}$  (CoA3). Prior to the  $\lambda$  estimation,  $T_{i\ CoA,Target}$  was rigidly registered to  $\bar{T}_{Control,initial}$ . Based on this approach,  $\lambda_W=9\text{mm}$  and  $\lambda_V=44\text{mm}$  were found to allow sufficient matching of  $\bar{T}_{Control,initial}$  with  $T_{i\ CoA,Target}$  and all other subjects, and were used to compute the final Control template (based on the 20 Control arch shapes)  $\bar{T}_{Control,final}$ .  $\bar{T}_{Control,final}$  was validated using 10-fold cross-validation. Further, gross geometric parameters of  $\bar{T}_{Control,final}$  (volume  $V$ , surface area  $A_{surf}$ , centreline length  $L_{cl}$  and median diameter along the centreline  $D_{med}$ ) were compared to the respective mean values of the Control population. After rigidly registering all CoA arch shapes to  $\bar{T}_{Control,final}$  via iterative closest point (ICP) registration, the transformations  $\phi_i$  of  $\bar{T}_{Control,final}$  towards each of the CoA subject shapes and thus the deformation vectors  $\beta$  were computed using the same set of  $\lambda$  parameters.

### 5.3.5 Analysing the transformations using PLS and PCA

The deformation vectors  $\beta$ , obtained from transforming  $\bar{T}_{Control,final}$  towards all Control and CoA shapes, constituted the input (predictors) for both PLS and PCA as detailed in Chapter 3.7. To first extract shape features predominantly related to *size* differences between subjects, an initial *PLS I* was performed with all deformation vectors  $\beta$  as predictors  $X_i$  and BSA of the subjects as response  $Y_i$ . A second *PLS II* was performed on the predictor residuals of *PLS I*,  $X_{i,resid}$  using the grouping parameter  $Y_{ii}$  ( $0 = Control$ ;  $1 = CoA$ ) as response. Residuals  $X_{i,resid}$  were defined as in Eq. 4.4. Thereby, dominant shape features related to size differences were removed prior to extracting the shape mode most related to the grouping parameter. PLS shape modes were computed in MATLAB and the mean squared prediction error (MSE, Eq. 4.5) was estimated using 10-fold cross-validation. Only one *PLS I* and *PLS II* mode was retained as MSE was not substantially decreased by adding more modes. Outliers were not removed here as the aim of this study was to detect these as highly abnormal shapes. By projecting each subject shape transformation onto the final shape mode *PLS II*, the *PLS II* shape vector  $f_{i,PLS}^m$  was derived (for  $m=1$ ). It contains subject-specific weights, describing how much the template  $\bar{T}_{Control,final}$  has to be deformed along the extracted *PLS II* mode in order to match template and subject shape as accurately as possible. I hypothesised that the weights associated with the *PLS II* shape mode yield a notion of how distant a specific subject shape is from the Control template shape – with large positive values representing subjects “far away” and small, negative numbers representing subjects “close” to the normal arch shape.

Furthermore, PCA was performed using the deformation vectors  $\beta$  deforming  $\bar{T}_{Control,final}$  towards all Control and CoA shapes as input, as described in Chapter 3.7.1. The PCA shape vectors  $f_{i,PCA}^m$  were computed for a total of  $K=N-1=39$  shape modes. Using the shape vectors, the subject-specific Mahalanobis distance  $Dist_{Mahal,i}$  (De Maesschalck et al., 2000) was computed as multi-dimensional distance metric in PCA shape space, typically used for outlier detection, here defined as (Jolliffe, I.T., 2002)

$$Dist_{Mahal,i} = \sum_{m=1}^K \frac{\{f_{i,m}\}^2}{Var(\{f_{i,m}\})} \quad (5.1)$$

With  $Var(\{f_{i,PCA}^m\})$  being the variance of the PCA shape vector for subject  $i$  of the  $m^{th}$  PCA shape mode. Essentially,  $Dist_{Mahal,i}$  is a measure of distance between a point and a distribution and can therefore be understood as a “multi-dimensional z-score”, measuring how many standard deviations a point is away from the mean of the distribution (De Maesschalck et al., 2000), (Elfadaly et al., 2016) and (Jolliffe, I.T., 2002). I assumed here that a higher  $Dist_{Mahal,i}$  relates to higher shape abnormality.

No clear guidance exists on how to choose  $m$  and  $K$  for calculating  $Dist_{Mahal,i}$ . Generally, either the “first few”, the “last few” or any reasonable number of principal components can be chosen (Jolliffe, I.T., 2002). Therefore, three types of  $Dist_{Mahal,i}$  were computed:  $Dist_{Mahal,first}$  for the first three components with  $m=1$  and  $K=3$ ;  $Dist_{Mahal,last}$  with  $m=37$  and  $K=39$  for the last three components; and  $Dist_{Mahal,90}$  for  $m=1$  and  $K=10$  covering all modes from 1 to 10, explaining a total of 90% of shape variability.

Correlations between the subject-specific entries of  $f_{i,PLS}^m$ ,  $Dist_{Mahal,first}$ ,  $Dist_{Mahal,last}$ ,  $Dist_{Mahal,90}$ ,  $CoAi$ ,  $A/T$  and the expert scores were assessed using Kendall’s  $\tau$  for non-parametric and ranked data. Non-parametric Mann-Whitney-U Test was applied to analyse differences in distributions of PLS shape vector and Mahalanobis distances between the two groups. Consistency between the expert ranking was assessed using the *Intraclass Correlation Coefficient* (ICC) assuming a 2-way mixed effects model. The significance level was set to  $p<.05$ . Statistical tests were carried out in SPSS (IBM SPSS Statistics, Chicago, IL).

## 5.4 Results

### 5.4.1 Control template

The final Control template showed a smooth, rounded aortic arch with a subtle tapering from ascending to descending aorta, Fig. 5.1a-c. Gross geometric parameters were close to their respective means measured on the entire Control population. Deviations ranged

from 0.3% (volume) to 1.94% (median diameter), resulting in an overall average deviation of 1.02%. Cross-validation revealed that the template shape was not substantially influenced by removing specific subjects from the analysis (Fig. 5.1d). Average surface distances between the full dataset shape and the reduced dataset shapes ranged from 0.14 to 1.22mm.

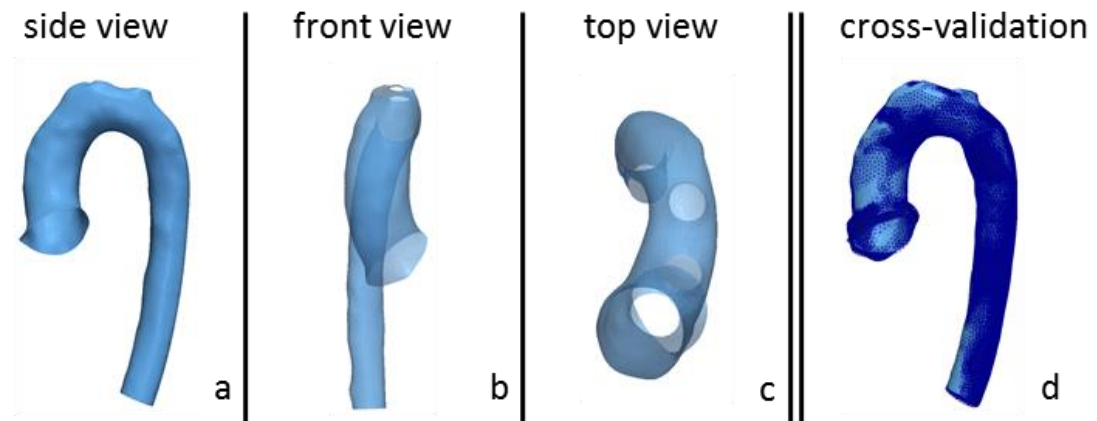


Fig. 5.1: Computed Control template aortic arch shape from different views (a-c) and cross-validated template shapes overlaid (d), adapted from (Bruse et al., 2016b)

#### 5.4.2 PLS and PCA results

*PLS I* extracted shape features most related to BSA such as overall differences in size between subjects. The model yielded a good fit of BSA based on the derived *PLS I* shape mode ( $r=0.70$ ;  $p \leq .001$ ), which accounted for 18% of shape variability. *PLS II* derived shape features most related to either the Control or the CoA group. The *PLS II* shape mode accounted for 21% of the remaining shape variability.

The *PLS II* shape vector values of Control subjects clustered closer together ( $-1036 \pm 252$ ; mean  $\pm$  standard deviation), whereas values derived for CoA subjects showed a larger spread ( $1036 \pm 1396$ ), related to more shape variability within the CoA group. The distribution of *PLS II* shape vector values was significantly different ( $p \leq .001$ ) between the two groups, Fig. 5.2. Control subjects were associated with weight values between  $-1521$  and  $-581$ ; CoA subjects ranged from  $-721$  to  $+3897$ , Fig. 5.3.

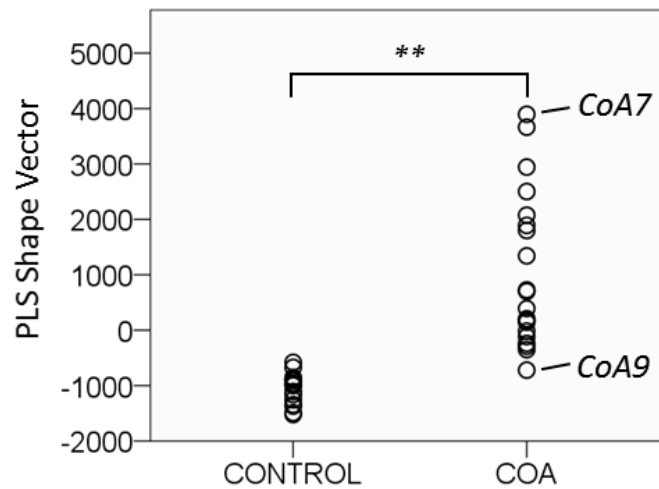


Fig. 5.2: Distributional differences between Control and CoA PLS shape vector entries (\*\* marks statistical significance at level  $p < .01$ ), adapted from (Bruse et al., 2016b)

Regarding the unsupervised results,  $Dist_{Mahal,first}$  ranged from 0.2 to 4.32 for the Control and from 0.23 to 11.68 for the CoA group. Distributions differed significantly ( $p = .017$ ). For  $Dist_{Mahal,last}$  values ranged between 0.09 and 10.52 for the Control and between 0.04 and 19.71 for the CoA group ( $p = .001$ ).  $Dist_{Mahal,90}$  ranged from 1.64 to 12.90 for the Control and from 4.93 to 26.74 for the CoA group ( $p < .001$ ).



Fig. 5.3: Computed shape abnormality ranking from low (blue) to high (red) abnormality according to PLS shape vector results, adapted from (Bruse et al., 2016b)

### 5.4.3 Comparison of expert ranking with SSM results

Qualitative shape rankings were consistent for experts 1 and 2 (mean scores 2.65 and 2.60), while expert 3 on average ranked CoA shapes farther away from normal (mean score 3.40). However, all experts applied a similar range of scores (all standard deviations 1.04). Average ranking was reliable with ICC=0.88 ( $p<.001$ ).

Expert shape scores correlated well with the computed PLS II shape vector for experts 1 and 2, and less for expert 3, Fig. 5.4. Average expert ranking however, showed reasonably good correlation (Kendall's  $\tau=0.36$ ,  $p=.033$ ).

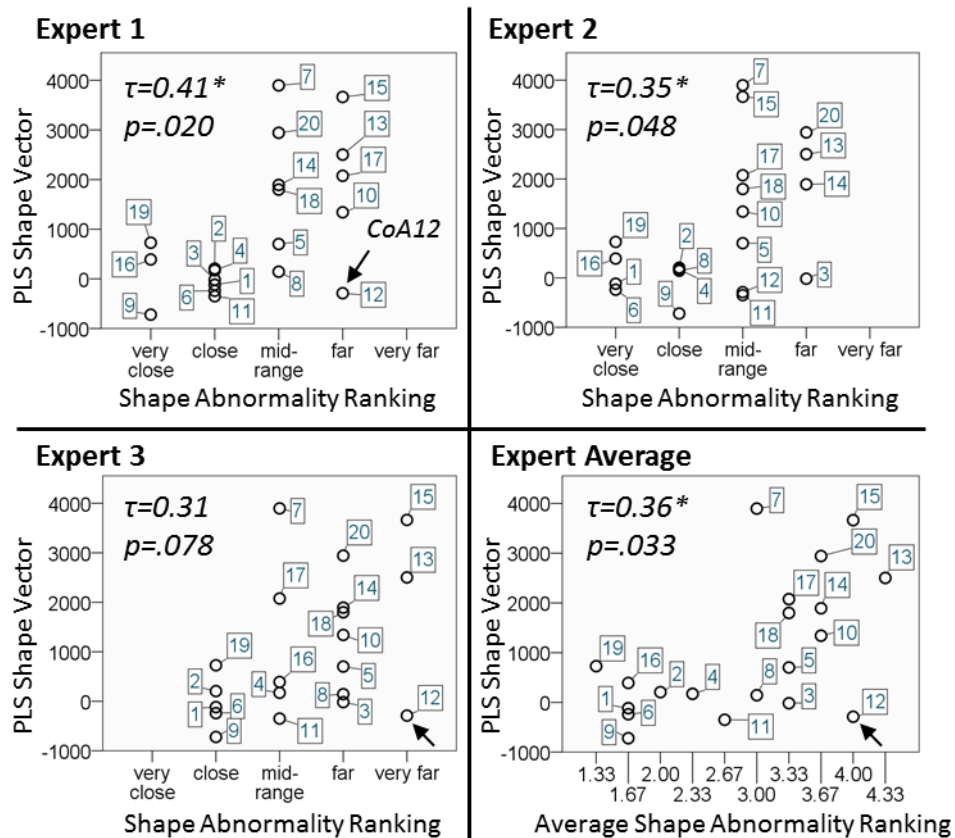


Fig. 5.4: Correlations between computed PLS shape vector and clinical expert ranking, outlying shape CoA12 marked (arrow), adapted from (Bruse et al., 2016b)

Among the Mahalanobis distances,  $Dist_{Mahal,first}$  correlated well with experts 1 and 2, however less with expert 3 and with the average expert ranking (Kendall's  $\tau=0.33$ ,  $p=.053$ ).  $Dist_{Mahal,last}$  did not correlate with any of the expert rankings significantly.  $Dist_{Mahal,90}$  however, showed good agreement with expert 3 and the average expert

ranking (Kendall's  $\tau=0.34$ ,  $p=.045$ ). On the contrary, conventional shape descriptors *CoAi* and *A/T* did not correlate significantly with the experts' ranking as shown in Tab. 5.1.

Tab. 5.1: Correlations between clinical expert shape ranking, computed PLS and PCA abnormality scores and traditionally used shape descriptors, adapted from (Bruse et al., 2016b)

Correlations Kendall's $\tau$ (p-value)	Expert 1	Expert 2	Expert 3	Expert Average
$f_{i,PLS}^m$	<b>0.41</b> (.020)*	<b>0.35</b> (.048)*	0.31 (.078)	<b>0.36</b> (.033)*
$Dist_{Mahal,first}$	<b>0.40</b> (.023)*	<b>0.35</b> (.048)*	0.26 (.135)	0.33 (.053)
$Dist_{Mahal,last}$	-0.27 (.128)	-0.09 (.633)	-0.19 (.278)	-0.22 (.200)
$Dist_{Mahal,90}$	0.29 (.097)	0.34 (.056)	<b>0.40</b> (.025)*	<b>0.34</b> (.045)*
<b>CoAi</b>	-0.11 (.520)	-0.04 (.838)	-0.22 (.222)	-0.11 (.533)
<b>A/T</b>	0.18 (.919)	0.13 (.453)	0.02 (.892)	0.06 (.718)

## 5.5 Discussion

In this chapter, I analysed the transformations of a “normal” template aorta shape towards surgically repaired CoA arch shapes via PLS and PCA in order to derive subject-specific quantitative measures of shape abnormality and assessed their agreement with clinical expert opinion. Both supervised PLS and unsupervised PCA approaches, using the full 3D shape information, performed better than traditional metrics in quantifying shape abnormality of CoA patients. Expectedly, the supervised PLS approach performed best, showing significant associations with two experts and the average expert ranking.

Particularly in extreme cases of CoA shapes being either very close or far away from normal, the derived *PLS II* shape vector reflected the expert ranking well. In the mid-range however, the method struggled to differentiate expert scores sufficiently. In particular one subject (CoA12) contributed to weak correlations between *PLS II* shape vector and expert rankings, Fig. 5.4. With a severe transverse narrowing and a highly localised indentation, subject CoA12 presents sophisticated shape features to be captured, Fig. 5.5. A decrease of the  $\lambda$  parameters might improve the method's accuracy – though at the expense of computation time.

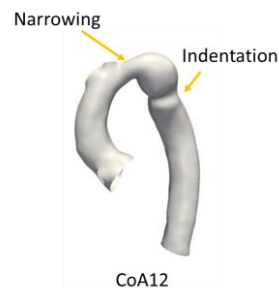


*Fig. 5.5: Outlying shape CoA 12 with challenging arch shape features (narrowed transverse arch and indentation)*

The main limitation of this study is the small sample size for both groups, which impeded applying more elaborate statistics and which should be addressed in future studies. Interestingly though, both the *PLS II* shape vector and the unsupervised Mahalanobis distance derived from PCA data seemed to reflect the experts' shape assessment better than conventional 2D arch shape descriptors as typically used in clinical practice. Further, *PLS II* shape vector and all Mahalanobis distance distributions showed statistically significant differences between the Control and the CoA group, suggesting the SSM results to be useful for classification tasks distinguishing healthy and diseased as well.

Overall, results suggest that the currents-based SSM accounts for more relevant 3D shape information and thus comes closer to intuitive human expert shape assessment. Ultimately, applying such techniques for clinical decision support could lead to more robust, efficient and objective diagnosis and risk stratification strategies in complex cardiac disease.

## 5.6 Summary

The main outcomes of this chapter were:

- Both supervised and unsupervised numerical results derived from the currents-based SSM were in better agreement with clinical expert opinion in terms of assessing overall 3D aortic arch shape abnormality than traditional shape descriptors.

- As expected, supervised PLS results performed slightly better than unsupervised PCA results and using either 10 PCA modes covering 90% of shape variability or the first three PCA modes yielded better results than using the last three PCA modes.
- To the best of my knowledge, this is the first study comparing 3D SSM results with expert opinion in complex cardiovascular disease. Future research should adopt such approaches in order to facilitate translation of computational techniques.

With an established protocol and the assurance that the currents-based SSM results are in line with both traditional metrics as well as clinical expert opinion, the proposed methods could be applied to answer clinically relevant questions in CoA in the following chapter.

## 6 Aortic arch shape and function post coarctation repair: deriving 3D shape biomarkers

*Part of the work described in this chapter has been published in: J. L. Bruse, A. Khushnood, K. McLeod, G. Biglino, M. Sermesant, X. Pennec, A. M. Taylor, T.-Y. Hsia, and S. Schievano. How successful is successful? Aortic arch shape following successful aortic coarctation repair correlates with left ventricular function, The Journal of Thoracic and Cardiovascular Surgery, vol. 153, pp. 418–427, Feb. 2017. (Bruse et al., 2017b). Copyright (2017) with permission of Elsevier.*

The two preceding chapters established robust protocols to run the currents-based statistical shape modelling (SSM) framework and demonstrated that extracted 3D shape features were in line with traditional shape descriptors and clinical expert opinion. Specifically, it was shown that distinct aortic arch shape features could be associated with cardiac functional surrogates such as LVEF in a cohort of 20 CoA patients, highlighting the possibility to use the SSM framework to derive novel shape biomarkers. While numerous clinical studies suggest associations between aortic arch shape and cardiac function in repaired CoA, these associations have never been investigated via an SSM making use of the full 3D shape information provided by medical image data. This chapter therefore applies the established SSM methods to a larger cohort of patients post CoA repair and includes additional functional parameters in order to investigate novel associations between 3D arch shape and cardiac function.

## 6.1 Abstract

*Background: Having a robust and validated currents-based SSM framework established (Chapter 4), I aimed to apply the developed methods to investigate relationships between aortic arch 3D shape features and clinically relevant functional data in a larger cohort of patients post CoA repair.*

*Methods: A total of 53 patients post CoA repair (age  $22.3 \pm 5.6$  years; 12-38 years after repair) were included and 3D arch shape models from CMR data were reconstructed. The currents-based SSM was used to compute the template aortic arch shape and to calculate deformation vectors of the template towards each patient's arch anatomy. Three-dimensional arch shape biomarkers most related to the functional parameters left ventricular ejection fraction (LVEF), indexed left ventricular mass (iLVM) and resting systolic blood pressure (BP), see Chapter 3.8, were extracted from the deformation vector data by means of partial least squares (PLS) regression.*

*Results: Distinct 3D arch shape features correlated significantly with LVEF ( $r=0.42$ ,  $p=.024$ ) and iLVM ( $r=0.44$ ,  $p=.014$ ). Indeed, low normal LVEF and elevated iLVM visually related to an overall arch shape with elongated ascending aorta with high arch height-to-width ratio, a relatively short proximal transverse arch, and a slightly dilated descending aorta. Elevated BP was associated with Gothic arch shape features, yet not significantly ( $r=0.32$ ,  $p=.160$ ).*

*Conclusions: The currents-based SSM in combination with PLS revealed that overall 3D aortic arch shape features of repaired CoA appear to be associated with left ventricular function. The method can thus be an adjunct to long-term risk assessment in patients following aortic arch operations.*

## 6.2 Introduction

As outlined earlier, coarctation of the aorta (CoA) has recently been described as a “complex” rather than simple cardiac lesion (Hauser, 2003), (De Caro et al., 2007), (Puranik et al., 2009). One reason for this is the high incidence of complications late after surgical repair, even though overall survival is improving (Brown et al., 2013). Apart from re-coarctation, patients can often suffer from hypertension (HT) and left ventricular (LV) hypertrophy, associated with increased cardiac afterload and diastolic heart failure, warranting regular screening (Puranik et al., 2009), (Brown et al., 2013), (O’Sullivan, 2014), (Canniffe et al., 2013). It is hence vital to look for factors contributing to long-term morbidity and mortality in this group of patients.

In assessing CoA repair, aortic arch shape has played a crucial role in the past decades. Residual discrete stenosis or narrowing (Ong et al., 1992), (Vriend et al., 2005), transverse arch hypoplasia (Weber et al., 1993), (Lee et al., 2012), (O’Sullivan, 2014) or the angulated, so-called “Gothic” arch with a high arch height-to-width ( $A/T$ ) ratio have all been associated with worse clinical outcomes (Ou et al., 2004), (Ou et al., 2007), (Ou et al., 2008a) compared to a more rounded “Romanesque” arch, see also Chapter 2.3.2. Yet, to date association between HT and a Gothic arch shape remains controversial (De Caro et al., 2007) and other studies advise to focus on transverse arch and isthmus hypoplasia instead (Lee et al., 2012), (Ntsinjana et al., 2013b).

Those discrepancies may in part be due to the fact that most clinical studies assessing arch shape were based on linear two-dimensional (2D) measurements of morphometric parameters. However, previous chapters have shown that 3D reconstructions of aortic arches post CoA repair cannot be fully captured using 2D morphometrics only. Gothic aortic arches with similar  $A/T$  ratio, for instance, may still differ considerably in other shape features such as dilatation, narrowing or hypoplasia from ascending down to the descending aorta. The complex 3D shape data therefore call for more sophisticated methods capable of analysing cardiac anatomy without restricting themselves to manually measured parameters.

In this chapter, I applied the currents-based SSM approach to a larger cohort of 3D aortic arch shape models of patients post CoA repair derived from CMR image data. Using the SSM, I sought to analyse 3D aortic arch shape post CoA repair in detail, based on the hypothesis that distinct arch shape features may be associated with functional parameters routinely acquired during follow-up CMR scans. The leading question to be answered by this chapter was:

- Which 3D arch shape features are associated with clinically relevant parameters in CoA repair?

## 6.3 Methods

### 6.3.1 Patient population

In order to increase the sample size from 20 analysed in Chapter 4, the current study included retrospective routine follow-up CMR image data of a total of 53 asymptomatic patients post-aortic CoA repair (mean age  $22.3 \pm 5.6$  years, Tab. 6.1), including scans from 2007 to 2015, Fig. 6.1.



Fig. 6.1: Input shape population of 53 aortic arch surface models and computed template shape (blue), adapted from (Bruse et al., 2017b)

The CMRs were obtained 12 to 38 years (mean  $20.6 \pm 5.0$  years) following initial CoA repair, and none of the patients had hemodynamically significant residual aortic arch

obstruction or CoA requiring revision/reintervention as determined by Doppler echocardiographic interrogation. 36 patients had initial repair during the first year of life (68%), 7 patients in the second year, and 10 patients more than 5 years after birth (with the oldest age at repair being 10 years). To ensure a coherent patient cohort, inclusion criteria were: no complex left-sided cardiac lesions; no distinct aneurysm or interrupted aortic arch; age between 15 and 40 years; and no image artefacts due to stents or valve implants. The majority of patients had undergone end-to-end (E-E) CoA repair shortly after birth (~80%), and around half of the cohort had a bicuspid aortic valve (BAV, Tab. 6.1).

*Tab. 6.1: Detailed clinical information about the included patient cohort post CoA repair for shape biomarker extraction, adapted from (Bruse et al., 2017b)*

Variables	Mean±SD (range)
Number of patients	53
Age at time of CMR [years]	22.3±5.6 (15.1-38.1)
Height [cm]	170.5±9.5 (147-188)
BSA [m <sup>2</sup> ]	1.83±0.21 (1.44-2.22)
Aortic valve morphology (TAV/BAV/fBAV)	(21/26/6)
Type of initial repair (E-E/ExtE-E/flap/patch/balloon)	(42/1/6/3/1)
LVEF [%]	64.1±7.3 (52-78)
iLVM [g/m <sup>2</sup> ]	64.1±14.7 (37-94)
Systolic resting BP [mmHg]	130.0±17.1 (92-163)

### 6.3.2 Functional parameters

Left ventricular ejection fraction (LVEF) and left ventricular mass (LVM) were calculated from the CMR short-axis stack, see Chapter 3.8 (Tab. 6.1). Systolic blood pressure (BP) was measured during CMR acquisition using a cuff in the right arm. LVEF, LVM and BP data was retrieved from GOSH CMR reports. Parameters were indexed with body surface area (BSA), where appropriate (denoted with a preceding lower case *i*).

### 6.3.3 Segmentation and pre-processing

Similar to the previous chapters, protocols established in Chapter 4 were followed: Aortic arch volumes were segmented and reconstructed semi-automatically from the CMR whole-heart data using Active Contours segmentation tools in ITKSnap

(Chapter 3.2.2), were exported as computational surface meshes and were cut consistently with a plane below the aortic root and at the level of the diaphragm. Head and neck vessels and coronary arteries were removed. Prior to 3D shape analysis, the obtained aortic arch shapes from all patients were rigidly registered to one subject using the iterative closest point ICP algorithm in VMTK. The meshed, cut and aligned 3D arch surface models constituted the input for the currents-based SSM, Fig. 6.1.

### 6.3.4 Statistical shape analysis method

Template shape and deformation vectors deforming the template towards each input shape were computed using the *Deformetrica* SSM framework (Durrleman et al., 2014) as opposed to the MATLAB-based *exoshape* framework used for the previous two chapters. *Deformetrica* allows much faster template and deformation estimation and therefore smaller  $\lambda_w$  and  $\lambda_v$  values than *exoshape*. Therefore, in this and the following studies, the matching criterion from Chapter 4.3.2.3 (>80% error reduction) was increased to >95%, resulting in lower  $\lambda$  values of  $\lambda_w=5\text{mm}$  and  $\lambda_v=20\text{mm}$ .

As in Chapter 3.7.2, partial least squares (PLS) regression was applied to the computed set of deformation vectors  $\beta$ , extracting the first PLS shape mode in order to determine those 3D shape features (i.e. shape deformations of the template) most correlated with a given external response parameter (LVEF, iLVM and BP). Prior to extracting shape features related to functional parameters, size effects due to differences in BSA between patients were removed with a first PLS regression, as described in Eq. 4.4. Results were visualised in ParaView, (Ahrens et al., 2005) by deforming the computed template arch shape along the PLS shape modes from *low* (-2 standard deviations, SD), to *high* (+2SD) values of the respective response parameter.

For numerical assessment, the subject-specific PLS shape vectors associated with each respective functional parameter were extracted via projection of each arch shape onto the respective PLS shape mode (Eq. 3.17). Associations between PLS shape vectors and parameters were then analysed via bivariate correlation analysis as described in Chapter 4.3.4.

The SSM template shape and patient-specific deformation vectors were computed based on the 53 input arch surface models. Similar to previous chapters, the template shape was validated as the representative mean shape of the population by comparing gross geometric characteristics (volume  $V$ , surface area  $A_{surf}$  and centerline length  $L_{CL}$ ) of the template against the respective mean values from the entire population extracted via VMTK. Secondly, the template shape was validated numerically via 10-fold cross-validation in order to verify independence of the included subjects, see Chapter 4.3.3.5.

### 6.3.5 Traditional 3D morphometrics

In order to allow for an additional quantitative shape assessment of the derived 3D shape patterns related to functional parameters, further morphometric parameters were measured manually on the computed PLS shape modes and on the obtained template aorta (Mimics, Materialise, Leuven, Belgium): arch height  $A$  to width  $T$  ratio ( $A/T$ ) just above the aortic root and, at the same level, the best fitting ascending and descending aortic diameter ( $D_{asc}$  and  $D_{desc}$ , respectively) ratio ( $D_{asc}/D_{desc}$ ).

### 6.3.6 Statistical analysis

Associations between functional parameters and PLS shape vectors describing 3D arch shape features were assessed via standard bi-variate correlation analyses. *Pearson's  $r$*  is reported for parametric, normally distributed data, while *Kendall's  $\tau$*  is reported for non-parametric data. Non-normality was assumed if the Shapiro-Wilk test was significant, assuming a significance level of  $p < .05$ .

For correlation analyses, computed p-values were adjusted for multiple comparisons via permutation tests with 100,000 permutations at  $\alpha$ -level .05 (Groppe et al., 2011). Note that in Chapter 4, p-values were not adjusted for multiple comparisons as the study was considered exploratory and the aim was to assess the usability of the SSM framework. On the contrary, here, the aim was to obtain novel, clinically relevant biomarkers from a larger population of CoA repair. As before, the Cook's distance (measuring the influence of a single subject on the final regression results) was computed for each PLS regression run. Subjects exceeding four times the mean Cook's distance were

considered to be influential and were subsequently removed from the respective shape feature extraction. Statistical tests were performed in MATLAB and SPSS (IBM SPSS Statistics, SPSS Inc., USA).

## 6.4 Results

### 6.4.1 Template aortic arch

For the following descriptions of aortic arch shape, “Gothic” denotes an arch with high  $A/T$  ratio and signs of a distinct *angulation* at the crest of the arch, while “Romanesque” denotes an arch with high height-to-width ratio, but a more rounded transverse arch (Ou et al., 2007).

The computed template aorta, representing the mean 3D shape of the CoA population, showed a moderately increased  $A/T$  ratio compared to the healthy aortic arch shape and overall non-angulated Romanesque-type arch shape with a rather slim transverse arch, yet without any distinct narrowing or re-coarctation, Fig. 6.1. Traditional morphometric parameters measured on the template shape were close to their respective mean values as calculated from the entire cohort, with an overall deviation  $\Delta$  of 3.3% (individual deviations  $\Delta V=5.6\%$ ,  $\Delta A_{surf}=3.0\%$ , and  $\Delta L_{CL}=1.4\%$ ). In addition, cross-validation confirmed that removing subjects randomly from the population did not change the template shape significantly (average surface distance between original template shape and cross-validated shapes  $D_{surf}=0.285\pm 0.07\text{mm}$ ). The template was thus validated as a representative anatomic mean shape of the cohort.

Prior to extracting shape features related to functional parameters, size effects were removed by regressing the computed deformation vectors with BSA. One subject had to be removed from subsequent analyses for being influential to the regression, following the Cook’s distance analysis.

### 6.4.2 Correlations of arch shape features with ejection fraction

Visualizing the PLS regression results showed lower – albeit in the “normal” range above 50% – LVEF to be associated with elevated  $A/T$  ratio ( $A/T=1.33$ , Tab. 6.2), a slim

ascending and shorter transverse arch and a slight size mismatch between a smaller isthmus and larger descending aorta. Instead, higher (normal) LVEF was associated with shorter, generally more rounded ( $A/T=0.93$ ) aortic arch shapes with larger ascending aorta ( $D_{asc}/D_{desc}=1.50$ ), Fig. 6.2. Correlation of the derived shape vector related to this shape change with LVEF revealed a significant association between those 3D shape features and LVEF after adjusting for multiple comparisons ( $r=0.42$ ,  $p=.024$ ). Two subjects were excluded according to the Cook's distance criterion.

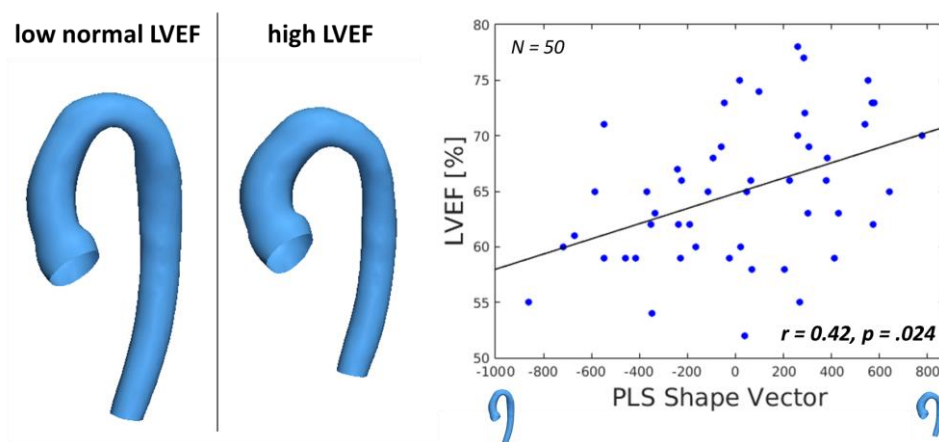


Fig. 6.2: Arch shape features associated with low and high LVEF as represented by LVEF shape mode deformations (left) and respective correlations between patient-specific shape vector values and LVEF, adapted from (Bruse et al., 2017b)

#### 6.4.3 Correlation of arch shape features with left ventricular mass

Arch shape features most associated with high and low iLVM were similar but exaggerated compared to those described for LVEF. High iLVM was significantly associated with a high  $A/T$  ratio arch ( $A/T=1.47$ ) with very slim ascending and nearly straight (i.e. edgy or crenel-like) transverse arch that tapered into a dilated and long descending aorta, creating a distinct size-mismatch at the isthmus region ( $r=0.44$ ,  $p=.014$ ,  $D_{asc}/D_{desc} = 0.96$ , Fig. 6.3). An overall even smaller, rounded arch ( $A/T=0.70$ ) with a slightly dilated ascending aorta that tapers into a relatively smaller distal transverse and isthmus arch continuation ( $D_{asc}/D_{desc}=1.96$ ) was associated with low iLVM. Two subjects were excluded following Cook's distance analysis.

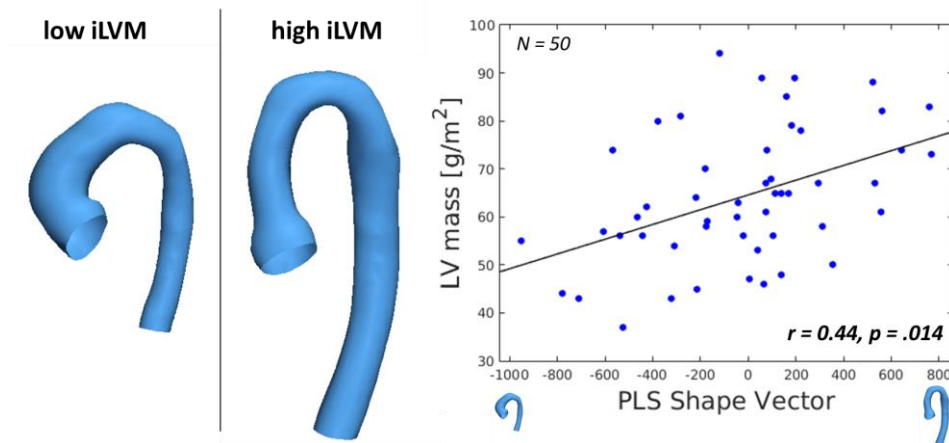


Fig. 6.3: Arch shape features associated with low and high iLVM (left) and respective correlations between shape vector and iLVM, adapted from (Bruse et al., 2017b)

#### 6.4.4 Correlation of arch shape features with resting blood pressure

High systolic resting BP was related to a Gothic-type arch shape (with arch angulation,  $A/T=1.41$ ) presenting with a mild ascending arch dilation and a narrow and short, angulated transverse arch, followed by a mild diameter increase from isthmus to descending aorta ( $D_{asc}/D_{desc} = 1.41$ , Fig. 6.4). The aortic arch shape associated with low BP was generally of similar size but showed a more crenel-like, slim ascending and straight and distally slim transverse arch. Yet, those shape associations, after adjusting for multiple comparisons, were not statistically significant ( $r=0.32$ ,  $p=.160$ ). Two subjects were excluded according to Cook's criterion.

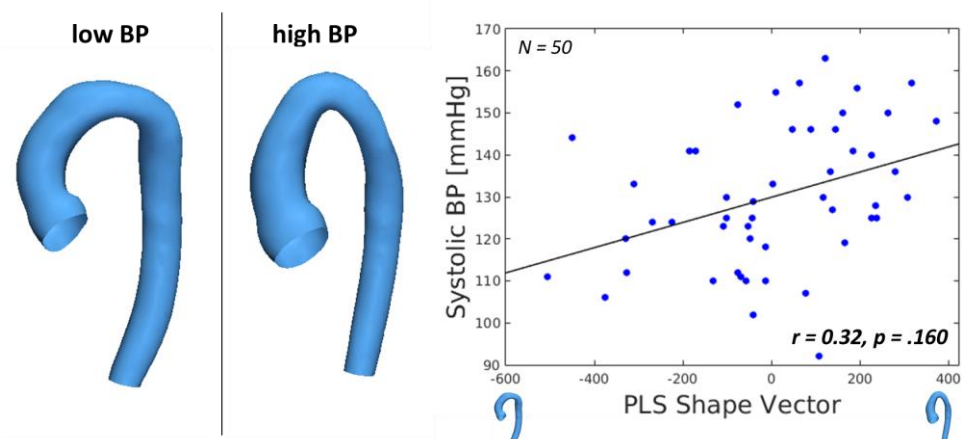


Fig. 6.4: Aortic arch shape features associated with low and high systolic resting BP (left) and respective correlations between PLS shape vector and BP, adapted from (Bruse et al., 2017b)

Tab. 6.2: Correlations between functional parameters and respective computed PLS shape vectors, adapted from (Bruse et al., 2017b)

Correlations Pearson's r (adj. p-value)	LVEF [%]	iLVM [g/m <sup>2</sup> ]	BP [mmHg]	LVEF Shape Vector	iLVM Shape Vector	BP Shape Vector
<b>LVEF</b> [%]	1.00 (.000)	0.08 (.992)	0.15 (.889)	<b>0.42</b> <b>(.024)*</b>	-0.34 (.108)	0.20 (.660)
<b>iLVM</b> [g/m <sup>2</sup> ]	0.08 (.990)	1.00 (.000)	0.01 (.995)	-0.36 (.084)	<b>0.44</b> <b>(.014)*</b>	-0.09 (.996)
<b>BP</b> [mmHg]	0.15 (.890)	0.01 (.999)	1.00 (.000)	-0.04 (.999)	0.02 (.999)	0.32 (.160)

## 6.5 Discussion

Late after coarctation repair, patients present with complex aortic arch shapes that deviate substantially from a healthy rounded aortic arch. While past research has shown that there is something about this shape that is reflected in long-term patient outcome, clinical analysis of arch shape to date has not lived up to the fact that elaborate 3D shape information of cardiac anatomy can be processed with novel, sophisticated analysis tools. Therefore, 3D aortic arch shape post CoA repair was analysed here in greater detail by applying the currents-based SSM, capable of extracting and visualizing complex shape features related to cardiac function.

Results suggest that a large, high *A/T* arch shape, particularly when combined with a slim ascending and short transverse, but long and dilated descending aorta, is significantly associated with impaired left ventricular function as implied by low left ventricular ejection fraction (LVEF) and elevated indexed left ventricular mass (iLVM). Note that LVEF was not actually “low” but “low normal” as the lowest LVEF in the cohort was 55% (highest 78%). An overall Gothic (angulated) arch shape seemed to be associated with high systolic resting blood pressure, yet not significantly.

### 6.5.1 Associations between aortic arch shape features and CMR-derived functional parameters

To my knowledge, previous studies have not focussed on aortic arch shape associations with LVEF post CoA repair – probably due to the fact that patients typically present with preserved, “normal” LVEF above 50%. Yet, results of this study suggest that apart from

known associations with increased iLVM and BP response, a high arch  $A/T$  ratio combined with low calibre ascending and short transverse arch may also relate to a diminished pumping efficiency of the left heart. This may be due to increased afterload posed by this specific arch geometry.

Arch shape features correlating with elevated iLVM were similar but showed an overall larger aorta with slim ascending and short transverse arch, and a narrowing at the isthmus region before tapering into a dilated descending aorta. Particularly the obtained high arch  $A/T$  ratio being associated with elevated iLVM is in accordance with the literature (Ou et al., 2004), (Ou et al., 2008a), (Ou et al., 2008b), (Donazzan et al., 2014), even though most of the mentioned studies associated high arch  $A/T$  with a Gothic, hence *angulated*, overall arch shape. I did not find such marked angulation, but found a more rounded crenel-like, yet short and slim transverse arch combined with a narrowing at the isthmus region to be related to elevated iLVM. Residual narrowing has been previously associated with higher iLVM by Ong et al (Ong et al., 1992). With correlations being rather strong (p-value not adjusted for multiple comparisons  $p=.0013$ ; adjusted  $p_{adj}=.014$ ), and elevated iLVM being a well-validated risk marker for increased cardiovascular morbidity, including coronary artery disease and cerebral vascular accidents (Levy et al., 1990), (Brown et al., 2013), the found “shape biomarkers” may constitute an important risk marker in patients post CoA repair.

One important aspect, which has not been addressed in previous studies, is the relevance of overall *size* (i.e. length from aortic valve down to the diaphragm) when assessing aortic arch shapes. Here, arch reconstructions were cut consistently at the level of the aortic root and at the level of the diaphragm and after removing effects due to differences in body size, smaller and more compact rounded arches seemed to be functionally superior. Yet, overall arch size is easily omitted when using traditional morphometrics. Therefore, relative overall size appearing to be functionally relevant, justifies assessing shape of cardiac anatomy as a whole.

### 6.5.2 Arch shape features and blood pressure response

Even though not statistically significant, elevated systolic resting blood pressure (BP) was found to be associated with a normal sized but slightly angulated, Gothic-type arch shape, showing slight dilation of the ascending aorta and some residual narrowing at the site of coarctation.

Gothicity and increased arch  $A/T$  ratio being related to elevated resting BP is in accordance with major studies of arch shape post CoA repair by Ou et al (Ou et al., 2004), as well as with studies focusing on exercise BP response (Ou et al., 2006), (Donazzan et al., 2014). However, other studies found residual narrowing and stenosis (Ong et al., 1992), (Vriend et al., 2005), transverse arch morphology (Weber et al., 1993) or both narrowing and transverse arch hypoplasia (Lee et al., 2012), (Ntsinjana et al., 2013b) to be related to HT. Interestingly, results of this study “combine” all these shape features within the derived 3D arch shape associated with elevated systolic resting BP, which suggests all of them to play a role in BP response post CoA repair. This circumstance and the fact that results were not statistically significant after adjusting for multiple comparisons, could explain inconclusive results from previous studies.

Not being able to pinpoint one specific arch shape feature directly related to HT, points towards another crux of restricting aortic arch shape analysis to traditional 2D morphometrics: all shapes associated with unfavourable functional behaviour in the study were visually associated with a high arch  $A/T$  ratio, yet this does not describe the obtained 3D shapes sufficiently. Apart from  $A/T$  ratio being high, derived shapes showed many more associated 3D shape features such as a dilated ascending or descending aorta, short transverse arch or a distinct angulation. Thus, a classification of arch shapes according to 2D metrics is limited – one needs to carefully distinguish between “Romanesque” or “Gothic” features and needs to assess the aorta as a whole, without restriction to one or a few parameters. This point is addressed by SSM, including all 3D shape information at hand.

Overall, caution is warranted when drawing conclusions about associations between HT and aortic arch shape, not least because reduced arterial compliance and distensibility (Lombardi et al., 2013), (Canniffe et al., 2013), (O’Sullivan, 2014) or other factors than aortic arch shape (Hauser et al., 2000) have been shown to affect BP response as well.

### **6.5.3 Limitations and future work**

The last point leads to one major limitation of this study: here, I purely focus on arch shape, without taking into account arterial wall properties such as reduced compliance or locally increased wall thickness, which have previously been associated with Gothic arches (Ou et al., 2007), (Ou et al., 2008a), (Donazzan et al., 2014) and elevated iLVM (Ou et al., 2008b). This would need to be addressed by future studies, including wave intensity analysis, for instance. Furthermore, results are observational or phenomenological only, without providing any direct functional insight. Studies involving computational fluid dynamics (CFD, see Chapter 3.9) or 4D flow CMR data as shown in (Frydrychowicz et al., 2011) at a larger scale may provide additional functional parameters such as energy loss or wall shear stress distributions, which could be included as functional response parameters to complement these results. Some aspects will be addressed in Chapter 7.

An interesting area of study would be to investigate and account for the effect of the surgical approach. Unfortunately, this was not pursuable in this cohort as the number of patients that had not had an E-E anastomosis but another type of initial repair (about 20%) was too low. In addition, the number of reoperations or catheter-based re-interventions remained low (20% of the cohort) and most patients on follow-up had little re-coarctation. For future multi-centre studies, the currents-based SSM methodology could be easily expanded to extract 3D shape patterns most associated with a certain surgical technique, number and type of re-intervention or even with a certain centre or surgeon, thus bearing the potential for in-depth analysis of surgical outcome.

## 6.6 Summary

The main outcomes of this chapter were:

- Previously not known associations between diminished (low normal) left ventricular ejection fraction and 3D aortic arch shape as well as between arch shape features and elevated left ventricular mass, i.e. novel 3D shape biomarkers were found.
- Overall larger aortic arches with high arch height-to-width ratio, slim ascending and short transverse arch seemed to be functionally inferior to more compact and rounded aortic arches.
- Results suggested a Gothic arch shape with a slightly dilated ascending aorta and some residual isthmus narrowing to be associated with elevated systolic resting blood pressure; this, however, was not statistically significant.
- This study confirmed previous literature in claiming that aortic arch shape in patients post CoA repair is related to cardiac function. Yet, results suggest that functional outcome is likely to be associated with a complex combination of 3D shape features, rather than a few morphometric parameters, which is why sophisticated shape analysis is advisable for assessing pathologic cardiac anatomy.
- In conclusion, it was shown that the currents-based SSM approach could constitute a valuable clinical tool for deriving clinically relevant shape biomarkers that may improve risk stratification during follow up of CoA patients.

As mentioned in the limitations, only phenomenological “shape biomarkers” were derived in this chapter based on the data provided, without any clear functional basis. In order to further understand shape and function correlation and address this issue, the next chapter aims to provide additional mechanistic insight in why the identified arch shapes may be functionally unfavourable.

## **7 Joint phenomenological and mechanistic computational modelling: CFD simulations on computed shape modes**

In the previous chapter, partial least squares (PLS) regression extracted 3D aortic arch shape features most associated with either high or low cardiac functional parameters. Along with numerical results, statistical shape modelling (SSM) results provided computed aortic arch shapes, i.e. template arch shapes were deformed along the respective PLS shape modes to visually represent 3D arch shape features most related to each functional parameter. These computed PLS shape mode arch shapes offer the possibility to perform mechanistic, fluid dynamics computational modelling in order to derive further functional parameters related to hemodynamic performance associated with each PLS shape mode. Although to date mechanistic computational modelling and SSM results have not yet been combined to provide further insight into disease mechanisms, it is likely that observational results have an underlying mechanistic explanation. In fact, meaningful associations between the SSM-derived PLS shape mode arch shapes and computed functional parameters would strengthen the phenomenological results identified in Chapter 6 by providing a potential mechanistic explanation. In this chapter, mechanistic and phenomenological modelling are therefore joined by performing computational fluid dynamics (CFD) analyses on the PLS shape modes in order to investigate whether shape modes associated with “worse” cardiac function are also related to “worse” hemodynamic performance, i.e. higher pressure drops and higher power losses.

## 7.1 Abstract

*Background: Computed unfavourable aortic arch shapes derived from partial least squares (PLS) regression for low left ventricular ejection fraction (LVEF), high indexed left ventricular mass (iLVM) and high systolic resting blood pressure (BP) may lead to higher flow resistance and energy loss across the arch than their more favourable counterparts. By performing CFD analyses on the computed shape modes, I sought to investigate whether there may be such mechanistic basis to the observational SSM results.*

*Methods: Six PLS shape modes corresponding to low/high LVEF, low/high iLVM and low/high BP as computed in Chapter 6 based on 53 patients post CoA repair were volume-meshed and served as input for CFD analyses in ANSYS FLUENT. Peak systolic flow conditions were modelled, maintaining the same flow boundary conditions for all models, in order to isolate the effect of arch shape alone. Pressure drop across the arch and local power loss were computed to quantify the energetic efficiency of each arch shape model.*

*Results: Peak systolic pressure drops across the arch were in the order of 10mmHg, with pressure drop reductions ranging from 13% for the iLVM low model compared to the iLVM high model to 27% reduction for the BP low compared to the BP high model. Similarly, power losses were reduced by 17% for the LVEF high model compared to its LVEF low counterpart and both the iLVM low model and the BP low model showed power loss reductions in the order of 23% compared to their counterpart.*

*Conclusions: The unfavourable aortic arch shapes computed by the SSM in Chapter 6 associated with low LVEF, high iLVM and high BP showed higher pressure drops and higher power losses than arch shape features that were linked to high LVEF, low iLVM and low BP. This study thus provides a potential mechanistic basis for the phenomenological results derived via the currents-based SSM approach in a cohort of patients post CoA repair.*

## 7.2 Introduction

Few studies to date combine both image-based phenomenological computational modelling with mechanistic modelling to analyse complex disease characteristics, even though a complementary approach may facilitate the transition from data to knowledge and more informed decision making (Lamata et al., 2014), (Frangi et al., 2016). SSM-driven analyses often remain observational, while mechanistic simulations are predominantly applied to a few cases only, thus usually lacking statistical backup of findings, see Chapter 2.4.2. Due to the complexity and high computational efforts of image-based *mechanistic* modelling, this chapter sought a reversed approach and uses mechanistic modelling to support observational findings from SSM results.

In the previous chapter, certain 3D aortic arch shape features have been linked to “better” or “worse” cardiac function as marked by high or low LVEF, low or high iLVM and low or high BP, respectively, via the currents-based SSM. Thereby, an overall large aortic arch with slim and long ascending, short transverse and slightly dilated descending aorta was found to be unfavourable in a cohort of 53 patients post CoA repair via PLS regression. The unfavourable arch shapes were essentially provided as computed 3D surface meshes in the form of PLS shape modes, deforming the template shape along the mode towards “high” (+2 standard deviations, SD) or “low” (-2SD) values of the respective functional response parameter, Fig. 7.1.

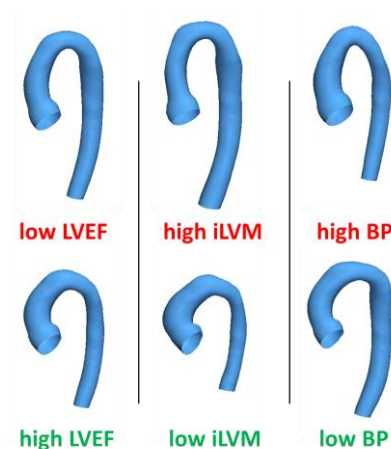


Fig. 7.1: Computed arch shape features associated with low or high values of cardiac functional parameters as determined in previous chapter, adapted from (Bruse et al., 2017b)

Previous studies suggest associations between low LVEF, high iLVM (i.e. LVH see Chapter 3.8.3), high BP (i.e. HT) and aortic arch obstruction, leading to higher flow resistance or higher afterload found in CoA (Lorell and Carabello, 2000), (Gardin and Lauer, 2004), (Rosenthal, 2005).

Approximating the aorta as a tube, basic fluid mechanic equations suitable for perfused tubes with circular cross-sections link energy loss due to friction (quantified by the pressure drop across the tube  $\Delta p$ ) to geometric parameters. Thereby, pressure drop  $\Delta p$  for a straight tube can be obtained by (Bohl and Elmendorf, 2014)

$$\Delta p_{tube, straight} = \frac{1}{2} \rho \bar{v}^2 \cdot \gamma \cdot \frac{L}{d} \quad (7.1)$$

with  $\rho$  being the (constant) fluid density,  $\bar{v}$  being the average fluid velocity,  $\gamma$  being the friction coefficient,  $L$  being the tube length and  $d$  being the tube diameter. Further, for a bended tube,  $\Delta p$  can be approximated by (Bohl and Elmendorf, 2014)

$$\Delta p_{tube, bended} = \frac{1}{2} \rho \bar{v}^2 \cdot \xi_B \quad (7.2)$$

With  $\xi_B$  being the resistance coefficient, which is a function of the relative curvature  $C_{rel} = R/d$  (with  $R$  being the curvature radius and  $d$  the tube diameter), the tube deflection angle  $\theta$ , the wall roughness  $k$  and the Reynolds number  $Re = f(\bar{v}, d, \text{fluid properties})$  (Bohl and Elmendorf, 2014)

$$\xi_B = f(C_{rel}, \theta, k, Re) \quad (7.3)$$

By roughly approximating an aortic arch as a bended tube, one can therefore assume high  $\Delta p$  to be related to high  $L$ , low  $d$  and high  $\xi_B$  (which is associated with high curvature and high deflection angle (Bohl and Elmendorf, 2014)).

Assuming such a mechanistic basis associating arch shape and hemodynamic performance, I hypothesised that the identified unfavourable arch shape features represented by the respective PLS shape modes for low LVEF, high iLVM and high BP would relate to higher pressure drops across the arch  $\Delta p$  (Nielsen et al., 2005) and higher

power losses  $PL$  (Hsia et al., 2004), (Dasi et al., 2008) compared to their respective high LVEF, low iLVM and low BP counterparts. Such associations between the computed PLS shape mode arch shapes and computed functional parameters  $\Delta p$  and  $PL$  would strengthen the purely observational results from Chapter 6 by providing a potential mechanistic explanation. The key question to be answered by this chapter was therefore:

- How do phenomenological SSM results compare to results from mechanistic computational modelling such as CFD?

## 7.3 Methods

### 7.3.1 Input shapes

Flow analysis was carried out on the 6 PLS shape mode models, derived for high and low LVEF, iLVM and BP, based on the 53 CoA patients presented in Chapter 6.4. Models are called “high LVEF”, “low LVEF” etc. in the following. All surface meshes were fitted with flow extensions for the upper head and neck vessels (HNV) according to their initial position and diameters as defined by the deformed template shape. Extensions for the HNV were set to 5 times the vessel diameter and for the inlet half times the root diameter. The boundaries were defined as “inlet”, “brachiocephalic (BCC)”, “left common carotid (LCC)”, “left subclavian arteries (LSC)” and “outlet” as shown in Fig. 7.2.

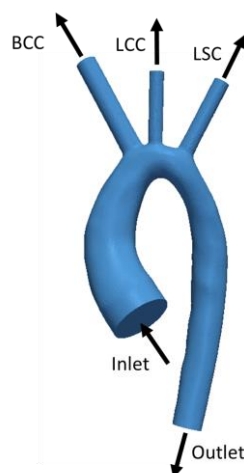


Fig. 7.2: Definition of inflow and outflow boundaries for CFD simulations

### 7.3.2 Volume meshing

The 6 PLS models were then meshed using an unstructured, centreline-adapted tetrahedral volume mesh in VMTK, which was improved by reducing skewed mesh elements in ANSYS ICEM CFD, see Chapter 3.3. In order to find an adequate overall mesh size, a mesh independence study was carried out. One model (high LVEF) was meshed from low ( $\sim 6$  cells/mm<sup>3</sup>) to high ( $\sim 25$  cells/mm<sup>3</sup>) volume mesh resolution and CFD simulations were run keeping all parameters constant except the mesh size. Output parameter of interest was power loss ( $PL$ ) across the arch, which was recorded for all runs. Fig. 7.3 shows that from a resolution of  $\sim 14$  cells/mm<sup>3</sup> onwards,  $PL$  did not change considerably (<2%) from one simulation to the other. Consequently, all other models were meshed with this resolution, resulting in mesh sizes between 900.000 to 1.2 million elements.

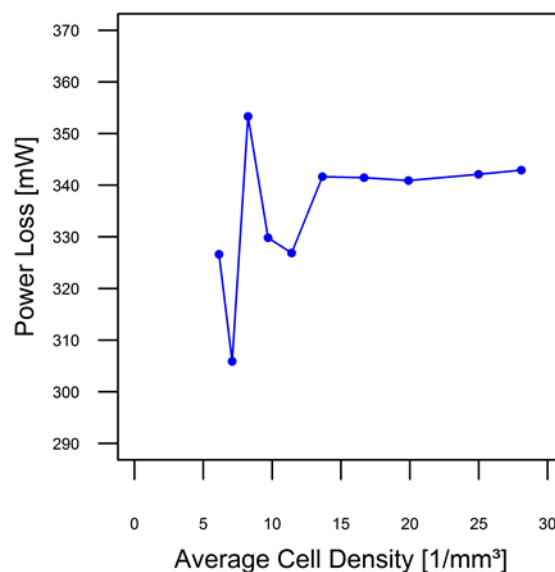


Fig. 7.3: Power loss relative to average volume mesh cell density for mesh independence study

### 7.3.3 Boundary conditions

ANSYS FLUENT v17 was used for all CFD analyses, with simulation parameters adopted from (Goubergrits et al., 2015), who have achieved good agreement between CFD results and catheterisation data in a cohort of 13 CoA patients. Since only the influence of aortic arch shape was of interest here, all 6 models were fitted with the same

boundary conditions. Further, in order to keep computational efforts low, only peak-systolic flow conditions were modelled with a mean peak-systolic inflow rate of 400ml/s prescribed at the inlet ((Goubergrits et al., 2015) measured  $389\pm 110.6$ ml/s in their cohort via CMR assessment), perpendicular to the inlet surface, using a flat velocity profile. 50% of the inflow was assumed to flow through the descending aorta to the outlet ((Goubergrits et al., 2015) measured  $50.3\pm 12.1\%$ ) and the other 50% towards the HNV. Since specific flow conditions in the HNV were not known, the fractions of flow through BCC, LCC and LSC were derived from the ratio of their respective vessel cross-sectional areas (Haggerty et al., 2014). Flow fractions were assigned to outlet, BCC, LCC and LSC via the *outflow* boundary condition in FLUENT. Vessel walls were assumed to be rigid, fulfilling the zero velocity no-slip condition.

Blood was modelled as a Newtonian, incompressible fluid with constant density of  $\rho=1050\text{kg/m}^3$  and viscosity of  $\eta=3.6\text{mPa s}$ . To account for non-laminar effects, a k- $\omega$  SST transition turbulence model (Goubergrits et al., 2015), (Goubergrits et al., 2014) was used. Simulations were run with second order precision until convergence was achieved (residuals  $<10\text{e-}04$ ).

Mean velocity  $\bar{v}$ , static pressure  $p_{static}$ , total pressure  $p_{total}$  and flow rate  $\dot{V}$  were extracted using surface monitors in ANSYS CFD-Post at the *inlet* and *outlet*. In order to derive which arch shape is likely to pose higher flow resistance (i.e. higher  $\Delta p$ ) to the ventricle and causes higher energy dissipation (i.e. higher  $PL$ ) in the arch at peak systole, the obtained output parameters were used to derive pressure drop  $\Delta p$  across the arch as

$$\Delta p = p_{static,inlet} - p_{static,outlet} \quad (7.4)$$

and power loss  $PL$  induced by friction defined as (Liu et al., 2004)

$$PL = p_{total,inlet} \cdot \dot{V}_{outlet} - p_{total,outlet} \cdot \dot{V}_{outlet}; p_{total} \cong p_{static} + \frac{1}{2} \rho \bar{v}^2 \quad (7.5)$$

Differences  $\Delta x$  between “high” and “low” models of the respective parameter  $x$  were computed as

$$\Delta x = \frac{x_{low} - x_{high}}{x_{high}} \cdot 100\% \quad (7.6)$$

## 7.4 Results

Velocity-encoded streamlines are shown for all 6 models in Fig. 7.4. High velocities in the order of 1.6m/s were obtained in the transverse arch section of the low LVEF and high iLVM model. The highest velocities, in the order of 1.9m/s were concentrated in the angulated section of the transverse arch in the high BP model.

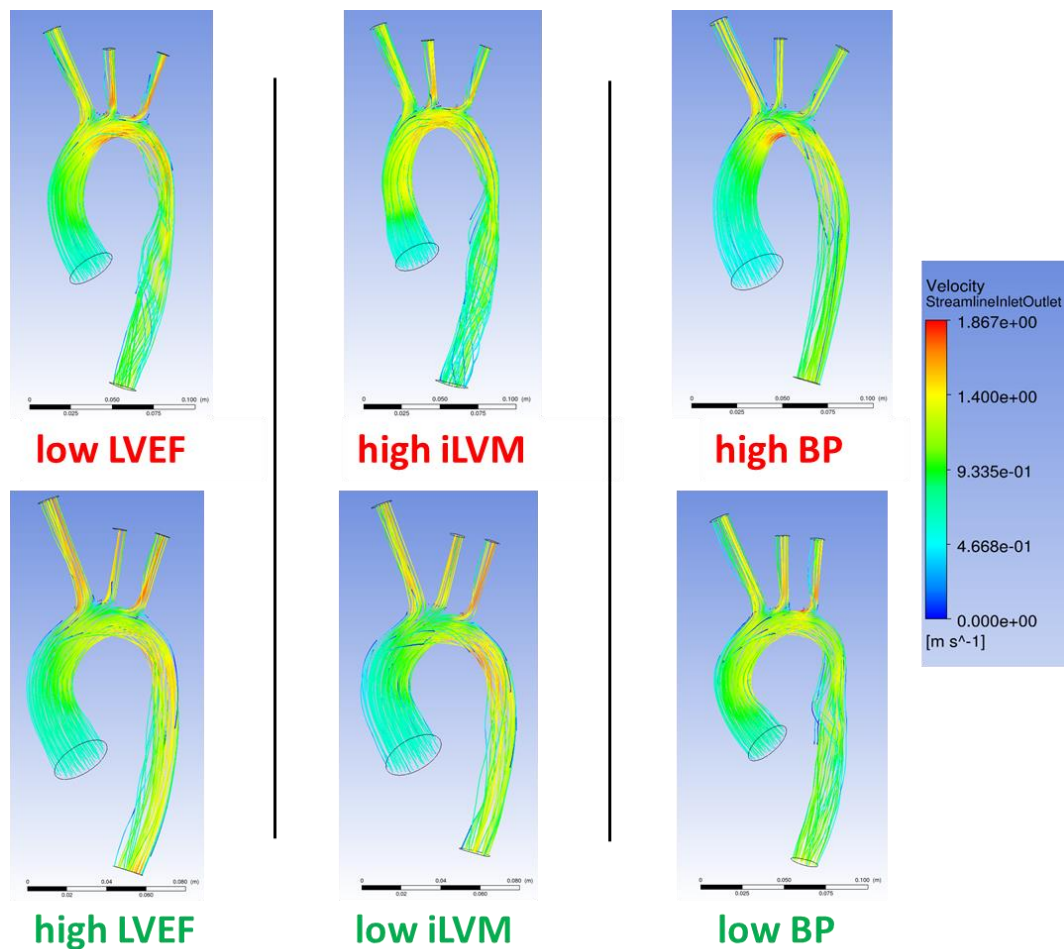


Fig. 7.4: Velocity encoded streamlines computed for the high/low arch shape cases derived by PLS in the previous chapter

Pressure drops  $\Delta p$  across the arch ranged from 8.55mmHg for the high LVEF model to 10.41mmHg for the high BP model and were thus all below the critical value of 20mmHg that would suggest a clinically significant obstruction. Differences in terms of  $\Delta p$  were all in accordance with expectations; the PLS computed functionally “better” arch shapes for high LVEF, low iLVM and low BP showed reduced pressure drops of 14.5%, 13.1% and 27.5%, respectively, compared to their functionally “worse” counterpart, Tab. 7.1.

In terms of  $PL$ , differences were even more pronounced with 16.8% reduced  $PL$  for the high LVEF model, 23.3% reduction for the low iLVM compared to the high iLVM model and 23.1% lower  $PL$  for the low BP compared to the high BP model. All  $\Delta p$  and  $PL$  values are shown in Tab. 7.1.

Tab. 7.1: Differences between computed hemodynamic parameters for respective PLS shape mode arch shapes associated with high or low functional parameters. Functional parameters associated with unfavourable cardiac function is highlighted in red; more favourable function in green.

PLS shape mode arch model	$\Delta p$ [mmHg]	$\Delta p$ % difference	$PL$ [mW]	$\Delta PL$ % difference
LVEF low	9.99	14.5%	418.8	16.8%
LVEF high	8.55		348.4	
iLVM high	9.03	13.1%	418.2	23.3%
iLVM low	7.85		320.9	
BP high	10.41	27.1%	405.1	23.1%
BP low	7.59		311.4	

## 7.5 Discussion

This study attempted to provide a mechanistic basis for the observational results obtained via SSM in the previous Chapter 6. To the best of my knowledge, for the first time, CFD simulations have been carried out using computed shape modes (from PLS regression) as input models, rather than patient-specific or simplified anatomical models.

The PLS shape modes were initially used to visualise 3D shape features most associated with functional response parameters. The computed surface meshes for high (+2SD) and low (-2SD) values of the response parameters LVEF, iLVM and BP (Chapter 3.8) were here re-used and volume-meshed for CFD analysis, all with the same boundary

conditions in order to investigate the influence of 3D arch shape alone on hemodynamic performance parameters.

Computed velocity fields and peak velocities were in similar order of magnitude as derived in previous simulations of CoA (Kim et al., 2009), (Olivieri et al., 2011), (LaDisa et al., 2011a). Highest velocities were found in the region of angulation of the PLS shape mode associated with high BP.

Furthermore, computed pressure drops across the arch  $\Delta p$  were in a physiological range of 9-10mmHg, in agreement with previous simulations (LaDisa et al., 2011a) and below the critical threshold of 20mmHg (Nielsen et al., 2005). This was expected, as only arches without clinically significant obstruction were included in the initial study, Chapter 6.

Interestingly, unfavourable arch shapes derived from the phenomenological SSM results for low LVEF, high iLVM and high BP all showed higher pressure drops and higher power losses than their respective “low” counterpart. Differences between “high” and “low” models were between 13% and 27%, which is considerably large given that some of the PLS shape modes (such as the high BP mode) did not show an obviously unfavourable arch shape (i.e. much longer, slimmer and/or much more curved arch, see Chapter 7.2) compared to its “better” counterpart.

The largest  $\Delta p$  was found in the high BP shape and the largest  $PL$  in the low LVEF arch shape, highlighting that a Gothic arch shape and shape features such as a slim, long ascending aorta with short transverse section and slightly dilated descending aorta as identified in Chapter 6.4.4 may indeed be functionally inferior, i.e. pose higher flow resistance to the pumping ventricle and result in higher energy losses. Previous results on a simplified Gothic arch geometry support these findings (Szopos et al., 2014).

The observational results derived in Chapter 6.4 may therefore have a functional, mechanistic basis – certain aortic arch shapes may lead to higher local flow resistance/energy loss and thus may be associated with increased iLVM, potentially diminished LVEF and higher BP. In fact, increased iLVM (i.e. left ventricular hypertrophy, LVH) has been linked to chronic pressure overload (Katz, 1990),

(Gardin and Lauer, 2004), (Rosenthal, 2005) and LVEF may also be affected by increased afterload (Gunther and Grossman, 1979), (Lorell and Carabello, 2000). Clear association between high BP (i.e. hypertension, HT) and arch obstruction has not been demonstrated, however hypotheses exist claiming that higher BP may be required to maintain flow through an obstructed arch (Maceira and Mohiaddin, 2012), leading to HT.

Whilst it is beyond the scope of this study to fully explain all potential cross-relationships between LVEF, iLVM, BP, energy loss and aortic arch shape, it has been shown here that there may be a mechanistic basis for the observational results discussed in Chapter 6. For the first time, SSM results and CFD results have been combined in an integrative manner, demonstrating that there is a sensible relationship between them.

### 7.5.1 Limitations and future work

There are several limitations to be considered. First, only peak-systolic (intransient) flow conditions were modelled, without including any blood flow pulsatility. However, the approach taken here has been shown to yield physiologic values for pressure drops across the arch and has previously shown good agreement with catheterisation measurements (Goubergrits et al., 2015). Similarly, simplified *outflow* boundary conditions were assumed, merely based on estimated flow fractions. Thus, only local hemodynamics in the arch were modelled, without taking into account any downstream vascular resistances or compliances, for example. More elaborate lumped-parameter-based boundary conditions may better account for these effects (Vignon-Clementel et al., 2010a).

This leads to one of the key limitations of this study: the material, i.e. elastic properties of the aorta were not taken into account at all. The aorta was modelled as a rigid shape, without including local differences in vessel elasticity; all included aortic arch shapes were acquired at mid-diastolic rest (see Chapter 3.1) i.e. at a certain fixed deformation stage. However, the aorta serves not only as a conduit distributing blood to the systemic vasculature, but also as an elastic reservoir, transforming pulsatile flow generated by the LV into a steady blood flow (Bogaert et al., 2012). Previous studies have shown

reduced compliance and distensibility in CoA (Ou et al., 2008b), (Lombardi et al., 2013), (Voges et al., 2016), which may also alter hemodynamic performance.

Future work should address the lack of vessel wall properties and perform CFD analyses including more elaborate boundary conditions and/or fluid structure interaction (FSI) simulations. It is to be taken into consideration that in this study, computed, SSM-derived arch shape models were used where e.g. wall properties or vascular resistances/compliances cannot be easily estimated. For these properties to be modelled correctly, a patient-specific approach could be adopted. Then, the 53 patients could be modelled via CFD analyses using patient-specific boundary conditions, which would provide patient-specific pressure or power loss data to be included as external parameters in the SSM. In this way, direct associations between 3D shape features and functional parameters could be established, without taking the “detour” via PLS shape modes. However, this requires substantial computational effort. Modern 4D flow CMR techniques (Markl et al., 2014) may provide a more efficient way to obtain realistic velocity and pressure maps in a large cohort of patients.

## 7.6 Summary

The main outcomes of this chapter were:

- Computed PLS shape mode arch shapes associated with clinically relevant functional parameters were used for CFD analyses in order to compute pressure and velocity fields allowing the derivation of further functional parameters.
- PLS shape mode arch shapes associated with “better” cardiac function as expressed by high LVEF, low iLVM and low BP yielded lower pressure drops and lower energy losses compared to their “worse” counterpart arch shapes.
- CFD results on PLS shape modes provided a mechanistic basis for the previously obtained phenomenological associations between aortic arch shape and function in CoA.
- To the best of my knowledge, this is the first study to date performing CFD analysis on SSM-derived results to join mechanistic and phenomenological

modelling, thus following the call for integrative and complementary approaches to transform mere data into information and knowledge (Frangi et al., 2016), see Chapter 2.4.2.

This chapter provided a mechanistic basis for the phenomenological results found in the cohort of 53 patients post CoA repair in Chapter 6, thus underlining that the 3D shape biomarkers derived via the currents-based SSM could be verified via deterministic, complementary modelling techniques. The analysis of the 3D shape biomarkers post CoA repair is completed with this chapter. In the next chapter, the modelling pipeline is extended towards detection of yet-to-be discovered structures and clusters within the 3D shape data via hierarchical clustering, which may allow placing a single pathological patient shape into the context of a population of pathological shapes.

## 8 Detecting meaningful anatomical shape clusters: metrics analysis for hierarchical clustering of aortic arch shapes

*Part of the work described in this Chapter has been published in: J. L. Bruse, M. A. Zuluaga, A. Khushnood, K. McLeod, H. N. Ntsinjana, T.-Y. Hsia, M. Sermesant, X. Pennec, A. M. Taylor, and S. Schievano. Detecting Clinically Meaningful Shape Clusters in Medical Image Data: Metrics Analysis for Hierarchical Clustering Applied to Healthy and Pathological Aortic Arches, IEEE Transactions on Biomedical Engineering, e-pub ahead of print, Feb. 2017. (Bruse et al., 2017c). Copyright (2017) with permission of IEEE.*

In the preceding chapters, methods to extract 3D shape biomarkers from medical image data combining the currents-based SSM approach with partial least squares (PLS) regression techniques have been developed, and have been applied to cohorts of patients post CoA repair. As seen in Chapter 7, this method has provided relevant clinical insight into the relationship between aortic shape and functional parameters. However, PLS being a supervised technique, certain external parameters need to be known prior to being able to extract shape biomarkers and outliers need to be accounted for. Shape biomarker results are visually provided in the form of computed shapes or numerically in the form of shape vectors, which may not be easily comprehensible. In this chapter, post-processing methods are extended towards hierarchical clustering, a data mining technique, which provides the possibility to detect previously unknown structures within a bulk data set, without any prior information. Hierarchical clustering provides results in the form of an intuitively understandable clustering tree, the dendrogram, showing which anatomical shapes form distinct clusters within the input dataset. Despite its potential, it remains unclear which parameter setting should be used to obtain meaningful clustering of the input data. This chapter constitutes a technical evaluation, assessing if and how meaningful clusters can be obtained by post-processing the deformation vector data generated by the currents-based SSM framework.

## 8.1 Abstract

*Background: Today's growing medical image databases call for novel processing tools to structure the bulk of data and extract clinically relevant information. Unsupervised hierarchical clustering may reveal clusters within anatomical shape data of patient populations as required for modern Precision Medicine strategies. Few studies have applied hierarchical clustering techniques to three-dimensional patient shape data and results depend heavily on the chosen clustering distance metrics and linkage functions. In this chapter, I therefore assessed clustering classification performance of various distance/linkage combinations and of different types of input data in a dataset where meaningful anatomical shape clusters are known a priori.*

*Methods: The currents-based SSM processing pipeline was extended by including automatic segmentation in the pre-processing and agglomerative hierarchical clustering in the post-processing step. The aim was to automatically subdivide a set of 60 aortic arch shapes derived from CMR data into three previously known groups, as defined by primary clinical diagnosis. After applying unsupervised clustering to the bulk of deformation vector data comprising all three (known) groups, results were evaluated via classification metrics against primary clinical diagnosis, traditional morphometrics and PCA results.*

*Results: The SSM pipeline achieved automatic division of input shape data according to primary clinical diagnosis with high F-score ( $0.902 \pm 0.042$ ) and Matthews Correlation Coefficient ( $0.851 \pm 0.064$ ) using the Correlation/Weighted distance/linkage combination. Meaningful subgroups within the three patient groups were obtained and benchmark scores for automatic segmentation and classification performance were reported.*

*Conclusion: Hierarchical clustering results varied depending on the distance/linkage combination used to structure the data. Yet, clinically relevant shape clusters and subgroups could be found with high specificity and low misclassification rates. Detecting novel, disease-specific clusters within medical image data may improve image-based risk assessment, treatment planning and medical device development in complex disease.*

## 8.2 Introduction

Currently, medical image databases are growing and valuable patient data are accumulating, calling for novel approaches to process and extract clinically relevant information not only on a case-by-case basis, but also considering entire patient populations (Völzke et al., 2012), (Medrano-Gracia et al., 2015), (Frangi et al., 2016).

Many computational image processing pathways focus on segmentation of body structures (Petitjean et al., 2015), (Cerroloza et al., 2015) or apply classification algorithms to automatically distinguish between healthy and disease (Zhao et al., 2009), (Zuluaga et al., 2015), (Kutra et al., 2012). Yet, to date few studies have looked at tools that can be applied *after* those two crucial steps; computational tools that can help understand a disease once anatomical shape information is given and once a diagnosis has been made.

Automated clustering techniques from the field of data mining have been widely used in genomics, taxonomy and chemoinformatics to structure large amounts of data into subgroups, thereby revealing previously unknown, yet relevant patterns within a given population (Eisen et al., 1998), (Murtagh and Contreras, 2012). Such an approach may prove beneficial as well for the analysis of complex three-dimensional (3D) anatomical models from medical image data in order to close the gap between mere data and useful knowledge, as desired in current Precision Medicine or “Precision Imaging” approaches (Frangi et al., 2016), Fig. 2.1.

Clinical image assessment of inner body structures usually reveals a patient’s dominant pathology, but it often remains unclear how individual image data relate to other patients with the same disease or primary diagnosis. Grouping patients according to anatomical similarity and taking into account clinical history and other functional or outcome parameters may ultimately allow refined, cluster-adapted treatment and follow-up strategies and could assist in risk-stratification when scanning a new patient with similar diagnosis.

Hierarchical clustering techniques seem to be an attractive way to discover anatomical subgroups from medical image data as they are inherently unsupervised, thus do not require any prior information about the study population and, unlike K-means clustering, do not require specifying an expected number of subgroups (Jain, 2010), (Hastie et al., 2009), (Halkidi et al., 2001). Furthermore, clustering results can be graphically summarised in a dendrogram that depicts in a tree-like diagram how similar subjects are grouped together, while dissimilar subjects are placed on different branches of the tree.

However, evaluation of subject similarity or dissimilarity and clustering results heavily depends on the choice of both similarity or *distance metric* (with low inter-subject distance relating to higher similarity) and *linkage function* determining how subjects are linked together to form a subgroup (Hastie et al., 2009), (Halkidi et al., 2001). Depending on the chosen distance/linkage combination, clustering results may vary substantially – potentially rendering meaningless results (Brun et al., 2007), (Dalton et al., 2009).

While previous studies have analysed clustering techniques based on generic shapes or two-dimensional (2D) shape data (Srivastava et al., 2005), few have assessed hierarchical clustering performance using actual patient data in a realistic setting, i.e. using three-dimensional (3D) anatomical models of healthy and pathological shapes derived from medical images (Dong et al., 2016), (Broggio et al., 2013). In general, medical image hierarchical clustering performance data including validation against known and clinically relevant clusters are sparse.

In this chapter, I aimed to investigate whether and how hierarchical clustering can be used to automatically divide a bulk of unlabelled clinically acquired cardiovascular magnetic resonance (CMR) image data into clusters and subgroups that could be of clinical relevance.

Specifically, I analysed here clustering classification performance of various distance/linkage combinations applied to a population of 60 aortic arch anatomical models, automatically segmented from CMR data, composed of three equally-sized subgroups of healthy aortic arches, arches post CoA repair (COA) (Ou et al., 2004) and

arches post arterial switch operation (ASO) (Lecompte et al., 1981). Both COA and ASO patients suffer from congenital heart disease (CHD), which manifests itself in abnormalities of the aorta, known to present shape patterns abnormal from healthy individuals (Ou et al., 2004), (Ntsinjana et al., 2014). COA and ASO image data provide an excellent platform to test unsupervised clustering algorithms, as newly found shape clusters or subgroups within those diseases may ultimately impact on novel diagnosis and treatment strategies.

To assure “meaningfulness” (here, clinical relevance) of unsupervised clustering results, I *externally validated* (Dalton et al., 2009), (Brun et al., 2007) results against clinical primary diagnosis, traditional morphometric parameters and PCA results. I aimed to find the distance metric/linkage function combination that achieved the highest classification performance, i.e. that was able to automatically divide the bulk CMR input data into the three clinically meaningful clusters of CTRL, COA and ASO arch shapes with low misclassification rates.

Furthermore, I hypothesised that such clinically meaningful clustering on a macrolevel yields meaningful shape subgroups (i.e. “clusters within clusters”) on lower-level hierarchies of the clustering tree as well, which may allow the detection of novel disease patterns in future studies. The key question behind this study was:

→ How could the currents-based SSM framework be used to detect previously unknown 3D anatomical shape clusters and subgroups from CMR image data?

### 8.3 Methods

Generally, pre-processing steps and SSM processing of the CMR data were performed according to the guidelines detailed in Chapter 4. The study outline is as follows: All aortic arch shape models were automatically segmented from CMR data and were parameterised within one common mathematical framework using the currents-based SSM. Based on this 3D shape data, principal component analysis (PCA, see Chapter 3.7.1) was applied for more detailed assessment of 3D shape features prior to cluster analysis. Hierarchical clustering was then performed on both the full, unprocessed shape data

and the reduced PCA dataset to determine the input and the distance/linkage combination yielding clustering closest to the clinical expert diagnosis with high classification performance. Lastly, the distance/linkage setting yielding the most meaningful division of the data (with highest *F-score* and *Matthews Correlation Coefficient*) was analysed in more detail.

### 8.3.1 Patient population

A total of 60 patients, who underwent routine CMR examination at GOSH were retrospectively included in the study. The cohort was divided into three subgroups according to their clinical primary diagnosis: 20 healthy subjects whose aortic arch shapes were reported as normal at cardiac assessment (control group CTRL, age  $15.2 \pm 2.03$  years, 3 female, already included in Chapter 5), 20 patients who had undergone surgical aortic arch reconstruction for treatment of CoA (COA,  $23.1 \pm 7.35$  years, 4 female, included in previous chapters) and 20 patients who had their aorta pushed back posteriorly in the Lecompte (Lecompte et al., 1981) manoeuvre for arterial switch operation (ASO,  $14.4 \pm 2.48$  years, 4 female, (Ntsinjana et al., 2013b)), Fig. 8.1.

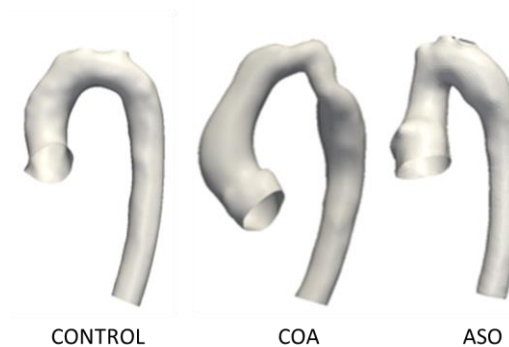


Fig. 8.1: Representative arch shape models from each of the included cohorts

### 8.3.2 Segmentation and registration

The aorta including the left ventricle (LV) was segmented automatically using the multi-atlas propagation segmentation approach, see Chapter 3.2.3 (Zuluaga et al., 2013), (Petitjean et al., 2015). For each group, a *leave-one-out* strategy was followed, where 19 manually labelled atlases of the respective group were used to segment one unseen subject, and dice similarity coefficients (DSC) were computed to

quantify automatic segmentation accuracy following  $DSC=2AB/(A+B)$ , where  $A$  is the obtained segmentation and  $B$  the corresponding ground truth. Automatic segmentation results were visually inspected and, if necessary, manually edited (i.e. cleaned up and improved) using ITKSnap.

Segmentation labels were exported as 3D computational surface meshes in the Visualization Toolkit (VTK) format (Schroeder et al., 2006) and visualised in ParaView. All models were cut consistently below the aortic root and at the level of the diaphragm using VMTK cutting tools, whilst coronary arteries and head and neck vessels were cut off as close as possible to the arch, see Chapter 4.3.2. All surface meshes were then rigidly registered to one healthy CTRL subject using the Iterative Closest Point (ICP) algorithm (Besl and McKay, 1992) prior to template computation. In order to remove bias due to misalignment of input shapes, a *Generalised Procrustes Analysis* (GPA) was adopted by computing an initial template, realigning the input shapes to the new template via ICP registration and recomputing the template until convergence, see Chapter 4.3.2.

### 8.3.3 Template and deformation matrix computation

The 60 aligned arch surface meshes constituted the input for the template computation using *Deformetrica* (Durrleman et al., 2014). Template and resulting template-dependent shape parameterisations were computed following protocols detailed in Chapters 4 and 6. Setting  $\lambda_w$  to 5mm and  $\lambda_v$  to 20mm resulted in a set of 300 deformation vectors  $\beta_i$  per patient. With each  $\beta_i$  having an  $x$ ,  $y$  and  $z$  entry, a final *deformation matrix*  $D_{Full} = \{\hat{\beta}\}_{deformation,full}$  from Eq. 3.9 of size  $N \times n$  with  $N=60$  included subjects and  $n=900$  deformation momenta comprised all 3D shape information of the input population and was used for further analysis via PCA and hierarchical clustering.

### 8.3.4 Morphometric analysis and PCA

To investigate whether arch shape characteristics related to *size* and *shape* were sufficiently different between the three groups (i.e. whether the three patient groups

translate into three actual *shape* groups), traditional morphometric analysis was carried out in 2D and in 3D, without controlling for size difference in this case, as size itself could be captured in the clustering as a descriptor of pathological paediatric patient arch shape as well.

In terms of size, aortic arch model volume  $V$ , surface to volume ratio  $S_{Vol} = A_{surf}/V$  and arch centreline length  $L_{CL}$  were derived automatically using VMTK and MATLAB. As shape parameters, I considered arch centreline tortuosity  $TO_{CL}$  (Piccinelli et al., 2009), ascending to descending aortic arch diameter ratio  $D_{asc,desc}$  and arch width  $T$ , manually measured as described in Chapter 6, (Ou et al., 2004).

Further, PCA was performed on the covariance matrix of the combined deformation vectors  $\{\hat{\beta}\}_{deformation}$  to extract the PCA shape modes, see 3.7.1. Each subject deformation  $\phi_i$  was projected onto each PCA shape mode to obtain the low-dimensional shape vector  $f_{i,PCA}^m$ ,  $m \in [1, K]$  (Mansi et al., 2011) for each shape mode  $m$  and subject  $i$ , whose entries parameterise the subject-specific PCA loadings. The  $f_{i,PCA}^m$  were compared between the three groups CTRL, COA and ASO, and the  $f_{i,PCA}^m$  of the first two PCA shape modes were plotted against each other to visualise potential grouping within the input shape data. The first  $m=19$  shape modes, explaining 90% of the total shape variability (determined by the proportion of sorted eigenvalues) were selected (Jolliffe, I.T., 2002) and the respective  $f_{i,PCA}^m$  combined constituted the reduced PCA shape loading matrix  $D_{PCA} = \{f_{i,PCA}^m\}$  of size  $N \times m$ , which described 3D population shape features in terms of the lower-dimensional PCA loadings.

### 8.3.5 Hierarchical clustering

The shape matrices  $D_{Full}$  and  $D_{PCA}$  constituted the input for the agglomerative hierarchical clustering algorithm (MATLAB). Based on a pre-defined distance (i.e. similarity) metric, clusters are formed by grouping subjects with similar features together, while subjects with distinctly different features are placed in other clusters. This unsupervised approach unveils “naturally occurring” subgroups within the data, without depending on prior user input (Hastie et al., 2009), (Srivastava et al., 2005).

Here, features of interest were 3D aortic arch shape features, parameterised by the entries of  $D_{Full}$  and  $D_{PCA}$ . The algorithm can be described as follows (Murtagh, 1983), (The Mathworks, Inc., 2016):

1. Compute distances between every pair of subjects within the input dataset to obtain a metric of pairwise subject similarity (treating each subject as its own cluster).
2. Form binary cluster from two closest (most similar) subjects (using distance metric) or clusters (using linkage function).
3. Re-compute distances between newly formed cluster and remaining subjects or clusters.
4. Return to Step 2 until all subjects are included in one large cluster, formed by a tree-like multi-level network of subclusters (dendrogram). At the lowest level, each subject forms its own cluster.
5. Cut off dendrogram branches at a specified level of the hierarchy to assign subjects below each cut to a specific cluster, generating partitions of the data.

To compute pairwise distances between the 60 patient shapes parameterised by deformation row vectors of  $D_{Full}$  or PCA shape vectors of  $D_{PCA}$ , the following commonly used distance (similarity) metrics  $dist$  between the vector pair  $x_s$  and  $x_t$  were computed (with  $D$  being of size  $N \times n$ , with  $N$  (1-by- $n$ ) row vectors  $x_i, i \in [1, N]$ ; for  $D_{Full}$  with  $n \in [1, \dots, 900]$  and for  $D_{PCA}$  with  $n \in [1, \dots, 19]$ ) (The Mathworks, Inc., 2016):

$$dist_{Euclidean} = \sqrt{\sum_{j=1}^n |x_{sj} - x_{tj}|^2} \hat{=} \|x_{sj} - x_{tj}\|_2 \quad (8.1)$$

$$dist_{StandardisedEuclidean} = \sqrt{\sum_{j=1}^n \frac{|x_{sj} - x_{tj}|^2}{s_j^2}} \quad (8.2)$$

with  $s_j$  being the standard deviation of the  $x_s$  and  $x_t$  over the sample set.

$$dist_{Cityblock} = \sum_{j=1}^n |x_{sj} - x_{tj}| \hat{=} \|x_{sj} - x_{tj}\|_1 \quad (8.3)$$

$$dist_{Chebychev} = \max_j \{ |x_{sj} - x_{tj}| \} \hat{=} \|x_{sj} - x_{tj}\|_{\infty} \quad (8.4)$$

$$dist_{Cosine} = 1 - \frac{x_s x_t'}{\sqrt{(x_s x_s')(x_t x_t')}} \hat{=} 1 - \frac{x_s \cdot x_t}{\|x_s\| \|x_t\|} \quad (8.5)$$

$$dist_{Correlation} = 1 - \frac{(x_s - \bar{x}_s)(x_t - \bar{x}_t)'}{\sqrt{(x_s - \bar{x}_s)(x_s - \bar{x}_s)'} \sqrt{(x_t - \bar{x}_t)(x_t - \bar{x}_t)'}}$$

$$\text{with } \bar{x}_s = \frac{1}{n} \sum_{j=1}^n x_{sj} \text{ and } \bar{x}_t = \frac{1}{n} \sum_{j=1}^n x_{tj} \quad (8.6)$$

$$dist_{Spearman} = 1 - \frac{(r_s - \bar{r}_s)(r_t - \bar{r}_t)'}{\sqrt{(r_s - \bar{r}_s)(r_s - \bar{r}_s)'} \sqrt{(r_t - \bar{r}_t)(r_t - \bar{r}_t)'}}$$

$$\text{where } \bar{r}_s = \frac{1}{n} \sum_j r_{sj} = \frac{(n+1)}{2} \text{ and } \bar{r}_t = \frac{1}{n} \sum_j r_{tj} = \frac{(n+1)}{2};$$

$$r_s \text{ and } r_t \text{ are the coordinate-wise rank vectors of } x_s \text{ and } x_t. \quad (8.7)$$

After defining a distance metric between *pairs of subject shapes*, a linkage function then uses the generated distance data to join *groups of subjects* together into binary clusters and link those to higher level larger clusters, until all subjects are linked together. The linkage function thus defines the similarity or distance between two groups of subjects and is used to generate the dendrogram. The order in which subjects are clustered together is determined by the type of linkage method.

For each distance metric, the following commonly used linkage methods were applied to generate a dendrogram. For subjects or clusters  $s$  and  $t$  joined into cluster  $s \cup t$ , the new distance between this cluster and another subject or cluster  $k$  is generally defined by the Lance-Williams dissimilarity update formula  $link(s \cup t, k)$  (Eq. 8.8), which defines different types of linkage methods, depending on the choice of the parameters  $\alpha_s$ ,  $\alpha_t$ ,  $\beta$  and  $\gamma$  as follows (Murtagh and Contreras, 2012):

$$\begin{aligned} link(s \cup t, k) &= \alpha_s dist(s, k) + \alpha_t dist(t, k) \\ &+ \beta dist(s, t) + \gamma |dist(s, k) - dist(t, k)| \end{aligned} \quad (8.8)$$

$$\begin{aligned} \text{link}(s \cup t, k)_{\text{Average}} : \alpha_s &= \frac{n_s}{n_s + n_t}, \alpha_t = \frac{n_t}{n_t + n_s}, \\ \beta &= 0, \gamma = 0 \end{aligned} \quad (8.9)$$

$$\begin{aligned} \text{link}(s \cup t, k)_{\text{Centroid}} : \alpha_s &= \frac{n_s}{n_s + n_t}, \alpha_t = \frac{n_t}{n_t + n_s}, \\ \beta &= -\frac{n_s n_t}{(n_s + n_t)^2}, \gamma = 0 \end{aligned} \quad (8.10)$$

$$\text{link}(s \cup t, k)_{\text{Complete}} : \alpha_s = \frac{1}{2}, \alpha_t = \frac{1}{2}, \beta = 0, \gamma = \frac{1}{2} \quad (8.11)$$

$$\text{link}(s \cup t, k)_{\text{Median}} : \alpha_s = \frac{1}{2}, \alpha_t = \frac{1}{2}, \beta = -\frac{1}{4}, \gamma = 0 \quad (8.12)$$

$$\text{link}(s \cup t, k)_{\text{Single}} : \alpha_s = \frac{1}{2}, \alpha_t = \frac{1}{2}, \beta = 0, \gamma = -\frac{1}{2} \quad (8.13)$$

$$\begin{aligned} \text{link}(s \cup t, k)_{\text{Ward}} : \alpha_s &= \frac{n_s + n_k}{n_s + n_t + n_k}, \alpha_t = \frac{n_t + n_k}{n_s + n_t + n_k}, \\ \beta &= -\frac{n_k}{n_s + n_t + n_k}, \gamma = 0 \end{aligned} \quad (8.14)$$

$$\text{link}(s \cup t, k)_{\text{Weighted}} : \alpha_s = \frac{1}{2}, \alpha_t = \frac{1}{2}, \beta = 0, \gamma = 0 \quad (8.15)$$

Note that *dist* can be any of the distance metrics defined in Eqs. (8.1-8.7);  $n_s, n_k, n_t$  is the number of subjects in cluster  $s, k, t$ , respectively. *Centroid, Median* and *Ward* linkage methods are appropriate for *Euclidean* distances only (The Mathworks, Inc., 2016). Cutting the dendrogram horizontally at a particular height or level partitions the data into shape subgroups (Hastie et al., 2009). Since I aimed to assess whether the clustering algorithm was able to distinguish between CTRL, COA and ASO groups, dendrograms were cut automatically at a level that yielded three large shape clusters.

### 8.3.6 Clustering classification performance measures

Based on the majority of group members associated with one cluster, each cluster was automatically labelled either CTRL ( $Class_1$ ), COA ( $Class_2$ ) or ASO ( $Class_3$ ) and numbers of

assigned subjects from each of the three classes were recorded in a *confusion matrix* to assess clustering classification performance. All correctly assigned subjects for each class are shown on the diagonal of the matrix. For each of the three classes  $Class_j, j \in [1,3]$ , the total number of *true positives* ( $TP_j$ , e.g. in case of the CTRL class, the actual CTRLs that were correctly classified as CTRL), *false positives* ( $FP_j$ , e.g. COA and/or ASO that were incorrectly classified as CTRL), *false negatives* ( $FN_j$ , e.g. CTRLs that were incorrectly classified as COA and/or ASO) and *true negatives* ( $TN_j$ , e.g. all remaining subjects, correctly classified as non-CTRL) were derived from the confusion matrices.

With these values, overall classification performance was computed using macroaveraging (denoted with subscript  $M$ ) (Sokolova and Lapalme, 2009) over  $L=3$  classes of the following performance measures:

$$Recall_M = \frac{\sum_{j=1}^L \frac{TP_j}{TP_j + FN_j}}{L} \quad (8.16)$$

$$Specificity_M = \frac{\sum_{j=1}^L \frac{TN_j}{FP_j + TN_j}}{L} \quad (8.17)$$

$$Precision_M = \frac{\sum_{j=1}^L \frac{TP_j}{TP_j + FP_j}}{L} \quad (8.18)$$

$$Accuracy_M = \frac{\sum_{j=1}^L \frac{TP_j + TN_j}{TP_j + FN_j + FP_j + TN_j}}{L} \quad (8.19)$$

To minimise chance findings and bias associated with those traditional measures, I also computed (macroaveraged) *Informedness*, which relates to the probability that there has been an informed classification as opposed to mere guessing, and *Markedness*, defined as (Powers D.M.W., 2011):

$$Informedness_M = \frac{\sum_{j=1}^L \frac{TP_j}{TP_j + FN_j} + \frac{TN_j}{FP_j + TN_j} - 1}{L} \quad (8.20)$$

$$Markedness_M = \frac{\sum_{j=1}^L \frac{TP_j}{TP_j + FP_j} + \frac{TN_j}{TN_j + FN_j} - 1}{L} \quad (8.21)$$

To provide a summary of the above measures, the macroaveraged  $F$ -score<sub>M</sub> (weighted harmonic mean of *Recall* and *Precision*) and *Matthew's Correlation Coefficient* ( $MCC_M$ ) (geometric mean of *Informedness* and *Markedness* (Baldi et al., 2000)) were computed as follows:

$$F - score_M = \frac{2Precision_M Recall_M}{Precision_M + Recall_M} \quad (8.22)$$

$$MCC_M = \frac{\sum_{j=1}^L \frac{TP_j TN_j - FP_j FN_j}{\sqrt{(TP_j + FP_j)(TP_j + FN_j)(TN_j + FP_j)(TN_j + FN_j)}}}{L} \quad (8.23)$$

$F$ -score<sub>M</sub> and  $MCC_M$  scores were used to evaluate overall classification performance of the various distance metric and linkage combinations. Note that  $F$ -score values range from 0 for worst to 1 for best classification performance, whereas  $MCC$  ranges from -1 for total disagreement over 0 for random guessing to +1 for perfect prediction of classes (Baldi et al., 2000). In the following, the qualitative term “best” refers to highest possible classification performance in terms of both  $F$ -score<sub>M</sub> and  $MCC_M$  score being close to the value 1.

### 8.3.7 Validation of clustering results

Clustering results were evaluated using 10-fold cross validation (CV), leaving out  $N/10$  randomly selected subjects, and re-computing template,  $D_{Full}$  and  $D_{PCA}$ , until each subject had been left out once see Chapter 4.3.3.5. Classification performance measures were calculated for each of the 10 CV runs, looping through all 49 distance metric/linkage combinations for the two different input matrices  $D_{Full}$  and  $D_{PCA}$ , respectively. All clustering runs were carried out on a 32GB workstation using one

2.3GHz core. The distance/linkage combination with the best classification performance based on mean  $F\text{-score}_M$  and  $MCC_M$  was chosen for further analyses of the full data matrix, comprising all  $N=60$  subjects. Results of this final clustering were visualised as a dendrogram and compared to PCA results.

### 8.3.8 Statistical analysis

For all analysed size, shape and PCA shape vector entries, mean and 95% confidence intervals (95CIs) based on the patient cohorts are reported. For classification performance measures, mean and 95CIs are reported based on the CV runs.

To compare distributional differences between the three patient groups CTRL, COA and ASO, independent analysis of variance (ANOVA) was performed. Prior to ANOVA, homogeneity of variance was assessed using Levene's test. In case homogeneity of variance was violated, Welch's test was performed. When ANOVA showed significance, post hoc tests were carried out for pairwise group comparisons and Bonferroni adjusted to control for Type I error rates. Statistical significance was assumed at level  $p < .05$ . All statistical tests were carried out using R v3.3.1 (R Foundation for Statistical Computing, Vienna, Austria).

## 8.4 Results

### 8.4.1 Segmentation

Average segmentation runtime was approximately two hours per patient (parallel processing on a 24 core, 2.3GHz, 32GB RAM workstation). Average DSC ( $\pm 95\text{CI}$ ) for the automatically computed segmentation labels compared to their respective ground truths were  $0.917 \pm 0.026$  for the CTRL,  $0.944 \pm 0.012$  for the COA and  $0.913 \pm 0.033$  for the ASO group. Final automatic segmentation labels required a maximum of 10 minutes manual clean-up.

### 8.4.2 Comparison of traditional shape parameters

In terms of size, significant distributional differences in  $V$  (Fig. 8.2a) were found between the COA and CTRL group ( $p=2e-07$ ), and the COA and ASO group ( $p=7e-06$ ).

$S_{Vol}$  distributions (Fig. 8.2b) differed significantly between the COA and CTRL group ( $p=1e-06$ ), and the COA and ASO group ( $p=3e-03$ ). Distributional differences in  $L_{Cl}$  (Fig. 8.2c) were found between the COA and CTRL group ( $p=5e-05$ ) and the COA and ASO group ( $p=1e-06$ ). Overall, COA aortic arches were significantly larger and more compact, whereas arch models from the CTRL and ASO group were of similar size. Following this analysis, I would expect the clustering algorithm to confuse CTRL and ASO shapes, while separating out well the COA group, if it mainly took into account size differences between input shapes.

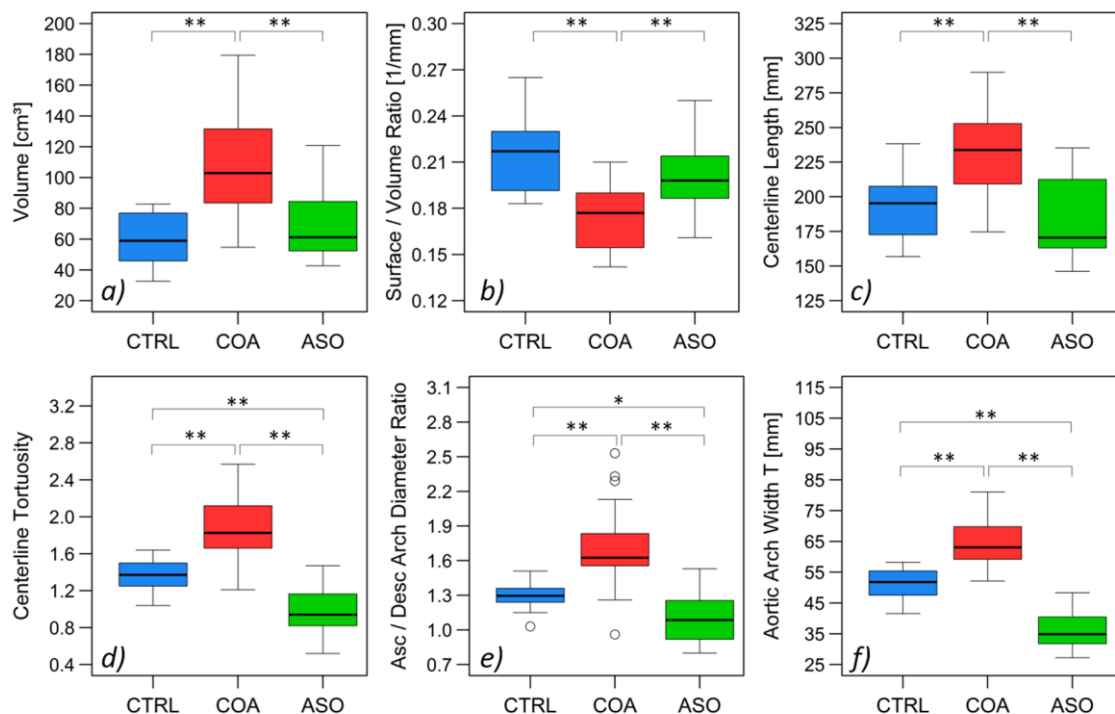


Fig. 8.2: Differences of aortic arch size (a-c) and shape (d-f) morphometric parameters between the three groups CTRL, COA and ASO, adapted from (Bruse et al., 2017c)

With regard to measured shape parameters, significant differences between all three groups were found for  $T_{O_{Cl}}$  following post hoc analyses ( $p=2e-07$  for COA vs CTRL,  $p=1e-14$  for COA vs ASO and  $p=1e-02$  for CTRL vs ASO, Fig. 8.2d). Similarly,  $D_{asc,desc}$  distributions ( $p=1e-05$  for COA vs CTRL,  $p=7e-10$  for COA vs ASO and  $p=4e-02$  for CTRL vs ASO, Fig. 8.2e) and  $T$  distributions differed significantly ( $p=6e-08$  for COA vs CTRL,  $p=2e-16$  for COA vs ASO and  $p=3e-09$  for CTRL vs ASO, Fig. 8.2e) between all three groups, with COA arches showing generally more tortuous and wider arch shapes with

higher ascending to descending aortic diameter ratios than the other two groups and ASO arches being the least wide, least tortuous with the lowest ascending to descending arch diameter ratios.

### 8.4.3 PCA of 3D shape features

The first three shape modes are visualised in Fig. 8.3a-c. PCA shape mode 1 accounted for 35.4% of shape variability. It described shape change from an overall small and short, ASO-like arch shape with narrow arch width towards a large, COA-like arch shape with high arch width, dilated root and ascending aorta, and more tortuous descending aorta continuation, Fig. 8.3a. In terms of  $f_{i,PCA}^{m=1}$  shape vector entry distributions, COA arches differed significantly from the CTRL group ( $p=4e-08$ ) and from the ASO group ( $p=3e-12$ ). CTRL and ASO shape vector entry distributions did not differ significantly ( $p=.050$ ).

PCA shape mode 2 described shape variability associated with more rounded and wide arches compared to more Gothic (Ou et al., 2004) arch shapes with similar arch height but smaller arch width. It accounted for 12.2% of the total shape variability, Fig. 8.3b. The  $f_{i,PCA}^{m=2}$  entry distribution for the ASO group differed significantly from the CTRL group ( $p=2e-08$ ) and from the COA group ( $p=1e-06$ ), while there was no significant difference between the CTRL and COA groups ( $p=.930$ ).

PCA shape mode 3 accounted for 7.4% of shape variability. It varied from arch shapes with lower arch height and slightly dilated root to arches with higher arch height but similar arch width and few diameter changes along the arch, Fig. 8.3c. For this mode, the  $f_{i,PCA}^{m=3}$  distribution of the CTRL group was significantly different from the COA group ( $p=2e-02$ ) and from the ASO group ( $p=3e-03$ ) but no significant difference was found between the COA and ASO group ( $p=.999$ ).

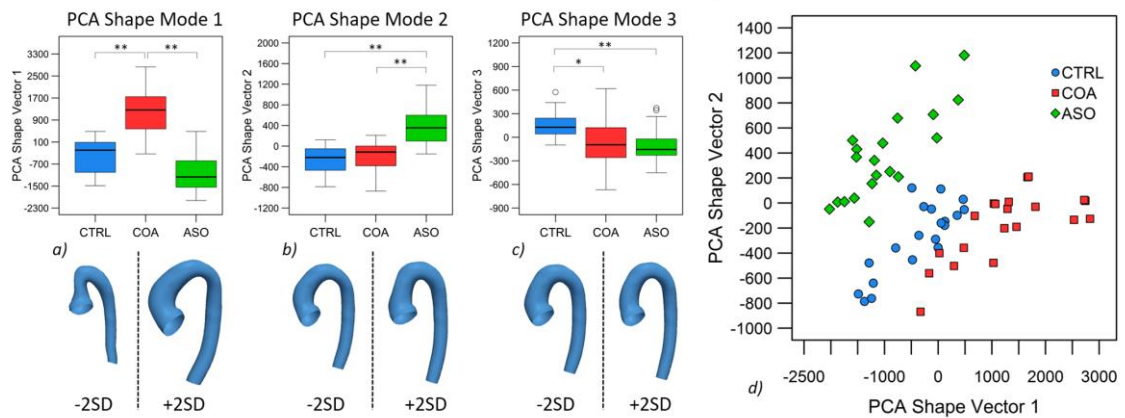


Fig. 8.3: PCA shape modes and shape vector differences between the three groups (a-c). Plotting the first two PCA modes against each other revealed clear grouping within the data according to primary diagnosis (d), adapted from (Bruse et al., 2017c)

Following the analysis of traditional shape parameters and the first three PCA shape modes, I concluded that all three selected patient groups were sufficiently different from each other, thus forming three distinct shape groups to be found by the clustering algorithm. Furthermore, plotting the  $f_{i,PCA}^{m=1}$  and  $f_{i,PCA}^{m=2}$  for PCA shape modes 1 and 2 against each other revealed a good split between the three groups in PCA 3D shape space (Fig. 8.3d), justifying the assumption of three large shape clusters within the cohort.

#### 8.4.4 Determining best performing input and distance/linkage combination

Macroaveraged classification performance measures  $F\text{-score}_M$  and  $MCC_M$  for various distance/linkage combinations and the input datasets  $D_{Full,CV}$  and  $D_{PCA,CV}$  are shown in Fig. 8.4. Note that only the linkage option which achieved highest  $F\text{-score}_M$  and  $MCC_M$  score is shown for each distance metric. Best performing linkages were the same for  $D_{Full,CV}$  and  $D_{PCA,CV}$ , except in the cases of *Cosine* and *Chebychev* distance metrics, where  $D_{PCA,CV}$  achieved higher scores using the *Average* linkage instead of *Weighted* linkage function.

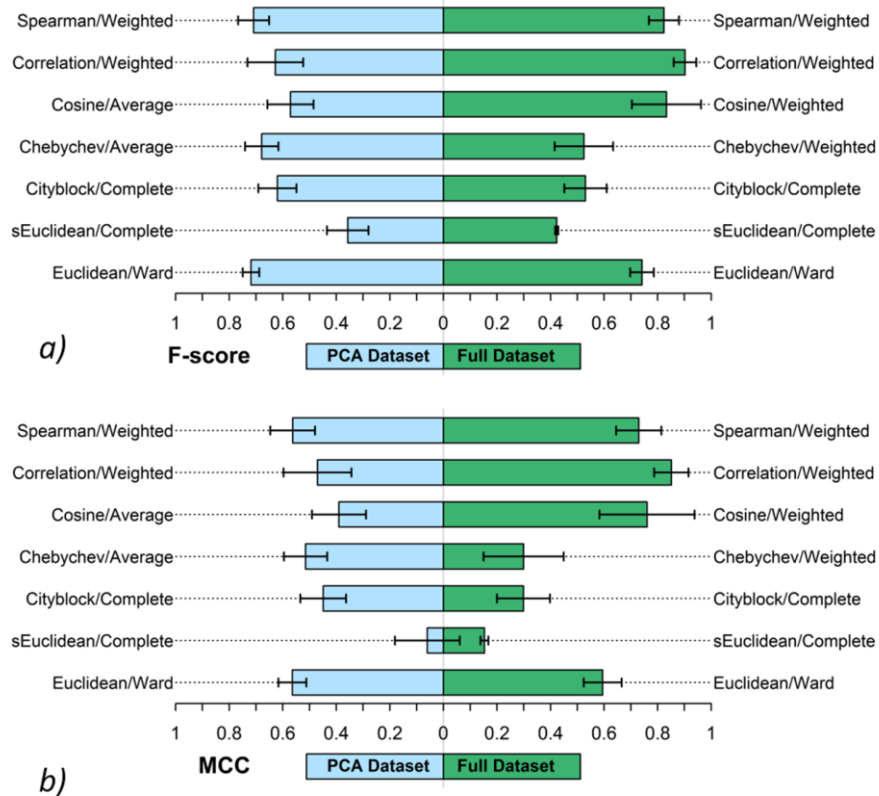


Fig. 8.4: Clustering classification performance in terms of F-score (a) and MCC (b) over 10 cross-validation runs for PCA dataset (light blue, left) and full deformation data. Only the respective best performing distance metric/linkage function is shown, adapted from (Bruse et al., 2017c)

In a one-to-one comparison, clustering using  $D_{Full,CV}$  yielded better classification performance both in terms of  $F-score_M$  and  $MCC_M$  than achieved with  $D_{PCA,CV}$ . Only the *Chebychev* and *Cityblock* distance metrics performed better for  $D_{PCA,CV}$ , yet scoring on average below 0.7 for  $F-score_M$  and below 0.6 for  $MCC_M$ . The worst performance was found for the *Standardised Euclidean* distance, even yielding negative (i.e. highly confused) results in terms of  $MCC_M$ .

On average, the best performing distance metrics (average  $F-score_M$  above 0.7 and average  $MCC_M$  above 0.5) were the *Spearman*, *Correlation* and *Cosine* metrics in combination with the *Weighted* linkage and the *Euclidean* distance in combination with the *Ward* linkage. However, particularly  $MCC_M$  scores revealed weaknesses such as large 95CIs for the *Cosine* metric, making it the most unreliable distance metric. Instead, *Spearman/Weighted*, *Correlation/Weighted* and *Euclidean/Ward* combinations

performed consistently well, with the *Correlation/Weighted* combination achieving on average the best classification performance with  $F\text{-score}_M=0.902\pm 0.042$  and  $MCC_M=0.851\pm 0.064$  for  $D_{Full,CV}$ . Therefore, the *Correlation/Weighted* distance/linkage combination applied to the full dataset  $D_{Full,CV}$  was found to yield the best overall shape clustering results with respect to the three patient groups and was chosen for further analysis.

#### 8.4.5 Analysis of best performing distance/linkage combination

Looking at individual classification performance metrics, the *Correlation/Weighted* distance/linkage combination performed consistently well, with average *Informedness<sub>M</sub>*, *Markedness<sub>M</sub>* and  $MCC_M$  scores above 0.8 and *Specificity<sub>M</sub>*, *Recall<sub>M</sub>*, *Precision<sub>M</sub>*,  $F\text{-score}_M$  and *Accuracy<sub>M</sub>* measures around 0.9, Fig. 8.5. Highest scores were achieved for *Specificity<sub>M</sub>* (i.e. proportion of patients correctly identified as *not* being a member of one of the three groups) with  $0.948\pm 0.023$ .

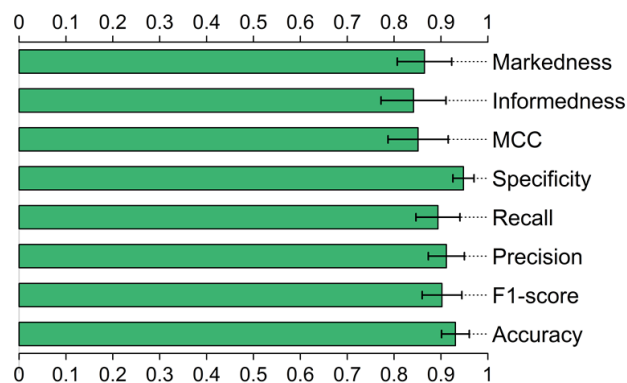


Fig. 8.5: Means and 95CIs of all computed clustering classification performance measures for best performing *Correlation* distance metric / *Weighted* linkage function combination, adapted from (Bruse et al., 2017c)

Detailed analysis of the derived confusion matrices for each CV run using the *Correlation/Weighted* combination and  $D_{Full,CV}$  revealed that on average 83% of CTRL arch shapes were correctly assigned to the CTRL group, while 13% were confused with COA and 4% were confused with ASO arch shapes, Tab. 8.1. For the COA group, on average 85% were correctly assigned and the remaining 15% were confused with CTRL arch shapes. ASO arch shapes were not confused with any other shape, thus 100% were placed correctly into one ASO cluster. Notably, neither were ASO and CTRL shapes

confused with high misclassification rates, nor were COA shapes always assigned correctly as one would have expected in case the clustering algorithm only took into account aortic arch size rather than shape.

Tab. 8.1: Confusion matrix for unsupervised hierarchical clustering classification performance, adapted from (Bruse et al., 2017c)

Group	CTRL, predicted	COA, predicted	ASO, predicted
CTRL, actual	83±13%	13±13%	4±6%
COA, actual	15±10%	85±10%	0
ASO, actual	0	0	100±0%

#### 8.4.6 Subgroup analysis – clusters within clusters

Finally, clustering classification performance was assessed using the *Correlation/Weighted* distance/linkage combination and  $D_{Full}$ , including all  $N=60$  patients. In this case, only two COA shapes (10%) were confused with CTRL arch shapes, while 100% of both CTRL and ASO arches were assigned to one respective cluster, Fig. 8.6.

In order to reveal more refined shape subgroups within the three larger clusters, which would add novel information about previously unknown patterns within the pathological shape clusters, branches were cut at a lower hierarchy level. Tree branches were cut at a height of 0.72, thus forming a total of 10 subgroups with a varying number of members in each larger cluster, Fig. 8.6. The CTRL group was divided into 5 smaller subgroups, the COA group into three and the ASO into two. Interestingly, the two confused COA shapes formed one distinct cluster within the CTRL group by themselves, marking them as being different from the other CTRL shapes.

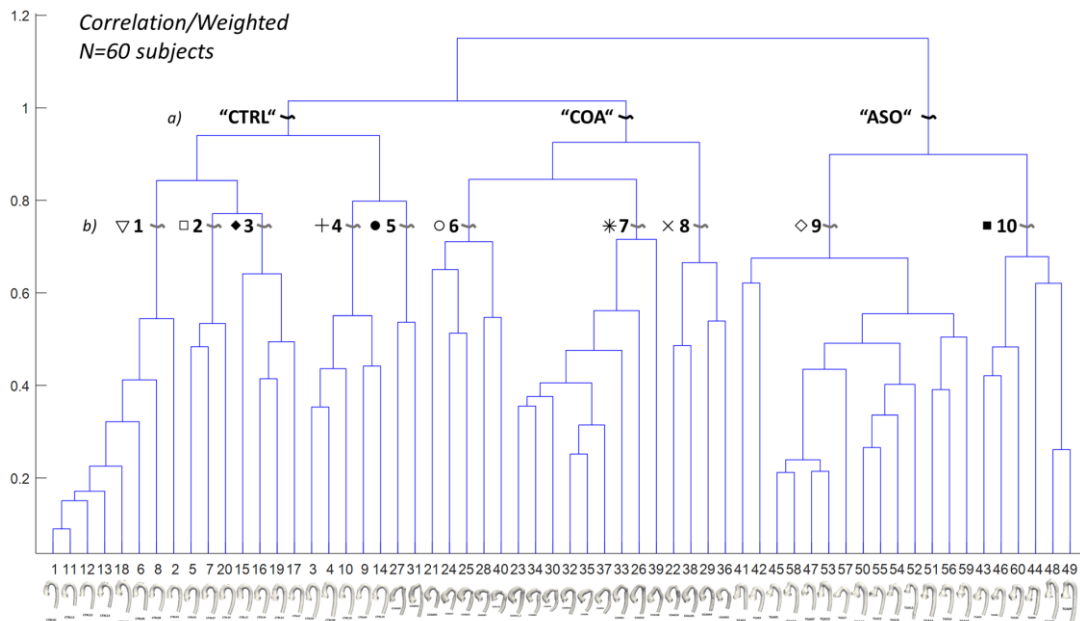


Fig. 8.6: Dendrogram obtained with the Correlation/Weighted distance/linkage combination on the full deformation dataset of 60 arch shapes. Cutting the dendrogram horizontally revealed known clusters (a) and novel subgroups (b), adapted from (Bruse et al., 2017c)

To evaluate whether the 10 subgroups related to meaningful 3D shape groups within the CTRL, COA and ASO clusters, I produced a scatter plot of the PCA shape space generated by the  $f_{i,PCA}^{m=1}$  and  $f_{i,PCA}^{m=2}$  associated with PCA shape modes 1 and 2 and symbol-coded the respective members of the 10 subgroups according to their subgroup affiliation, Fig. 8.7.

This plot revealed that novel and meaningful shape subgroups within the three larger (known) shape clusters could be found, since arch shapes that were clustered together by the hierarchical clustering algorithm were also clustered closer together in terms of their 3D aortic arch shapes as described by the PCA loadings. These findings confirmed that the pipeline can be used to detect to date unknown anatomical subgroups and patterns within pathological arch shape populations, which may prove to differ in terms of clinical outcome in future studies of larger, homogeneous patient cohorts.

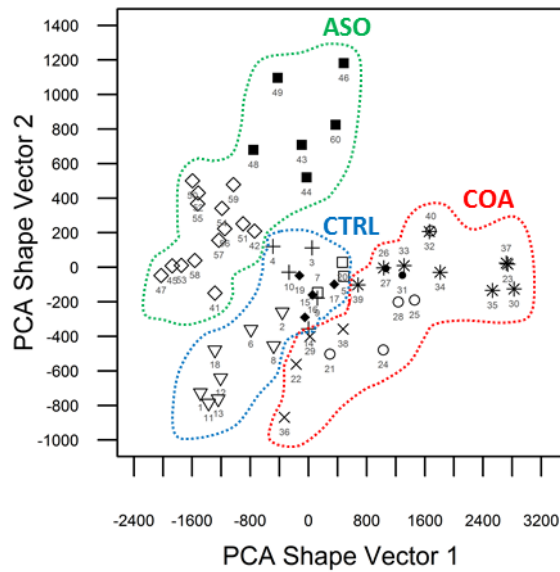


Fig. 8.7: Scatterplot of PCA shape vector entries for modes 1 and 2 revealed that patients with similar 3D arch shape were grouped together by both PCA and the clustering algorithm (individual patients are symbol-coded according to subgroups obtained from cutting the dendrogram as in Fig. 8.6b), adapted from (Bruse et al., 2017c)

## 8.5 Discussion

In this study, the modelling pipeline was extended by adding automatic segmentation and hierarchical clustering for post-processing of the generated shape data. Comparing different types of input data for the unsupervised clustering pipeline, results showed that a preceding dimensionality reduction via PCA yielded overall lower macro  $F\text{-score}_M$  and  $MCC_M$  scores than the raw deformation vector data. PCA thus did not yield improved clustering classification performance, which is in accordance with previous studies (Yeung and Ruzzo, 2001).

### 8.5.1 Optimal distance metric and linkage function

Using the full deformation vector data as input, the distance/linkage combinations *Spearman/Weighted*, *Correlation/Weighted* and *Euclidean/Ward* showed overall good ability to automatically structure the bulk input data into the three clinically defined groups as measured by average  $F\text{-scores}_M$  above 0.7 and  $MCC_M$  scores above 0.5, following 10-fold cross-validation. This is in accordance with early observations from Lance and Williams (Lance and Williams, 1967) stating that the *Correlation* distance is

suitable for comparing shapes, while the *Euclidean* distance is generally compatible with many clustering scenarios, probably due to being invariant under translations of the origin and under rotations of the pattern space (Dubes and Jain, 1976). The *Correlation* metric may here have resulted in best classification performance as it predominantly measures interrelationships between features (rather than absolute values or magnitudes) – here parameterised by shape deformation vectors of a template shape defined in a common mathematical framework. In accordance with this study, *Correlation* and *Euclidean* distance metrics have previously been found appropriate for various hierarchical clustering tasks (Dalton et al., 2009), (Lance and Williams, 1967), (Dougherty et al., 2002) and so has the *Ward* linkage, specifically when clustering anatomical structures (Cerrolaza et al., 2015), (Boyer et al., 2015), (Schecklmann et al., 2012). The *Correlation/Weighted* combination performed best with average  $Specificity_M$ ,  $Recall_M$ ,  $Precision_M$  and  $Accuracy_M$  scores around 0.9 and small confidence intervals – considerably higher than previously reported accuracies (Singh and Singh, 2012).

Note however, that this study has demonstrated again that clustering results do depend on the setting of clustering parameters and on the type of input data. PCA shape mode loadings (i.e. shape vectors  $f_{i,PCA}^m$ ) represent another input datatype than deformation vector data as provided by *Deformetrica* and indeed showed different clustering performance and different optimal distance/linkage combinations. Therefore, caution is warranted when performing hierarchical clustering on untested datatypes – ideally, a parametric study such as presented here, aiming to find appropriate, datatype-specific distance metrics and linkage functions should be carried out prior to reporting clustering results.

### 8.5.2 Classification performance

Averaged over all cross-validation runs, 17% of CTRL shapes, 15% of COA shapes and 0% of ASO shapes were misclassified. Those were lower misclassification rates than reported earlier for hierarchical clustering by Dalton (21% to 28%) (Dalton et al., 2009), and Brun (13% to 48%) (Brun et al., 2007). Applied to the full dataset of 60 patients, only

two COA arch shapes that showed highly localised deformation of the transverse aortic arch were confused with CTRL shapes. This suggests that some subtle 3D arch shape features may not be taken into account sufficiently when computing inter-subject distances. This could be addressed in future studies by a weighting of local 3D shape features, depending on which section of the arch (i.e. which anatomical region) is subject of interest. As expected though, ASO arches seemed to constitute a distinctly different shape cluster, allowing for 0% of misclassification, which is a notable performance for an unsupervised and automated approach. Following the overall good classification results for the unsupervised pipeline used here, it can further be assumed that trained, supervised approaches would perform even better in case classification of shapes is desired.

### **8.5.3 Subgroup detection**

Furthermore, hierarchical clustering results were compared to results from PCA statistical shape analysis and found that both methods compared well in determining shape clusters and subgroups based on the deformation data. More importantly, apart from distinguishing the three clinically known groups (CTRL, COA, ASO) mostly correctly, the clustering algorithm was able to cluster together subjects with similar 3D arch shape on lower levels of the clustering tree as well. This allowed for detection of previously unknown “clusters within the cluster”, i.e. novel anatomical patterns within the pathological COA and ASO clusters. While I refrained from analysing those subgroups further due to a limited subgroup sample size, such subgroups may be discovered in future studies of larger patient cohorts via the proposed pipeline and may generate novel hypotheses of clinical relevance.

### **8.5.4 Limitations and future work**

For broad application of hierarchical clustering algorithms to become reality, large medical image databases are required, which leads to one of the limitations of this study – the relatively small sample size. Yet, this study constitutes a first step showcasing that clinically meaningful clustering of medical image data can be achieved once clustering

parameters are set correctly. The next chapter will address this issue by focusing on one larger cohort of CoA patients.

Here, I aimed to automate data processing as much as possible. Yet, steps such as isolating the structure of interest after segmentation (here the aortic arch) were performed using manual cutting tools. This is another limitation, which may be addressed by providing segmentation atlases specifically adapted to the structure of interest. Further, some automatic segmentation results had to be edited manually due to insufficient input image quality or artefacts. With sophisticated automatic segmentation algorithms currently being on the rise (Zhuang, 2013), I expect drastic improvement in this area in the near future. In this regard, this study reports one of the largest datasets of automatically segmented pathological structures affected by CHD and the reported Dice Similarity Coefficients could be used as reference values for further algorithm development.

## 8.6 Summary

In this chapter, the SSM pipeline was extended by including automatic segmentation and hierarchical clustering. The main outcomes include:

- By applying a specific set of distance metric and linkage function, clustering classification results yielded clinically meaningful shape clusters and subgroups.
- To the best of my knowledge, this is the first study evaluating 3D hierarchical shape clustering performance on realistic, clinically acquired cardiovascular image data.
- The techniques implemented in the pipeline could be used to progress from a case-by-case image-based diagnosis towards assessing a patient in the context of a patient population as an integral component of current Precision Medicine or “Precision Imaging” (Frangi et al., 2016) strategies.

In this chapter, I have set up an automated processing pipeline for hierarchical clustering and have determined a suitable setting of distance metric and linkage function yielding clinically meaningful shape clusters and allowing detection of novel subgroups within 3D

shape data generated by *Deformetrica*. Hierarchical clustering thus proved to be an attractive alternative to shape feature regression via PLS regression. The next step was to apply the pipeline to a larger cohort of pathological shapes in order to detect novel clusters and subgroups within the bulk data and to assess whether such clusters differ in terms of cardiac functional parameters.

## **9 Hierarchical clustering applied to a patient population of repaired coarctation**

In the previous chapter, the SSM methods were extended by adding hierarchical clustering as a data post-processing technique. Optimal parameter setting in terms of distance metric and linkage function to process the generated deformation vector data was determined, yielding meaningful anatomical shape clusters according to primary clinical diagnosis. With evidence that the currents-based SSM in combination with PLS regression is able to detect patterns of 3D aortic arch shape features associated with cardiac functional parameters from Chapter 3.8 and a validated hierarchical clustering pipeline being set up, I sought to apply the techniques developed in the previous chapter to a larger cohort of patients post CoA repair, where anatomical shape clusters and subgroups are generally unknown. Only few studies to date have applied unsupervised hierarchical clustering techniques to medical image data with the aim of gaining clinically relevant insight about potential disease subgroups characterised by anatomical similarities. In this chapter, I therefore investigate whether automatically derived anatomical shape clusters differ with regard to clinically relevant functional parameters.

## 9.1 Abstract

*Background: The externally validated clustering pipeline established in the previous chapter was here applied to a larger cohort of patients post CoA repair, in order to assess its potential to detect previously unknown, clinically relevant anatomical shape clusters.*

*Methods: Image data from 67 patients post CoA repair were processed following protocols established in Chapter 8 in order to generate 3D aortic arch surface models that were processed via the currents-based SSM. Hierarchical clustering of the generated deformation data was performed using the Correlation/Weighted distance metric/linkage function combination, as established in Chapter 8. Morphometric shape descriptors and clinically relevant functional parameters were included to evaluate respective distributional differences between derived clusters via Kruskal-Wallis and Dunn tests.*

*Results: After cutting the computed clustering dendrogram, six larger anatomical shape clusters emerged, constituting six groups of aortic arch shape within the dataset. Visually, sensible clustering of the 3D arch shapes was achieved, which was reflected in significant differences between clusters in terms of traditional shape descriptors. Furthermore, inter-cluster differences in LVEF distributions were found, with the cluster predominantly comprising long, wide and slim arch shapes showing low ( $57.7 \pm 9.32\%$ ) LVEF.*

*Conclusions: Hierarchical clustering of 3D anatomical shape data yielded visually meaningful clustering of a cohort of pathological arch shapes post CoA repair into six previously unknown groups. Results suggest differences in cardiac function between certain shape clusters, making hierarchical clustering a potentially attractive tool for image-based risk assessment in complex cardiac disease.*

## 9.2 Introduction

As demonstrated in the previous chapter, hierarchical clustering offers the possibility to detect novel anatomical clusters and disease subgroups based on 3D shape information in a set of unlabelled CMR image data. In addition, Chapters 4 and 6 have shown that, in patients post CoA repair, certain patterns of aortic arch shape features seem to exist, which relate to cardiac functional parameters. One can therefore hypothesise that hierarchical clustering may be able to unveil similarities and dissimilarities within a set of patients with known primary diagnosis in terms aortic arch shape, which coincide with functional similarities or dissimilarities. Such newly discovered subgroups may thus improve risk stratification and follow-up strategies in complex structural cardiac disease as they allow placing a newly scanned patient into the context of an associated pathologic population.

Hierarchical clustering has previously been applied to assess patterns within functional magnetic resonance imaging (fMRI) data (Filzmoser et al., 1999), (Cordes et al., 2002), (Garreffa et al., 2006), but application to traditional 3D CMR or CT anatomical data is still rare. Kang et al applied hierarchical clustering and found significant associations between phenotypes in bicuspid aortic valve (BAV) patients and valvular dysfunction (Kang et al., 2013). However, clustering input data was generated by subjective classification and manual aortic arch diameter measurements. Few studies include 3D anatomical shape information and fully unsupervised approaches. Broggio et al applied hierarchical clustering and principal component analysis (PCA) to a population of 76 3D heart models and found new “shape families” (Broggio et al., 2013). Their approach however, lacked external validation (see Chapter 8) of the clustering technique and did not include any comparison of morphometric or functional parameters between the derived shape clusters.

In this chapter, I aimed to apply the validated hierarchical clustering pipeline as presented in Chapter 8 to a larger set of CMR image data of patients post CoA repair, in order to detect novel clusters and subgroups and assess functional differences between them. The leading questions was therefore:

→ Can clinically relevant clusters or patterns be found in a larger patient cohort affected by CoA?

## 9.3 Methods

### 9.3.1 Patient population and image processing

A total of 67 patients (age  $22.36 \pm 6.18$  years) post CoA repair that underwent routine whole heart CMR assessment were included in this study, 53 of which had been included in the work presented in Chapter 6. Patients with complex left-sided cardiac lesions and image artefacts due to stents or valve implants were excluded. The majority (78% of patients) had had End-to-End (E-E) CoA repair and 57% had bicuspid or functionally bicuspid aortic valve (BAV) morphology. Details are provided in Tab. 9.1. As functional parameters, LVEF, iLVM, systolic resting BP and MVR (LVM/EDV, see Chapter 3.8.3) were included. Aortic arch shapes were automatically segmented from the whole heart image data using the multi-atlas propagation segmentation method (Chapter 3.2.3) and pre-processed as described in Chapter 4.3.2 to obtain re-meshed, cut and aligned input 3D arch models to be used for template computation in *Deformetrica*. Conventional arch shape descriptors centreline length  $L_{CL}$ , centreline tortuosity  $To_{CL}$  and ascending to proximal descending aortic arch diameter  $D_{asc}/D_{desc}$  were measured in VMTK and manually on the image slices as detailed earlier Chapter 4.3.1.

Tab. 9.1: Detailed information about the included patient cohort post CoA repair for anatomical shape clustering

Variables	Mean±SD (range)
Number of patients	67
Age at time of CMR [years]	$22.36 \pm 6.18$ (11.8-38.1)
Height [cm]	$170.2 \pm 9.73$ (147-188)
BSA [m <sup>2</sup> ]	$1.83 \pm 0.21$ (1.44-2.22)
Aortic valve morphology (TAV/BAV/fBAV)	(29/28/10)
Type of initial repair (E-E/ExtE-E/flap/patch/balloon)	(52/1/9/4/1)
LVEF [%]	$64.3 \pm 7.17$ (44-80)
iLVM [g/m <sup>2</sup> ]	$67.7 \pm 20.5$ (37-161)
Systolic resting BP [mmHg]	$129.1 \pm 17.5$ (90-163)
MVR (LVM/EDV) [g/ml]	$0.852 \pm 0.227$ (0.34-1.33)

### 9.3.2 Hierarchical clustering analysis

Hierarchical clustering analysis was run on the computed deformation matrix  $D_{Full}$ , following the protocols established in the previous chapter. The *Correlation* distance metric and *Weighted* linkage function combination was used since it yielded most meaningful automatic division of the data as demonstrated in Chapter 8.4. The computed dendrogram was plotted in MATLAB and cut horizontally to obtain clustering of the shape data.

### 9.3.3 Statistical analysis

Depending on the dendrogram cuts, patients were associated with their respective cluster; distributional differences of traditional shape descriptors as well as of functional parameters between the clusters were analysed via non-parametric Kruskal-Wallis tests. If Kruskal-Wallis tests showed significance, Bonferroni-adjusted Dunn post-hoc tests were run. Statistical significance was assumed at level  $p < .05$ . All statistical tests were performed in R v3.3.1.

## 9.4 Results

Based on the computed dendrogram presented in Fig. 9.1, the anatomical shape data could be divided into two large groups, which were then split further by cutting the dendrogram horizontally such that 6 shape clusters of reasonable size emerged. On visual assessment, patients presenting with similar aortic arch shape were clustered together well Fig. 9.5. Thereby, group 1 included overall normal-sized arch shapes with few diameter changes along the arch, group 2 included smaller, but rounded arches with slightly dilated ascending aorta, group 3 clustered larger arches with long and relatively dilated descending aorta together, group 4 included tortuous, large and Gothic-type arches with high shape variability, group 5 included arches with dilated ascending aorta and group 6 clustered overall large and wide, but overall slim arches together.

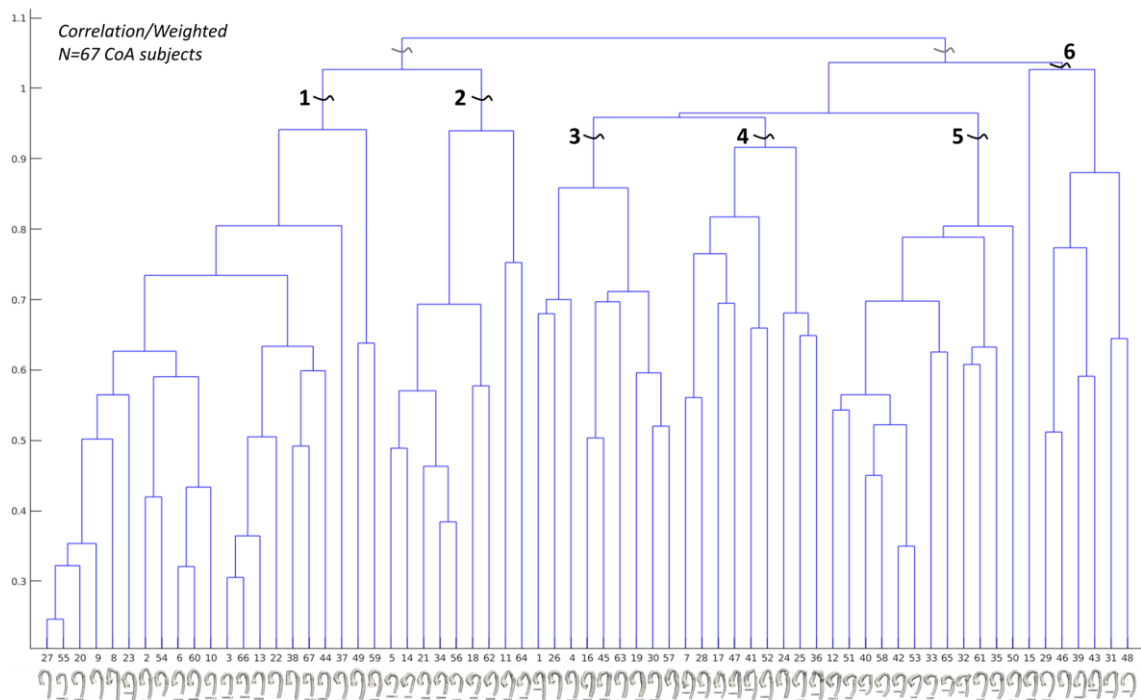


*Fig. 9.1: Clustering dendrogram of 67 aortic arch shapes post CoA repair. Horizontal cutting revealed six larger shape clusters*

This visual assessment was supported by significant distributional differences between the 6 cluster groups regarding traditional arch shape descriptors. In terms of  $L_{CL}$ , group 1 was significantly different compared to groups 4 (all adjusted  $p=7.7e-06$ ), 5 ( $p=5.5e-04$ ) and 6 ( $p=7.4e-03$ ) and so was group 2 to groups 4 ( $p=4.8e-05$ ), 5 ( $p=1.9e-03$ ) and 6 ( $p=1.0e-02$ ) following Dunn post-hoc tests; distributions are presented in Fig. 9.2. For  $To_{CL}$ , only group 1 differed significantly from group 4 ( $p=.007$ ) and for  $D_{asc}/D_{desc}$ , group 2 differed from group 3 ( $p=.010$ ) and group 3 from group 5 ( $p=.010$ ).

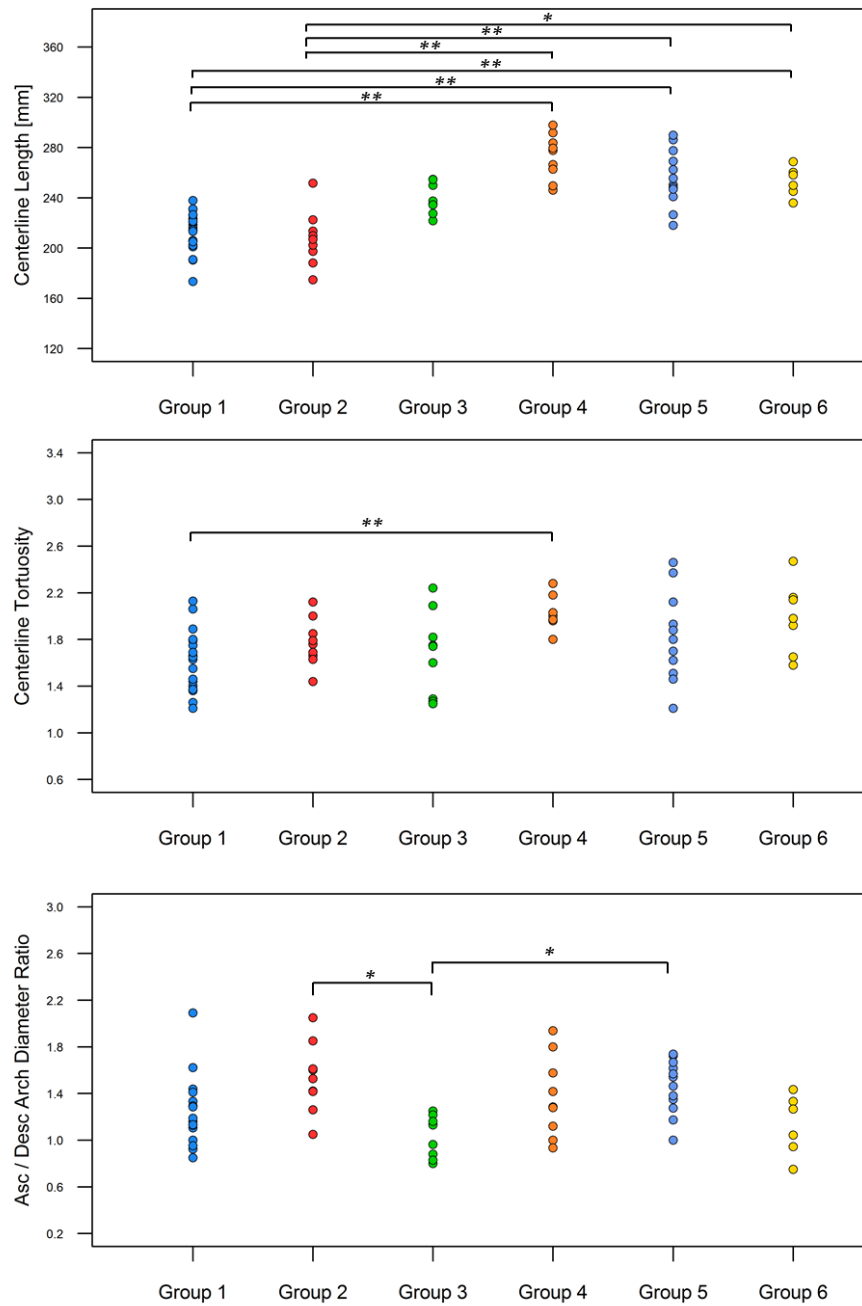


Fig. 9.2: Distributional differences in morphometric parameters between the six derived arch shape groups from hierarchical clustering from Fig. 9.1 (\*\* marks statistical significance at level  $p < .01$ ; \* at level  $p < .05$ )

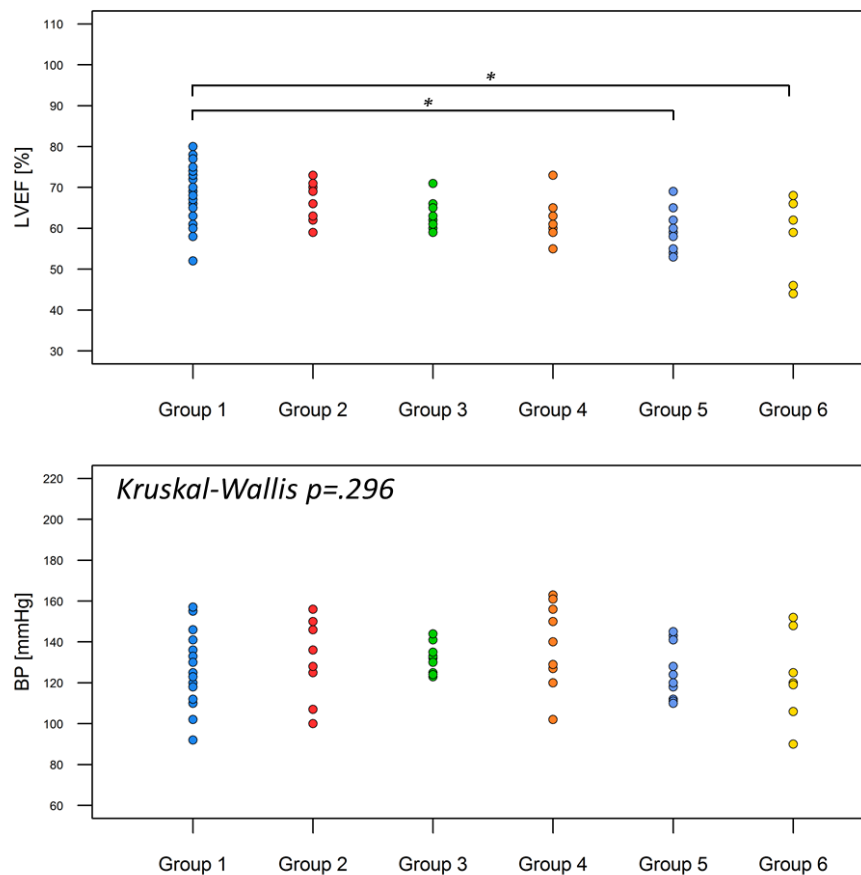


Fig. 9.3: Distributional differences of cardiac functional parameters LVEF and systolic resting BP between the six derived shape clusters from Fig. 9.1 (\* marks statistical significance at level  $p < .05$ )

Most functional parameters did not show significant distributional differences on Kruskal-Wallis assessment (Fig. 9.3, Fig. 9.4); for iLVM significance was  $p = .154$ ; for BP  $p = .296$  and for MVR  $p = .147$ . However, LVEF did achieve significance on Kruskal-Wallis assessment ( $p = .003$ ) and specifically showed significant differences between groups 1 and 5 ( $p = .016$ ) and groups 1 and 6 ( $p = .044$ ), with group 1 having larger LVEF ( $68.9 \pm 7.16\%$ , number of subjects in group  $n = 21$ ) than group 5 ( $60.8 \pm 5.43\%$ ,  $n = 12$ ) and than group 6 ( $57.7 \pm 9.32\%$ ,  $n = 7$ ).

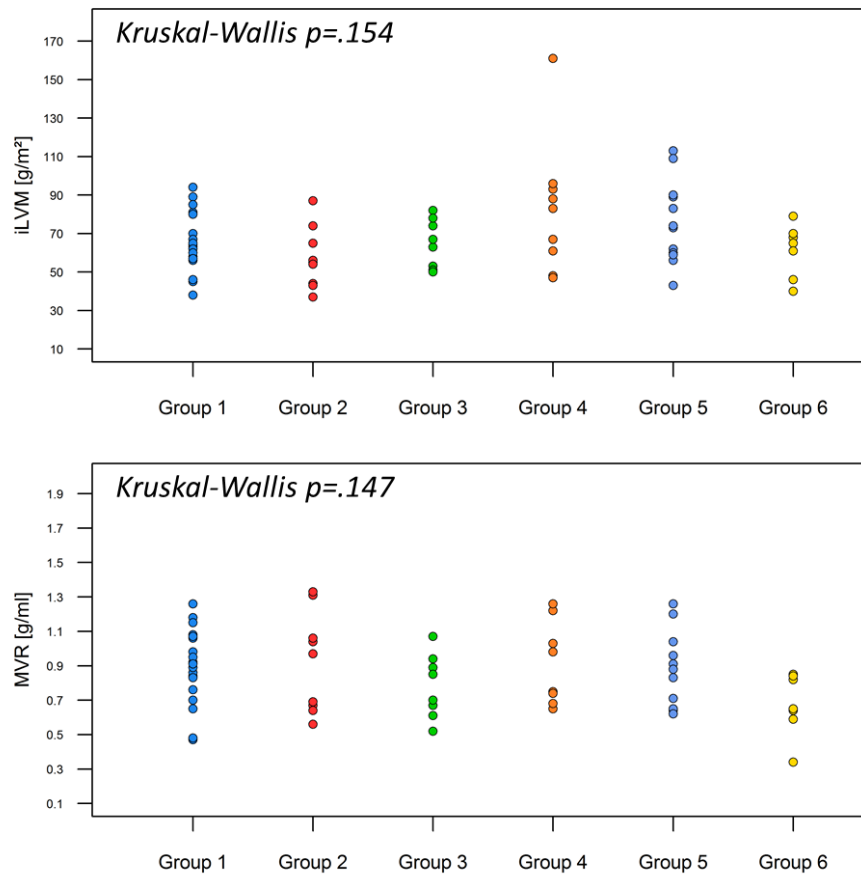


Fig. 9.4: Distributional differences of cardiac functional parameters iLVM and MVR between the six derived shape groups from Fig. 9.1

## 9.5 Discussion

In this study, the previously validated hierarchical clustering pipeline presented in Chapter 8 was applied to a larger cohort of patients post CoA repair in order to unveil novel clusters and subgroups based on aortic arch shape features. It constitutes the first study that attempts to cluster CMR-derived 3D anatomical shape data in complex cardiac disease in an automated and unsupervised fashion and, at the same time, compared derived shape clusters in terms of morphometric and functional parameters related to cardiac function.

On visual assessment, hierarchical clustering yielded sensible clustering of the 67 input arch shapes into 6 subgroups of reasonable size ( $N \geq 7$ ), each grouping aortic arches with similar 3D shape features together. One factor that seemed to play an important role

was overall arch size, which I considered to be a relevant descriptor of arch shape in patients affected by CHD. Visual clustering results were supported by significant distributional differences in terms of morphometric shape descriptors between computed shape clusters.



Fig. 9.5: Six CoA anatomical shape groups derived by the hierarchical clustering pipeline, see dendrogram in Fig. 9.1

Significant differences in the functional parameter LVEF were found between three clusters; with one cluster (number 6, Fig. 9.5) grouping together relatively large, wide and slim aortic arch shapes showing diminished, yet low normal LVEF ( $57.7 \pm 9.32\%$ ) compared to other clusters. Some of these arch shape features, such as a long and slim ascending aorta have been previously associated with low LVEF in Chapter 6.4. The other functional parameters iLVM, BP and MVR did not show significant differences between the six clusters. Yet, particularly in MVR distributions, within clusters, distributions visually showed further grouping, thus suggesting potential subclusters within each cluster. Subclusters were not analysed due to their small sample sizes.

Compared to two previous studies applying hierarchical clustering for assessment of cardiac anatomy (Broggio et al., 2013), (Kang et al., 2013), this study followed a completely unsupervised and automated approach, which has been externally validated in Chapter 8, analysing the entire aortic arch shape as a 3D entity without relying on landmarks or manual measurements and aimed to assess clinical meaningfulness by including relevant functional parameters. The discovered functional differences between the reported six anatomical shape clusters suggest that patients associated to a shape cluster may share cardiac functional similarities, which may prove beneficial for risk stratification of patients with a common disease. However, differences between clusters with regard to critical risk markers such as elevated BP, iLVM and MVR were not statistically significant.

### **9.5.1 Limitations and future work**

The key limitation of this study is the relatively small sample size, which hinders further statistical analyses of intra-cluster or inter-cluster distributional differences of functional parameters. Furthermore, the included patient cohort was rather inhomogeneous in terms of CoA repair and aortic valve morphology. Future studies involving a significantly larger number of patients may reveal anatomical arch similarities or dissimilarities between patients that share a certain arch repair and/or valve type. Potential differences in cardiac function need to be investigated in more detail in larger cohorts. On the technical side, automatic segmentation techniques may obtain improved segmentation results if cluster-specific atlases are used. Further, applying clustering techniques to cardiac disease that requires implantation of medical devices could allow improved and more cost-effective cluster-adapted cardiac device design in a “few-sizes-fit-all” fashion, whenever patient-specific approaches are not feasible (Bruse et al., 2017d). Found clusters could be used to compute cluster-specific subtemplates (i.e. mean anatomical shapes) that provide geometric boundary conditions for cardiac device design, which may be suitable for an entire subgroup of patients.

## 9.6 Summary

This study demonstrated how hierarchical clustering could be used for detecting previously unknown anatomical shape clusters within a patient cohort sharing a common aortic arch pathology. The main outcomes were:

- In a cohort of 67 patients post CoA repair, six arch shape clusters were discovered based on 3D aortic arch shape features parameterised within the currents-based SSM.
- Shape clusters were meaningful on visual assessment, which was corroborated by traditional morphometrics.
- Only few clear and significant differences between clusters were found in terms of functional parameters. Specifically, low (normal) LVEF was associated with one computed shape cluster comprising overall large and wide but slim aortic arch shapes.

This chapter constitutes the last study carried out within the scope of this thesis and shows that although larger cohorts are necessary to further investigate the clinical relevance of anatomical clusters, disease-specific anatomical shape clustering may prove beneficial for risk stratification as well as cardiac device design. Overall, I have developed protocols and techniques to extract 3D shape biomarkers and anatomical shape clusters from medical image data in cohorts of patients suffering from CHD. Functional and clinical relevance of 3D aortic arch shape features in patients post CoA has been demonstrated by combining state-of-the-art image analysis, computational modelling and data mining techniques. The next and last chapter reiterates the main outcomes of this thesis, presents conclusions and potential topics to be addressed in future studies.

## **10 Conclusions and future work**

This chapter summarises the main findings and outcomes of this thesis and highlights my contributions to the field of biomedical engineering. General limitations of this work are discussed and potential starting points for future research are outlined. Final remarks conclude this thesis.

## 10.1 Contributions overview

This thesis aimed to investigate associations between shape and function in congenital heart disease (CHD) by combining state-of the art medical image processing, computational modelling and data mining tools. In particular, I sought to analyse if and how a novel statistical shape modelling (SSM) framework based on parameterising shape with mathematical currents can be used to explore relationships between 3D anatomical shape features and cardiac functional parameters. As a clinically relevant example, I focussed on cohorts of patients post aortic coarctation repair (CoA) since earlier work suggested associations between aortic arch shape features and cardiac function in this group of patients. By combining and evaluating engineering and data analytic methods and by applying them to the clinically relevant question of cardiovascular magnetic resonance (CMR)-based shape assessment for risk stratification in complex cardiac disease, I hoped to promote translation of such computational approaches into clinical research.

Overall, I set up protocols on how to run the currents-based SSM to extract novel 3D shape biomarkers and unknown anatomical shape clusters from the input CMR-image data. I showed that computed SSM results were in agreement with traditional morphometric shape descriptors and with clinical expert opinion. For the first time, I joined both SSM and computational fluid dynamics (CFD) modelling to provide a mechanistic basis for SSM results. Regarding image-based risk assessment of patients post CoA repair, I identified novel 3D arch shape biomarkers and anatomical shape clusters to be associated with impaired cardiac function.

In conclusion, it has been shown that the presented methods and tools for the analysis of shape and function have the potential to contribute to a better understanding of complex structural disease, which may lead to the development of novel diagnosis and risk stratification strategies and, potentially, of new surgical approaches.

## 10.2 Detailed contributions and outcomes

Previous work in the literature on the currents-based SSM framework highlighted the ability of this method to visually and numerically analyse complex 3D anatomical shape variability as typically found in CHD. To make this shape analysis tool more accessible to the broader engineering and clinical research community, I started my work by outlining general concepts behind such phenomenological computational modelling methodology (**Chapter 2**) and in particular by describing the currents-based SSM framework conceptually, rather than mathematically as found in previous relevant publications (**Chapter 3**).

I then moved on to determine an efficient and robust way to run the SSM framework with the aim of extracting anatomical shape biomarkers from CMR image data (**Chapter 4**). Specifically, it was investigated how user-determined parameters such as surface mesh size and kernel resolutions affect both computation time and final template shape (i.e. the anatomical mean shape), and new strategies were derived to set these parameters appropriately. Further, I proposed a way to detect and handle shape outliers within the input shape population. In order to assess the validity of the results, I then compared the SSM results with traditionally measured 2D and 3D morphometric parameters (typically used for shape assessment in clinical practice), which resulted in good agreement. This being established, preliminary results on a cohort of 20 CoA patients demonstrated the method's potential of extracting novel shape biomarkers via partial least squares (PLS) regression, since previously unknown associations between aortic arch shape features and left ventricular ejection fraction (LVEF) were found. To summarise, major contributions from Chapter 4 were:

1. Protocols were established, guiding the user through the the currents-based SSM analysis in order to extract 3D shape biomarkers from CMR image data.
2. For the first time, agreement between traditional shape descriptors and the computed SSM results was demonstrated.

3. A preliminary analysis on 20 CoA subjects suggested aortic arch shape features such as an overall large aorta with slim ascending and transverse arch section to be associated with low LVEF.

Few studies to date have quantitatively analysed correlations between computed SSM results and clinical expert opinion: with the established protocol, validated versus the measurable shape descriptors, I sought to assess how such computed results compare to subjective clinical expert opinion. Therefore, a ranking of shape abnormality comparing CoA patients to healthy Controls was computed and compared to an abnormality ranking carried out by experienced clinical experts (**Chapter 5**). This was the first study comparing the currents-based SSM results to human opinion in a quantitative manner and suggested that such computational approaches may become a valuable tool in image-based risk assessment. The main outcome of this study was:

4. Computed 3D shape abnormality values of a cohort of CoA patients were in better agreement with clinical expert opinion than traditionally used arch shape descriptors.

With the SSM results being in agreement with traditional morphometrics and human expert opinion, I aimed to extract novel 3D shape biomarkers in a larger cohort of CoA patients using the currents-based approach (**Chapter 6**). Applying the methods developed in Chapter 4, a total of 53 patients post CoA repair were analysed and shape biomarkers associated with clinically relevant functional parameters were extracted from the CMR input data. Such information may assist in image-based clinical risk stratification of CoA patients, who are known to face complications later in life. This study constituted the first 3D SSM of the aorta affected by CHD and demonstrated its usefulness for clinical research aiming to analyse complex cardiac anatomy. In particular, the main findings were:

5. Low (normal) LVEF and high indexed left ventricular mass (iLVM) were significantly associated with overall larger aortic arch shapes with slim ascending and transverse arch, slightly dilated descending aorta and high arch height to

width ratio. More compact and rounded arch shape patterns were found to be functionally favourable.

6. The previously reported Gothic aortic arch shape with high height to width ratio and angulated transverse section seemed to be associated with higher BP, however results remained inconclusive as statistical significance was not achieved after adjusting for multiple comparisons.

A large part of biomedical engineering research has been focussing on investigating associations between cardiac shape and function using mechanistic computational modelling by simulating cardiac anatomy and function dependent on physical laws. This thesis, however, concentrates on phenomenological i.e. observational computational modelling via the currents-based SSM framework in combination with data mining techniques. Recent studies suggest that research should aim to join both mechanistic and phenomenological approaches in order to extract most information and knowledge out of the provided data to inform clinical decision making. In **Chapter 7**, I therefore sought to investigate whether the associations between arch shape and “better” or “worse” functional parameters identified in Chapter 6 may have a mechanistic basis. CFD simulations, replicating peak systolic blood flow conditions in the arch were carried out on the computed arch shapes most associated with low/high LVEF, iLVM and BP (Chapter 7). CFD results were in line with results from phenomenological SSM as computed hemodynamic parameters pressure drop  $\Delta p$  and power loss  $PL$  were found to be higher for the functionally “worse” arch shapes derived with the currents-based SSM approach. This study demonstrated that the combination of mechanistic and phenomenological computational modelling may be complementary and may provide additional insight, which could in turn increase the credibility of purely phenomenological results within the clinical community. To the best of my knowledge, this was the first study performing CFD analyses directly on SSM-derived shape modes. Specifically, the main outcomes of Chapter 7 were:

7. Overall large aortic arches with slim ascending and transverse section and slightly dilated descending aorta showed increased pressure drop  $\Delta p$  and power loss  $PL$

in the order of 15-25% compared to their respective functionally better counterpart arch shape pattern as determined by SSM.

8. In agreement with the literature, the Gothic-type arch shape with angulated transverse section was found to be the functionally worst arch shape, showing 23% higher pressure drop and 27.5% higher power loss than the computed crenel-type arch shape associated with lower BP.

Having established and extensively applied the SSM-based shape biomarker extraction via PLS regression, I then aimed to explore the SSM framework's capabilities when combined with other data mining techniques. I included hierarchical clustering as an unsupervised data processing technique, which, unlike PLS, does not require prior assumptions about the input data and provides intuitively comprehensible results in the form of a dendrogram showing anatomical clusters within the data. Hierarchical clustering has not been applied extensively in the field of medical image analysis, which is why practical protocols on how to set clustering parameters (i.e. distance metric and linkage function) were missing. In a first technical evaluation, I therefore externally validated a data processing pipeline, comprising automatic segmentation, the currents-based SSM and hierarchical clustering using a dataset of known aortic arch shape clusters of healthy Control subjects and further two patient cohorts affected by CHD as defined by clinical diagnosis (**Chapter 8**). In this way, the *Correlation* distance metric and *Weighted* linkage function were found to yield most meaningful unsupervised division of the input data into the three groups with low misclassification rates. This was a notable performance for an unsupervised approach compared to previously reported data. This chapter constituted the first study externally validating hierarchical clustering performance of cardiac anatomy against clinical diagnosis and results from principal component analysis (PCA). Hierarchical clustering thus provided a notion of the "natural" grouping or structure within the input shape data, for generating future hypotheses about previously unknown clusters and subgroups within cohorts of patients affected by CHD. Such approaches could provide additional information to clinicians, who would know that a patient suffers from a certain congenital defect, yet who may not know how this patient relates to other, similar patients affected by the

same defect. The reported classification performance measures and Dice Similarity Coefficients (DSC) for automatic segmentation of aorta and left ventricle can be used as benchmark scores for future algorithm development. Specific outcomes of this chapter were:

9. Protocols on how to perform hierarchical clustering on the shape data generated by the currents-based SSM were established; the full deformation vector data showed overall better clustering classification results than shape vector data generated by PCA.
10. The *Correlation* distance metric and *Weighted* linkage function as well as the *Spearman/Weighted* and *Euclidean/Ward* distance/linkage combinations yielded overall good and reliable automatic clustering with relatively high *F-score* and *Matthew's Correlation Coefficient (MCC)* values. The best performing combination was *Correlation/Weighted* with average *F-score*=0.902±0.042 and *MCC*=0.851±0.064.
11. The hierarchical clustering pipeline achieved overall low misclassification rates of around 15±10% and automatic segmentation DSCs above 0.9 for both healthy and diseased cohorts.

The clustering results from Chapter 8 also suggested that novel subgroups, i.e. “clusters within the cluster” could be derived for arch shape populations affected by CHD. This idea motivated the last study carried out in this thesis in **Chapter 9**, where I applied the validated hierarchical clustering pipeline to a larger cohort of 67 patients affected by CoA. The aim was to determine previously unknown anatomical shape clusters within a coherent pathological shape cohort and assess whether found clusters differed in terms of cardiac functional parameters. Similar studies have been carried out recently, however without analysing the full 3D anatomical shape information provided by CMR image data. The clustering pipeline found six larger anatomical arch shape clusters in the dataset, which differed significantly in terms of morphometric parameters. Although clear differences with regard to functional parameters were not found, one shape cluster comprising overall large and wide but slim aortic arch shapes showed statistically

significant distributional differences in terms of LVEF compared to two other clusters. Results corroborated earlier findings from PLS regression and demonstrated how clustering could be used to detect novel anatomical shape clusters within a certain disease. Such approaches may prove a useful adjunct in image-based risk stratification, moving away from a confined case-by-case assessment towards analysing a patient in the context of similar cases. Furthermore, anatomical shape clusters may contribute to more cost-effective medical device design and development by providing a range of cluster-specific devices rather than cost-intensive patient-specific solutions (Bruse et al., 2017d). The main outcomes of this chapter were:

12. On visual assessment, SSM-based hierarchical clustering yielded six larger meaningful anatomical shape clusters for a cohort of 67 patients affected by CoA.
13. Significant distributional differences were found in terms of morphometric parameters, but not regarding the included cardiac functional parameters iLVM, BP and mass to volume ratio (MVR). One cluster containing large, wide and slim aortic arches showed significantly lower LVEF than two other shape clusters containing generally more rounded arch shapes.
14. Larger patient cohorts need to be analysed via hierarchical clustering in order to be able to draw conclusions about functional differences between clusters.

This last point leads to some limitations that need to be considered when evaluating the outcomes of this work. Those are addressed in the next section.

## **10.3 Limitations and future work**

### **10.3.1 Sample size and patient populations**

The first major limitation of this work is the relatively small sample size of patients post CoA repair included in the shape abnormality computation (Chapter 5), the CFD study (Chapter 7) and the clustering according to functional parameters (Chapter 9). Studies on larger cohorts need to confirm findings from these chapters.

Given that six larger anatomical shape clusters were found in the cohort of 67 CoA patients, many more patients would be necessary to assess distributional differences of functional parameters between these clusters. Further, more clinically relevant functional or outcome parameters (such as data from cardiopulmonary exercise testing, CPET) should be included in order to find clusters of high or low risk.

Generally, it is to be taken into account that all results presented in this thesis suffer from the inherent demographic bias of only including patient populations with rare congenital heart diseases enrolled at GOSH, London, UK. Inclusion of patients from other clinical centres would be advisable and would also contribute to increasing sample sizes for increased statistical power.

Multi-centre studies however, need to be approached with caution. In this thesis, all patients were assessed via CMR imaging using the same scanner type, scanning protocols and sequences and it has not been investigated how any variation of these would affect the final SSM results. Future research should also investigate the possibility of increasing sample sizes by pooling image data from different imaging modalities.

### **10.3.2 Automation and parameter setting**

In terms of the currents-based SSM framework, future work should aim at automating the entire processing pipeline further. Ideally, a newly scanned patient's shape is immediately added to a local or cloud-based SSM database, which would allow immediate comparison of this patient with respect to a chosen population; shape biomarker values, abnormality scores or clustering visualisations could be directly obtained and included in the diagnosis process. To increase processing speed and improve automation, atlases adapted to the structure of interest could be used for automatic segmentation, reducing manual cutting operations. Subsequent alignment (i.e. rigid registration) prior to template computation could be integrated into one coherent software framework. A highly attractive solution of speeding up and automating the process further, would be to be able to run the entire analysis on the image data (or binary segmentation labels) themselves, without taking the detour of surface meshes. One could think of a representation of the segmentation labels in the

space of currents that allows direct template computation as a “template segmentation” and associated template segmentation deformations, which could then be exported as 3D surface mesh for further processing. For the correct setting of the kernel resolution ( $\lambda$ ) parameters, the process could be automated further by performing an a priori matching of an assumed template shape with each input shape and iteratively adjusting the  $\lambda$  parameters until optimal matching between deformed template and each patient shape is guaranteed. In general, future studies could investigate whether different kernel settings allow for improved agreement between experts and computed shape abnormality scores or for improved clustering classification results.

### **10.3.3 Post-processing of the data**

For the PLS regression, techniques could be extended to include not only one but several parameters such that 3D shape features most associated with differences in several functional or outcome parameters are derived simultaneously. Since Mansi et al (Mansi et al., 2011) have initially used the proposed methods for the creation of statistical growth models, future work should follow up on this idea by generating growth models of healthy versus diseased or operated anatomy, for example (Zacur et al., 2015). In this way, local differences in growth patterns could be visualised and models could be applied to a new patient for growth prediction.

In terms of shape abnormality score computation, other pathological shapes or structural defects and a larger group of clinical experts, potentially from other clinical centres, could be included. In fact, when assessing the performance of new algorithms for risk assessment, such comparisons with human expert opinion should always be included in order to promote acceptance and translation of the proposed methods.

For a more elaborate analysis, joining both phenomenological and mechanistic computational modelling, hemodynamic parameters could be computed for each input arch shape. This would generate patient-specific hemodynamic data that could be included into a PLS regression, similar to the clinical parameters used in this thesis. In that way, direct associations between arch shape features and mechanistic parameters could be investigated. Since such large-scale CFD simulations require a large amount of

(computation) time and effort to be set up and run, 4D flow analyses providing both anatomical and blood flow related data from one CMR scan may be a more efficient approach to generate large amounts of data.

Regarding the hierarchical clustering, its use for medical device design could be exploited further by computing subtemplates for cluster subgroups that could be used for mechanical in silico or in vitro testing in order to design “few-sizes-fit-all” devices, adapted to their respective anatomical cluster. Potentially, the clustering approach could be changed fundamentally, by not assuming shape to be the prior but by running the clustering on a joint dataset containing both shape and functional data to find relevant novel clusters.

With the promising unsupervised classification results found in Chapter 8, I expect supervised classification approaches to perform even better. This could be exploited for various disease classification tools. Generally, post-processing methods could be extended by other data mining and machine learning tools, such as neural networks or support vector machines to enable outcome prediction, for instance (Dawes et al., 2017).

To further promote translation of the proposed computational approaches, more studies with direct clinical insight are necessary. Dissemination into other medical domains where shape plays an important role such as neuroscience or plastic and reconstructive surgery may be feasible and has already shown to yield promising results (Tenhagen et al., 2016), (Rodriguez-Florez et al., 2017).

## 10.4 Final remarks

I have shown that the combination of image processing, engineering and data analytics tools and specifically statistical shape modelling (SSM) provides a powerful platform to analyse associations between shape and function in complex structural disease. The methods presented in this thesis can be extended beyond the analysis of aortic arch shapes (Bruse et al., 2016c) and beyond cardiac applications to investigate other anatomical structures (Rodriguez-Florez et al., 2017), (Dall’Asta et al., 2017).

By demonstrating its validity, meaningfulness and its broad applicability, I hope that this work contributes to the dissemination of computational SSM-based approaches with potential research, clinical, technical and commercial applications. In research, SSM-based computational modelling could help better understand diseases by providing means to derive novel shape biomarkers and detect yet-to-be-discovered disease patterns. This, in turn, could ultimately assist clinicians in decision-making and risk stratification, particularly in complex or rare diseases. Large cloud-based image databases – in combination with immediate online clustering following image acquisition – could allow for comparison of a newly scanned patient to individuals with the same clinical history or disease in order to detect “outliers” or similarities. On the technical side, clustering could be used for shape-retrieval systems and found clusters could be used to compute subtemplates (i.e. representatives of a subgroup), which may improve atlas-based image segmentation of highly varying anatomy. Finally, regarding commercial applications, subtemplate anatomical models could allow for more cost effective “few-sizes-fit-all” rather than patient-specific approaches for device design and development, which may be particularly appealing in complex structural disease (Bruse et al., 2017d).

To conclude, computational SSM-based tools that are able to detect and extract shape clusters, outliers and shape biomarkers could eventually be integrated in clinical decision support systems (Richardson et al., 2010). These may pave the way for moving from mere data towards information and knowledge (Fig. 2.1), which could contribute to a better understanding of complex structural disease and ultimately may impact on improved diagnosis, risk stratification and treatment strategies. However, as with all computational algorithm-based approaches, it is crucial for the best clinical care not to rely entirely on one computed number, but to critically assess results and put them into context before taking a decision. Computational results should only be used as an addition to inform, back up or challenge clinical expert opinion and assist in assessing complex cases where only few data are available. As human beings are the centre of medicine, humans should also be the centre of clinical decision making, relying on their intuition and experience and always assessing all provided information with critical eyes.

## 11 Bibliography

Agnoletti, G., Ou, P., Celermajer, D.S., Boudjemline, Y., Marini, D., Bonnet, D., and Aggoun, Y. (2008). Acute angulation of the aortic arch predisposes a patient to ascending aortic dilatation and aortic regurgitation late after the arterial switch operation for transposition of the great arteries. *J. Thorac. Cardiovasc. Surg.* *135*, 568–572.

Ahrens, J., Geveci, B., and Law, C. (2005). ParaView: An End-User Tool for Large-Data Visualization. *Vis. Handb.* 717.

ANSYS Inc. (2016). ANSYS FLUENT v17 Documentation.

Antiga, L., and Steinman, D.A. (2004). Robust and objective decomposition and mapping of bifurcating vessels. *IEEE Trans. Med. Imaging* *23*, 704–713.

Antiga, L., Piccinelli, M., Botti, L., Ene-Iordache, B., Remuzzi, A., and Steinman, D.A. (2008). An image-based modeling framework for patient-specific computational hemodynamics. *Med. Biol. Eng. Comput.* *46*, 1097–1112.

Baldi, P., Brunak, S., Chauvin, Y., Andersen, C.A.F., and Nielsen, H. (2000). Assessing the accuracy of prediction algorithms for classification: an overview. *Bioinformatics* *16*, 412–424.

Baretta, A., Corsini, C., Yang, W., Vignon-Clementel, I.E., Marsden, A.L., Feinstein, J.A., Hsia, T.-Y., Dubini, G., Migliavacca, F., Pennati, G., et al. (2011). Virtual surgeries in patients with congenital heart disease: a multi-scale modelling test case. *Philos. Transact. A Math. Phys. Eng. Sci.* *369*, 4316–4330.

Beg, M.F., Miller, M.I., Trouvé, A., and Younes, L. (2005). Computing Large Deformation Metric Mappings via Geodesic Flows of Diffeomorphisms. *Int. J. Comput. Vis.* *61*, 139–157.

Beier, S., Ormiston, J., Webster, M., Cater, J., Norris, S., Medrano-Gracia, P., Young, A., and Cowan, B. (2016). Impact of bifurcation angle and other anatomical characteristics on blood flow – A computational study of non-stented and stented coronary arteries. *J. Biomech.* *49*, 1570–1582.

Besl, P.J., and McKay, N.D. (1992). A method for registration of 3-D shapes. *IEEE Trans. Pattern Anal. Mach. Intell.* *14*, 239–256.

Bhatia, R.S., Tu, J.V., Lee, D.S., Austin, P.C., Fang, J., Haouzi, A., Gong, Y., and Liu, P.P. (2006). Outcome of Heart Failure with Preserved Ejection Fraction in a Population-Based Study. *N. Engl. J. Med.* *355*, 260–269.

Biglino, G., Capelli, C., Bruse, J., Bosi, G.M., Taylor, A.M., and Schievano, S. (2017). Computational modelling for congenital heart disease: how far are we from clinical translation? *Heart* *103*, 98–103.

Bluemke, D.A., Kronmal, R.A., Lima, J.A.C., Liu, K., Olson, J., Burke, G.L., and Folsom, A.R. (2008). The Relationship of Left Ventricular Mass and Geometry to Incident Cardiovascular Events: The MESA Study. *J. Am. Coll. Cardiol.* 52, 2148–2155.

Bogaert, J., Dymarkowski, S., and Taylor, A.M. (2012). *Clinical Cardiac MRI* (Berlin; New York: Springer).

Bohl, W., and Elmendorf, W. (2014). *Technische Strömungslehre* (Vogel Business Media).

Bookstein, F.L. (1989). Principal warps: thin-plate splines and the decomposition of deformations. *IEEE Trans. Pattern Anal. Mach. Intell.* 11, 567–585.

Bosmans, B., Huysmans, T., Wirix-Speetjens, R., Verschueren, P., Sijbers, J., Bosmans, J., and Vander Sloten, J. (2013). Statistical Shape Modeling and Population Analysis of the Aortic Root of TAVI Patients. *J. Med. Devices* 7, 040925–040925.

Boyer, D.M., Puente, J., Gladman, J.T., Glynn, C., Mukherjee, S., Yapuncich, G.S., and Daubechies, I. (2015). A New Fully Automated Approach for Aligning and Comparing Shapes. *Anat. Rec.* 298, 249–276.

Broggio, D., Moignier, A., Ben Brahim, K., Gardumi, A., Grandgirard, N., Pierrat, N., Chea, M., Derreumaux, S., Desbrée, A., Boiserie, G., et al. (2013). Comparison of organs' shapes with geometric and Zernike 3D moments. *Comput. Methods Programs Biomed.* 111, 740–754.

Brown, M.L., Burkhart, H.M., Connolly, H.M., Dearani, J.A., Cetta, F., Li, Z., Oliver, W.C., Warnes, C.A., and Schaff, H.V. (2013). Coarctation of the Aorta: Lifelong Surveillance Is Mandatory Following Surgical Repair. *J. Am. Coll. Cardiol.* 62, 1020–1025.

Brun, M., Sima, C., Hua, J., Lowey, J., Carroll, B., Suh, E., and Dougherty, E.R. (2007). Model-based evaluation of clustering validation measures. *Pattern Recognit.* 40, 807–824.

Bruse, J.L., McLeod, K., Biglino, G., Ntsinjana, H.N., Capelli, C., Hsia, T.-Y., Sermesant, M., Pennec, X., Taylor, A.M., Schievano, S., et al. (2016a). A statistical shape modelling framework to extract 3D shape biomarkers from medical imaging data: assessing arch morphology of repaired coarctation of the aorta. *BMC Med. Imaging* 16, 40.

Bruse, J.L., McLeod, K., Biglino, G., Ntsinjana, H.N., Capelli, C., Hsia, T.-Y., Sermesant, M., Pennec, X., Taylor, A.M., and Schievano, S. (2016b). A Non-parametric Statistical Shape Model for Assessment of the Surgically Repaired Aortic Arch in Coarctation of the Aorta: How Normal is Abnormal? In O. Camara et Al. (Eds.): *Statistical Atlases and Computational Models of the Heart 2015*, (Munich: Springer International Publishing Switzerland 2016), pp. 21–29.

Bruse, J.L., Ntsinjana, H., Capelli, C., Biglino, G., McLeod, K., Sermesant, M., Pennec, X., Hsia, T.-Y., Schievano, S., and Taylor, A. (2016c). CMR-based 3D statistical shape modelling reveals left ventricular morphological differences between healthy controls and arterial switch operation survivors. *J. Cardiovasc. Magn. Reson.* *18*, 1–3.

Bruse, J.L., Cervi, E., McLeod, K., Biglino, G., Sermesant, M., Pennec, X., Taylor, A.M., Schievano, S., Hsia, T.-Y., Taylor, A., et al. (2017a). Looks Do Matter! Aortic Arch Shape After Hypoplastic Left Heart Syndrome Palliation Correlates With Cavopulmonary Outcomes. *Ann. Thorac. Surg.* *103*, 645–654.

Bruse, J.L., Khushnood, A., McLeod, K., Biglino, G., Sermesant, M., Pennec, X., Taylor, A.M., Hsia, T.-Y., Schievano, S., Taylor, A.M., et al. (2017b). How successful is successful? Aortic arch shape after successful aortic coarctation repair correlates with left ventricular function. *J. Thorac. Cardiovasc. Surg.* *153*, 418–427.

Bruse, J.L., Zuluaga, M., Khushnood, A., McLeod, K., Ntsinjana, H., Hsia, T.Y., Sermesant, M., Pennec, X., Taylor, A., and Schievano, S. (2017c). Detecting Clinically Meaningful Shape Clusters in Medical Image Data: Metrics Analysis for Hierarchical Clustering applied to Healthy and Pathological Aortic Arches. *IEEE Trans. Biomed. Eng.* e-pub ahead of print.

Bruse, J.L., Giusti, G., Baker, C., Cervi, E., Hsia, T.-Y., Taylor, A.M., and Schievano, S. (2017d). Statistical Shape Modeling for Cavopulmonary Assist Device Development: Variability of Vascular Graft Geometry and Implications for Hemodynamics. *J. Med. Devices.* e-pub ahead of print.

Caballero, A.D., and Laín, S. (2013). A Review on Computational Fluid Dynamics Modelling in Human Thoracic Aorta. *Cardiovasc. Eng. Technol.* *4*, 103–130.

Canniffe, C., Ou, P., Walsh, K., Bonnet, D., and Celermajer, D. (2013). Hypertension after repair of aortic coarctation — A systematic review. *Int. J. Cardiol.* *167*, 2456–2461.

Capelli, C., Bosi, G.M., Cerri, E., Nordmeyer, J., Odenwald, T., Bonhoeffer, P., Migliavacca, F., Taylor, A.M., and Schievano, S. (2012). Patient-specific simulations of transcatheter aortic valve stent implantation. *Med. Biol. Eng. Comput.* *50*, 183–192.

Casciaro, M.E., Craiem, D., Chironi, G., Graf, S., Macron, L., Mousseaux, E., Simon, A., and Armentano, R.L. (2014). Identifying the principal modes of variation in human thoracic aorta morphology. *J. Thorac. Imaging* *29*, 224–232.

Cerrolaza, J.J., Reyes, M., Summers, R.M., González-Ballester, M.Á., and Linguraru, M.G. (2015). Automatic multi-resolution shape modeling of multi-organ structures. *Med. Image Anal.* *25*, 11–21.

Chiu, P., Lee, H.P., Venkatesh, S.K., and Ho, P. (2013). Anatomical characteristics of the thoracic aortic arch in an Asian population. *Asian Cardiovasc. Thorac. Ann.* *21*, 151–159.

Cohen, M., Fuster, V., Steele, P.M., Driscoll, D., and McGoon, D.C. (1989). Coarctation of the aorta. Long-term follow-up and prediction of outcome after surgical correction. *Circulation* *80*, 840–845.

Collins, F.S., and Varmus, H. (2015). A New Initiative on Precision Medicine. *N. Engl. J. Med.* *372*, 793–795.

Coogan, J.S., Chan, F.P., LaDisa Jr., J.F., Taylor, C.A., Hanley, F.L., and Feinstein, J.A. (2013). Computational fluid dynamic simulations for determination of ventricular workload in aortic arch obstructions. *J. Thorac. Cardiovasc. Surg.* *145*, 489–495.e1.

Cook, A.C. (2001). The spectrum of fetal cardiac malformations. *Cardiol. Young* *11*, 97–110.

Cootes, T., Hill, A., Taylor, C., and Haslam, J. (1994). Use of active shape models for locating structures in medical images. *Image Vis. Comput.* *12*, 355–365.

Cordes, D., Haughton, V., Carew, J.D., Arfanakis, K., and Maravilla, K. (2002). Hierarchical clustering to measure connectivity in fMRI resting-state data. *Magn. Reson. Imaging* *20*, 305–317.

Craiem, D., Chironi, G., Redheuil, A., Casciaro, M., Mousseaux, E., Simon, A., and Armentano, R.L. (2012a). Aging Impact on Thoracic Aorta 3D Morphometry in Intermediate-Risk Subjects: Looking Beyond Coronary Arteries with Non-Contrast Cardiac CT. *Ann. Biomed. Eng.* *40*, 1028–1038.

Craiem, D., Casciaro, M.E., Graf, S., Chironi, G., Simon, A., and Armentano, R.L. (2012b). Effects of aging on thoracic aorta size and shape: A non-contrast CT study. In 2012 Annual International Conference of the IEEE Engineering in Medicine and Biology Society (EMBC), pp. 4986–4989.

Crepaz, R., Cemin, R., Romeo, C., Bonsante, E., Gentili, L., Trevisan, D., Pitscheider, W., and Stellin, G. (2005). Factors affecting left ventricular remodelling and mechanics in the long-term follow-up after successful repair of aortic coarctation. *Cardiol. Young* *15*, 160–167.

Cuspidi, C., Vaccarella, A., Negri, F., and Sala, C. (2010). Resistant hypertension and left ventricular hypertrophy: an overview. *J. Am. Soc. Hypertens.* *4*, 319–324.

Dall'Asta, A., Schievano, S., Bruse, J.L., Paramasivam, G., Kaihura, C.T., Dunaway, D., and Lees, C.C. (2017). Quantitative analysis of fetal facial morphology using 3D ultrasound and statistical shape modelling: a feasibility study. *Am. J. Obstet. Gynecol.* e-pub ahead of print.

- Dalton, L., Ballarin, V., and Brun, M. (2009). Clustering Algorithms: On Learning, Validation, Performance, and Applications to Genomics. *Curr. Genomics* 10, 430–445.
- Dasi, L.P., Pekkan, K., Katajima, H.D., and Yoganathan, A.P. (2008). Functional analysis of Fontan energy dissipation. *J. Biomech.* 41, 2246–2252.
- Daszykowski, M., Kaczmarek, K., Vander Heyden, Y., and Walczak, B. (2007). Robust statistics in data analysis — A review: Basic concepts. *Chemom. Intell. Lab. Syst.* 85, 203–219.
- Dawes, T.J.W., Marvao, A. de, Shi, W., Fletcher, T., Watson, G.M.J., Wharton, J., Rhodes, C.J., Howard, L.S.G.E., Gibbs, J.S.R., Rueckert, D., et al. (2017). Machine Learning of Three-dimensional Right Ventricular Motion Enables Outcome Prediction in Pulmonary Hypertension: A Cardiac MR Imaging Study. *Radiology*. e-pub ahead of print.
- De Caro, E., Trocchio, G., Smeraldi, A., Calevo, M.G., and Pongiglione, G. (2007). Aortic Arch Geometry and Exercise-Induced Hypertension in Aortic Coarctation. *Am. J. Cardiol.* 99, 1284–1287.
- De Maesschalck, R., Jouan-Rimbaud, D., and Massart, D.L. (2000). The Mahalanobis distance. *Chemom. Intell. Lab. Syst.* 50, 1–18.
- Demertzis, S., Hurni, S., Stalder, M., Gahl, B., Herrmann, G., and Van den Berg, J. (2010). Aortic arch morphometry in living humans. *J. Anat.* 217, 588–596.
- Donazzan, L., Crepaz, R., Stuefer, J., and Stellin, G. (2014). Abnormalities of Aortic Arch Shape, Central Aortic Flow Dynamics, and Distensibility Predispose to Hypertension After Successful Repair of Aortic Coarctation. *World J. Pediatr. Congenit. Heart Surg.* 5, 546–553.
- Dong, A., Honnorat, N., Gaonkar, B., and Davatzikos, C. (2016). CHIMERA: Clustering of Heterogeneous Disease Effects via Distribution Matching of Imaging Patterns. *IEEE Trans. Med. Imaging* 35, 612–621.
- Dougherty, E.R., Barrera, J., Brun, M., Kim, S., Cesar, R.M., Chen, Y., Bittner, M., and Trent, J.M. (2002). Inference from clustering with application to gene-expression microarrays. *J. Comput. Biol. J. Comput. Mol. Cell Biol.* 9, 105–126.
- Dubes, R., and Jain, A.K. (1976). Clustering techniques: The user's dilemma. *Pattern Recognit.* 8, 247–260.
- Durrleman, S. (2010). Statistical models of currents for measuring the variability of anatomical curves, surfaces and their evolution. University of Nice-Sophia Antipolis. PhD Thesis
- Durrleman, S. (2014). *Deformetrica User's Manual*. [http://www.deformetrica.org/?page\\_id=108](http://www.deformetrica.org/?page_id=108) accessed 06.11.2014, 19:18.

Durrleman, S., Pennec, X., Trouvé, A., and Ayache, N. (2007). Measuring brain variability via sulcal lines registration: a diffeomorphic approach. *Med. Image Comput. Comput.-Assist. Interv. MICCAI Int. Conf. Med. Image Comput. Comput.-Assist. Interv.* *10*, 675–682.

Durrleman, S., Pennec, X., Trouvé, A., and Ayache, N. (2009). Statistical models of sets of curves and surfaces based on currents. *Med. Image Anal.* *13*, 793–808.

Durrleman, S., Prastawa, M., Charon, N., Korenberg, J.R., Joshi, S., Gerig, G., and Trouvé, A. (2014). Morphometry of anatomical shape complexes with dense deformations and sparse parameters. *NeuroImage* *101*, 35–49.

Eisen, M.B., Spellman, P.T., Brown, P.O., and Botstein, D. (1998). Cluster analysis and display of genome-wide expression patterns. *Proc. Natl. Acad. Sci. U. S. A.* *95*, 14863–14868.

Elfadaly, F.G., Garthwaite, P.H., and Crawford, J.R. (2016). On point estimation of the abnormality of a Mahalanobis index. *Comput. Stat. Data Anal.* *99*, 115–130.

Farrar, G., Suinesiaputra, A., Gilbert, K., Perry, J.C., Hegde, S., Marsden, A., Young, A.A., Omens, J.H., and McCulloch, A.D. (2016). Atlas-based ventricular shape analysis for understanding congenital heart disease. *Prog. Pediatr. Cardiol.* *43*, 61–69.

Feinstein, J.A., Benson, D.W., Dubin, A.M., Cohen, M.S., Maxey, D.M., Mahle, W.T., Pahl, E., Villafañe, J., Bhatt, A.B., Peng, L.F., et al. (2012). Hypoplastic Left Heart Syndrome: Current Considerations and Expectations. *J. Am. Coll. Cardiol.* *59*, S1–S42.

Filzmoser, P., Baumgartner, R., and Moser, E. (1999). A hierarchical clustering method for analyzing functional MR images. *Magn. Reson. Imaging* *17*, 817–826.

Fonseca, C.G., Backhaus, M., Bluemke, D.A., Britten, R.D., Chung, J.D., Cowan, B.R., Dinov, I.D., Finn, J.P., Hunter, P.J., Kadish, A.H., et al. (2011). The Cardiac Atlas Project—an imaging database for computational modeling and statistical atlases of the heart. *Bioinforma. Oxf. Engl.* *27*, 2288–2295.

Frangi, A.F., Taylor, Z.A., and Gooya, A. (2016). Precision Imaging: more descriptive, predictive and integrative imaging. *Med. Image Anal.* *33*, 27–32.

Fratz, S., Chung, T., Greil, G.F., Samyn, M.M., Taylor, A.M., Buechel, E.R.V., Yoo, S.-J., and Powell, A.J. (2013). Guidelines and protocols for cardiovascular magnetic resonance in children and adults with congenital heart disease: SCMR expert consensus group on congenital heart disease. *J. Cardiovasc. Magn. Reson.* *15*, 51.

Frydrychowicz, A., Markl, M., Hirtler, D., Harloff, A., Schlensak, C., Geiger, J., Stiller, B., and Arnold, R. (2011). Aortic Hemodynamics in Patients With and Without Repair of Aortic Coarctation: In Vivo Analysis by 4D Flow-Sensitive Magnetic Resonance Imaging. *Investig. Radiol.* May 2011 *46*, 317–325.

Gardin, J.M., and Lauer, M.S. (2004). Left Ventricular Hypertrophy: The Next Treatable, Silent Killer? *JAMA* 292, 2396–2398.

Garreffa, G., Ken, S., Macrì, M.A., Giulietti, G., Giove, F., Colonnese, C., Venditti, E., De Cesare, E., Galasso, V., and Maraviglia, B. (2006). BOLD signal and vessel dynamics: a hierarchical cluster analysis. *Magn. Reson. Imaging* 24, 411–418.

Go, A.S., Mozaffarian, D., Roger, V.L., Benjamin, E.J., Berry, J.D., Borden, W.B., Bravata, D.M., Dai, S., Ford, E.S., Fox, C.S., et al. (2013). AHA Statistical Update. *Circulation* 127, e6–e245.

Goubergrits, L., Riesenkampff, E., Yevtushenko, P., Schaller, J., Kertzscher, U., Berger, F., and Kuehne, T. (2014). Is MRI-Based CFD Able to Improve Clinical Treatment of Coarctations of Aorta? *Ann. Biomed. Eng.* 43, 168–176.

Goubergrits, L., Riesenkampff, E., Yevtushenko, P., Schaller, J., Kertzscher, U., Hennemuth, A., Berger, F., Schubert, S., and Kuehne, T. (2015). MRI-based computational fluid dynamics for diagnosis and treatment prediction: Clinical validation study in patients with coarctation of aorta. *J. Magn. Reson. Imaging* 41, 909–916.

Grimshaw, G.M., and Thompson, J.M. (1995). The abnormal aorta: A statistical definition and strategy for monitoring change. *Eur. J. Vasc. Endovasc. Surg.* 10, 95–100.

Groppe, D.M., Urbach, T.P., and Kutas, M. (2011). Mass univariate analysis of event-related brain potentials/fields I: A critical tutorial review. *Psychophysiology* 48, 1711–1725.

Guibert, R., McLeod, K., Caiazzo, A., Mansi, T., Fernández, M.A., Sermesant, M., Pennec, X., Vignon-Clementel, I.E., Boudjemline, Y., and Gerbeau, J.-F. (2014). Group-wise construction of reduced models for understanding and characterization of pulmonary blood flows from medical images. *Med. Image Anal.* 18, 63–82.

Gunther, S., and Grossman, W. (1979). Determinants of ventricular function in pressure-overload hypertrophy in man. *Circulation* 59, 679–688.

Hager, A., Kanz, S., Kaemmerer, H., Schreiber, C., and Hess, J. (2007). Coarctation Long-term Assessment (COALA): Significance of arterial hypertension in a cohort of 404 patients up to 27 years after surgical repair of isolated coarctation of the aorta, even in the absence of restenosis and prosthetic material. *J. Thorac. Cardiovasc. Surg.* 134, 738–745.e2.

Haggerty, C.M., Restrepo, M., Tang, E., de Zélicourt, D.A., Sundareswaran, K.S., Mirabella, L., Bethel, J., Whitehead, K.K., Fogel, M.A., and Yoganathan, A.P. (2014). Fontan hemodynamics from 100 patient-specific cardiac magnetic resonance studies: A computational fluid dynamics analysis. *J. Thorac. Cardiovasc. Surg.* 148, 1481–1489.

- Halkidi, M., Batistakis, Y., and Vazirgiannis, M. (2001). On Clustering Validation Techniques. *J. Intell. Inf. Syst.* *17*, 107–145.
- Hastie, T., Tibshirani, R., and Friedman, J. (2009). *The Elements of Statistical Learning* (New York, NY: Springer New York).
- Hauser, M. (2003). Exercise blood pressure in congenital heart disease and in patients after coarctation repair. *Heart* *89*, 125–126.
- Hauser, M., Kuehn, A., and Wilson, N. (2000). Abnormal responses for blood pressure in children and adults with surgically corrected aortic coarctation. *Cardiol. Young* *10*, 353–357.
- Haycock, G.B., Schwartz, G.J., and Wisotsky, D.H. (1978). Geometric method for measuring body surface area: A height-weight formula validated in infants, children, and adults. *J. Pediatr.* *93*, 62–66.
- Heimann, T., and Meinzer, H.-P. (2009). Statistical shape models for 3D medical image segmentation: A review. *Med. Image Anal.* *13*, 543–563.
- Hsia, T.-Y., Migliavacca, F., Pittaccio, S., Radaelli, A., Dubini, G., Pennati, G., and de Leval, M. (2004). Computational fluid dynamic study of flow optimization in realistic models of the total cavopulmonary connections 1. *J. Surg. Res.* *116*, 305–313.
- Hsia, T.-Y., Cosentino, D., Corsini, C., Pennati, G., Dubini, G., and Migliavacca, F. (2011). Use of Mathematical Modeling to Compare and Predict Hemodynamic Effects Between Hybrid and Surgical Norwood Palliations for Hypoplastic Left Heart Syndrome. *Circulation* *124*, S204–S210.
- Hughes, M.L., Tsang, V.T., Kostolny, M., Giardini, A., Muthurangu, V., Taylor, A.M., and Brown, K. (2011). Lessons from inter-stage cardiac magnetic resonance imaging in predicting survival for patients with hypoplastic left heart syndrome. *Cardiol. Young* *21*, 646–653.
- Huysmans, T., Sijbers, J., and Verdonk, B. (2010). Automatic Construction of Correspondences for Tubular Surfaces. *IEEE Trans. Pattern Anal. Mach. Intell.* *32*, 636–651.
- Izenman, A. J. (2008). *Modern Multivariate Statistical Techniques - Regression, Classification, and Manifold Learning* (Springer Science+Business Media LLC).
- Jain, A.K. (2010). Data clustering: 50 years beyond K-means. *Pattern Recognit. Lett.* *31*, 651–666.
- Johnston, B.M., Johnston, P.R., Corney, S., and Kilpatrick, D. (2004). Non-Newtonian blood flow in human right coronary arteries: steady state simulations. *J. Biomech.* *37*, 709–720.

Jolliffe, I.T. (2002). *Principal Component Analysis* (Springer-Verlag New York, Inc.).

Kang, J.-W., Song, H.G., Yang, D.H., Baek, S., Kim, D.-H., Song, J.-M., Kang, D.-H., Lim, T.-H., and Song, J.-K. (2013). Association Between Bicuspid Aortic Valve Phenotype and Patterns of Valvular Dysfunction and Bicuspid Aortopathy: Comprehensive Evaluation Using MDCT and Echocardiography. *JACC Cardiovasc. Imaging* 6, 150–161.

Kass, M., Witkin, A., and Terzopoulos, D. (1988). Snakes: Active contour models. *Int. J. Comput. Vis.* 1, 321–331.

Katz, A.M. (1990). Cardiomyopathy of Overload. *N. Engl. J. Med.* 322, 100–110.

Kim, H.J., Vignon-Clementel, I.E., Figueroa, C.A., LaDisa, J.F., Jansen, K.E., Feinstein, J.A., and Taylor, C.A. (2009). On Coupling a Lumped Parameter Heart Model and a Three-Dimensional Finite Element Aorta Model. *Ann. Biomed. Eng.* 37, 2153–2169.

Knauth, A.L., Gauvreau, K., Powell, A.J., Landzberg, M.J., Walsh, E.P., Lock, J.E., Nido, P.J. del, and Geva, T. (2008). Ventricular size and function assessed by cardiac MRI predict major adverse clinical outcomes late after tetralogy of Fallot repair. *Heart* 94, 211–216.

Kowalik, G.T., Steeden, J.A., Pandya, B., Odille, F., Atkinson, D., Taylor, A., and Muthurangu, V. (2012). Real-time flow with fast GPU reconstruction for continuous assessment of cardiac output. *J. Magn. Reson. Imaging* 36, 1477–1482.

Krieger, E.V., Clair, M., Opatowsky, A.R., Landzberg, M.J., Rhodes, J., Powell, A.J., Colan, S.D., and Valente, A.M. (2013). Correlation of Exercise Response in Repaired Coarctation of the Aorta to Left Ventricular Mass and Geometry. *Am. J. Cardiol.* 111, 406–411.

Kutra, D., Saalbach, A., Lehmann, H., Groth, A., Dries, S.P.M., Krueger, M.W., Dössel, O., and Weese, J. (2012). Automatic Multi-model-Based Segmentation of the Left Atrium in Cardiac MRI Scans. In *Medical Image Computing and Computer-Assisted Intervention – MICCAI 2012*, N. Ayache, H. Delingette, P. Golland, and K. Mori, eds. (Springer Berlin Heidelberg), pp. 1–8.

LaDisa, J.F., Alberto Figueroa, C., Vignon-Clementel, I.E., Jin Kim, H., Xiao, N., Ellwein, L.M., Chan, F.P., Feinstein, J.A., and Taylor, C.A. (2011a). Computational Simulations for Aortic Coarctation: Representative Results From a Sampling of Patients. *J. Biomech. Eng.* 133, 091008-091008-9.

LaDisa, J.F., Dholakia, R.J., Figueroa, C.A., Vignon-Clementel, I.E., Chan, F.P., Samyn, M.M., Cava, J.R., Taylor, C.A., and Feinstein, J.A. (2011b). Computational simulations demonstrate altered wall shear stress in aortic coarctation patients treated by resection with end-to-end anastomosis. *Congenit. Heart Dis.* 6, 432–443.

Lamata, P., Lazdam, M., Ashcroft, A., Lewandowski, A.J., Leeson, P., and Smith, N. (2013). Computational mesh as a descriptor of left ventricular shape for clinical diagnosis. In *Computing in Cardiology Conference (CinC)*, 2013, pp. 571–574.

Lamata, P., Casero, R., Carapella, V., Niederer, S.A., Bishop, M.J., Schneider, J.E., Kohl, P., and Grau, V. (2014). Images as drivers of progress in cardiac computational modelling. *Prog. Biophys. Mol. Biol.* *115*, 198–212.

Lance, G.N., and Williams, W.T. (1967). A General Theory of Classificatory Sorting Strategies 1. Hierarchical Systems. *Comput. J.* *9*, 373–380.

Lecheler, S. (2014). *Numerische Strömungsberechnung* (Wiesbaden: Springer Fachmedien Wiesbaden).

Lecompte, Y., Zannini, L., Hazan, E., Jarreau, M.M., Bex, J.P., Tu, T.V., and Neveux, J.Y. (1981). Anatomic correction of transposition of the great arteries. *J. Thorac. Cardiovasc. Surg.* *82*, 629–631.

Lee, M.G.Y., Kowalski, R., Galati, J.C., Cheung, M.M.H., Jones, B., Koleff, J., and d'Udekem, Y. (2012). Twenty-four-hour ambulatory blood pressure monitoring detects a high prevalence of hypertension late after coarctation repair in patients with hypoplastic arches. *J. Thorac. Cardiovasc. Surg.* *144*, 1110–1118.

Levy, D., Garrison, R.J., Savage, D.D., Kannel, W.B., and Castelli, W.P. (1990). Prognostic Implications of Echocardiographically Determined Left Ventricular Mass in the Framingham Heart Study. *N. Engl. J. Med.* *322*, 1561–1566.

Lewandowski, A.J., Augustine, D., Lamata, P., Davis, E.F., Lazdam, M., Francis, J., McCormick, K., Wilkinson, A.R., Singhal, A., Lucas, A., et al. (2013). Preterm Heart in Adult Life Cardiovascular Magnetic Resonance Reveals Distinct Differences in Left Ventricular Mass, Geometry, and Function. *Circulation* *127*, 197–206.

Liu, X., Pu, F., Fan, Y., Deng, X., Li, D., and Li, S. (2009). A numerical study on the flow of blood and the transport of LDL in the human aorta: the physiological significance of the helical flow in the aortic arch. *Am. J. Physiol. - Heart Circ. Physiol.* *297*, H163–H170.

Liu, Y., Pekkan, K., Jones, S.C., and Yoganathan, A.P. (2004). The Effects of Different Mesh Generation Methods on Computational Fluid Dynamic Analysis and Power Loss Assessment in Total Cavopulmonary Connection. *J. Biomech. Eng.* *126*, 594–603.

Lombardi, K.C., Northrup, V., McNamara, R.L., Sugeng, L., and Weismann, C.G. (2013). Aortic Stiffness and Left Ventricular Diastolic Function in Children Following Early Repair of Aortic Coarctation. *Am. J. Cardiol.* *112*, 1828–1833.

Lorell, B.H., and Carabello, B.A. (2000). Left Ventricular Hypertrophy. *Circulation* *102*, 470–479.

Lorenz, C., and Berg, J. von (2006). A comprehensive shape model of the heart. *Med. Image Anal.* *10*, 657–670.

Maceira, A.M., and Mohiaddin, R.H. (2012). Cardiovascular magnetic resonance in systemic hypertension. *J. Cardiovasc. Magn. Reson.* *14*, 28.

MacLeod, R.S., Stinstra, J.G., Lew, S., Whitaker, R.T., Swenson, D.J., Cole, M.J., Krüger, J., Brooks, D.H., and Johnson, C.R. (2009). Subject-specific, multiscale simulation of electrophysiology: a software pipeline for image-based models and application examples. *Philos. Trans. R. Soc. Math. Phys. Eng. Sci.* *367*, 2293–2310.

Mansi, T. (2010). Modèles physiologiques et statistiques du cœur guidés par imagerie médicale : application à la tétralogie de Fallot. École Nationale Supérieure des Mines de Paris. PhD Thesis.

Mansi, T., Durrleman, S., Bernhardt, B., Sermesant, M., Delingette, H., Voigt, I., Lurz, P., Taylor, A.M., Blanc, J., Boudjemline, Y., et al. (2009). A Statistical Model of Right Ventricle in Tetralogy of Fallot for Prediction of Remodelling and Therapy Planning. In *Medical Image Computing and Computer-Assisted Intervention – MICCAI 2009*, G.-Z. Yang, D. Hawkes, D. Rueckert, A. Noble, and C. Taylor, eds. (Springer Berlin Heidelberg), pp. 214–221.

Mansi, T., Voigt, I., Leonardi, B., Pennec, X., Durrleman, S., Sermesant, M., Delingette, H., Taylor, A.M., Boudjemline, Y., Pongiglione, G., et al. (2011). A Statistical Model for Quantification and Prediction of Cardiac Remodelling: Application to Tetralogy of Fallot. *IEEE Trans. Med. Imaging* *30*, 1605–1616.

Marelli, A.J., Mackie, A.S., Ionescu-Ittu, R., Rahme, E., and Pilote, L. (2007). Congenital Heart Disease in the General Population Changing Prevalence and Age Distribution. *Circulation* *115*, 163–172.

Markl, M., Schnell, S., and Barker, A.J. (2014). 4D Flow Imaging: Current Status to Future Clinical Applications. *Curr. Cardiol. Rep.* *16*, 1–9.

McGregor, R., Szczerba, D., Siebenthal, M. von, Muralidhar, K., and Székely, G. (2008). Exploring the Use of Proper Orthogonal Decomposition for Enhancing Blood Flow Images Via Computational Fluid Dynamics. In *Medical Image Computing and Computer-Assisted Intervention – MICCAI 2008*, D. Metaxas, L. Axel, G. Fichtinger, and G. Székely, eds. (Springer Berlin Heidelberg), pp. 782–789.

McLeod, K., Mansi, T., Sermesant, M., Pongiglione, G., and Pennec, X. (2013). Statistical Shape Analysis of Surfaces in Medical Images Applied to the Tetralogy of Fallot Heart. In *Modeling in Computational Biology and Biomedicine*, F. Cazals, and P. Kornprobst, eds. (Berlin, Heidelberg: Springer Berlin Heidelberg), pp. 165–191.

Medrano-Gracia, P., Cowan, B.R., Bluemke, D.A., Finn, J.P., Lima, J.A.C., Suinesiaputra, A., and Young, A.A. (2013). Large Scale Left Ventricular Shape Atlas Using Automated Model Fitting to Contours. In *Functional Imaging and Modeling of the Heart*, S. Ourselin, D. Rueckert, and N. Smith, eds. (Springer Berlin Heidelberg), pp. 433–441.

Medrano-Gracia, P., Ormiston, J., Webster, M., Beier, S., Ellis, C., Wang, C., Young, A.A., and Cowan, B.R. (2014). Construction of a Coronary Artery Atlas from CT Angiography. In *Medical Image Computing and Computer-Assisted Intervention – MICCAI 2014*, (Springer International Publishing), pp. 513–520.

Medrano-Gracia, P., Cowan, B.R., Suinesiaputra, A., and Young, A.A. (2015). Challenges of Cardiac Image Analysis in Large-Scale Population-Based Studies. *Curr. Cardiol. Rep.* *17*, 1–7.

Mitchell, S.C., Korones, S.B., and Berendes, H.W. (1971). Congenital Heart Disease in 56,109 Births Incidence and Natural History. *Circulation* *43*, 323–332.

Moeller, T. (2013). *Pocket Atlas of Sectional Anatomy, Volume II: Thorax, Heart, Abdomen and Pelvis: 2* (Stuttgart ; New York: Thieme Medical Publishers).

Murtagh, F. (1983). A Survey of Recent Advances in Hierarchical Clustering Algorithms. *Comput. J.* *26*, 354–359.

Murtagh, F., and Contreras, P. (2012). Algorithms for hierarchical clustering: an overview. *Wiley Interdiscip. Rev. Data Min. Knowl. Discov.* *2*, 86–97.

Nielsen, J.C., Powell, A.J., Gauvreau, K., Marcus, E.N., Prakash, A., and Geva, T. (2005). Magnetic Resonance Imaging Predictors of Coarctation Severity. *Circulation* *111*, 622–628.

Ntsinjana, H.N., Tann, O., and Taylor, A.M. (2013a). Trends in pediatric cardiovascular magnetic resonance imaging. *Acta Radiol.* *54*, 1063–1074.

Ntsinjana, H.N., Biglino, G., Capelli, C., Tann, O., Giardini, A., Derrick, G., Schievano, S., and Taylor, A.M. (2013b). Aortic arch shape is not associated with hypertensive response to exercise in patients with repaired congenital heart diseases. *J. Cardiovasc. Magn. Reson. Off. J. Soc. Cardiovasc. Magn. Reson.* *15*, 101.

Ntsinjana, H.N., Capelli, C., Biglino, G., Cook, A.C., Tann, O., Derrick, G., Taylor, A.M., and Schievano, S. (2014). 3D morphometric analysis of the arterial switch operation using in vivo MRI data. *Clin. Anat.* n/a-n/a.

Olivieri, L.J., de Zelicourt, D.A., Haggerty, C.M., Ratnayaka, K., Cross, R.R., and Yoganathan, A.P. (2011). Hemodynamic Modeling of Surgically Repaired Coarctation of the Aorta. *Cardiovasc. Eng. Technol.* *2*, 288–295.

Ong, C.M., Canter, C.E., Gutierrez, F.R., Sekarski, D.R., and Goldring, D.R. (1992). Increased stiffness and persistent narrowing of the aorta after successful repair of coarctation of the aorta: Relationship to left ventricular mass and blood pressure at rest and with exercise. *Am. Heart J.* *123*, 1594–1600.

O’Sullivan, J. (2014). Late Hypertension in Patients with Repaired Aortic Coarctation. *Curr. Hypertens. Rep.* *16*, 1–6.

Ou, P., Bonnet, D., Auriacombe, L., Pedroni, E., Balleux, F., Sidi, D., and Mousseaux, E. (2004). Late systemic hypertension and aortic arch geometry after successful repair of coarctation of the aorta. *Eur. Heart J.* *25*, 1853–1859.

Ou, P., Mousseaux, E., Celermajer, D.S., Pedroni, E., Vouhe, P., Sidi, D., and Bonnet, D. (2006). Aortic arch shape deformation after coarctation surgery: Effect on blood pressure response. *J. Thorac. Cardiovasc. Surg.* *132*, 1105–1111.

Ou, P., Celermajer, D.S., Mousseaux, E., Giron, A., Aggoun, Y., Szezepanski, I., Sidi, D., and Bonnet, D. (2007). Vascular Remodeling After “Successful” Repair of Coarctation: Impact of Aortic Arch Geometry. *J. Am. Coll. Cardiol.* *49*, 883–890.

Ou, P., Celermajer, D.S., Raisky, O., Jolivet, O., Buyens, F., Herment, A., Sidi, D., Bonnet, D., and Mousseaux, E. (2008a). Angular (Gothic) aortic arch leads to enhanced systolic wave reflection, central aortic stiffness, and increased left ventricular mass late after aortic coarctation repair: Evaluation with magnetic resonance flow mapping. *J. Thorac. Cardiovasc. Surg.* *135*, 62–68.

Ou, P., Celermajer, D.S., Jolivet, O., Buyens, F., Herment, A., Sidi, D., Bonnet, D., and Mousseaux, E. (2008b). Increased central aortic stiffness and left ventricular mass in normotensive young subjects after successful coarctation repair. *Am. Heart J.* *155*, 187–193.

Oxford University Press (2014). Oxford Dictionary (Online Version - accessed: 30/10/2014 - 14:00).

Petitjean, C., Zuluaga, M.A., Bai, W., Dacher, J.-N., Grosgeorge, D., Caudron, J., Ruan, S., Ayed, I.B., Cardoso, M.J., Chen, H.-C., et al. (2015). Right ventricle segmentation from cardiac MRI: A collation study. *Med. Image Anal.* *19*, 187–202.

Piccinelli, M., Veneziani, A., Steinman, D.A., Remuzzi, A., and Antiga, L. (2009). A framework for geometric analysis of vascular structures: application to cerebral aneurysms. *IEEE Trans. Med. Imaging* *28*, 1141–1155.

Powers D.M.W. (2011). Evaluation: From Precision, Recall and F-Measure to ROC, Informedness, Markedness & Correlation. *J. Mach. Learn. Technol.*

Presbitero, P., Demarie, D., Villani, M., Perinetto, E.A., Riva, G., Orzan, F., Bobbio, M., Morea, M., and Brusca, A. (1987). Long term results (15-30 years) of surgical repair of aortic coarctation. *Br. Heart J.* *57*, 462–467.

Puranik, R., Tsang, V.T., Puranik, S., Jones, R., Cullen, S., Bonhoeffer, P., Hughes, M.L., and Taylor, A.M. (2009). Late magnetic resonance surveillance of repaired coarctation of the aorta. *Eur. J. Cardiothorac. Surg.* *36*, 91–95.

Quail, M.A., and Taylor, A.M. (2013). Computer Modeling to Tailor Therapy for Congenital Heart Disease. *Curr. Cardiol. Rep.* *15*, 1–7.

- Ralovich, K., Itu, L., Vitanovski, D., Sharma, P., Ionasec, R., Mihalef, V., Krawtschuk, W., Zheng, Y., Everett, A., Pongiglione, G., et al. (2015). Noninvasive hemodynamic assessment, treatment outcome prediction and follow-up of aortic coarctation from MR imaging. *Med. Phys.* *42*, 2143–2156.
- Razavi, R.S., Hill, D.L.G., Muthurangu, V., Miquel, M.E., Taylor, A.M., Kozerke, S., and Baker, E.J. (2003). Three-dimensional magnetic resonance imaging of congenital cardiac anomalies. *Cardiol. Young* *13*, 461–465.
- Richardson, J.E., Ash, J.S., Sittig, D.F., Bunce, A., Carpenter, J., Dykstra, R.H., Guappone, K., McCormack, J., McMullen, C.K., Shapiro, M., et al. (2010). Multiple Perspectives on the Meaning of Clinical Decision Support. *AMIA. Annu. Symp. Proc.* *2010*, 1427–1431.
- Robbers-Visser, D., Boersma, E., and Helbing, W.A. (2009). Normal biventricular function, volumes, and mass in children aged 8 to 17 years. *J. Magn. Reson. Imaging JMRI* *29*, 552–559.
- Rodriguez-Florez, N., Göktekin, Ö.K., Bruse, J.L., Borghi, A., Angullia, F., Knoop, P.G.M., Tenhagen, M., O'Hara, J.L., Koudstaal, M.J., Schievano, S., et al. (2017). Quantifying the effect of corrective surgery for trigonocephaly: A non-invasive, non-ionizing method using three-dimensional handheld scanning and statistical shape modelling. *J. Cranio-Maxillofac. Surg.* *45*, 387–394.
- Rosenthal, E. (2005). Coarctation of the aorta from fetus to adult: curable condition or life long disease process? *Heart* *91*, 1495–1502.
- Rowley, J. (2007). The wisdom hierarchy: representations of the DIKW hierarchy. *J. Inf. Sci.* *33*, 163–180.
- Rueckert, D., and Aljabar, P. (2010). Nonrigid Registration of Medical Images: Theory, Methods, and Applications [Applications Corner]. *IEEE Signal Process. Mag.* *27*, 113–119.
- Sarikouch, S., Peters, B., Gutberlet, M., Leismann, B., Kelter-Kloepping, A., Koerperich, H., Kuehne, T., and Beerbaum, P. (2010). Sex-Specific Pediatric Percentiles for Ventricular Size and Mass as Reference Values for Cardiac MRICLINICAL PERSPECTIVE. *Circ. Cardiovasc. Imaging* *3*, 65–76.
- Schecklmann, M., Lehner, A., Poepl, T.B., Kreuzer, P.M., Hajak, G., Landgrebe, M., and Langguth, B. (2012). Cluster analysis for identifying sub-types of tinnitus: A positron emission tomography and voxel-based morphometry study. *Brain Res.* *1485*, 3–9.
- Schievano, S., Coats, L., Migliavacca, F., Norman, W., Frigiola, A., Deanfield, J., Bonhoeffer, P., and Taylor, A.M. (2007a). Variations in right ventricular outflow tract morphology following repair of congenital heart disease: implications for percutaneous pulmonary valve implantation. *J. Cardiovasc. Magn. Reson. Off. J. Soc. Cardiovasc. Magn. Reson.* *9*, 687–695.

Schievano, S., Migliavacca, F., Coats, L., Khambadkone, S., Carminati, M., Wilson, N., Deanfield, J.E., Bonhoeffer, P., and Taylor, A.M. (2007b). Percutaneous Pulmonary Valve Implantation Based on Rapid Prototyping of Right Ventricular Outflow Tract and Pulmonary Trunk from MR Data. *Radiology* 242, 490–497.

Schievano, S., Taylor, A.M., Capelli, C., Lurz, P., Nordmeyer, J., Migliavacca, F., and Bonhoeffer, P. (2010). Patient specific finite element analysis results in more accurate prediction of stent fractures: Application to percutaneous pulmonary valve implantation. *J. Biomech.* 43, 687–693.

Schroeder, W., Martin, K., and Lorensen, B. (2006). *Visualization Toolkit: An Object-Oriented Approach to 3D Graphics*, 4th Edition (Clifton Park, N.Y.: Kitware).

Sermesant, M., Chabiniok, R., Chinchapatnam, P., Mansi, T., Billet, F., Moireau, P., Peyrat, J.M., Wong, K., Relan, J., Rhode, K., et al. (2012). Patient-specific electromechanical models of the heart for the prediction of pacing acute effects in CRT: A preliminary clinical validation. *Med. Image Anal.* 16, 201–215.

Singh, N.S.D., and Singh, D. (2012). Performance Evaluation of K-Means and Hierarchical Clustering in Terms of Accuracy and Running Time. *Int. J. Comput. Sci. Inf. Technol.* 3, 4119–4121.

Singh, N., Thomas Fletcher, P., Samuel Preston, J., King, R.D., Marron, J.S., Weiner, M.W., and Joshi, S. (2014). Quantifying anatomical shape variations in neurological disorders. *Med. Image Anal.* 18, 616–633.

Sluysmans, T., and Colan, S.D. (2005). Theoretical and empirical derivation of cardiovascular allometric relationships in children. *J. Appl. Physiol.* 99, 445–457.

Sokolova, M., and Lapalme, G. (2009). A systematic analysis of performance measures for classification tasks. *Inf. Process. Manag.* 45, 427–437.

Sørensen, T.S., Körperich, H., Greil, G.F., Eichhorn, J., Barth, P., Meyer, H., Pedersen, E.M., and Beerbaum, P. (2004). Operator-Independent Isotropic Three-Dimensional Magnetic Resonance Imaging for Morphology in Congenital Heart Disease. *Circulation* 110, 163–169.

Srivastava, A., Joshi, S.H., Mio, W., and Liu, X. (2005). Statistical shape analysis: clustering, learning, and testing. *IEEE Trans. Pattern Anal. Mach. Intell.* 27, 590–602.

Styner, M.A., Rajamani, K.T., Nolte, L.-P., Zsemlye, G., Székely, G., Taylor, C.J., and Davies, R.H. (2003). Evaluation of 3D Correspondence Methods for Model Building. In *Information Processing in Medical Imaging*, C. Taylor, and J.A. Noble, eds. (Springer Berlin Heidelberg), pp. 63–75.

Sugawara, J., Hayashi, K., Yokoi, T., and Tanaka, H. (2008). Age-Associated Elongation of the Ascending Aorta in Adults. *JACC Cardiovasc. Imaging* 1, 739–748.

- Szopos, M., Poussineau, N., Maday, Y., Canniffe, C., Celermajer, D.S., Bonnet, D., and Ou, P. (2014). Computational modeling of blood flow in the aorta—insights into eccentric dilatation of the ascending aorta after surgery for coarctation. *J. Thorac. Cardiovasc. Surg.* *148*, 1572–1582.
- Takx, R.A.P., Vliegenthart, R., Schoepf, U.J., Nance, J.W., Bamberg, F., Abro, J.A., Carr, C.M., Litwin, S.E., and Apfaltrer, P. (2017). Prognostic value of CT-derived left atrial and left ventricular measures in patients with acute chest pain. *Eur. J. Radiol.* *86*, 163–168.
- Tan, J.-L., Babu-Narayan, S.V., Henein, M.Y., Mullen, M., and Li, W. (2005). Doppler Echocardiographic Profile and Indexes in the Evaluation of Aortic Coarctation in Patients Before and After Stenting. *J. Am. Coll. Cardiol.* *46*, 1045–1053.
- Tavakoli, V., and Amini, A.A. (2013). A survey of shaped-based registration and segmentation techniques for cardiac images. *Comput. Vis. Image Underst.* *117*, 966–989.
- Taylor, C.A., and Figueroa, C.A. (2009). Patient-Specific Modeling of Cardiovascular Mechanics. *Annu. Rev. Biomed. Eng.* *11*, 109–134.
- Tenhagen, M., Bruse, J.L., Rodriguez-Florez, N., Angullia, F., Borghi, A., Koudstaal, M.J., Schievano, S., Jeelani, O., and Dunaway, D. (2016). Three-Dimensional Handheld Scanning to Quantify Head-Shape Changes in Spring-Assisted Surgery for Sagittal Craniosynostosis. *J. Craniofac. Surg.* *27*, 2117–2123.
- The Mathworks, Inc. (2016). MATLAB R2016 Help Documentation.
- Thompson, D.W. (1945). *On growth and form* (p. 1064: Cambridge : University Press ; New York : Macmillan).
- Vaillant, M., and Glaunès, J. (2005). Surface Matching via Currents. In *Information Processing in Medical Imaging*, G.E. Christensen, and M. Sonka, eds. (Springer Berlin Heidelberg), pp. 381–392.
- Vakili, B.A., Okin, P.M., and Devereux, R.B. (2001). Prognostic implications of left ventricular hypertrophy. *Am. Heart J.* *141*, 334–341.
- Verdecchia, P., Schillaci, G., Borgioni, C., Ciucci, A., Gattobigio, R., Zampi, I., Reboldi, G., and Porcellati, C. (1998). Prognostic Significance of Serial Changes in Left Ventricular Mass in Essential Hypertension. *Circulation* *97*, 48–54.
- Vergales, J.E., Gangemi, J.J., Rhueban, K.S., and Lim, D.S. (2013). Coarctation of the Aorta - The Current State of Surgical and Transcatheter Therapies. *Curr. Cardiol. Rev.* *9*, 211–219.
- Viceconti, M. (2015). Biomechanics-based in silico medicine: The manifesto of a new science. *J. Biomech.* *48*, 193–194.

Vignon-Clementel, I., Figueroa, C.A., Jansen, K.E., and Taylor, C.A. (2010a). Outflow boundary conditions for 3D simulations of non-periodic blood flow and pressure fields in deformable arteries. *Comput. Methods Biomech. Biomed. Engin.* *13*, 625–640.

Vignon-Clementel, I.E., Marsden, A.L., and Feinstein, J.A. (2010b). A primer on computational simulation in congenital heart disease for the clinician. *Prog. Pediatr. Cardiol.* *30*, 3–13.

Voges, I., Kees, J., Jerosch-Herold, M., Gottschalk, H., Trentmann, J., Hart, C., Gabbert, D.D., Pardun, E., Pham, M., Andrade, A.C., et al. (2016). Aortic stiffening and its impact on left atrial volumes and function in patients after successful coarctation repair: a multiparametric cardiovascular magnetic resonance study. *J. Cardiovasc. Magn. Reson. Off. J. Soc. Cardiovasc. Magn. Reson.* *18*, 56.

Völzke, H., Schmidt, C.O., Hegenscheid, K., Kühn, J.-P., Bamberg, F., Lieb, W., Kroemer, H.K., Hosten, N., and Puls, R. (2012). Population Imaging as Valuable Tool for Personalized Medicine. *Clin. Pharmacol. Ther.* *92*, 422–424.

Vriend, J.W.J., Zwinderman, A.H., Groot, E. de, Kastelein, J.J.P., Bouma, B.J., and Mulder, B.J.M. (2005). Predictive value of mild, residual descending aortic narrowing for blood pressure and vascular damage in patients after repair of aortic coarctation. *Eur. Heart J.* *26*, 84–90.

Warnes, C.A., Liberthson, R., Danielson Jr, G.K., Dore, A., Harris, L., Hoffman, J.I.E., Somerville, J., Williams, R.G., and Webb, G.D. (2001). Task Force 1: the changing profile of congenital heart disease in adult life. *J. Am. Coll. Cardiol.* *37*, 1170–1175.

Weber, H.S., Cyran, S.E., Grzeszczak, M., Myers, J.L., Gleason, M.M., and Baylen, B.G. (1993). Discrepancies in aortic growth explain aortic arch gradients during exercise. *J. Am. Coll. Cardiol.* *21*, 1002–1007.

Wolak, A., Gransar, H., Thomson, L.E.J., Friedman, J.D., Hachamovitch, R., Gutstein, A., Shaw, L.J., Polk, D., Wong, N.D., Saouaf, R., et al. (2008). Aortic Size Assessment by Noncontrast Cardiac Computed Tomography: Normal Limits by Age, Gender, and Body Surface Area. *JACC Cardiovasc. Imaging* *1*, 200–209.

Worz, S., von Tengg-Kobligk, H., Henninger, V., Rengier, F., Schumacher, H., Böckler, D., Kauczor, H.-U., and Rohr, K. (2010). 3-D Quantification of the Aortic Arch Morphology in 3-D CTA Data for Endovascular Aortic Repair. *IEEE Trans. Biomed. Eng.* *57*, 2359–2368.

Yeung, K.Y., and Ruzzo, W.L. (2001). Principal component analysis for clustering gene expression data. *Bioinformatics* *17*, 763–774.

Young, A.A., and Frangi, A.F. (2009). Computational cardiac atlases: from patient to population and back. *Exp. Physiol.* *94*, 578–596.

Yushkevich, P. (2016). ITK-SNAP Video Documentation,. <http://www.itksnap.org/Pmwiki/pmwiki.php?n=Videos.SNAP3> accessed 01 March 2017.

Yushkevich, P.A., Piven, J., Hazlett, H.C., Smith, R.G., Ho, S., Gee, J.C., and Gerig, G. (2006). User-guided 3D active contour segmentation of anatomical structures: Significantly improved efficiency and reliability. *NeuroImage* 31, 1116–1128.

Zacur, E., Wong, J., Razavi, R., Geva, T., Greil, G., and Lamata, P. (2015). Revealing Differences in Anatomical Remodelling of the Systemic Right Ventricle. In *Functional Imaging and Modeling of the Heart*, H. van Assen, P. Bovendeerd, and T. Delhaas, eds. (Springer International Publishing), pp. 99–107.

Zhao, F., Zhang, H., Wahle, A., Thomas, M.T., Stolpen, A.H., Scholz, T.D., and Sonka, M. (2009). Congenital Aortic Disease: 4D Magnetic Resonance Segmentation and Quantitative Analysis. *Med. Image Anal.* 13, 483–493.

Zhuang, X. (2013). Challenges and Methodologies of Fully Automatic Whole Heart Segmentation: A Review. *J. Healthc. Eng.* 4, 371–407.

Zuluaga, M.A., Cardoso, M.J., Modat, M., and Ourselin, S. (2013). Multi-atlas Propagation Whole Heart Segmentation from MRI and CTA Using a Local Normalised Correlation Coefficient Criterion. In *Functional Imaging and Modeling of the Heart*, S. Ourselin, D. Rueckert, and N. Smith, eds. (Springer Berlin Heidelberg), pp. 174–181.

Zuluaga, M.A., Burgos, N., Mendelson, A.F., Taylor, A.M., and Ourselin, S. (2015). Voxelwise atlas rating for computer assisted diagnosis: Application to congenital heart diseases of the great arteries. *Med. Image Anal.* 26, 185–194.

## 12 List of publications arising during this thesis

### 12.1 Peer reviewed journal articles directly related to this work

1. J. L. Bruse, M. A. Zuluaga, A. Khushnood, K. McLeod, H. N. Ntsinjana, T.-Y. Hsia, M. Sermesant, X. Pennec, A. M. Taylor, and S. Schievano. *Detecting Clinically Meaningful Shape Clusters in Medical Image Data: Metrics Analysis for Hierarchical Clustering Applied to Healthy and Pathological Aortic Arches*, IEEE Transactions on Biomedical Engineering, e-pub ahead of print, Jan. 2017
2. J. L. Bruse, G. Giusti, C. Baker, E. Cervi, T.-Y. Hsia, A. M. Taylor, and S. Schievano. *Statistical Shape Modeling for Cavopulmonary Assist Device Development: Variability of Vascular Graft Geometry and Implications for Hemodynamics*, Journal of Medical Devices, e-pub ahead of print, Jan. 2017
3. G. Biglino, C. Capelli, J. L. Bruse, G. Bosi, A. M. Taylor, and S. Schievano. *Computational modeling for congenital heart disease: How far are we from clinical translation?*, Heart, vol. 103, no. 2, pp. 98-103, Jan. 2017
4. J. L. Bruse, A. Khushnood, K. McLeod, G. Biglino, M. Sermesant, X. Pennec, A. M. Taylor, T.-Y. Hsia, and S. Schievano. *How successful is successful? Aortic arch shape following successful aortic coarctation repair correlates with left ventricular function*, The Journal of Thoracic and Cardiovascular Surgery, vol. 153, no. 2, pp. 418-427, Feb. 2017
5. J. L. Bruse, E. Cervi, K. McLeod, G. Biglino, M. Sermesant, X. Pennec, A. M. Taylor, S. Schievano, and T.-Y. Hsia. *Looks do matter! Aortic arch shape after hypoplastic left heart syndrome palliation correlates with cavopulmonary outcomes*, The Annals of Thoracic Surgery, vol. 103, no. 2, pp. 645-654, Feb. 2017

6. J. L. Bruse, K. McLeod, G. Biglino, H. N. Ntsinjana, C. Capelli, T.-Y. Hsia, M. Sermesant, X. Pennec, A. M. Taylor, and S. Schievano. *A statistical shape modelling framework to extract 3D shape biomarkers from medical imaging data: assessing arch morphology of repaired coarctation of the aorta*, BMC Medical Imaging, vol. 16, no. 40, May 2016
7. J. L. Bruse, K. McLeod, G. Biglino, H. N. Ntsinjana, C. Capelli, T.-Y. Hsia, M. Sermesant, X. Pennec, A. M. Taylor, and S. Schievano. *A non-parametric statistical shape model for assessment of the surgically repaired aortic arch in coarctation of the aorta: How normal is abnormal?*, Proceedings of STACOM 2015, vol. 9534, Editors: Camara, Mansi, Pop, Rhode, Sermesant, Young, Jan. 2016

## **12.2 Peer reviewed journal articles not directly related to this work**

1. B. Biffi, J. L. Bruse, M. A. Zuluaga, H. N. Ntsinjana, A. M. Taylor, and S. Schievano. *Investigating Cardiac Motion Patterns using Synthetic High Resolution 3D Cardiovascular Magnetic Resonance images and Statistical Shape Analysis*, Frontiers in Pediatrics, e-pub ahead of print, Feb. 2017
2. Dall'Asta, S. Schievano, J. L. Bruse, G. Paramasivam, C. Kaihura, D. Dunaway, and C. Lees. *Quantitative analysis of fetal facial morphology using 3D ultrasound and statistical shape modelling: a feasibility study*, American Journal of Obstetrics and Gynecology, e-pub ahead of print, Feb. 2017
3. N. Rodriguez-Florez, Ö. K. Göktekin, J. L. Bruse, A. Borghi, F. Angullia, P. G. M. Knoop, M. Tenhagen, J. L. O'Hara, M. J. Koudstaal, S. Schievano, O. Jeelani, G. James and D. Dunaway. *Quantifying the effect of corrective surgery for trigonocephaly: A non-invasive, non-ionizing method using three-dimensional handheld scanning and statistical shape modelling*, Journal of Cranio-Maxillofacial Surgery, vol. 45, no. 3, pp. 387-394, Mar. 2017

4. M. Tenhagen, J. L. Bruse, N. Rodriguez-Florez, F. Angullia, A. Borghi, M. J. Koudstaal, S. Schievano, O. Jeelani, and D. Dunaway. *Three-dimensional handheld scanning to quantify head-shape changes in spring-assisted surgery for sagittal craniosynostosis*, Journal of Craniofacial Surgery, vol. 27, no. 8, pp. 2117-2123, Nov. 2016

### **12.3 Peer reviewed conference publications directly related to this work**

1. J. L. Bruse, Y. Benzadon, K. McLeod, G. Biglino, T.-Y. Hsia, M. Sermesant, X. Pennec, A. M. Taylor, and S. Schievano. *Exploring local growth patterns in surgically reconstructed and healthy aortic arches*, 22<sup>nd</sup> Congress of the European Society of Biomechanics, 10-13 July, 2016, Lyon, France (oral)
2. J. L. Bruse, K. McLeod, E. Cervi, G. Biglino, T.-Y. Hsia, M. Sermesant, X. Pennec, A. M. Taylor, and S. Schievano. *Discovering clusters in pathologic cardiac morphology: MR-based hierarchical 3D shape clustering of surgically repaired aortic arches*, 30<sup>th</sup> International Congress and Exhibition of Computer Assisted Radiology and Surgery, 21-25 June, 2016, Heidelberg, Germany (oral)
3. J. L. Bruse, K. McLeod, G. Biglino, M. Sermesant, X. Pennec, T.-Y. Hsia, A. M. Taylor, and S. Schievano. *Shape does matter: 3-D statistical shape analysis of the aortic arch after coarctation repair reveals shape correlation with left ventricular function*, 96<sup>th</sup> Annual Meeting of the American Association for Thoracic Surgery, 14-18 May, 2016, Baltimore, MD, USA (oral)
4. J. L. Bruse, A. Khushnood, T.-Y. Hsia, A. M. Taylor, V. Muthurangu, and S. Schievano. *Exploring abnormal arch shape patterns using CMR-based hierarchical 3D shape clustering: Application to a generic imaging population of repaired coarctation of the aorta*, 24<sup>th</sup> Annual Meeting & Exhibition of the International Society for Magnetic Resonance in Medicine, 07-13 May, 2016, Singapore (electronic poster)

5. J. L. Bruse, H. N. Ntsinjana, C. Capelli, G. Biglino, K. McLeod, M. Sermesant, X. Pennec, T.-Y. Hsia, S. Schievano, and A. M. Taylor. *CMR-based 3D statistical shape modelling reveals left ventricular morphological differences between healthy controls and arterial switch operation survivors*, 19th Annual Scientific Sessions of the Society for Cardiovascular Magnetic Resonance, 27-30 January, 2016, Los Angeles, CA, USA (walking poster)
6. J. L. Bruse, E. Cervi, K. McLeod, G. Biglino, M. Sermesant, X. Pennec, A. M. Taylor, S. Schievano, and T.-Y. Hsia. *Looks do matter! Aortic arch shape following hypoplastic left heart syndrome palliation correlates with cavopulmonary physiology and outcomes*, 52<sup>nd</sup> Annual Meeting of The Society of Thoracic Surgeons, 23-27 January, 2016, Phoenix, AZ, USA (poster)
7. J. L. Bruse, K. McLeod, G. Biglino, H. N. Ntsinjana, C. Capelli, T.-Y. Hsia, M. Sermesant, X. Pennec, A. M. Taylor, and S. Schievano. *A non-parametric statistical shape model for assessment of the surgically repaired aortic arch in coarctation of the aorta: How normal is abnormal?*, 2015 International Workshop on Statistical Atlases and Computational Modeling of the Heart, MICCAI 2015, 9<sup>th</sup> October, 2015, Munich, Germany (oral; Best Paper Award)
8. J. L. Bruse, K. McLeod, G. Biglino, X. Pennec, M. Sermesant, T.-Y. Hsia, A. M. Taylor, and S. Schievano. *Making sense of streamlines: A statistical shape-modelling approach to detect flow patterns in the aorta*, 3<sup>rd</sup> CMR 4D flow workshop, 29-30 June, 2015, Oxford, UK (poster)
9. J. L. Bruse, K. McLeod, G. Biglino, E. Cervi, T.-Y. Hsia, X. Pennec, M. Sermesant, A. M. Taylor, S. Schievano. *A statistical shape atlas of the surgically reconstructed aortic arch in patients with hypoplastic left heart syndrome*, 7<sup>th</sup> World Congress of Biomechanics, 7-11 July, 2014, Boston, MA, USA (poster)
10. J. L. Bruse, K. McLeod, G. Biglino, E. Cervi, T.-Y. Hsia, X. Pennec, M. Sermesant, A. M. Taylor, S. Schievano. *Statistical shape atlas of the surgically reconstructed aortic arch in children with hypoplastic left heart syndrome*, Shape 2014 - Symposium on Statistical Shape Models & Applications, 11-13 June, 2014, Delémont, Switzerland (poster)

11. J. L. Bruse, K. McLeod, G. Biglino, E. Cervi, T.-Y. Hsia, X. Pennec, M. Sermesant, A. M. Taylor, S. Schievano. *Shape atlas of the surgically reconstructed aortic arch in patients with hypoplastic left heart syndrome*, 4<sup>th</sup> International Conference on Engineering Frontiers in Pediatric and Congenital Heart Disease, 21-22 May, 2014, Paris, France (oral, Young Investigator Award)

## 13 Copyright permissions

Page Number	Type of work	Source work	Copyright holder & year	Work out of copyright
Pages 22-38, Chapter 2	Excerpts	(Biglino et al., 2017)	© 2017 BMJ Publishing Group Ltd.	✓
Page 27	Figure	(Biglino et al., 2017)	© 2017 BMJ Publishing Group Ltd.	✓
Page 31	Figure	(Ou et al., 2004)	© 2004 Oxford University Press	✓
Pages 72-101, Chapter 4	Whole paper	(Bruse et al., 2016a)	© 2016 BMC Springer Nature	✓
Page 102-114, Chapter 5	Excerpts	(Bruse et al., 2016b)	© 2016 Springer	✓
Page 115-129, Chapter 6	Whole paper	(Bruse et al., 2017b)	© 2017 Elsevier	✓
Page 143-168, Chapter 8	Whole paper	(Bruse et al., 2017c)	© 2017 IEEE	✓